A FUNDAMENTAL STUDY OF CHAR OXIDATION KINETICS USING MODEL MATERIALS

Thesis by

Yiannis Angelo Levendis

In Partial Fulfillment of the Requirements

for the Degree of

Doctor of Philosophy

California Institute of Technology

Pasadena, California

1988

(Submitted September 28, 1987)

ΙΘΑΚΗ

Σὰ βγεῖς στὸν πηγαιμὸ γιὰ τὴν 'Ιθάκη,
νὰ εὔχεσαι νάναι μακρὺς ὁ δρόμος,
γεμάτος περιπέτειες, γεμάτος γνώσεις.
Τοὺς Λαιστρυγόνας καὶ τοὺς Κύκλωπας,
τὸν θυμωμένο Ποσειδῶνα μὴ φοβᾶσαι,
τέτοια στὸν δρόμο σου ποτέ σου δὲν θὰ βρεῖς,
ἂν μέν' ἡ σκέψις σου ὑψηλή, ἂν ἐκλεκτὴ
συγκίνησις τὸ πνεῦμα καὶ τὸ σῶμα σου ἀγγίζει.
Τοὺς Λαιστρυγόνας καὶ τοὺς Κύκλωπας,
τὸν ἄγριο Ποσειδῶνα δὲν θὰ συναντήσεις,
ἂν δὲν τοὺς κουβανεῖς μὲς στὴν ψυχή σου,
ἂν ἡ ψυχή σου δὲν τοὺς στήνει ἐμπρός σου.

Νὰ εὔχεσαι νάναι μακρὺς ὁ δρόμος.
Πολλὰ τὰ καλοκαιρινὰ πρωϊὰ νὰ εἶναι
ποὺ μὲ τί εὐχαρίστησι, μὲ τί χαρὰ
θὰ μπαίνεις σὲ λιμένας πρωτοειδωμένους·
νὰ σταματήσεις σ' ἐμπορεῖα Φοινικικά,
καὶ τὲς καλὲς πραγμάτειες ν' ἀποκτήσεις,
σεντέφια καὶ κοράλλια, κεχριμπάρια κ' ἔβενους,
καὶ ἡδονικὰ μυρωδικὰ κάθε λογῆς,
ὅσο μπορεῖς πιὸ ἄφθονα ἡδονικὰ μυρωδικά·
σὲ πόλεις Αἰγυπτιακὲς πολλὲς νὰ πᾶς,
νὰ μάθεις καὶ νὰ μάθεις ἀπ' τοὺς σπουδασμένους.

Πάντα στὸν νοῦ σου νάχεις τὴν 'Ιθάκη.
Τὸ φθάσιμον ἐκεῖ εἶν' ὁ προορισμός σου.
Ἀλλὰ μὴ βιάζεις τὸ ταξεῖδι διόλου.
Καλλίτερα χρόνια πολλὰ νὰ διαρκέσει·
καὶ γέρος πιὰ ν' ἀράξεις στὸ νησί,
πλούσιος μὲ ὅσα κέρδισες στὸν δρόμο,
μὴ προσδοκῶντας πλούτη νὰ σὲ δώσει ἡ 'Ιθάκη.

'Η 'Ιθάκη σ' ἔδωσε τ' ὡραῖο ταξεῖδι.
Χωρὶς αὐτὴν δὲν θἄβγαινες στὸν δρόμο.
Ἄλλα δὲν ἔχει νὰ σὲ δώσει πιά.

Κι ἂν πτωχικὴ τὴν βρεῖς, ἡ 'Ιθάκη δὲν σὲ γέλασε.
Ἔτσι σοφὸς ποὺ ἔγινες, μὲ τόση πεῖρα,
ἤδη θὰ τὸ κατάλαβες ἡ 'Ιθάκες τί σημαίνουν.

ITHAKA

As you set out for Ithaka
hope your road is a long one,
full of adventure, full of discovery.
Laistrygonians, Cyclops,
angry Poseidon—don't be afraid of them:
you'll never find things like that on your way
as long as you keep your thoughts raised high,
as long as a rare excitement
stirs your spirit and your body.
Laistrygonians, Cyclops,
wild Poseidon—you won't encounter them
unless you bring them along inside your soul,
unless your soul sets them up in front of you.

Hope your road is a long one.
May there be many summer mornings when,
with what pleasure, what joy,
you enter harbors you're seeing for the first time;
may you stop at Phoenician trading stations
to buy fine things,
mother of pearl and coral, amber and ebony,
sensual perfume of every kind—
as many sensual perfumes as you can;
and may you visit many Egyptian cities
to learn and go on learning from their scholars.

Keep Ithaka always in your mind.
Arriving there is what you're destined for.
But don't hurry the journey at all.
Better if it lasts for years,
so you're old by the time you reach the island,
wealthy with all you've gained on the way,
not expecting Ithaka to make you rich.

Ithaka gave you the marvelous journey.
Without her you wouldn't have set out.
She has nothing left to give you now.

And if you find her poor, Ithaka won't have fooled you.
Wise as you will have become, so full of experience,
you'll have understood by then what these Ithakas mean.

Poem of K. P. Kavafis

Written in 1911

ACKNOWLEDGEMENTS

I would like to thank my advisor Richard Flagan for his million ideas and suggestions and active participation in my project; my co-advisor George Gavalas for the many in depth discussions on a multitude of issues in my work; Michael Hoffmann for his friendship and assistance and Rolf Sabersky for his goodhearted attitude. I also gratefully acknowledge the professional advice, assistance, encouragement and frienship from my co-workers and friends: Elton Daily, Sten Samson, Pat Kohen, Joe Fontana, Glen Cass, Rich Eastvedt, Concetto Geremia, Hellmut Eckert, Bob Johnson, Larry Henling, Dimitri Papantoniou, Chris Pilinis, Bob Hously, Adel Sarofim, Leonard Montenegro, John Lee, Mark Cohen, Dale Waren, Carol Jones, Scott Northrop, Ranajit Sahu, Mike Loewenberg, Yorgos Stylianos, Hung Nguyen, Suzanne McIntyre, Brian Wong, Panos Georgopoulos, Panos Papanicolaou, Sandy Brooks, Carol Garland, Rayma Harrison, Joan Mathews, Jim Morgan, Elaine Granger, Michael Karyeaclis, J.J. Wu, Anne Staunton, Giuseppe Levendis and many others.

to my parents

ABSTRACT

A fundamental study concerning the reactivity of carbon to oxygen, under conditions pertinent to the combustion of pulverized fuel particles, was conducted. Model, man-made materials have been synthesized and produced to aid in understanding the events that occur during pyrolysis and oxidation of chars. The benefit of employing synthetic materials, along with natural fuels, was that they allowed control of the purity and composition of the chars, as well as enabled production of particles of specific physical properties relevant to modeling combustion processes.

Monodisperse, spherical, glassy carbon particles, of various sizes, were manufactured from spraying and thermally treating a carbon-yielding, highly crosslinked polymer. Various pore-forming agents were introduced and copolymerized, aiming to alter the pore structure, density and pore size distribution of the materials. Characterization of the chars, at various stages of pyrolysis and partial oxidation, employed widely varying techniques such as mercury intrusion, gas sorption, helium pycnometry, wide and small-angle scattering and nuclear magnetic resonance. Upon characterization, the influence of the physical factors on the combustion behavior was accounted for and the intrinsic reaction rates of the chars were correlated with their chemical nature. The mechanisms of pore coarsening, opening of pore restrictions and development of a large accessible pore surface area in the interior of the particles, in conjunction to the kinetics of structural ordering and graphitization, have been shown to influence critically the reactivity of chars. Furthermore, experiments with calcium treated chars revealed that the catalytic effect of mineral matter on enhancing the combustion rate is very important.

TABLE OF CONTENTS

LIST OF TABLES

LIST OF FIGURES

FIGURES: page

FIGURES/APPENDICES

CHAPTER 1

INTRODUCTION

1 *Problem Statement*

Coal is a material of vital technological interest inasmuch as it is the most abundant fossil fuel in the world. Numerous investigations on the combustion of coal have been undertaken in the last decades or even centuries, going all the way back to the Industrial Revolution. The aim of such studies was to develop rational methods for designing equipment to suit the fuel available. Today, everpressing constraints related to efficient energy utilization and enviromental concerns have necessitated a greater basic understanding of combustion and concomitant heat transfer processes.

It is well established (Mulcahy and Smith, 1969; Timothy et al., 1982; McLean et al., 1981; and Seeker et al., 1981) that burning of pulverized fuel particles occurs in two stages: evolution and combustion of volatiles and subsequent heterogeneous oxidation of the carbonaceous residue (char). Although these two stages frequently overlap (Howard and Essenhigh, 1967 and our own studies) it is the second stage that has the longest duration. It is very important, in the studies of char oxidation to determine whether the particle combustion is controlled by mass transfer or by chemical kinetics. The second case is more complex and requires determination of the chemical mechanisms involved, where in the particle they occur, and in what manner they are influenced by particular combustor operating conditions.

The present work is concerned with the kinetics of the combustion of chars. Coal chars, however, are very intricate materials by nature, derived from disintegrated and geologically altered plant tissue, and contain almost any mineral found on Earth's crust as well as entangled networks of pores. A first step in understanding the behavior of such a complicated system is to understand the behavior of a simpler system that approximates most of the properties of coal chars: synthetic, laboratory-made, model chars.

Based on the development of glassy carbons for catalyst supports, Senior and Flagan (1984) adopted such materials as model compounds for simulating char combustion in order to study the vaporization of ash that takes place at elevated temperatures. Similar materials were used in this investigation to study the reactivity of chars.

2 *Outline of the present work*

The objective of this project is to employ synthetic chars that are to a large extent free of impurities and to study the effect of various physical and chemical parameters on the oxidation kinetics. In Chapter 2 we will see how monodisperse, spherical particles were manufactured and combusted in order to study the effects of particle size variability and total surface area on the combustion behavior, given a well-described shape (sphere).

Chapter 3 outlines the methods according to which glassy carbons of variable physical and chemical properties were produced and carefully characterized with the objective to understand the development and extent of these properties in the course of pyrolysis, carbonization and partial oxidation of the materials.

Chapter 4 carries the characterization methods one step further by describing how Nuclear Magnetic Resonance techniques were employed to probe into the chemical structure of the chars. One of the findings of this particular study is that the chemical structure of the pyrolyzed synthetic chars is indeed similar to coal chars.

Chapter 5 describes modifications of an existing laboratory furnace necessary both for providing means of carbonizing and partially oxidizing quantities of material, adequate for the characterization processes, and enabling measurement of the particle surface temperature history from ignition to extinction. For the latter purpose a two-color infrared pyrometer was constructed and evaluated.

Chapter 6 is the focus of the thesis, describing the combustion behavior of the

chars and deducing their intrinsic (chemical) reactivities following the model of Smith and Tyler (1974). In Chapter 7 a more detailed evaluation of the reactivity of the chars is attempted, based on the model of Gavalas (1981).

In Chapter 8 ignition mechanisms of coal chars are investigated with pyrometry techniques, aided by the experience gained from studying the behavior of the synthetic chars.

Chapter 9 includes both the conclusions of the investigation and attempts for suggestions of future work.

As an epilogue to the present work chapter 10 is included and describes work performed mostly after the thesis defence. This chapter is concerned with studying the catalyzed kinetics of calium treated synthetic and coal chars.

The six Appendices that follow describe technical aspects of the various particle production and characterization techniques. Appendix 8 describes an independent study on characterization and reactivity of bituminus coal chars.

3 *References*

1. Gavalas, G. R. (1981). "Analysis of Char Combustion Including the Effect of Pore Enlargement." *Combustion Science and Technology* **24**, 197.

2. Howard, J. B. and Essenhigh, R. H. (1967). *Eleventh Symposium (International) on Combustion*, The Combustion Institute, 399.

3. McLean, W. J., Hardesty, D. R. and Pohl, J. H. (1981)."Direct Observations of Devolatilizing Pulverized Coal Particles in a Combustion Environment." *Eighteenth Symposium (International) on Combustion*, The Combustion Institute, 1239.

4. Mulcahy, M. F. R. and Smith I. W. (1969). "Kinetics of Combustion of Pulverized Fuel: A Review of Theory and Experiment." *Reviews of Pure and*

Applied Chemistry **19**, 81.

5. Senior, C. L. and Flagan, R. C. (1984). "Synthetic Chars for the Study of Ash Vaporization." *Twentieth Symposium (International) on Combustion*, The Combustion Institute, 921.

6. Seeker, W. R., Samuelsen, G. S., Heap, M. P. and Trolinger, J. D. (1981). "Thermal Decomposition of Pulverized Coal Particles." *Eightteenth Symposium (International) on Combustion*, The Combustion Institute, 1213.

7. Smith, I. W. and Tyler, R. J. (1974). "The Reactivity of a Porous Brown Coal Char to Oxygen between 630 and 1812 K." *Combustion Science and Technology* **9**, 87.

8. Timothy, L. D., Sarofim, A. F. and Béer, J. M. (1982). "Characteristics of Single Particle Coal Combustion." *Nineteenth Symposium (International) on Combustion*, The Combustion Institute, 1123.

CHAPTER 2

Combustion Science & Technology **53**, 117, (1987).

Combust. Sci. and Tech., 1987, Vol. 53, pp. 117–136
Photocopying permitted by license only

Combustion of Uniformly Sized Glassy Carbon Particles

YIANNIS A. LEVENDIS and RICHARD C. FLAGAN *Environmental Engineering Science, California Institute of Technology 138–78, Pasadena, California 91125*

(Received August 18, 1986; in final form January 5, 1987)

Abstract—A method for production of spherical particles of glassy carbon has been developed. The particles exhibit some differences in surface structure, but are otherwise uniform in size and shape. In drop-tube combustion experiments at wall temperatures ranging from 1200 K to 1600 K, some particles ignited and burned rapidly, reaching temperatures several hundred degrees higher than the wall temperature, while others burned as much as two orders of magnitude more slowly at temperatures only slightly higher than that of the reactor wall. In spite of these differences in ignition behavior, the particles burned with an intrinsic reaction rate that was in close agreement with the Nagle and Strickland-Constable rate for pyrolytic graphite as well as rates previously measured for carbon black and coal char oxidation. X-ray diffraction measurements show that graphitization occurs rapidly in a hot oxidizing atmosphere. Rapid annealing of the carbon structure might account for the similarity of the high temperature oxidation rates of carbons from different sources.

INTRODUCTION

Efforts to understand the kinetics of char oxidation are impeded by the variability of char chemistry and physical structure, nonuniform distribution of mineral matter, and the inability to control particle size with sufficient precision to insure that all particles will burn with the same temperature. Smith (1978) has reported that, even after correcting for the surface area of the char and the diffusional resistance of the pore structure, the apparent intrinsic reactivities of chars vary as much as four orders of magnitude at a given temperature. Some of this variability may reflect real differences in the chemical nature of the char, but particle-to-particle variability and imperfect description of the nature of the porous structure are also likely contributors.

Recent advances in the modeling of the combustion of porous chars (Gavalas, 1980; Gavalas, 1981; Simons, 1982) have the potential to reduce the uncertainty considerably. Validation of such models is dependent upon the ability to perform carefully controlled experiments that allow independent examination of the effects of the porous structure and of the intrinsic chemical structure of the char. One approach to such experimental studies is the use of model materials rather than chars produced from natural fuels. Several possibilities for such a surrogate char exist. Senior and Flagan (1984) have used glassy carbons with added minerals in the study of ash vaporization mechanisms. In that study, the synthetic chars afforded control of the mineral composition independently from the porous structure of the char. Low BET surface area chars burned with little apparent development of porosity, while the micropores of similar materials with high initial BET surface areas enlarged enough to be clearly visible at the surface of the char. The rates of silica volatillization from the two materials were widely different, primarily due to the differences in the temperatures reached by the particles during combustion in similar environments. Detailed combustion rate measurements were not made.

The synthetic char used in that study was still far from an ideal medium for the study of the rate determining factors in char oxidation. The char was produced in bulk and then pulverized for combustion studies. Even after sieving, the char particle size and shape varied widely eliminating some of the benefits of the otherwise homogeneous chars in the study of char kinetics.

An alternate approach has been applied to the production of synthetic solid fuels. By atomizing suspensions of carbon black in water using a vibrating orifice aerosol generator, Szekely and Faeth (1982) produced carbon black slurry droplets of uniform size. The problems of variable particle size are thus minimized, but the extent to which the chemical and physical structure of the carbon matrix can be varied is limited by the range of carbon black properties. The pore structure of the particle that results when a carbon black slurry droplet dries, i.e., a low density agglomerate of small spherical units differs substantially from that of coal char particles, particularly cenospheres derived from swelling coals.

In this paper, we report on the development of model fuel particles for the study of char oxidation processes. Uniformly sized, spherical, glassy carbon particles have been generated and characterized. The combustion behavior and oxidation kinetics of these particles have been examined.

EXPERIMENTAL METHODS

Particle Synthesis and Generation

The chars generated in this study can be characterized as glassy carbons. The method for their synthesis has previously been described in detail (Senior, 1984) so it will only be briefly summarized here. Furfuryl alcohol was polymerized at 60°C for 1/2 h while stirring constantly, using p-toluene sulfonic acid as a catalyst. A separatory funnel was used to separate the water that is produced during polymerization from the resultant polymer.

The production of uniformly sized glassy carbon particles involved atomization of the polymer into uniformly sized droplets that were then dried and cured to generate solid particles. Acoustic excitation of the instability of a capillary jet was used to break a fine stream of liquid into monodisperse droplets, in a manner similar to the vibrating orifice aerosol generator of Berglund and Liu (1973). The device used in the present study is illustrated in Figure 1. Liquid was fed at a constant rate through a small, 50 to 100 μm diameter, orifice using a syringe pump. A bimorph piezoelectric crystal cemented on a stainless steel membrane (75 μm thick) caused the stream to break into uniformly sized droplets. An air flow through an orifice coaxial with the droplet stream disperses the droplets and minimizes coagulation.

The polymer produced from furfuryl alcohol was too viscous for effective atomization through the orifice so the viscosity was reduced by dissolving the polymer in acetone, typically at a mass ratio of 2 to 1. Even after dissolution, the orifice rapidly plugged unless centrifugation was used to eliminate residual polymer particles from the solution. A tube was incorporated in the cavity of the aerosol generator (Figure 1 detail) to minimize sedimentation of polymer particles and impurities on the orifice, thereby further reducing orifice plugging. Using a 75 μm orifice, 150 μm solution droplets were generated. Upon drying and curing glassy carbon particles with typical diameters of 45 μm were produced.

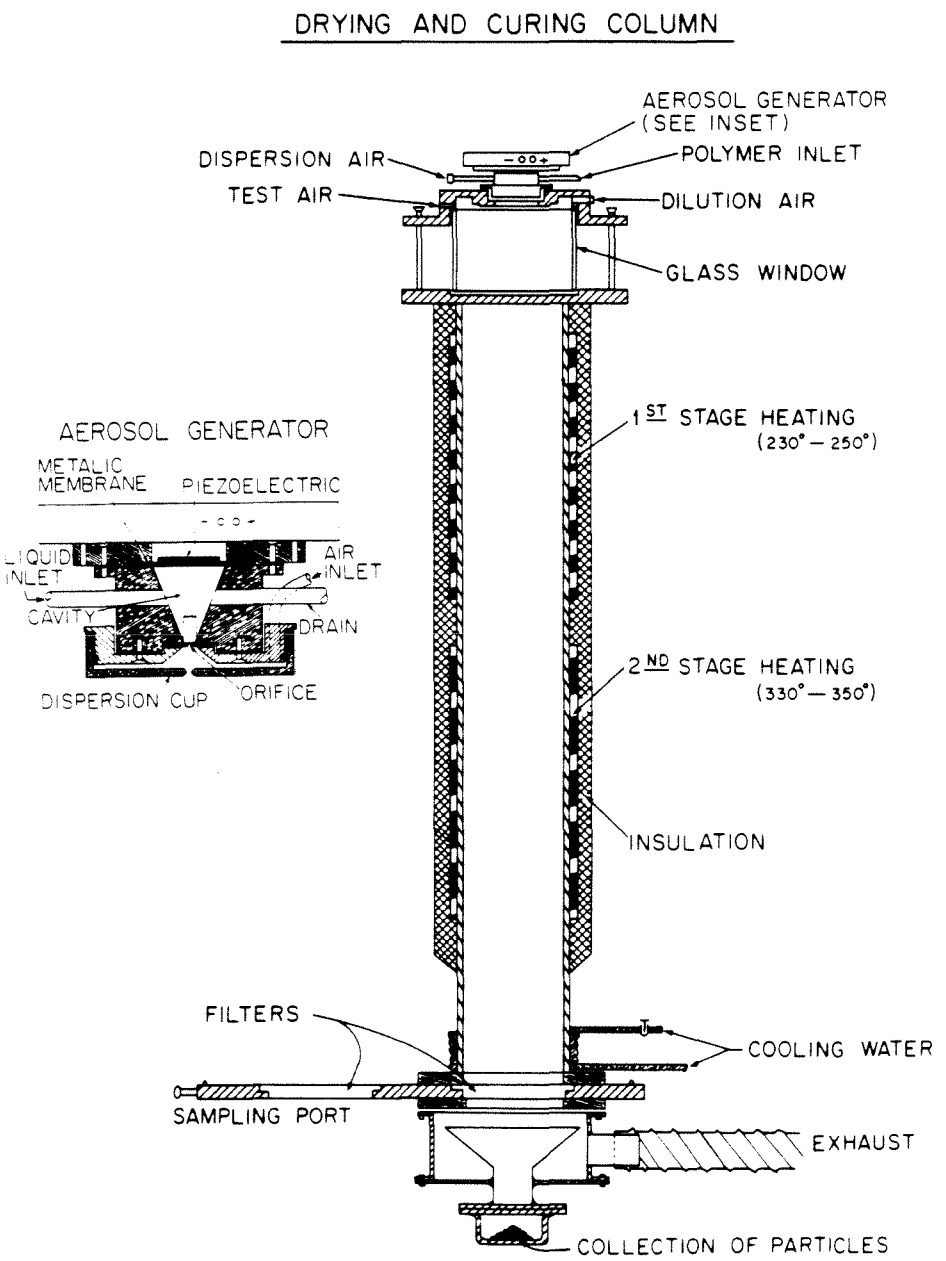

FIGURE 1 Schematic diagram of the particle generation, drying, and curing system.

Successful production of spherical glassy carbon particles required that the solvent be evaporated and the polymer cured while the particles remain entrained in a gas flow. In a previous study Senior and Flagan (1984) cured batches of approximately 40 gm of polymer in porcelain boats requiring approximately 12 h and temperatures as high as 500°C. The small droplets used in this work reduce the mass transfer resistance to solvent evaporation, so much shorter drying and curing times are possible. In the present study, the polymer droplets were dried and cured in a nitrogen flow introduced coaxially with the droplets into the column illustrated in Figure 1. The main column is a 15 cm i.d. stainless steel tube that is 1.7 m long. A short pyrex section (10 cm long) is mounted at the top of the column to facilitate observation of the jet and verification of monodisperse droplet production.

The main column was heated in two stages, with average centerline temperatures of 250 to 280°C for the upper stage and 350 to 380°C for the lower stage. In the 4 to 5 s residence time in the column the polymer dried into dense droplets and then solidified. Particles were collected by sedimentation at the bottom of the column, typically at a rate of 1 gm/hr. Microscope analysis of the collected powder revealed that, in addition to the primary particles, there were small numbers of particles with volumes 2, 3, or even 4 times the volume of the primary particles. These larger particles were again dense solid spheres, suggesting that, in spite of the dispersion of the droplet stream, there was some coagulation of the droplets. This probably occurred early in the curing column where the enlarged particles would still be sufficiently fluid to coalesce fully prior to curing.

While the collected particles were solid enough to retain their spherical shape and could be separated, they were somewhat sticky. The particles were, therefore, further cured by heating in nitrogen at 500°C for 1.5 h. Water vapor and volatile hydrocarbon evolution during this time resulted in a mass loss of 44 percent. This final curing temperature was selected based on previous work on bulk glassy

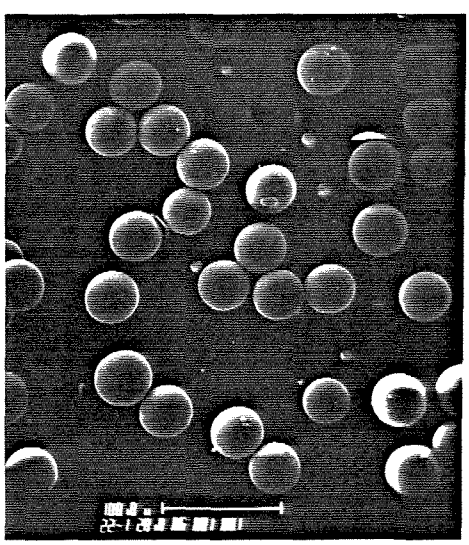

FIGURE 2 Scanning electron microscope picture of synthetic char particles after curing at 500°C. The space bar denotes 100 μm.

carbons in which it was noted that the greatest mass loss occurs between 350°C and 450°C. After this additional heat treatment, the particles were no longer sticky and could readily be separated mechanically. Singlet particles were separated from the doublets and larger particles by dry sieving in a mechanical shaker. These additional processing steps resulted in a dry powder of monodisperse, nonagglomerated, spherical glassy carbon particles as shown in Figure 2.

The cured particles contained 87.8 percent carbon and 3.25 percent hydrogen, i.e., C/H molar ratio of 2.26, as shown in Table I. The particle density was 1.435 gm/cm^3 as determined by helium displacement and 1.247 gm/cm^3 by mercury displacement, indicating a porosity of $\varepsilon = 0.16$. The BET surface area was 1.92 m^2/gm, considerably larger than the 0.24 m^2/gm surface area of the powder that was not subjected to the additional heat treatment but comparable to the 1.8 m^2/gm, measured for mineral containing glassy carbon that had been processed in bulk. (Senior, 1984) Thus, it is apparent that the curing introduced some additional porosity.

TABLE I
Properties of synthetic chars

	"As collected"	Cured at 500°C N_2	Cured at 1200°C N_2	Partially combusted air 1200°C	Partially combusted air 1000°C
C (wt %)	73.7	87.8	97.0	97.05	90.78
H (wt %)	5	3.25	1.1	0.82	1.39
O (by difference)	~ 20	9	1.9	2.1	7
Helium density (g/cm^3)	1.380	1.435	1.912	2.205	1.715
Apparent density (g/cm^3)	1.228	1.247	1.520	1.590	1.503
Total porosity		17.5%	21%	38%	22%
N_2 surface area (m^2/g)	0.24	1.956	7.286	504.7	477
Hg surface area (m^2/g)		7.195	9.134	4.617	8.622

Combustion Experiments

Studies of the combustion behavior of the glassy carbon particles were performed in an externally heated laminar flow furnace, illustrated in Figure 3. This system has been described in detail (Senior, 1984) so it will only be briefly described here. The fuel particles were introduced along the centerline of a 5 cm internal diameter alumina tube that was heated with Kanthal Super 33 molybdenum disilicide resistance heating elements, providing a hot zone of 20 cm length over which the wall temperature varied by no more than 25 K. The wall temperature was measured with thermocouples permanently installed on the outside of the tube, and using a disappearing filament optical pyrometer to measure the temperatures on the inside wall and also on the injector insulation and the flow straightener. A water cooled, gas dilution sampling probe mounted at the bottom of the hot zone was used to collect particle samples in experiments where combustion was not complete.

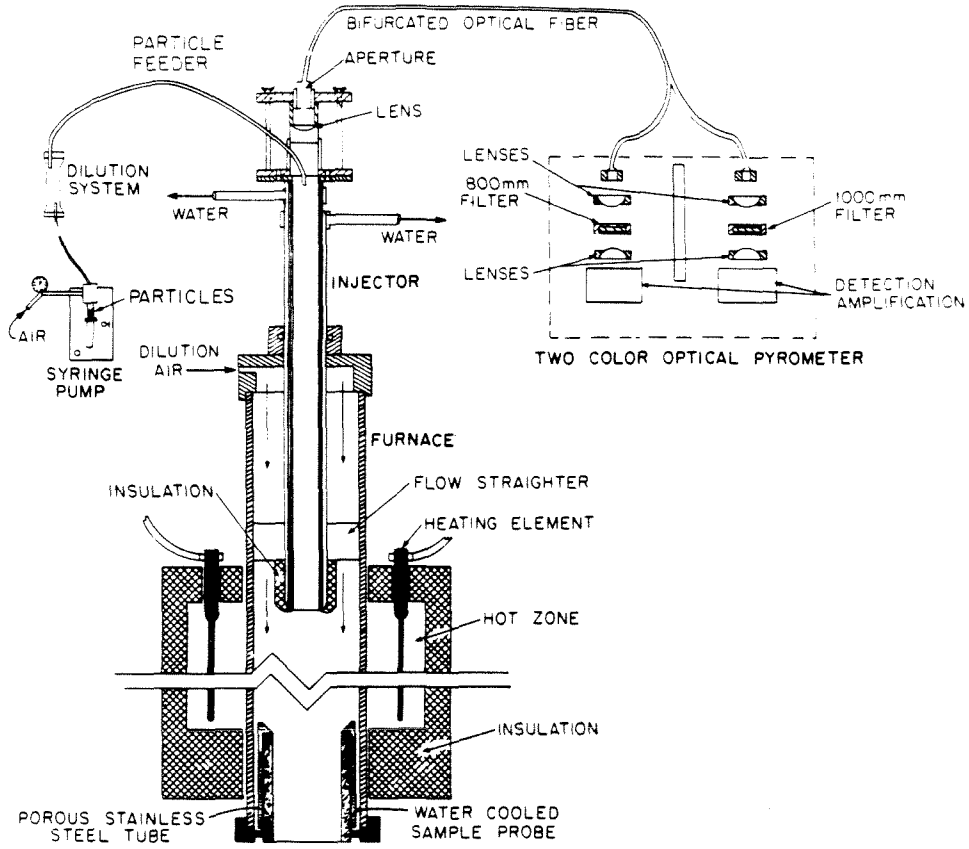

FIGURE 3 Schematic diagram of the combustion and two color optical pyrometer.

Consistent measurements of the gas temperature distribution in the reactor were obtained by two methods: (i) suction pyrometer; and (ii) bare type S thermocouple with correction for radiation being made using the known distribution of wall temperatures. Particle temperatures were measured using the two color optical pyrometer illustrated in Figure 3, viewing down the axis of the reactor in the manner of previous single particle history measurements by Timothy *et al.* (1982). A lens mounted at the top of a large bore, water-cooled injector focused the radiation emitted by burning particles onto the end of a bifurcated optical fiber bundle. The system was designed to view individual burning particles against a cold background at the bottom of the sample collection probe, thereby minimizing interference from radiation emitted from the hot reactor walls.

The particle radiation was conveyed via the bifurcated optical fiber bundle to two silicon detectors (Hamamatsu S1336-5BQ). Broad band optical filters (bandwidth 70 nm) centered about 800 nm and 1000 nm were used to select the two wavelengths for measurements. Broad band filters were selected to obtain adequate signals from small particles observed at large distance. The pyrometer was calibrated in place using a variety of sources mounted directly below the furnace; the most common being the melting point of a platinum wire (1750°C).

The particle feed system has previously been described by Senior (1984). A nominal feed rate of 1 gm/h was used in the experiments involving bulk samples. Particle pyrometry required that only one particle be in the view volume at a time in order to measure the temperature-time history of the burning particle. To feed particles at this low rate, a small boat containing a small amount of the fuel was installed in the injector line, and particles were entrained into the gas flow one at a time by lightly tapping the boat.

EXPERIMENTAL RESULTS AND DISCUSSION

The combustion of the glassy carbon particles was studied for a variety of oxygen partial pressures and wall temperatures in the laminar flow reactor. Except where noted below the particles burned were 45 μm diameter, monodisperse, glassy carbon spheres that had undergone the 500°C curing in nitrogen.

The particles collected at the bottom of the curing column were, as previously noted, virtually identical smooth spheres. After the 500°C curing, most particles showed little change in appearance but small structures appeared on the surfaces of some of the particles. This surface structure and the increase in surface area suggest that the internal structure of the particles was also altered. The changes in surface structure can be seen in Figure 4. The particle on the left has a smooth surface with only a few craters that may have formed as a result of bursting of bubbles in the char. The particle on the right has a number of small mounds on its surface. These mounds appear to have evolved from the interior of the char, possibly as a result of gas evolution forming bubbles near the particle surface. In spite of these apparent differences, the cured particles are still very uniform in size, indicating that there has not been major variation in the quantity of vapor released from different particles.

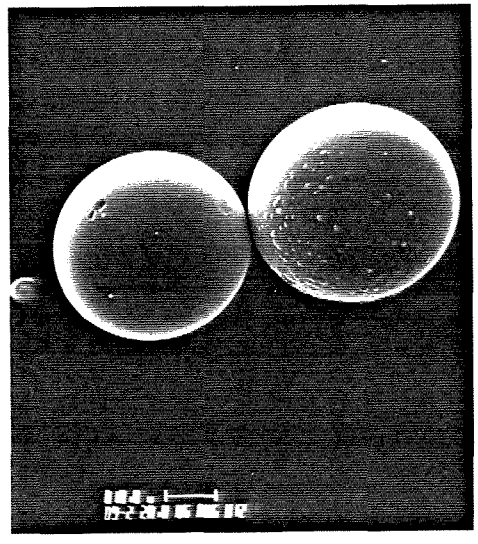

FIGURE 4 Scanning electron microscope picture of monodisperse spherical char particles cured at 500°C. The space bar denotes 10 μm.

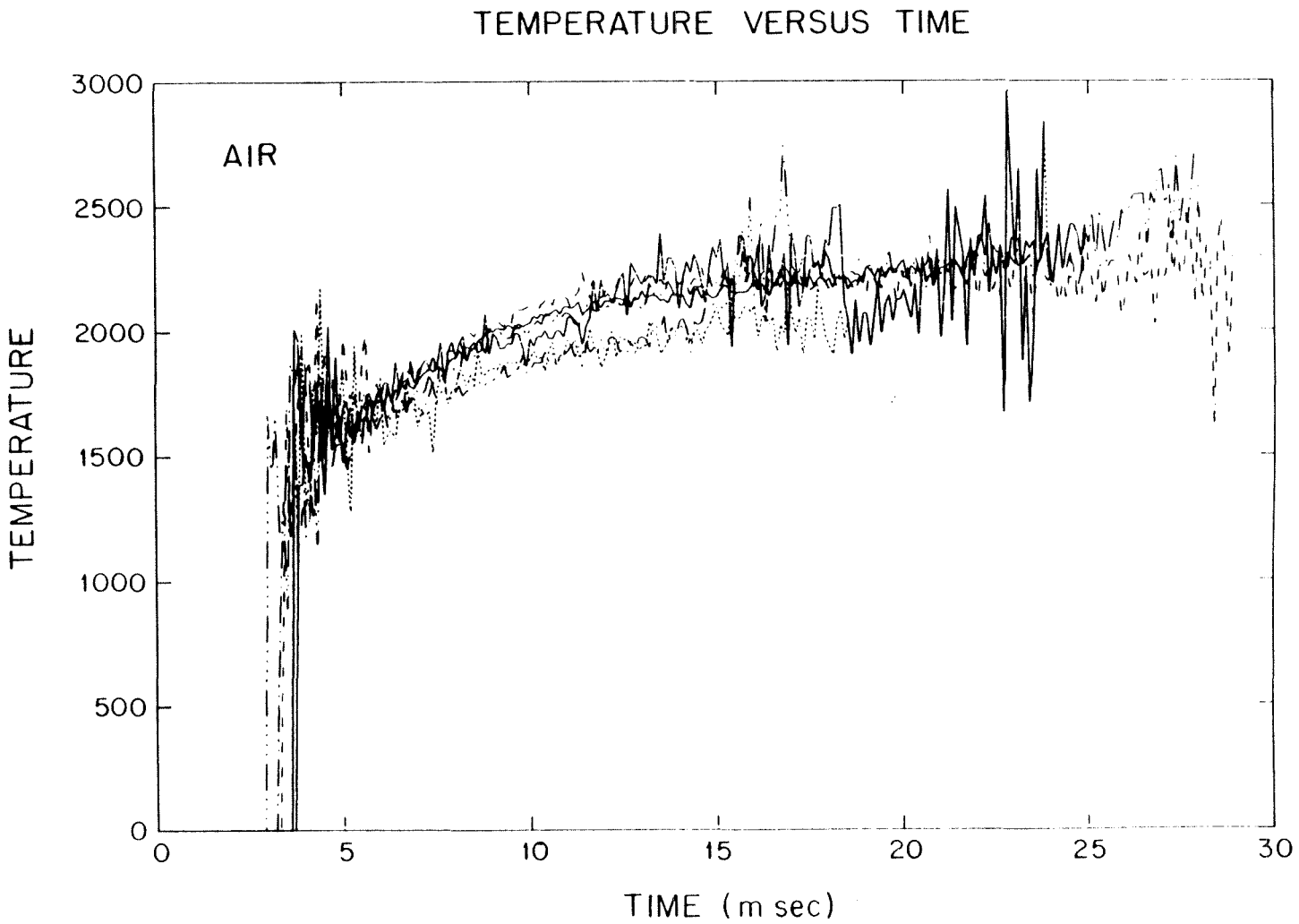

FIGURE 5 Temperature–time profiles of 45 μm spherical particles burning in air at a furnace temperature of 1500 K as measured by two color optical pyrometry.

From these photographs we see that, in spite of our efforts to produce uniform particles, the particles vary from one another in their physical structure. It should be noted, however, that the particle-to-particle variability among these glassy carbon spheres is substantially less than that of chars produced by other means. In particular, the particles have similar chemical structure and a very narrow range of sizes. The major differences among these particles appear to be in the initial internal physical structure, with some particles having open macropores near the carbon surface while others have no apparent large pores on their surfaces.

Visual observation of particles as they passed through the reactor revealed large variability in the particle combustion behavior. While some particles (estimated to be 5 to 10 percent of the total) ignited and burned in bright brief flashes, most of the particles (90 to 95 percent of the total) survived for long times, burning slowly at temperatures near the wall temperature. The fraction of the particles that burn completely is roughly equivalent to the fraction of the particles that exhibit pronounced surface structures in the SEM observations.

Several superimposed two-color optical pyrometry measurements for the individual particles burning in air with a reactor wall temperature of 1500 K are shown in Figure 5. The temperature profiles for those particles that ignite and burn completely at high temperature appear to be clustered in groups, with most of the particles following the higher temperature trend and 20 to 30 percent of the particles observed with the pyrometer burning at temperatures approximately 200 K lower. The large fluctuations seen early and late in the temperature history are attributed to the low emission intensities during those parts of the process. The total burn duration observed in these experiments was on the order of 30 ms. At the low velocities used in these experiments, this corresponds to complete combustion in the first few millimetres below the injector outlet.

One possible explanation for the brief high temperature luminosity is that volatiles released upon heating to high temperature resulted in soot formation as has been observed in coal combustion. To examine this possibility, particles were passed through the furnace in a nitrogen carrier gas with a furnace wall temperature of 1500 K. The two seconds residence at this high temperature provides adequate time for any devolatilization that is likely to occur. The devolatized particles were collected with filters. The mass loss in this process was 12 percent. Two subsequent passes of these particles through the furnace in inert atmosphere yielded mass loss of 0.8 and 0.6 percent, probably more indicative of losses in the injection and collection processes than of additional devolatilization. The devolatilized particles yielded qualitatively similar time–temperature histories to those observed for the original glassy carbon particles, demonstrating that the flashes observed with the pyrometer were the result of char oxidation rather than soot formation and burnout.

As noted above, most of the particles burned more slowly, allowing a carbonaceous residue to remain unburned at the end of the reactor hot zone. Filter samples were collected to determine the extent of conversion and the characteristics of the partially burned char after combustion of 60 and 45 μm diameter particles in air, at furnace temperatures ranging from 1300 to 1600 K. The residence time was also varied by increasing the flow rate from 2 lpm to 10 lpm. The residence times were calculated based on the gas velocity in the tube furnace integrating over the gas temperature profile and correcting for any additional particle sedimentation effects for the corresponding gas temperatures and particle sizes. The impact of the particle feeder outlet jet on the furnace flow field was negligible due to the large bore and the low gas temperatures in the water-

cooled injector. At the outlet of the injector, the feeder and the furnace gas flows were set to be approximately isokinetic. The results of these partial combustion experiments are summarized in Figure 6. Burnout was a strong function of temperature and residence time. A weak dependence on fuel feed rate was also noted, possibly the result of locally high particle concentrations near the center of the reactor, depleting the oxygen slightly as has been previously observed by Field (1967).

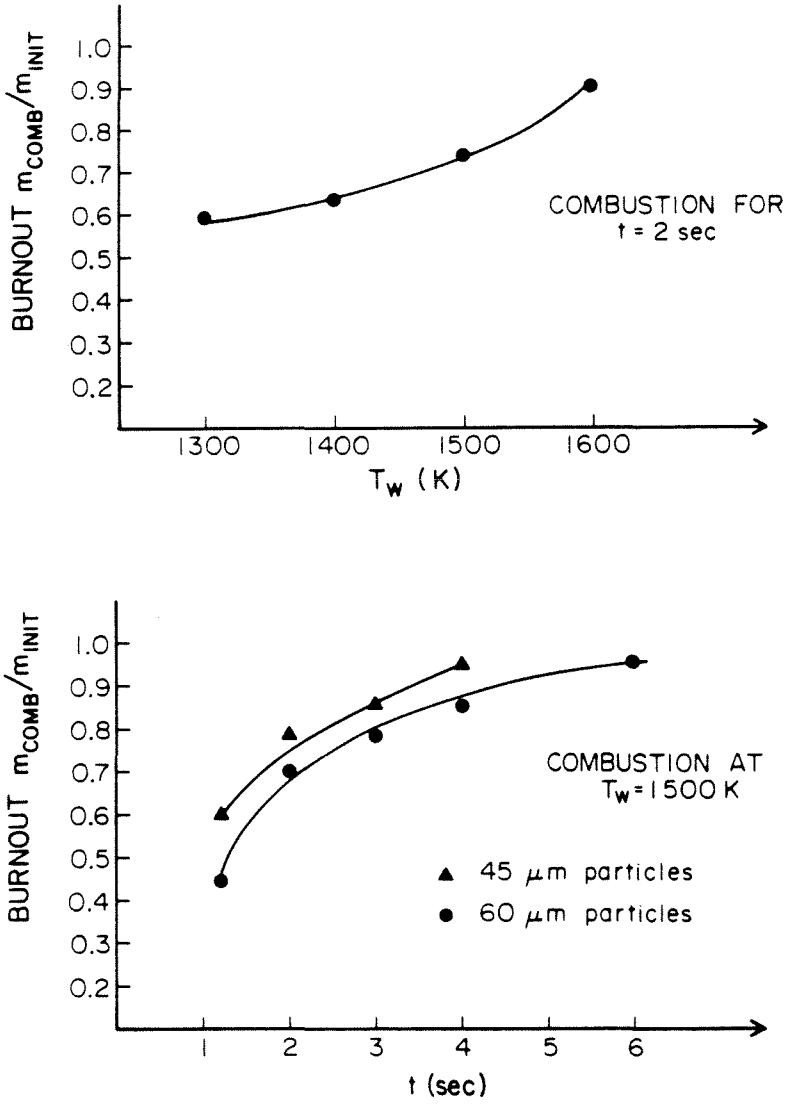

FIGURE 6 Particle burnout (residual mass over initial mass) as a function of (a) Furnace wall temperature at a fixed residence time, two seconds, for 60 μm particles. (b) Residence time at a fixed wall temperature 1500 K, 45 and 60 μm particles.

Scanning electron micrographs of particles collected at the combustor outlet provide important insights into the way these particles burn. Figure 7a shows particles that have been partially burned at a reactor temperature of 1300 K. The particles appear to have decreased in both diameter, from 45 μm to 40 μm, and apparent density, as exhibited by the open macropores on the particle surface. The particles that survive the furnace remain fairly uniform in size. Even at this low wall temperature, however, a small number of particles were observed to undergo rapid, high temperature combustion.

Further reduction in size (to about 30 μm final size) was observed in the particles that were partially burned at a reactor temperature of 1400 K but as can be seen in Figure 7b, the particles are no longer so uniform in size. The pores also became more pronounced. Combustion in a 1500 K furnace reduced the particles to about 20 μm diameter, Figure 7c, and resulted in some fragmentation. The fractured particle near the center of this picture reveals an internal structure typical of char cenospheres for this particular particle. Using mercury porosimetry and helium density measurements the total porosity of these partially combusted particles (1500 K) was estimated to be $\varepsilon = 0.38$. When the glassy carbon was burned in air in a 1600 K furnace, no char survived to be collected on the filter.

A summary of the properties of the char particles from these partial combustion experiments is presented in Table I. One of the most striking features is that the total BET area increases by more than two orders of magnitude with oxidation. Similar trends in surface area increase have been observed at the onset of oxidation of coal chars (Northrop 1986). To investigate further the development of total surface area and porosity with the extent of combustion, particles were oxidized in various oxygen partial pressures. At the completion of every oxidation run, nitrogen BET surface area was measured. Burnout was estimated from measurements of size reduction and density changes of the monodisperse particles as well as from mass loss measurements both methods being in good agreement. The variation of the BET area are plotted versus burnout in Figure 8. The total area increases rapidly with conversion from an initial 2 m^2/gm to 20 m^2/gm at 5 percent conversion (1 order of magnitude higher), reaches a maximum of about 500 m^2/gm (an increase of more than 2 orders of magnitude) at approximately 60 percent conversion and then drops to 430 m^2/gm at 90 percent conversion.

Assuming the pores to be uniformly sized and cylindrical in shape, the mean pore radius is given by (Wheeler, 1951)

$$\bar{r}_p = 2\varepsilon \frac{\tau^{1/2}}{A_G \sigma_a} \tag{1}$$

where ε is the porosity, σ_a is the apparent or mercury density (gm/cm^3), A_G is the total surface area m^2/gm and τ is the tortuosity which is usually assumed to be $\tau = 2$ (Smith, 1978). The initial pore diameter is estimated to be 400 nm decreasing to 3 nm at 60 percent conversion due to the large increase in total surface area. The appearance of the vast network of micropores after partial oxidation could result from opening of initially inaccessible pores during combustion. The existence of closed micropores in the glassy carbon is consistent with the findings of Fitzer *et al.* (1969) who, by using small-angle scattering, observed that furfuryl alcohol-based glassy carbon that had been heat treated at 500°C possessed a network of 2.5 nm diameter micropores. The slight reduction of area at high conversions has also been reported by Smith (1982) and is probably due to enlargement of pores.

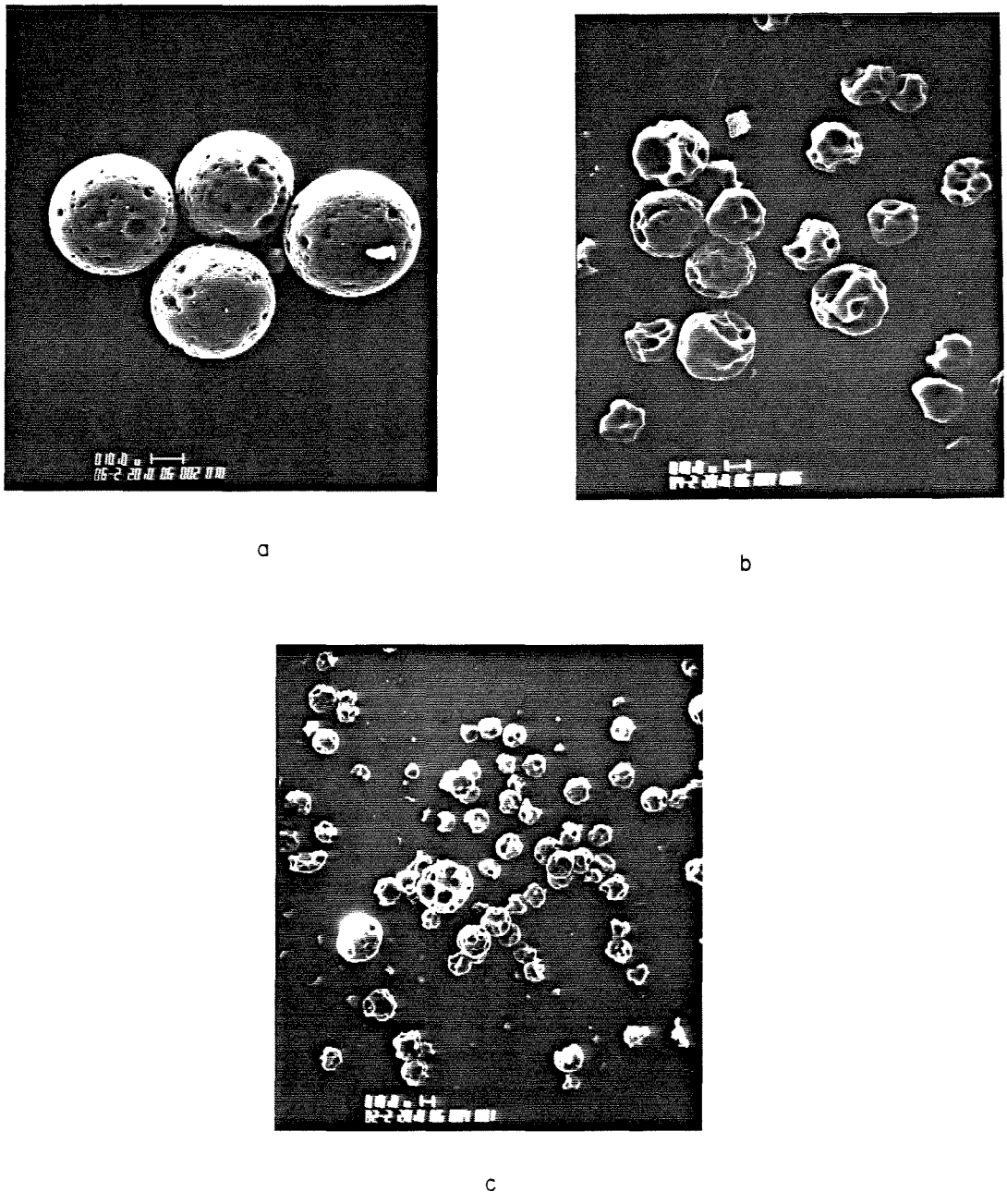

FIGURE 7 Scanning electron microscope of partially consumed synthetic chars following combustion in air at an average combustor wall temperature of (a) 1300 K, (b) 1400 K, (c) 1500 K. The space bar denotes 10 μm.

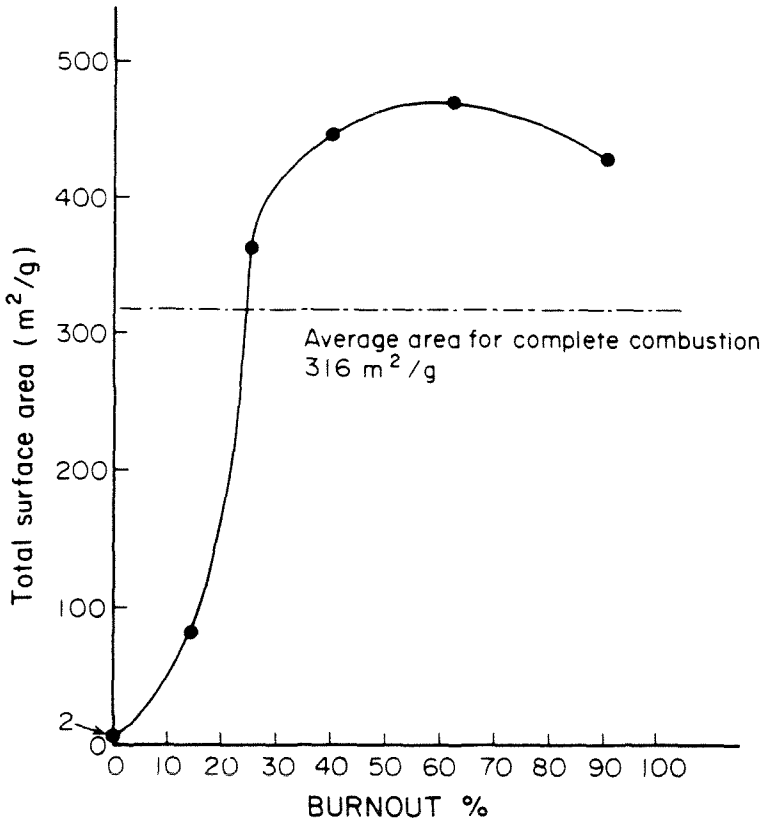

FIGURE 8 N_2 BET surface area versus burnout achieved by varying the oxygen concentration at a constant wall temperature of 1500 K.

The development of large smooth craters on the glassy carbon particle surfaces is apparent in Figure 7 and was previously observed by Senior and Flagan (1984) in the combustion of mineral-containing particles. Here, however, the complications associated with the foreign inclusions are avoided. Close examination of the partially burned particles reveals that there are a number of distinct particle types: (i) spheres with only small pits in their surfaces; (ii) more severely scalloped particles of generally smaller size; and (iii) fragments in a range of sizes. The development of these structures appears to be related to the opening of pores in the carbon as it burns, possibly due to the particle-to-particle variations in the distribution of the macropore structure near the particle surface. Similar particle-to-particle variations have been observed in combustion of semi-anthracite particles (Smith and Tyler, 1972), where some particles retained their original shape, while others developed a type of cellular or lacy structure.

X-ray powder diffraction studies using a Copper-K alpha source indicated that the "as collected" material and the cured materials at both 500 and 1200°C were completely amorphous, or glassy. Upon partial combustion, however, strong graphite diffraction lines appear. These lines become sharper and more intense with increasing reactor temperature. The most prominent line is a strong line at

3.37 Å corresponding to the 002 band of graphite, with weaker lines at 2.13 Å and 1.68 Å corresponding to 100 and 004 graphite bands respectively. The spectra produced from the present material do not contain all of the diffraction lines of highly structured pyrolytic graphite. This is consistent with previous findings (Hutcheon, 1970) that the majority of manufactured graphites consist of microcrystalline graphitic regions in an essentially amorphous matrix. Bosse and Bragg (1975) suggest that the apparent amorphous structure observed in small-angle X-ray scattering studies of glassy carbon results from X-ray scattering from pores rather than from the randomly distorted graphitic layers hypothesized by Jenkins *et al.* (1972). Furthermore, the observation that graphite appears after partial combustion is consistent with studies of graphitization reported by Noda and Inagaki (1964) which show that the presence of an oxidizing gas can catalyze the graphitization process.

CHAR OXIDATION KINETICS

The vastly different particle temperatures and burn durations observed for particles that initially appear to be so similar has yet to be explained. Are there subtle differences between the particles that lead in oxidation kinetics, or is this variation the result of differences in the ignition behavior? To explore the cause of this variability we have examined the char reaction kinetics. From measurements of the mass loss rate and of the burn duration, the apparent char oxidation rate ρ_a (mass per unit external surface area per unit time) can easily be estimated. The primary surface reaction in char oxidation is thought to be (Smith, 1982).

$$C(s) + \frac{1}{2}O_2 \rightarrow CO$$

The rate of surface reaction must equal the rate of oxygen transport to the char surface, so, for a particle of radius a,

$$\rho_a = \nu\, h_m (C_\infty - C_s) \tag{2}$$

where ν is the stoichiometric coefficient for reaction [1], h_m is the mass transfer coefficient ($h_m = D/a$ for small particle Reynold's numbers where D is the external diffusion coefficient) and C_∞ and C_s are the oxygen concentration in the free stream and at the char surface respectively. The apparent reaction rate may also be expressed in terms of the apparent nth order reactivity i.e.,

$$\rho_a = R_a C_s^n \tag{3}$$

For a spherical particle, the rate of change of the radius is:

$$\frac{da}{dt} = -\frac{\rho_a}{\sigma_a} \tag{4}$$

where σ_a is the apparent density of the particle as determined by mercury displacement. Assuming R_a to be constant over the burn duration and combining (2) and (3) to eliminate the unknown C_s, substituting into (4) and integrating between the initial and final radii, one can calculate an average apparent reaction

rate, ρ_a. | Char oxidation takes place on the carbon surface both exterior and inside the pores. We follow the approach of Smith and account for pore diffusion by using an effectiveness factor η defined as the ratio of the actual combustion rate to the rate attainable (all else being equal) if no pore diffusion existed. The reaction rate becomes:

$$\rho_a = \eta\gamma\sigma_T A_G R_i C_s{}^m \quad (\mathrm{gm/m^2 s}) \tag{5}$$

where R_i is the intrinsic reaction rate coefficient, γ the characteristic length of the particle defined as the ratio of the volume over the external surface area. A_G is the total surface area ($\mathrm{cm^2/gm}$), σ_T the true (Helium) density ($\mathrm{gm/cm^3}$), m the true reaction order and is related to the apparent order n by $m = 2n - 1$. The method for calculating the effectiveness factor is described in detail by Smith and Tyler (1974), Smith (1982). Briefly, η is a function of the Thiele (1939) modulus ϕ which depends on the intrinsic reactivity of the material R_i and is given as

$$\phi = \gamma(A_G\sigma_T R_i C_s^{m-1} D_e^{-1})^{1/2} \tag{6}$$

where D_e is the effective diffusivity through the pore structure. Since the pore size is appreciably smaller than the mean free path of oxygen molecule it is suitable to assume Knudsen diffusion. From Wheeler's model (1959) the effective diffusivity can be estimated as:

$$D_e = 9.7 \times 10^3 \bar{r}_p \left(\frac{T_p}{M}\right)^{1/2} \frac{\varepsilon}{\tau} \quad (\mathrm{cm^2/s}) \tag{7}$$

$\bar{r}_p$ is the mean pore radius, T_p is the particle temperature and M is the molecular weight of the diffusing gas. Combining e.g. (6) and (7):

$$\eta\phi^2 \frac{m+1}{2} = \gamma\rho_a \frac{m+1}{4\, D_e\, C_s}. \tag{8}$$

The terms on the right-hand side can be estimated from experimental data; thence the left-hand side is calculated and η can be found using the relations between η and $\eta\phi^2 (m+1)/2$ given by Mehta and Aris (1971). The intrinsic reaction rate is therefore:

$$\rho_i = R_i C_s{}^m \quad (\mathrm{gm/cm^2 s}) \tag{10}$$

and is the rate of reaction on pore walls in the absence of any mass transfer or pore diffusion limitations and can be calculated from Eq. (5).

For the present work the true reaction order was estimated to be 0.6 from results obtained from partial combustion experiments by measuring the relation between ρ_a and C_∞. This value is in good agreement with orders calculated for other similar graphitizing carbons (Smith, 1977). The estimated effectiveness factor ranged from 0.5 to 5×10^{-3} depending on temperature and apparent reaction rates corresponding the particles burning in regime II. The intrinsic reactivities were calculated assuming a shrinking core model of combustion and integrating the rate equation over the particle burning history to the observed burnout. Cylindrical pores of 3 nm in diameter were assumed throughout the calculation and no correction for pore enlargement with conversion was applied. The 3 nm diameter

value is also supported by pore size distribution measurements from N_2 absorption and capillary condensation for partially combusted chars using the method of Yan and Zhang (1985).

Mass loss rates were estimated from the burn duration determined by optical pyrometry for those particles that burned at high temperatures, and from the change in weight or particle size and porosity for those particles that were not completely consumed. Mean optical pyrometer temperatures were applied in both cases. Using both the two color pyrometer and observations from below the furnace with a disappearing filament brightness pyrometer, the incompletely burned particles were observed to burn very close to the wall temperature.

Because of the relatively low initial surface area of the synthetic char the combustion rates were well below the diffusion limit, and reliable kinetic rate estimates could be made. The intrinsic char oxidation rates estimates are presented in Figure 9. In addition to the data obtained in the flow reactor experiments, a low

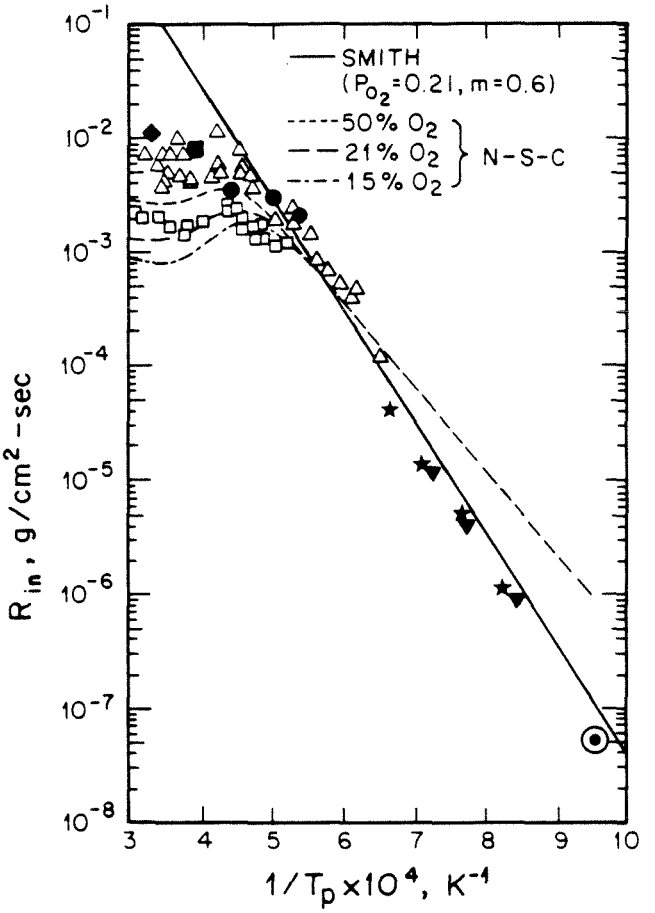

FIGURE 9 Intrinsic reactivity of the synthetic char particles as inferred from complete combustion using the two color pyrometer ●, from the partial combustion measurements of mass loss ▼ and size and density change ★ and from low temperature thermogravimetric analysis ⊙. Comparison with models of Smith (1) and Nagle/Strickland-Constable (10) (1: p_{O_2} = 0.15; 2: 0.21; 3: 0.5 atm) and data (open points □, △) of Park and Appleton (11).

temperature measurement obtained using a DuPont Thermogravimetric analyzer is shown. The uncertainty in the drop tube furnace reaction rates is estimated to be 10 to 20 percent due to the estimates of mass loss rates. There is an uncertainty of order 100 K in the particle temperatures and 4 ms in the burn duration time for the particles that burn completely. In addition there are uncertainties in estimating pore sizes and effective diffusivities. Also shown for comparison are two previously published intrinsic rate constants: (i) a rate estimated by Smith (1978) based on the study of oxidation rates of a number of chars derived from coal and other materials; and (ii) the Nagle-Strickland-Constable apparent rate determined for the combustion of pyrolytic graphite (1962). Previously reported oxidation rate measurements of carbon black particles (Park and Appleton, 1973) are shown as open points. The present results are in close agreement with the N—S—C oxidation rates at high temperatures reproducing the plateau in the rate at around 2000 K and in fair agreement with Smith's rates at lower temperatures.

At the present time, the cause of the widely varying combustion characteristics of the particles remains unclear. The consistency of the combustion kinetics with previous observations of carbon oxidation rates over a wide range of temperatures suggests that the difference is one of ignition behavior rather than of combustion rates. It seems likely that the small differences in the physical structure of the original char played a major role in the variable ignition. The small initial porosity of these synthetic chars could make particle-to-particle variations in the extent to which the vast inside micropore network is exposed to the hot oxidizing atmosphere. For the particles with limited surface exposed initially, early ignition is not achieved, allowing the rapid transformation of the amorphous carbon to a graphitic structure that is likely to be much less reactive. Such a decrease in the intrinsic reactivity could be the reason that the reaction does not accelerate so rapidly as the surface area increases later in the combustion process. Thus in the middle particle temperature range (1000–1500 K) intrinsic rates three times lower than those predicted by N—S—C have been observed. These reaction rates however are in excellent agreement with rates reported by Smith for highly purified carbons having an activation energy of 60 kcal/mol.

CONCLUSIONS

Highly uniform, spherical carbon particles were produced by acoustically excited atomization of a low viscosity solution of the polymer precursor for glassy carbon. After curing the char, the only apparent difference between particles was the appearance on the surfaces of some particles of a few small bubble-like structures or pits. In spite of the similarities of the particles, the combustion behavior varied widely from particle to particle. In drop tube combustion experiments in which the temperature histories of individual particle were followed, some particles would ignite and burn rapidly at high temperature while other particles would burn slowly at temperatures only slightly higher than that of the furnace wall and gas. The apparent combustion rate varied from particle to particle by as much as two orders of magnitude for combustion in air at reactor temperatures between 1200 K and 1500 K. Soot formation from devolatilization was ruled out as the source of the brief high temperature luminosity of some particles, by heating some char particles in nitrogen at 1500 K for 6 s prior to combustion. Like the original char, some particles ignited and burned rapidly at high temperature while others burned more slowly.

Since all particles were formed from a homogeneous solution of the same precursor, major chemical property variations seem unlikely. Estimates of the intrinsic oxidation kinetics support this hypothesis. In spite of the large range over which the overall oxidation rates varied, the intrinsic rates seem to be consistent when individual particle temperatures are taken into account. The reaction rate is in close agreement with one proposed by Nagle and Strickland-Constable (1962) for the oxidation of pyrolytic graphite, as well as with the combustion of carbon black (Park and Appleton, 1972) for high temperatures and the Smith's measurements of the kinetics of oxidation of a variety of purified carbons at medium temperatures (1978).

The cause of the particle-to-particle variability is at the present time still unclear. The consistency of the combustion kinetics with previous observations of carbon oxidation rates over a wide range of temperatures suggests that the difference is one of ignition behavior rather than of combustion rates. Due to the large activation energy for the char oxidation, the temperature increase associated with rapid reaction would accelerate the combustion dramatically.

It seems likely that the small differences in the physical structure of the original char played a major role in the variable ignition. The small initial macroporosity of these synthetic chars result in particle-to-particle variations in the surface area of the char that is initially exposed to a hot oxidizing atmosphere. The amorphous carbon, in the presence of oxygen, rapidly transforms to a graphitic structure that is likely to be much less reactive. This transformation may be the reason that the reaction does not accelerate so rapidly as the surface area increases later in the combustion process. Data on the properties of individual char particles prior to combustion experiments on the same particles would be required to test this hypothesis unambiguously. While such data are not presently available, the use of single particle levitation systems for thermogravimetric analysis, such as that developed by Spjut *et al.* (1985) should make such measurements possible in the near future.

The apparent consistency of the intrinsic high temperature oxidation kinetics of this synthetic char and a wide range of carbonaceous materials derived from other sources suggests that, if the pore microstructure of different chars is taken into account appropriately, a single rate expression for the intrinsic surface oxidation kinetics may be valid. The large increase in the surface area during combustion clearly indicates the need for pore structure models to take the changes in the porous nature of the char along the oxidation process into account. Further studies of role and evolution of the porous structure in char oxidation, both synthetic materials and chars derived from natural fuels, as well as more information about active sites are needed to determine the extent to which a single rate expression can be used to describe high temperature char oxidation of chars and to resolve these questions.

ACKNOWLEDGEMENT

This research was supported by U.S. Department of Energy University Coal Programs Grant Number DE-FG22-84PC70775. The authors gratefully acknowledge technical discussions and assistance from George Gavalas, Patrick Koen, Scott Northrop, Ranajit Sahu, and Adel Sarofim.

REFERENCES

Berglund, R. N., and Liu, B. Y. H. (1973). Generation of monodisperse aerosol standards. *Environmental Science and Technology* 7, 147.

Bose, S., and Bragg, R. M. (1975). Preprints of 2nd Carbon Conference, Baden-Baden. *Deutche Keramisc Gesellschaft*, p. 205.

Field, M. A. (1967). Rate of combustion of size-graded fractions of char from a low-rank coal between 1200 K and 2000 K. *Combustion and Flame* **13**, 237–252.

Fitzer, E., Schaefer, W., Yamada, S. (1969). The Formation of Glasslike Carbon by Pyrolysis of Polyfurfuryl Alcohol and Phenolic Resin. *Carbon* **7**, pp. 643–648.

Gavalas, G. R. (1980). A random capillary model with application to char gasification at chemically controlled rates. *AIChE Journal* **26**, 1477.

Gavalas, G. R. (1981). Analysis of char combustion including the effect of pore enlargement. *Combustion Science and Technology* **24**, 197–210.

Hutcheon, J. M. (1970). Polycrystalline Carbon and Graphite from *Modern Aspects of Graphite Technology*. L. C. F. Blackman (Ed.), Academic Press, London, p. 2

Jenkins, G. M., Kawamura, K., and Ban, L. L. (1972). *Proc. Roy. Soc.* **A327**, 501.

McEnaney, B., and Willis, M. A. (1976). Some Effects of Heat-treatment in the Range 1000–3000 K on Porosity and Reactivity in Carbon and Graphites from *High Temperature Chemistry of Inorganic and Ceramic Materials*, p. 102.

Metha, B. N., and Aris (1971). Communication on the Theory of Diffusion and Reaction—VII. The Isothermal p-th Order reaction. *Chemical Engineering Science* **26**, p. 1699.

Nagle, J., and Strickland-Constable, R. F. (1962). Oxidation of carbon between 1000–2400C. *Proceedings of the Fifth Carbon Conference*, Vol. 1, p. 154, Pergamon Press, Oxford.

Noda, T., and Inagaki, M. (1964). Effect of Gas Phase on Graphitization of Carbon. *Carbon* **2**, 127–130.

Northrop, P. S. (1986). Personal communication.

Park, C., and Appleton, J. P. (1973). Shock-tube measurement of soot oxidation rates. *Combustion and Flame* **20**, 369–379.

Senior, C. L. (1984). Submicron aerosol production during combustion of pulverized coal, Ph.D. Thesis, California Institute of Technology.

Senior, C. L. (1984). Synthetic Chars for the Study of Ash Vaporization. *Twentieth Symposium (International) on Combustion*, The Combustion Institute, Pittsburgh, PA, pp. 921–929.

Simons, G. A. (1982). The pore tree structure of porous char. *Nineteenth Symposium (International) on Combustion*, The Combustion Institute, Pittsburgh, PA, pp. 1067–1076.

Simons, G. A. (1979). Char gasification: Part I—Transport model. *Combustion Science and Technology* **20**, 107–116.

Smith, I. W., and Tyler, R. J. (1972). Internal burning of pulverized semi-anthracite: the relation between particle structure and reactivity. *Fuel* **51**, 312–321.

Smith, I. W., and Tyler, R. J. (1974). The Reactivity of a Porous Brown Coal Char to Oxygen between 630 and 1812 K. *Combustion Science and Technology* **9**, 87–94.

Smith, I. W. (1978). The intrinsic reactivity of carbons to oxygen. *Fuel* **57**, 409.

Smith, I. W. (1982). Combustion Rates of Coal Chars: A Review. *Nineteenth Symposium (International) on Combustion*, The Combustion Institute, Pittsburg, PA, pp. 1045–1065.

Spjut, R. E., Sarofim, A. F., and Longwell, J. P. (1985). Laser Heating and Particle Temperature Measurement in an Electrodynamic Balance. *Langmuir* **1**, 355.

Szekely, G. A., Jr., and Faeth, G. M. (1982). Reaction of carbon black slurry agglomerates in combustion gases. *Nineteenth Symposium (International) on Combustion*, The Combustion Institute, Pittsburgh, PA, pp. 1077–1085.

Thiele, E. W. (1939). Relation between Catalytic Activity and Size of the Particle. *Ind. Eng. Chem.* **31**, p. 916.

Timothy, L. D., Sarofim, A. F., and Beer, J. M. (1982). Characteristics of single particle coal combustion. *Nineteenth Symposium (International) on Combustion*, The Combustion Institute, Pittsburgh, PA, pp. 1123–1130.

Yan, J., and Zhang, Q. (1985). Pore Structure Analysis of Porous Particles by Equivalent Model, *Particle Characterization* **3**, 20–25.

Wheeler, A. (1951). Reaction Rates and Selectivity in Catalyst Pores, *Advances in Catalysis* **3**, 249.

NOTATION

A_G	specific total surface area	cm^2/gm
a	particle radius	cm
C_∞	oxygen concentration in bulk gas	gm/cm^3
C_s	oxygen concentration on the outer particle surface	gm/cm^3

D	external diffusion coefficient	cm^2/sec
D_e	effective diffusion coefficient	cm^2/sec
h_m	mass transfer coefficient—carbon oxide flux	cm/s
M	molecular weight	g/g mol
m	true order of reaction	
n	apparent order of reaction	
R_a	rate coefficient per unit external surface area	$g/cm^2/s$
R_i	intrinsic rate coefficient	$g/cm^2/s$
$\bar{r}_p$	mean pore radius	cm
T_p	particle temperature	K
γ	characteristic dimension of particle	cm
ε	porosity	
η	effectiveness factor	
ν	stoichiometric coefficient	
ρ_a	reaction rate per unit external area	$g/cm^2/s$
ρ_i	intrinsic reaction rate	$g/cm^2/s$
σ_a	apparent (mercury) density	g/cm^3
σ_T	true (helium) density	g/cm^3
τ	tortuosity of pores	
ϕ	Thiele modulus	

CHAPTER 3

Submitted to *Carbon*

Synthesis, Formation and Characterization of Glassy Carbon Spheres of Various Properties

Yiannis A. Levendis and Richard C. Flagan
Environmental Engineering Science 138-78
California Institute of Technology
Pasadena, California 91125

Abstract

A method of producing glassy carbons of variable physical and chemical properties has been developed. Production times are very brief, in the order of seconds to minutes. The particles are spheres of uniform size made out of a carbon-yielding polymer and heat-treated to 800 K, with sizes ranging from a few microns to several tens of microns. The porosity, the pore size distribution and the surface areas of these chars are controlled by the addition of various liquid and solid pore-forming agents. Both solid and hollow spheres can be produced depending on the nature and the concentration of the pore former. The surface areas vary by two orders of magnitude, the porosities vary by a factor of five, and the pore size distributions include both micro and transitional pores. The heat treatment temperature, in the range of 800 to 1600 K, as well as the degree of oxidation strongly influence all of the glassy carbon properties. As the temperature rises, the size and the volume of the micropores increase at the expense of the skeletal volume. The size distribution of the micropores becomes more uniform and their shapes more rounded. The presence of an oxidizer gas, at elevated temperatures, opens and enlarges existing porosity and catalyzes multiphase graphitization of many of the copolymer chars.

1 Introduction

Glassy or vitreous carbons are materials of scientific and technological interest. Their name is due to their high luster and fracture properties and they are produced by pyrolysis and heat treatment of thermosetting organic polymers. It has been shown[1] that these glasslike carbons can be formed from a variety of starting polymer materials, regardless of chemical composition as long as they are highly crosslinked. The microstructure of glassy carbons contains a significant volume of micropores, which contributes to their molecular sieve properties and high adsorption capacity. Their large total surface areas, thermal stability under inert conditions, and high degree of purity has rendered them excellent supports for metallic catalysts [2,3,4]. The porous microstructure of glassy carbons can be controlled during synthesis [3,5,6,7]. Other attributes of the glassy carbons include their good electrical conductivity, hardness and resistance to corrosion.

The synthesis of bulk glassy carbons is a time consuming process due to the slow curing required to generate the solid carbon from the polymeric precursor. In a previous study[8], we have demonstrated that small polymer droplets can be cured in a matter of seconds in an entrained flow reactor operated at temperatures as low as 350°. Uniformly sized, spherical particles were produced and used as coal char surrogates for studies of combustion kinetics. The uniform particle size eliminates ambiguities in data interpretation since the external mass transfer resistances are the same for all particles. Uniformly sized particles would also be valuable for the study of catalytic processes for the same reasons. The particles synthesized for that study were microporous, with no apparent meso- or macropores. For use as catalyst supports, however, increased porosity and larger pore sizes are often needed.

In this paper, we report on methods for the control of the porous microstructure of monodisperse, spherical, glassy carbon particles. Particles ranging in size from a few microns in diameter to more than 200 microns have been generated using

the atomizing method of Levendis and Flagan [8]. The pore size distribution is controlled by addition of a variety of liquid and solid pore-forming agents and by the degree of activation through partial oxidation of the carbons.

2 Experimental Methods

All of the chars produced for this work had a common glassy carbon matrix. They were formed from a partially polymerized carbon-yielding binder, pore-forming agents and a volatile solvent that served as a mixing agent and also facilitated flow and atomization. The binder was furfuryl alcohol and was partially polymerized at 60° C under constant stirring, using p-toluene sulfonic acid as a catalyst. The resulting polymer was water-washed and thinned with acetone at a typical mixing ratio of two parts of acetone to one part of polymer by weight to lower its viscosity.

The pore-formers were liquid or solid materials that either dissolve or suspend in the acetone-polymer mixture. The materials that dissolve in the mixture were the following organics: decalin, glycerol, polyethylene glycol, tannic acid, benzoic acid, isopropyl alcohol and triton X-100 (isoctyl phenoxy polyethoxy ethanol). The reasoning behind using such materials is that, due to their high boiling or decomposition temperatures, they may be expected to evolve from the polymer when it is at the verge of solidification, thereby creating a network of pores. The foundations of this technique were laid by Hucke[5], who used colloidal suspensions of the pore-forming agent. Here, however, the presence of acetone and the constraints associated with the subsequent atomization limit the choice of pore formers to those that dissolve in the solvent.

A different way to create porosity is to suspend submicron-sized solid particles (e.g., carbon black) in the polymer/acetone mixture[6,10]. The solid used in the present study was carbon black having an average particle size of 22 nm. To delay

the agglomeration and settling of the carbon black in the mixture, Triton X-100 was used as a dispersion agent. A general overview of the technique is shown in Fig. 1.

2.1 Particle Generation and Curing

The polymer-acetone-pore-former mixtures were poured into syringes and, under constant agitation, were fed through a syringe pump to an aerosol generator. The mixtures were subsequently sprayed into the thermal reactor, shown in Fig. 2, where the solvent was evaporated and the residue was solidified. To generate uniformly sized particles, the syringe pump fed the liquid through a small orifice mounted at the bottom of the aerosol generator as shown in Fig. 2. A bimorph piezoelectric crystal cemented on a thin (75μm) metal membrane was used to excite instabilities in the capillary jet eminating from the orifice, thereby causing the stream to break up into uniformly sized droplets[11]. Orifices ranging from 50μm to 100μm in diameter were used depending on the desired final particle size and the mixture being atomized. Carbon black containing mixtures required larger orifices to prevent plugging. A small tube was inserted in the cavity to reduce the likelihood of plugging by polymer particles or carbon black agglomerates that would otherwise settle on the orifice. The operating frequency was adjusted to control particle size and to ensure that monodisperse particles would be generated. A small nitrogen jet was used to deflect the particle stream in order to verify monodispersivity[11]. The atomizer was mounted at the top of a thermal reactor (curing column) and a short pyrex window was inserted to facilitate observation of this testing. After the optimal frequency was selected a nitrogen flow was used to disperse the droplets through an additional coaxial orifice and minimize coagulation. A second nitrogen stream was used to dilute the flow and regulate the residence time in the reactor.

The thermal reactor was a 15 cm i.d. stainless steel tube 1.7 m long. The column

was externally heated in three stages as shown in Fig. 2. The maximum centerline temperature of 650 K occurred at the middle section of the column. A large orifice (2 cm in diameter) was inserted below the observation window and above the curing column to prevent the buoyant hot gases of the reactor from entering the cooler upper space and creating turbulence that would disturb the jet.

The collection stage at the bottom of the column incorporates a virtual impactor designed to collect particles bigger than 5 μm with a 75% efficiency. Thus, any small particles produced during atomization (satellites) or during curing by homogeneous nucleation were not collected. A sampling port was also incorporated to verify production of monodisperse aerosol. The residence time of the particles in the reactor was approximately 4 sec. Production rates varied between 5 g/hr and a fraction of a gram per hour, depending upon the size of the particles produced. The collected particles were solid spheres but were somewhat sticky, so they were further cured in nitrogen at 800 K for one hour in porcelain boats in a muffle-tube furnace. This heat treatment resulted in a loss of 40% of the mass of the particles because of devolatilization. The heat treatment temperature was selected on the basis of previous work on glassy carbons, which shows that most of the volatile loss occurs between 600 and 700 K[1]. The resulting dry particles were subsequently sieved to remove any doublets and triplets, generated by coagulation and fusion of liquid droplets in the drying column. The resulting monodisperse spheres were stored in dessicators.

Some of the materials were activated by partial oxidation either at high temperatures in the externally heated drop tube furnace described in[8], or at lower temperatures ($T < 1000$ K) in a muffle-tube furnace. Partially oxidized particles from the drop tube furnace were collected on glass fiber filters.

2.2 Particle Characterization

Total surface areas were measured by adsorption of nitrogen at 77 K and carbon dioxide at room temperature, using a rapid pseudo-static technique of deriving gas adsorption isotherms by continous addition of adsorbate gas to the sample[12]. The apparatus was calibrated using carbon and alumina standards. Sample quantities of at least 0.1 g were used to minimize uncertainties.

Apparent densities, porosities, pore volume, and pore surface distributions were determined by mercury intrusion, using a *Quantachrome Autoscan-60* porosimeter capable of achieving maximum pressures of 230 MPa corresponding to penetration into 5.5 nm diameter pores. Distributions of smaller pores were determined from multilayer adsorption and capillary condensation of nitrogen, using the method of Yan and Zhang[13] to calculate the pore size distribution. True or helium densities were determined on vacuum-dried samples by helium displacement at room temperature.

Unreacted and partially burned particles were examined by both optical and scanning electron microscopy (SEM). The resolution of the scanning electron microscope (*ETEC Autoscan*) was 7 nm and the operating voltage 20 kV. Transmission electron microscopy (TEM) studies were conducted with a *Phillips EM 430* microscope. Several samples were cast in epoxy and then ground and polished in a *Minimet* automatic grinder in order to facilitate optical examination of the interior of the particles.

Elemental analysis (C, H, N, O) was performed by combusting a few milligrams of sample in a *Perkin Elmer* analyzer. Combustion was performed in oxygen at 1173 K and subsequent reduction at 973 K in the presence of a copper catalyst. Sulfur determination was performed in a *Leco* furnace by burning the sample at 1450 K.

Wide-angle x-ray diffraction spectra were obtained by means of a Guinier powder

camera. A focusing quartz monocromator was used to filter CuKα radiation at 45 kV and 25 mA. The sample thickness was approximately 0.20 mm. Diffraction line position was measured using a high accuracy vernier, and line intensity profiles were measured with an *Ultrascan XL* Laser Densitometer.

Small-angle x-ray scattering (SAXS) data was recorded, from 0.25° to 10°, using *Siemens D500/501* Diffractometer. CuKα radiation at 40 kV 30 mA was used in conjunction with a Kβ Nickel filter. The slits were arranged to approximate an infinite slit geometry condition. The detector was a scintillation counter and data was recorded with an IBM microcomputer. The samples were spread on a thin low-absorption carbon film and the sample thickness was kept constant for all runs at a value approximately equal to $1/\mu = 966\mu$m, where μ is the linear absorption coefficient for carbon. Corrections were made to account for the geometry of the system, polarization and absorption effects, air scattering and slit height. Background corrections were also made.

3 Experimental Results and Discussion

3.1 Microscopy and Sorption Studies

3.1.1 *Particle size and density*

While a range of particle sizes have been generated by the methods described above, most of the characterization studies were performed with a single particle size, 45 μm, to facilitate comparison of the different materials. Scanning electron micrographs of groups of plain polymer particles 45 μm in diameter are shown in Fig. 3. Cenospheres, i.e., hollow spheres can be produced with high concentration of tannic acid pore former or pure tannic acid alone. Some of these cenospheres, shown in Fig. 4a, have blowholes caused the abrupt release of gases contained within the particle during heat treatment. Highly porous particles were created using various

concentrations of carbon black. In Fig. 4b a particle containing 25% carbon black (as measured in the mixture precursor) is shown. The most striking feature of these particles is the rough porous surface, in contrast with the smooth surfaces of all the other particles produced. Partial combustion usually altered the particle morphology by creating pits and craters as well as enlargement of surface pores. A plain polymer particle that was oxidized in air at 1500 K to approximately 40% burnout is shown in Fig. 5a. Polished sections of partially burned particles, Fig. 5b, show a dense interior that contains only pores with sizes less than 7 nm (resolution of the SEM instrument). TEM micrographs of thin chips of particles, at a magnification where the atomic layers can be resolved, are shown in Fig. 6. In Figs. 6a and 6b plain polymer chars carbonized at 1500 K and partially combusted in air at the same temperature, respectively, are shown.

Apparent densities, σ_a, were determined by low pressure (101 kPa) mercury porosimetry and signify the density of the solid plus any pores smaller than 7 μm. Mercury densities, σ_{Hg}, were measured by high pressure mercury intrusion and represent the density of the solid plus any pores with radii less than 32 Å. The helium density, σ_{He}, is considered to be approximately the true density of the solid, since micropore openings as small as 4 Å are accessible to helium. The above densities along with associated porosities are presented in Table Ia. Total macro and transitional pore volumes, as measured from mercury penetration, are also tabulated. The percentages given in this table, as well as in the text, for the content of the pore formers in the chars correspond to mass fractions in the polymer precursor - pore former mix. Density and porosity data for some partially burned materials is shown in Table Ib. The oxidized materials have higher porosities and helium densities, but their apparent densities are similar to the ones of the starting materials.

3.1.2 *Surface areas*

Surface areas, A_G, measured by nitrogen adsorption at 77 K after the 800 K heat treatment of the chars in nitrogen, are shown in Table II. The initial area of the plain polymer char was 2 m^2/g. Except for decalin and isopropyl alcohol, the effect of the additives was to increase the area. Addition of 18% PEG created an initial area of 79 m^2/g while addition of 25% carbon black increased the area to 184 m^2/g. Upon partial combustion, the area increased dramatically. Figure 7 shows the variation of the surface area of the plain polymer char with burnout. From an initial value of 2 m^2/g, the area of this char increased by more than two orders of magnitude to 480 m^2/g after 60% combustion. From this last value of surface area and the measured porosity $\epsilon = 0.3$, an average pore radius was calculated to be 14 Å using Wheeler's model[14] :

$$\bar{r}_p = \frac{2\epsilon}{A_G \sigma_A}(r.f)(1-\epsilon), \qquad (1)$$

where ϵ is the total porosity and (r.f) is a roughness factor, here taken as 2 after Wheeler.

The areas of the chars made with other copolymer additives follow trends similar to the plain polymer chars, increasing to high values after partial combustion. In particular, addition of Triton X-100 and glycerol causes a two fold increase in surface area, over that of the plain polymer. SAXS analysis of the unburned Triton/glycerol copolymer revealed an unusually high concentration of extremely fine pores which enlarged upon combustion at elevated temperatures. The reduction of the average pore size of the starting material made by the addition of Triton X-100 was previously observed by Moreno-Castilla[3] for chars containing transitional pores only. Addition of PEG also increased the extent of microporosity, as indicated by SAXS and the increase in BET area with oxidation, but to a lesser amount. The high initial surface area of the carbon black impregnated particles prior to oxidation (184 m^2/g) cannot be explained by the presence of carbon black particles alone,

since their surface area is 113 m^2/g (all external). 25% carbon black, by weight in the polymer, can contribute only 30 m^2/g. It appears, therefore, the higher area is due to pores or microcracks that develop in the polymer matrix around the carbon black spheres during carbonization, as a result of thermally induced stresses. To investigate this point further, materials containing various concentrations of carbon blacks were generated. Nitrogen BET and mercury surface areas as well as mercury-penetrated pore volumes are presented in Table III. The mercury surface area is calculated from the volume measurements as follows:

$$A_{Hg} = \int (\frac{2dV_{Hg}}{rdr}) dr. \tag{2}$$

The results indicate that both the total pore volume accessible to mercury and the mercury surface area increase with carbon black content because of augmented transitional porosity. The BET area increases with carbon black concentration, reaches a maximum at around 17% carbon black, and then decreases again. This behavior suggests that the polymeric carbon itself is responsible for most of these high areas. Initially, the increasing concentration of carbon black inclusions stresses the matrix more and more, thereby creating accessible porosity. Once a threshold concentration is reached, however, the displacement of the polymer matrix by the carbon black dominates, and the BET area falls.

3.1.3 *Pore size distribution*

Pore size distributions were measured from mercury intrusion plots assuming cylindrical pores and using the Washburn Equation[16]

$$r_p = \frac{-2\sigma cos\alpha}{P}, \tag{3}$$

where σ is the surface tension of mercury and α is the contact angle, taken to be 140°. For distributions of pores having diameters less than 64 Å but larger than 15 Å, nitrogen adsorption and capillary condensation techniques were used. The

results indicate that all of the chars produced, with the exception of the one containing carbon black, have porosity consisting mainly of micropores. The average radius of these micropores, deduced from eq. (1) for partially burned materials, varies from 14 Å for the char that contains 20% glycerol to 9 Å for the char containing 18% tannic acid. The char that contained carbon black particles and the dispersing agent triton X-100 had a bimodal pore size distribution consisting of micropores in the range of 10-13 Å and transitional pores that exhibit a clear peak at 75 Å radius; the latter was observed in distributions obtained by both mercury intrusion and nitrogen adsorption. The transitional pores appear to have been produced by structural imperfections induced in the carbon binder by the carbon black inclusions. Their diameters are roughly the same size as the carbon black spheres. Pore size distributions for the plain polymer char and the one containing 25% carbon black and 2% triton X-100 are shown in Fig. 8.

3.1.4 *Compressibility of Glassy Carbons*

It has been suggested that carbonaceous materials are compressible at the high pressures encountered in the mercury porosimeter[17]. When the intruded volume increases linearly with pressure, compressibility of the samples is a likely cause. It is not certain to what extent the present materials are compressible, since the intrusion-pressure relationships (after making the appropriate corrections for the instrument) do not exhibit an extended linear range. The best approximation to linearity occurs at the middle range pressures 700-1500 atm and from this region a coefficient of compressibility is estimated to be between 2×10^{-8} m^2/N for plain polymer and 4×10^{-9} m^2/N for the material containing glycerol and Triton. The compressibility of the partially burned materials is roughly an order of magnitude smaller than that of the starting materials. Partially burned samples of the tannic acid containing materials behave differently; their compressibility decreases with

tannic acid mass fraction and tends to zero for mass fractions higher than 18%. These materials, however, undergo plastic deformation and pore crushing as indicated by a large ireversible intrusion that occurs abruptly when the pressure reaches approximately 2100 atm.

3.1.5 *Elemental analysis*

Carbon and hydrogen contents and carbon-to-hydrogen ratios for the chars are given in Table IV. The remaining mass is mostly oxygen which, however, was not measured directly in this study. The amount of carbon in the copolymer formed from tannic acid decreases with increasing amount of tannic acid, since pure tannic acid chars are shown to have a much lower carbon content than the plain polymer. The oxygen content of the heat-treated tannic acid appears to be very large ($\approx$20%) as might be anticipated for an oxygen rich starting material ($C_{76}H_{52}O_{46}$). Upon partial combustion, of the materials most of the oxygen and hydrogen leave, and the carbon concentrations assume very high values. The nitrogen content in the particles was very low, below 0.25%. Sulfur was introduced in the particles by the polymerization catalyst (p-toluene sulfonic acid), but Leco analysis indicated that sulfur levels were quite low (0.08%).

3.2 X-Ray Diffraction

Glassy carbons are classified as "hard" carbons since they only partially graphitize as a result of the isotropy, fine scale, and high degree of imperfection of their structure. Perret and Ruland[18] and Jenkins et al.[19] have proposed a model for the structure of glassy carbons. According to this model the glassy carbons consist of randomly distorted, graphitic layers in interwined ribbon-like arrays. The end-to-end distances of these molecules are considerably larger than the crystallite size, L_a, values estimated from X-ray diffraction line broadening. The graphitization

kinetics of glassy carbons have been shown by Fischbach[20] to be rather slow, and a true graphitic structure is never reached even at heat treating temperatures in excess of 3000 K. The interlayer spacing $\bar{d}$ decreases from 4.0 Å at 1000 K to a limiting value of 3.43 Å at 3500 K. These spacings are significantly larger than the 3.354 Å spacing of the three-dimensionally ordered graphite. If graphitization involves joining small layer planes together to form larger ones and then rotating and translating these larger planes to appropriate stacking registry (alternate layers are laterally displaced) with neighboring planes and, at the same time, eliminating defects in the planes[20], then the long molecules and the high porosity of glassy carbons will limit the extend of crystallization since extensive reorganization will be required. TEM studies show crystallization of the materials at 3000 K in the form of randomly distorted turbostratic layers[19].

The x-ray diffraction spectra of glassy and other disordered carbons typically contain *(002)* peaks that result from stacks of parallel layer planes, and *(hk)* peaks that result from the two-dimensional structure within the individual layer plane segments[20]. Three-dimensional peaks are rarely present, indicating minimal or nonexistent stacking order of parallel layers. Even after heat treatment for 2 s at temperatures as high as 1600 K the diffraction spectra for the materials produced in the present study show no signs of graphitization, as expected. At small angles there is a very strong scattering region, which is attributed to x-ray scattering by the extensive pore network[18]. At larger angles there are three broad peaks corresponding to $\bar{d}_{002}$, $\bar{d}_{100}$ and $\bar{d}_{110}$ spacings. These peaks become slightly sharper and shift to higher angles with heat treatment temperature, as shown in Fig. 9. Table V shows the average interlayer spacings and crystallite sizes, derived assuming disorganized graphitic structures[21]: basal plane dimension L_a, and height L_c, normal to the *(002)* planes calculated using the Scherrer-type modified Warren equation[22] for line broadening at 3/4 of the peak height. The observed line breadth

was corrected for instrumental line broadening[21,23], although, for the very broad peaks in these materials, this correction is almost negligible.

The interlayer spacings decrease and the crystallite dimensions increase with heat treatment. The interlayer spacings ($\bar{d}_{002}$) are rather large when compared to to the average interlayer spacing of 3.364 Åtypically observed for "turbostratic" carbons, i.e, carbons with graphite layers randomly stacked. The apparent crystallite dimensions are also rather small in comparison to those of graphitizing carbons. These low values, however, are to be expected, given the moderate heat treatment temperatures and short time durations of the present experiments. Moreover, the significance of L_a and L_c is ambigous. In particular, the basal plane dimension L_a should be best interpreted as an indication of relative layer flatness and perfection, not as real crystallite layer diameters[20]. Hence, layers that are bent or perforated, will give small L_a values even though the extent of the structure may be large. The crystallite dimensions of the present chars are consistent with with values reported for glassy carbons produced for a phenolic resin[19], indicating similar physical properties for glassy carbons made from different starting materials as postulated by Fitzer et al.[1]. Partial combustion in air at 1600 K for 2 s, promoted structural ordering as evidenced by the appearance of the *(100)* peak, shown in Fig. 9. Heat treatment at higher oxygen levels (30% O_2) enhanced crystal formation indicated by the presence of taller and narrower peaks. The particles did not ignite at a reactor temperature of 1600 K and oxygen levels below 30%, but rather burned at particle temperatures close to that of the furnace. The small temperature rise was confirmed by optical pyrometry. The calculated temperature rise due to measured surface reaction rates is small (< 15 K) for oxygen levels below 21%. Hence, the enhanced graphitization cannot be explained by temperature differences alone. Catalysis of graphitization by oxidizing gases has been previously reported by Noda and Inagaki[24]. At higher oxygen levels (21 - 30%), the temperature rise

may become more significant; it is estimated to be 40 K at 30% O_2. It was not posible to measure such a small temperature rise accurately in the present experiments. Hence, the roles of temperature and oxygen level on catalyzing graphitization cannot be separated in the higher oxygen level experiments. The powdery nature of the chars also helped promote graphitization[25] and allowed O_2 to penetrate the interior of the particles effectively. The TEM micrographs of Fig. 6 support the argument of O_2 induced graphitization. The partially combusted sample (6b) possesses regions where crystallites are oriented parallel to each other (and parallel to the electron beam); meanwhile, the carbonized (in N_2 at the same temperature) sample (6a) appears completely disordered.

The effect of O_2 on graphitization of the copolymer chars was variable. Some of the copolymers underwent substantial graphitization upon partial combustion in air at 1600 K for 2 s. For these chars, a sharp graphitic and/or turbostratic component appears superimposed on the broad *(002)* band of the disordered carbon matrix as shown in Fig. 9. The onset of this limited (two or three phase) graphitization appears suddenly over a fairly narrow range of treatment temperatures. The narrow diffraction peaks indicate the appearance of large crystallites. The particles formed from 17% tannic acid and 83% polyfurfuryl alcohol (PFA) possess a turbostratic *(002)* component ($\bar{d}$=3.49Å). The particles formed from 50% tannic acid and PFA exhibited a graphitic *(002)* component ($\bar{d}$=3.356Å) and the particles formed from 18% PEG and PFA showed a turbostratic together with a faint graphitic component. For the last two materials, *(hk)* peaks appeared, indicative of two-dimensional ordering. Appearance of the *(103)* peak for the 18% PEG material signifies the onset of three-dimensional ordering.

The origin and relative amounts of graphitic phases in the copolymer chars is uncertain at present. The graphitic phases may originate from the pore former materials themselves as they decompose upon oxidative heating. It has been pro-

posed[26] that extensive graphitization of carbons occurs only if the carbonizing mass passes through a plastic state during which anisotropic droplets that contain highly oriented polynuclear molecules separarated from the fluid mass, known as "mesophase," are formed. SEM observations suggest that some of the copolymer materials and, in particular, those containing tannic acid have undergone partial melting and resolidification during the course of the 1600 K oxidation. Tannic acid melts at temperatures around 800 K. Hence if the mesophase arises from the molten components, graphitic crystals might result even at 1600 K aided by O_2 catalysis. A polished section of a 50% tannic acid particle is shown in Fig. 10a. The dark ridges might be due to a separated, decomposed phase of tannic acid. Figure 10b shows a 50% tannic acid particle after partial burning. Many submicron spherical particles are embedded on the surface of the latter particle. Previous work on sucrose and rayon carbons suggests that such spheres might be the graphitizing crystallites[27]. Franklin[28] suggests that the formation of the minor graphitic phase is due to temperature-dependent internal stresses induced by differential thermal expansion of the small anisotropic crystallites, which are strongly bound together by extensive cross-link bonding. At high temperatures these crystallites rupture their cross-linked bonds and rearrange into highly oriented graphitic aggregates under the compressive stresses imposed by the surrounding carbon matrix.

Particles formed from 25% carbon black spheres as filler in the PFA resin also develop of a second crystalline phase upon partial combustion, as indicated by faint *(002)* peak and a few "two-dimensional" peaks. Since the resin alone, carbonized under the same conditions, did not exhibit any crystalline peaks, it appears that the graphitization of the binder was induced by the filler. Previous investigators have reported that furfuryl acohol and other resins graphitized significantly when mixed with natural and artificial graphite and carbon black fillers[29,30]. Moreover, the graphitization of carbon fiber/glassy carbon composites starts at the boundary

between the matrix and the fiber and proceeds into the matrix[31]. This was attributed to stress accumulation that was caused by a large volume shrinkage (47%) observed during carbonization.

The transitional pore network existing in this material could also have contributed to the formation of the crystalline phase by differential expansion of the isotropic matrix and the carbon around the pores. Kawamura and Tsuzuku[32] observed that high-porosity glassy carbons graphitize more readily than low-porosity ones. Kamiya and Suzuki[33] reported a preferential alignment of carbon layers around macropores in phenol formaldehyde resin char that graphitized upon treatment to high temperatures (2700 K).

3.2.1 *X-Ray Density*

The density of the materials is estimated from x-ray diffraction data[34]:

$$\sigma_{x-ray} = \frac{ZAm_H}{a_c(a_c\sqrt{(3/2)})C} = \frac{7.627}{\bar{d}_{(002)}} \qquad \mathrm{g/cm^3}, \tag{4}$$

where Z=4 denotes the number of carbon atoms in a unit cell, A=12 is the atomic weight of carbon, $m_H = 1.66 \times 10^{-24}$ is the mass of a hydrogen atom, a_c=2.456 is the lattice constant of graphite. X-ray densities for partially burned materials are tabulated in Table V. Since some of the copolymer chars exhibit multiphase graphitization, two density values have been reported, one corresponding to the disordered carbon matrix and one corresponding to the crystalline phase. If more than one crystalline phase is present, the density corresponding to the strongest peak is tabulated. The density of the unoxidized plain polymer sample is 1.7 g/cm^3 and the density of the disordered component of the partially oxidized samples varies between 1.91 to 1.96 g/cm^3. The density of the crystalline component varies between 2.1 to to 2.27 g/cm^3, the last value being the density of graphite. Since the relative amounts of the different phases present are not known, an average value cannot be

deduced. However, it is expected that the average value will be very close to the density of the dominant disordered phase.

3.3 Small Angle X-Ray Scattering

Inhomogeneities in solids can be detected using small angle x-ray scattering (SAXS). Because of the reciprocity between interatomic distance and "$\sin\theta$," where θ is the x-ray glancing angle, inhomogeneities significantly larger than the incident radiation wavelength generate x-ray scattering and interference effects at very small angles. For solid polymers, the inhomogeneities responsible for the scattering at small angles are microvoids dispersed throughout the mattrix.

3.3.1 *Analysis of SAXS Data*

SAXS intensity profiles have been used in several studies to determine the shape and size of pores of glassy carbons [18,34,35,36,37,38]. For an isotropic medium, the scattered intensity at low angles is given by Guinier[39]:

$$I(h) = V(\rho(r))^2 \int_0^\infty \gamma_0(r) \frac{\sin hr}{hr} 4\pi r^2 dr, \tag{5}$$

where $\rho(r)$ is the electron density of the diffracting body, $\mathbf{h}$ is the wave vector of the scattered intensity ($\mid \mathbf{h} \mid = 4\pi/\lambda \sin\theta$; 2θ = angle of scattering). V is the volume of the voids, and the characteristic fuction $\gamma_0(r)$ is the probability that a point at a distance r in an arbitrary direction from a given point in a void will itself be in the void.

In the so-called Guinier region at very small angles, $h \rightarrow 0$, and the scattered intensity becomes

$$I(h) = V\rho^2 \exp(-h^2 R_g^2/3), \tag{6}$$

where R_g is the electron radius of gyration about the center of electronic charge. For a dilute concentration of homogeneously distributed scattering voids, the radius

of gyration can be determined from

$$\frac{d \ln I}{dh^2} = -R_g^2/3. \tag{7}$$

For large angles in SAXS, the so-called Porod region, and for infinitely long and narrow slits, $h \rightarrow \infty$ and

$$I(h) = \pi^2 \rho^2 S/h^3, \tag{8}$$

where S is the total surface area of the matter contained in the volume V. For this region, Porod's range of inhomogeneity, l_m can be defined as:

$$l_m = \frac{\int_o^\infty hI(h)dh}{\lim_{h\rightarrow\infty} h^2 I(h)}. \tag{9}$$

Then the total surface area per unit mass becomes

$$S = \frac{4 \times 10^4 \epsilon(1-\epsilon)}{\sigma_a} \frac{lim_{h\rightarrow\infty}[h^2 I(h)]}{\int_0^\infty hI(h)\,dh} \qquad \mathrm{m}^2/\mathrm{g}, \tag{10}$$

where ϵ is volume fraction of the pores. Care must be exercized in evaluating the integral in the denominator of the above equation. The lower limit poses no problem, since at values of h close to zero, $hI(h)$ is very small regardless of the value of $I(h)$. For large values of $hI(h)$, however, errors can become significant since the intensity values, $I(h)$, are small and may be influenced by other sources of extraneous and parasitic radiation (Compton, thermal, and atomic structure scattering). The area measurements have significance only if it is verified that the product $h^3 I(h)$ is constant over a large interval. In this case the above integral can be approximated[35] as:

$$\int_0^\infty hI(h)dh = \int_0^{h_0} hI(h)dh + \int_{h_0}^\infty hk/h^3 dh, \tag{11}$$

where k is the limiting value of $h^3 I(h)$, and h_0 must be within the range of applicability of Porod's law where $d \ln I / d \ln h = -3$ as $h \rightarrow \infty$.

An alternative approach of determining x-ray parameters is due to Debye and coworkers[40] and applies to completely random two phase systems. The characteristic function is given as:

$$\gamma_0(r) = \exp(-r/a), \tag{12}$$

and the intensity for point optics is given as:

$$I(h) = \frac{A}{\left[1 + \left(\frac{4\pi a\theta}{\lambda}\right)^2\right]^2}, \tag{13}$$

where A is a constant and 2θ is the scattering angle. The correlation distance, a, can be obtained from a plot of $I^{-1/2}$ against $(2\theta)^2$, which should yield a straight line, if the material is indeed random. Then:

$$a = \frac{\lambda}{2\pi}\left(\frac{slope}{intercept}\right)^{1/2}, \tag{14}$$

The correlation distance, a, has been shown to be similar to the range of inhomogeneity, l_m, and the total surface area of the voids per unit mass is defined as before. Other secondary parameters that can be calculated from l_m or a, if the pore volume fraction ϵ is known, are: d_{voids} which corresponds to the average dimension of segments in the voids and is given by:

$$d_{voids} = l_m/(1-\epsilon), \tag{15}$$

and d_{solid} is defined as the average distance between pore walls within the carbon matrix and is given by:

$$d_{solid} = l_m/\epsilon, \tag{16}$$

All of the above parameters apply to both dense and dilute void concentrations with the exception of R_g, which applies only to dilute systems.

3.3.2 *Results and Discussion*

Several experimental x-ray profiles are shown in Fig. 11. It can be observed that the intensity of scattered radiation exhibits a continous profile, decreasing with the angle

of scattering. The intensity increases with heat treatment temperature and with the degree of oxidation as indicated from the plain polymer profiles. It also varies with the nature of the copolymer, depending on the concentration, and, presumably, size and shape of the voids. The fact that the carbon formed from glycerol-Triton and PFA exhibits the highest scattering is due partly on its enhanced porosity and partly on the degree of conversion that is the highest of all carbons in this figure.

The experimental curves were corrected for smearing effects, using the method of Schmidt and Hight[41] but with a unity weighting function that approximates a negligible slit width-to-height ratio[42]. The resulting intensity curve approximates the scattering that would have been observed from point collimation under the same conditions. The Debye plots generated for various copolymers, shown in Fig. 12, are reasonably linear. Correlation length values, a, have been estimated and summarized in Table VI. Values of the mean cord intercept length for the pores and the solid were calculated from the values of a. Most of the void sizes are below 10Å, being in good agreement with previously reported values[18,36,38] for glassy carbons that have undergone similar heat treatment. The voids in the 18% PEG char are exceptionally large, indicating the presence of a number of pores large enough to be penetrated by nitrogen at 77 K. These results are in good agreement with the large BET area observed for this material (Table III). The fact that the slope in the Debye plot for this last material is steep only for a limited range of scattering angles and then becomes milder at higher angles shows the existence of smaller voids along with the large ones. The Debye plot for the 25% carbon black containing material shows two or three distinct void sizes; the largest one, indicated by scattering at very small angles, corresponds to 150Å (diameter) pores in excellent agreement with the porosimetry data. The smallest pores correspond to the values measured for the plain polymer matrix. Guinier plots for the copolymers exhibit a narrow angular range of linearity, suggesting a rather broad pore size

distribution. Radii of gyration for the linear region are included in Table VI. Porod plots indicate significant deviation from Porod's Law ($d\ln I/d\ln h \propto -3$) at the tail of the scattering curve, suggesting anisotropic density fluctuations[18]. Furthermore the Porod invariant plots exhibited no maximum in the $h^3I(h)$ value suggestive of interfaces with sharp edges and corners[43,44]. Since the Porod Law does not hold, the range of inhomogeneity was not calculated. Total surface areas were computed based on Debye's parameter a.

The scattered radiation from the materials heat-treated at elevated temperatures increases with temperature and degree of oxidation. This intensity increase is due to both the increase of the amount of the inhomogeneity and the enhancement in contrast between the two regions that produce the heterogeneity. The amount of inhomogeneity increases because the voids augment in number and size, the contrast is due to the expulsion of volatiles from the pores. As shown in Fig. 13 Porod's law holds well at large angles for all of the materials. especially the partially burned ones. This suggests that the materials become progressively more homogeneous with heat treatment,as reported previously[18,39]. The Porod Invariant, $h^3I(h)$, tends to limiting values at large angles, indicating a smoothing of the interfaces with pyrolysis temperature and oxidation (Fig. 14). The resulting l_m values are in good agreement with Debye's correlation lengths a for the various materials, as shown in Table VII. Also shown are values for the mean cord intercepts, d, for the voids and the solid, and surface areas calculated from the l_m values. The average void size is seen to increase with heat treatment and, degree of oxidation at the expense of the solid matrix in between voids. As also suggested by Perret and Ruland[18], the average thickness of the carbon matrix between the pore walls, of the oxidized materials, d_{solid}, is comparable to the layer stack height, L_c, obtained from wide-angle scattering measurements (Table V). This indicates that pores are separated by only one stack carbon layers and supports the hypothesis of Jenkins

and Perret and Ruland [19,18] regarding the structure of glassy carbons.

Guinier plots for the heat treated materials are shown in Fig. 15. Guinier's law holds well for a large range of scattering angles indicating a narrow pore size distribution. At very small angles, the scattered intensities increases, probably because of enlargement of surface pores by the combustion process. Calculated radii of gyration are listed in Table VII. These values, however, are questionable since the void fraction in glassy carbons is more than a few percent and Guinier's Law is applicable only to dilute systems. Surface area calculations indicate the development of a large amount of porosity upon heat treatment. If one compares the 616 m^2/g measured by SAXS to the 9 m^2/g measured by BET for the material pyrolyzed to 1500 K, it is apparent that these pores are closed to N_2. Partial oxidation causes an initial increase in surface areas because of pore openning, followed by a continous drop in areas upon further oxidation because of pore enlargement. The value of surface area for the plain polymer that has been partially burned in air at 1500 K is in excellent agreement with the N_2 BET surface area (see Fig. 7), suggesting the development of a well-interconnected and open network of micropores.

In summary, the results of SAXS indicate that the initial materials which were heat-treated to 800 K possess a vast network of micropores that have an average size of less than 10 Å. The only exeptions are the materials containing carbon black spheres and large amounts of PEG. The size distributions of pores are broad and the pores are anisotropically distributed within the particle. The voids are not very well developed, formed between ribbon like layers of glassy carbon, and contain sharp edges and corners. As the carbonizing temperature increases, the void size increases because of evolution of heavy volatile hydrocarbons, structural ordering and densification of the carbon matrix. The data suggests that the voids become more rounded but not necessarily spherical[37], and more uniform in size and spatial distribution. The pore openings are small, and most of this porosity is closed to

N_2 at 77 K and open only to CO_2 at 195 K[38]. Upon partial combustion, the pores enlarge because of the combined effect of heterogeneous reaction between the carbon at the pore walls and the oxidizer and enhanced structural rearangement caused by the catalytic effects of O_2. After this treatment, the pore openings are sufficiently large for N_2 to penetrate in BET measurements.

3.4 Additional Sorption Measurements

To show that elevated temperature treatment and oxidation both contribute to the enlargement of pores, the following experiment was performed: Plain polymer material heat treated to 800 K was divided into two parts; part (a) was oxidized in air at 800 K to 20% burnout, and part (b) was first pyrolyzed to 1500 K and then oxidized similarly to part (a). The N_2 BET area of part (a) was 300 m^2/g, whereas the area of the part (b) was 580 m^2/g. The fact that the first area is smaller than the second indicates that oxidation alone is not sufficient to open and enlarge the pores enough for the N_2 to completely penetrate the particles. Pore opening for part (b) seems to be complete since the BET area coincides with the SAXS area for 20% burnout at 1500 K.

Void volumes of the above materials were measured by CO_2 adsorption at room temperature and subsequent analysis of the resulting isotherms with the potential theory equations of Polanyi-Dubinin. The value of this void volume represents pores whose diameters range from about 30Å to the kinetic diameter of carbon dioxide (3.3Å)[45]. The resulting volume of material from part (a) above is 0.220 cm^3/g ($\epsilon = 0.27$), and for the material from part (b) the void volume is 0.257 cm^3/g ($\epsilon = 0.32$). The void fraction of the second material is in good agreement with the corresponding value derived from helium and apparent density measurements; therefore, the porosity of this material is completely open to CO_2. By comparison, the material of part (b) contains either closed porosity or small pores. The

total surface areas of these two materials derived from Medek's[46] equation, using Dubinin's parameters is 560 m^2/g for part (a) and 684 m^2/g for part (b).

Pore volume measurements by means of CO_2 adsorption at 297 K were also applied to the unoxidized material that was pyrolyzed to 800 K. The void volume was 0.0223 cm^2/g, corresponding to a porosity of $\epsilon = .03$, which is less than that determined with helium ($\epsilon = 0.11$). These values show that the voids of the initial material are small and impermeable. The CO_2 surface area for this material was calculated to be 59 m^2/g.

4 Conclusions

Uniform size glassy carbon spheres have been manufactured by controlled atomization. The polymer precursor was furfuryl alcohol, but other highly crosslinked polymers can also be used. The production and curing time required to generate solid particles are very brief because of the small size of the spheres. The sphere size can be varied, and both solid and hollow spheres can be produced.

The pore structure and the chemical properties of the particles can be varied by the addition of pore-forming agents. The particles carbonized at 800 K contain a vast network of micropores of very fine size (less than 10Å). These micropores are closed and inaccessible to N_2 at 77 K. The shape of these pores is rather irregular and their size distribution is broad. Upon carbonization at elevated temperatures, the carbon matrix shrinks. This densification makes space for the voids to grow. The void shapes become more rounded, and the pore size distribution narrows. Oxidation accelerates pore growth by the combined effect of catalysis of graphitization reactions and by heterogeneous reaction that leads to gasification of the carbon matrix. In addition, oxidation enlarges the pore openings and reduces the resistance to pore diffusion in the particle. Oxidation at elevated temperatures induces multiphase graphitization to some of the copolymer particles.

All of the glassy carbon materials produced in this study possess micropores only, with the exception of the carbon black containing particles that also possess transitional pores superimposed on the micropore network, and the cenospheres that contain macropores and large voids (bubbles). Finally, the glassy carbon spheres produced are hard, and their compressibility varies from very small values to zero depending on the copolymer nature and the heat treatment. Bulk quantities of spherical glassy carbon chars can be produced by an array of acoustically excited aerosol generators, and if monodispersivity is not a requirement, they can be produced by a high output spray nozzle.

5 Acknowledgements

This research was supported by the U.S. Department of Energy University Coal Programs Grant Number DE-FG22-84PC70775. The authors gratefully acknowledge technical assistance from Scott Northrop, George Gavalas, Patric Kohen, Bob Hously, Bob Johnson, Sten Samson and Larry Henling.

6 Notation

SYMBOL	DESCRIPTION	UNITS
a	correlation distance	Å
a_c	lattice constant	Å
A_G	specific total area	m^2/g
A_{Hg}	specific Mercury area	m^2/g
$\bar{d}$	interlayer spacing	Å
d_{void}	av. segment dimension in voids	Å
d_{solid}	av. segment dimension in solid	Å
h	wave vector magnitude	1/Å

$I(h)$	relative radiation intensity	
l_m	range of inhomogeneity	Å
L_a	crystallite stack width	Å
L_c	crystallite stack height	Å
m	mass	g
P	pressure	atm
r	radial distance	cm
r_p	pore radius	cm
R_g	radius of gyration	Å
$\mathbf{R}$	universal gas constant	atm cm^3/mole K
S	SAXS total surface area	m^2/g
V	inhomogeneity volume	cm^3/g
V_{Hg}	specific Mercury pore volume	cm^3/g
α	contact angle	
$\gamma_0(r)$	probability	
ϵ	porosity	
ρ_u	electron density	
σ_a	apparent density	g/cm^3
σ_{Hg}	Mercury density	g/cm^3
σ_{He}	true(Helium) density	g/cm^3
σ_{x-ray}	x-ray density	g/cm^3
σ	surface tension of mercury	dyne/cm

7 References

1. E. Fitzer, W. Schaefer and S. Yamada, *Carbon* **7**, 643 (1969).

2. C. Moreno-Castilla, O. P. Mahajian, H. J. Jung, M. A. Vannice, and P. L. Walker, Jr., Absts. 14th Biennial Conf. on Carbon, Pennsylvania State University (1979), p.26.

3. C. Moreno-Castilla, O. P. Mahajian and P. L. Walker, Jr., *Carbon* **18**, 271 (1980).

4. C. N. Satterfield, "Mass Transfer in Heterogeneous Catalysis," Massachussets Institute of Technology Press (1970).

5. E. E. Hucke, United States Patent Publication 3,859,421 (1975).

6. J. L. Schmitt, Jr., P. L. Walker, Jr. and G. A. Castellion, United States Patent Publication 3,978,000 (1976).

7. P. L. Walker, Jr., A. Oya, O. P. Mahajan, *Carbon* **18**, 377 (1980).

8. Y. A. Levendis and R. C. Flagan, *Combust. Sci. and Tech.* **53**, 117 (1987).

9. I. Fernandez-Morales, A. Guerrero-Ruiz, F. J. Lopez-Garzon, I. Rodriguez-Ramos and C. Moreno-Castilla *Carbon* **22**, 3, 301 (1984).

10. C. L. Senior and R. C. Flagan, *Twentieth Symposium (International) on Combustion*, The Combustion Institute, Pittsburg, PA. p.921 (1986).

11. R. N. Berglund and B. Y. H. Liu, *Environ. Sci. and Tech.* **7**, 147 (1973).

12. P. S. Northrop, R. G. Gavalas and R. C. Flagan, *Langmuir* **3**, 300 (1987).

13. J. Yan and Q. Zhang, *Particle Characterization* **3**, 20 (1986).

14. A. Wheeler *Adv.in Catalysis* **3**, 249 (1951).

15. I. W. Smith and R. J. Tyler, *Fuel* **51**, 312 (1972).

16. J. J. F. Scholten, from *Porous Carbon Solids*, edited by R. L. Bond, Academic Press, London (1967).

17. P. Zwietering and D. W. van Krevelen, *Fuel* **33**, 331 (1954).

18. R. Perret and W. Ruland, *J. Appl. Cryst. 5*, 183 (1972).

19. G. M. Jenkins, K. Kawamura and L. L. Ban, *Proc. R. Soc. Lond. A.* **327**, 501 (1972).

20. D. B. Fischbach, *Chem. and Phys. of Carbon* **7**, 1 (1971).

21. J. Morgan and B. E. Warren, *J. Chem. Phys.* **6**, 666 (1938)

22. M. A. Short and P. L. Walker, Jr., *Carbon* **1**, 3 (1963).

23. B. E. Warren, *Phys. Rev.* **59**, 693 (1941).

24. T. Noda and M. Inagaki, *Carbon* **2**, 127 (1964).

25. D. B. Fischbach and M. E. Rorabaugh, *Carbon* **21**, 429 (1983).

26. J. D Brooks and G. H. Taylor, *Chem. and Phys. of Carbon* **4**, 243 (1968).

27. P. A. Oberlin and F. Rousseaux, *J. Appl. Cryst.* **1**, 218 (1968).

28. R. E. Franklin, *Proc. Roy. Soc. (London)* **A209**, 196 (1951).

29. S. Nakamura, T. Ishii and S. Yamada, *Symposium on Carbon, Tokyo* (1964).

30. P. Cornuault, F. du Chaffaut, J. Rappeneau, M. Yvars and A. Fillatre, *Carbon* **6**, 857 (1968).

31. Y. Hishiyama, M. Inagaki, S. Kimura and S. Yamada, *Carbon* **12**, 249 (1974).

32. K. Kawamura and T. Tsuzuku, *Carbon* **12**, 352 (1973).

33. K. Kamiya and K. Suzuki, *Carbon* **13**, 317 (1975).

34. M. M. Dubinin, G. M. Plavnik and E. D. Zaverina, *Carbon* **2**, 261 (1964).

35. S. Bose and R. H. Bragg, *Carbon* **19**, 289 (1981).

36. G. D. Wignal and C. J. Pings, *Carbon* **12**, 51 (1974).

37. W. S. Rothwell, *J. Appl. Phys.* **39**, 3, 1840 (1968).

38. R. G. Jenkins and P. L. Walker, Jr., *Carbon* **14**, 7 (1976).

39. A. Guinier and G. Fournet, *Small Angle Scattering of X-Rays* John Wiley, New York (1955).

40. P. Debye, H. R. Anderson and H. Brumberger, *J. Appl. Phys.* **28**, 679 (1957).

41. P. W. Schmidt and R. Hight, Jr., *Acta Cryst.* **13**, 480 (1960).

42. B. Chu and D. M. Tan Creti, *Acta Cryst.* **18**, 1083 (1964).

43. G. Porod, *Small Angle X-Ray Scattering* edited by H. Brumberger, Gordon & Beach, New York (1969).

44. D. Tchoubar and J. Mering, *J. Appl. Cryst.* **2**, 128 (1969).

45. M. M. Dubinin, *Chem. Rev.* **60**, 235 (1960).

46. J. Medek, *Fuel* **56**, 131 (1977)

8 List of figures

1. Schematic of the char production technique.
2. Schematic of the particle generation system and thermal reactor.
3. SEM photographs of plain polymer particles.
4. SEM photographs of (a) a cenosphere made from 18% tannic acid and PFA (b)a particle made from 25% carbon black and PFA.
5. SEM photographs of partially burned plain polymer (PFA). particles at 1500 K for 2 sec in air (a) surface, (b) section.
6. TEM photographs of plain polymer chars (a) carbonized at a particle temperature of $\approx$ 1500 K in N_2 for 2 sec and (b) partially burned in air at a particle temperature of $\approx$ 1500 K for 2 sec.
7. BET and SAXS surface area versus burn-off for plain polymer chars.
8. Mercury porosimetry pore size distribution.
9. Wide-angle x-ray diffraction profiles of carbonized and partially combusted glassy carbons.
10. SEM photographs of particles made from 18% tannic acid and PFA a)section of unoxidized particle, b)detail of partially burned particle.
11. Experimental SAXS intensity profiles for carbonized and partially burned glassy carbons (apperture of slits 0.1°, 0.1°, 0.1° and 0.018°).
12. Debye plot for glassy carbons.
13. Porod plot for heat-treated and activated glassy carbons.

14. Porod invariant plot for heat-treated and activated glassy carbons.

15. Guinier plot for heat-treated and activated glassy carbons.

TABLE Ia
DENSITIES AND POROSITIES

Polymer with Pore Former	σ_a Apparent solid and pores less than 7μm g/cm^3	σ_{Hg} Mercury solid and pores less than 32Å g/cm^3	σ_{He} Helium g/cm^3	$\mathcal{E}$ Total porosity %	$\mathcal{E}$ below 32Å radius porosity %	V_{pore} macro and transitional pores cm^3/g
PLAIN POLYMER	1.23	1.28	1.37	11	6.8	0.08
DECALIN (21%)	1.17	1.21	1.36	14	11	----
DECALIN (37%)	1.25	1.29	1.35	8	4	0.032
GLYCEROL (20%)	1.24	1.30	1.39	11	6.3	0.029
GLYCEROL (20%) TRITON (3%)	1.24	1.29	1.37	10	6.4	0.028
GLYCEROL (35%) TRITON (7%)	1.26	1.29	1.33	6	3	0.027
GLYCEROL (20%) TRITON (3%) PEG (3%)	1.25	1.28	1.32	6	3.2	0.026
PEG (9%)	1.23	1.26	1.43	14	12	0.030
PEG (18%)	1.17	1.25	1.39	16	10.5	0.054
TANNIC ACID (8%)	1.31 ave.	1.35 ave.	1.38	6.0 ave.	2.5 ave.	0.031
TANNIC ACID (17%)	1.33	1.35	1.39	4	2.5	0.010
TANNIC ACID (50%)	1.35	1.37	1.40	----	----	----
PLAIN TANNIC ACID	----	----	1.45	----	----	----
CARBON BLACK (25%)	0.88	1.28	1.45	39	11.6	0.358
PURE CARBON BLACK	----	----	1.86	----	----	----

TABLE Ib
PARTIALLY BURNED MATERIALS

PEG (9%)	1.25	1.31	2.0	37	34	0.041
TANNIC ACID (8%)	1.21	1.5	2.1	42	28	0.043
TANNIC ACID (17%)	1.205	1.85	2.2	45	16	0.00
GLYCEROL (20%) TRITON (3%) PEG (3%)	1.21	1.25	2.1	39.5	37.5	0.023

TABLE II
SURFACE AREAS (N_2 –BET)

POLYMER WITH PORE FORMER	$A_G(m^2/g)$ Initial	$A_G(m^2/g)$ after 1500K Partial Combustion	Conversion
PLAIN POLYMER	~2 (1.83)	480	60%
DECALIN (21%)	1.87	471	60%
DECALIN (37%)	2.18	480	60%
GLYCEROL (20%)	16.36	360	60%
GLYCEROL (20%) TRITON (3%)	3.54	490	67%
GLYCEROL (35%) TRITON (7%)	4.75	788	72%
GLYCEROL (20%) TRITON (3%) PEG (3%)	1.76	688	63%
PEG (9%)	3.42	638	60%
PEG (18%)	79.0	493	85%
TANNIC ACID (8%)	48.6	229	65%
TANNIC ACID (17%)	12.3	500	67%
TANNIC ACID (50%)	6.01	345	85%
PLAIN TANNIC ACID	18	----	
CARBON BLACK (25%)	184	----	
PURE CARBON BLACK	113	----	

TABLE III
MATERIALS CONTAINING CARBON BLACK AND PEG

POLYMER WITH PORE FORMER	BET AREA (m^2/g)	Hg AREA (m^2/g)	Hg PORE VOLUME (cm^3/g)	APPARENT DENSITY (g/cm^3)	He DENSITY (g/cm^3)
CARBON BLACK (2%)	58.6	----	----	----	----
CARBON BLACK (8%)	90.5	24.4	0.078	1.22	1.38
CARBON BLACK (14%)	91.5	48	0.136	----	1.42
CARBON BLACK (17%)	232.6	71.6	0.304	1.05	1.43
CARBON BLACK (25%)	184	109	0.358	0.88	1.45
PEG (18%)	79	16.5	0.054	1.17	1.39

TABLE IV
CHEMICAL COMPOSITION

POLYMER WITH PORE FORMER	C%	H%	C/H
PLAIN POLYMER	85.85	3.45	2.07
DECALIN (25%)	87.80	3.32	2.18
TANNIC ACID (8%)	91.02	1.92	3.83
TANNIC ACID (17%)	87.17	2.98	2.44
TANNIC ACID (50%)	82.56	3.08	2.23
PURE TANNIC ACID CURED AT 800K	76.92	2.52	2.54
PEG (9%)	87.48	3.25	2.44
PEG (18%)	87.26	3.36	2.16
GLYCEROL (20%)	87.21	3.20	2.27
GLYCEROL (20%) TRITON X-100 (2%)	85.8	3.52	2.03
GLYCEROL (35%) TRITON X-100 (7%)	85.95	3.83	2.12
GLYCEROL (20%) PEG (3%) TRITON (3%)	84.60	3.41	2.07
CARBON BLACK (25%)	92.49	1.38	----
PLAIN POLYMER CURED AT 1500K IN N_2	97.0	1.1	7.35
PLAIN POLYMER PARTIALLY BURNED AT 1500K	97.05	0.82	9.86

TABLE V
WIDE ANGLE X-RAY DIFFRACTION DATA

MATERIAL	T_{HT}* (K)	GAS (% vol)	$\bar{d}_{002}$ Disor. Å	$\bar{d}_{002}$ Cryst. Å	$L_c(002)$ Å	$L_a(100)$ Å	Density Disor. g/cm^3	Density Cryst. g/cm^3
PL. POL.	800	N	---	---	---	---	---	---
PL. POL.	1600	N	4.5	---	13	---	1.70	---
PL. POL.	1600	Air	3.95	---	13	37	1.93	---
PL. POL.	1600	.4 O_2 .6 N_2	3.96	3.56 weak	16	38	1.96	2.14
PL. POL. with 17% TAN. AC.	1600	Air	3.95	3.49 v. strong	13	29	1.93	2.19
50% TAN. AC.	1400	Air	4.0	---	13	26	1.91	---
50% TAN. AC.	1600	Air	3.96	3.36 strong	16	37	1.93	2.27
18% PEG	1600	Air	4.0	3.69 strong	12.4	30	1.91	2.1
25% CARBON BLACK	1600	Air	3.90	3.55 medium	12.5	27	1.96	2.15

* T_{HT} = HEAT TREATMENT TEMPERATURE

TABLE VI

SMALL ANGLE PARAMETERS FOR GLASSY CARBONS

POLYMER WITH PORE FORMER	a (Å)	R_g (Å)	ℓ_m (Å)	d_{VOIDS} (Å)	d_{SOLID} (Å)	S (m^2/g)	ϵ	σ_{Hg}
PLAIN POLYMER	7.2	11	----	8	65	(442)	0.11	1.23
TANNIC ACID (17%)	8.3	11.5	----	8.6	207	(140)	0.04	1.33
TANNIC ACID (50%)	11.0	12.5	----	11.5	275	(103)	0.04	1.35
GLYCEROL (35%) TRITON (7%)	5.2	11	----	5.5	87	(325)	0.06	1.26
GLYCEROL (20%) TRITON (3%) PEG (3%)	7.7	15	----	8.2	128	(234)	0.06	1.25
GLYCEROL (20%) TRITON (3%)	5.4	----	----	6.0	60	(537)	0.1	1.24
PEG (18%)	28	24	----	33	175	(164)	0.16	1.17
CARBON BLACK (25%)	{128 / 6.5}	----	----	{164 / 8}	{580 / 43}	({15 / 367})	~0.11 ~0.24	0.88

TABLE VII

SMALL ANGLE PARAMETERS FOR HEAT TREATED AND PARTIALLY BURNED GLASSY CARBONS

(2 sec. TREATMENT TIMES AT 1500K)

POLYMER WITH PORE FORMER	a (Å)	R (Å)	ℓ_m (Å)	d_{VOIDS} (Å)	d_{SOLID} (Å)	S (m^2/g)	ϵ	σ_{Hg}
PLAIN POLYMER H.T. NITROGEN	8.3	14	8.3	10.4	41	616	0.2	1.22
PLAIN POLYMER 16% PART COM. 2% O_2	----	12.5	8.7	11.4	36	687	~0.22	1.21
PLAIN POLYMER 23% PART COM. 5% O_2	9	13	9	12.5	32	537	0.28	1.20
PLAIN POLYMER 65% PART COM. AIR	17.2	17	15	23	44	498	0.34	1.22
TANNIC ACID (17%) 67% PART COM. AIR	19	14	14	23	35	360	0.42	1.18
GLYCEROL (35%) TRITON (7%) 72% PART COM. AIR	16	14.5	16.5	26.6	41	625	0.50	1.0
PEG (9%) 60% PART COM. AIR	13.2	12	12	18	34	606	0.35	1.25

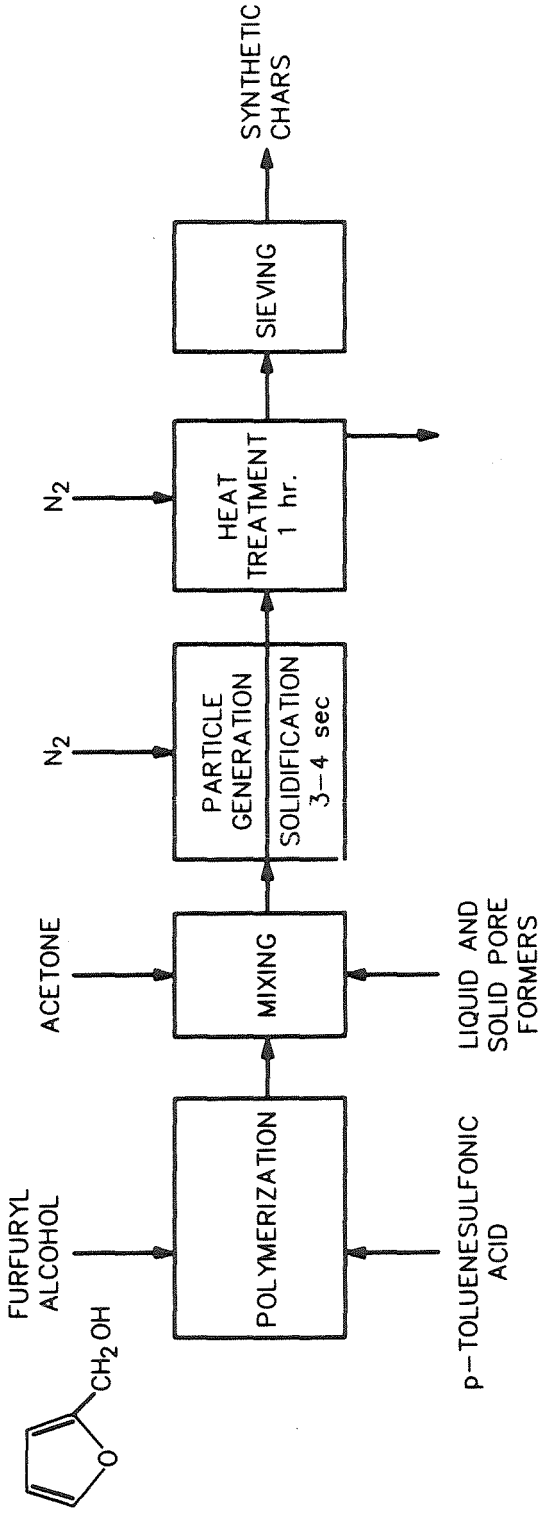

Figure 1: Schematic of the char production technique.

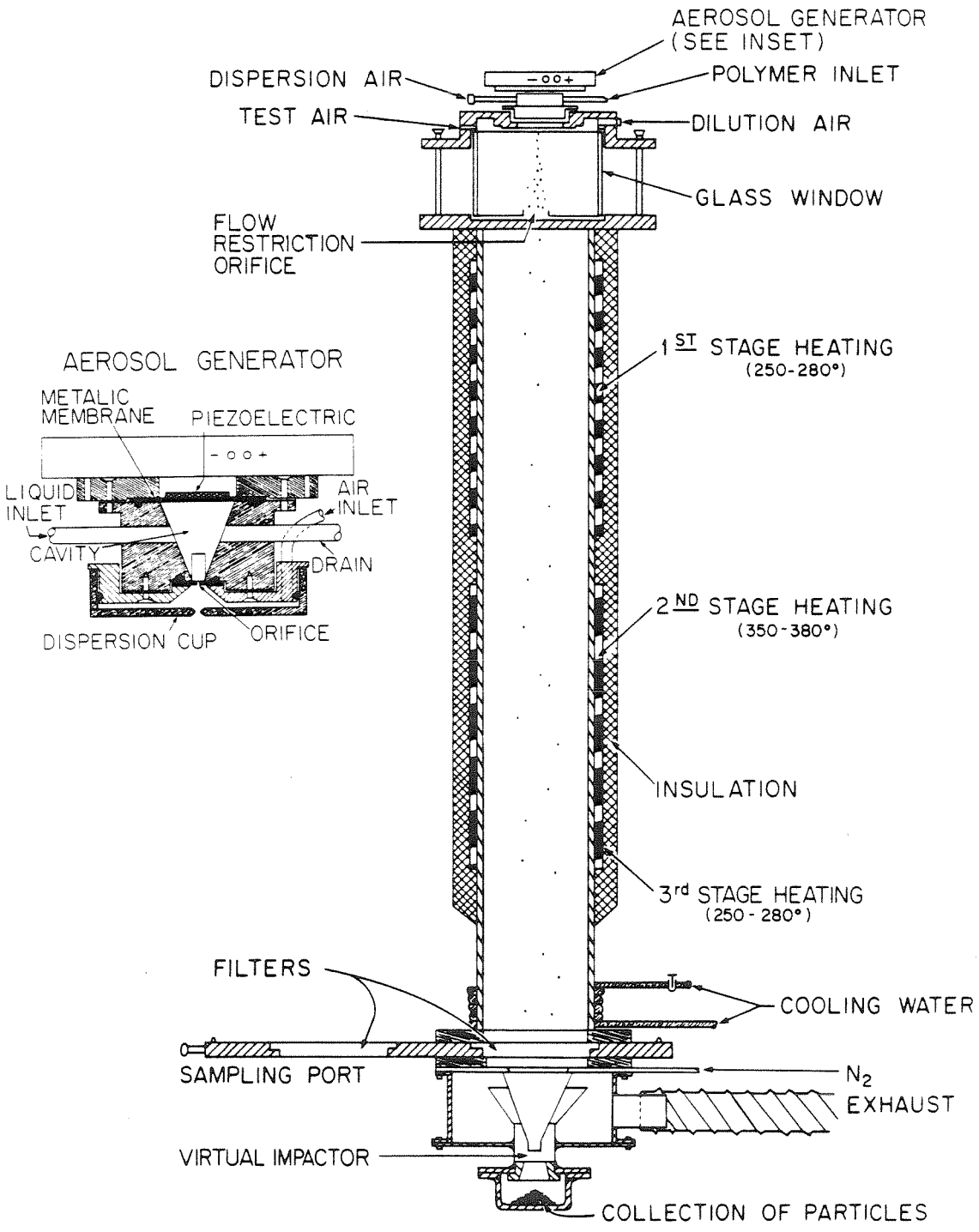

Figure 2: Schematic of the particle generation system and thermal reactor.

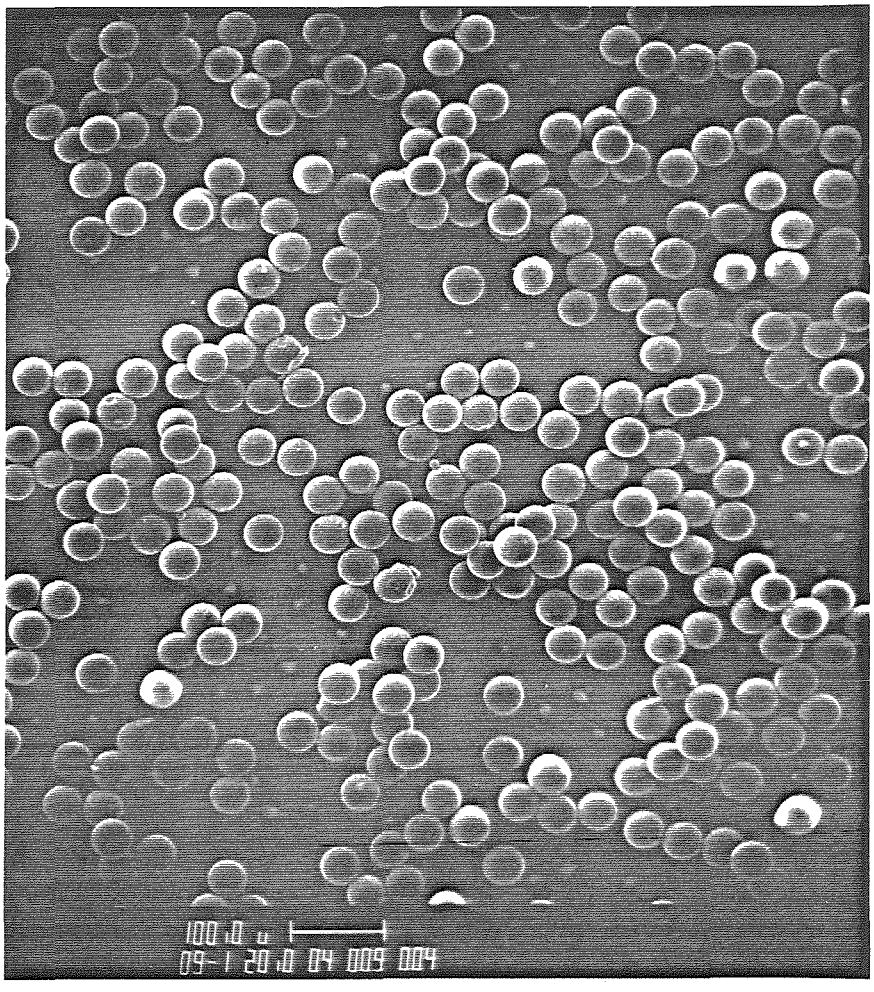

Figure 3: (a) SEM photograph of plain polymer particles

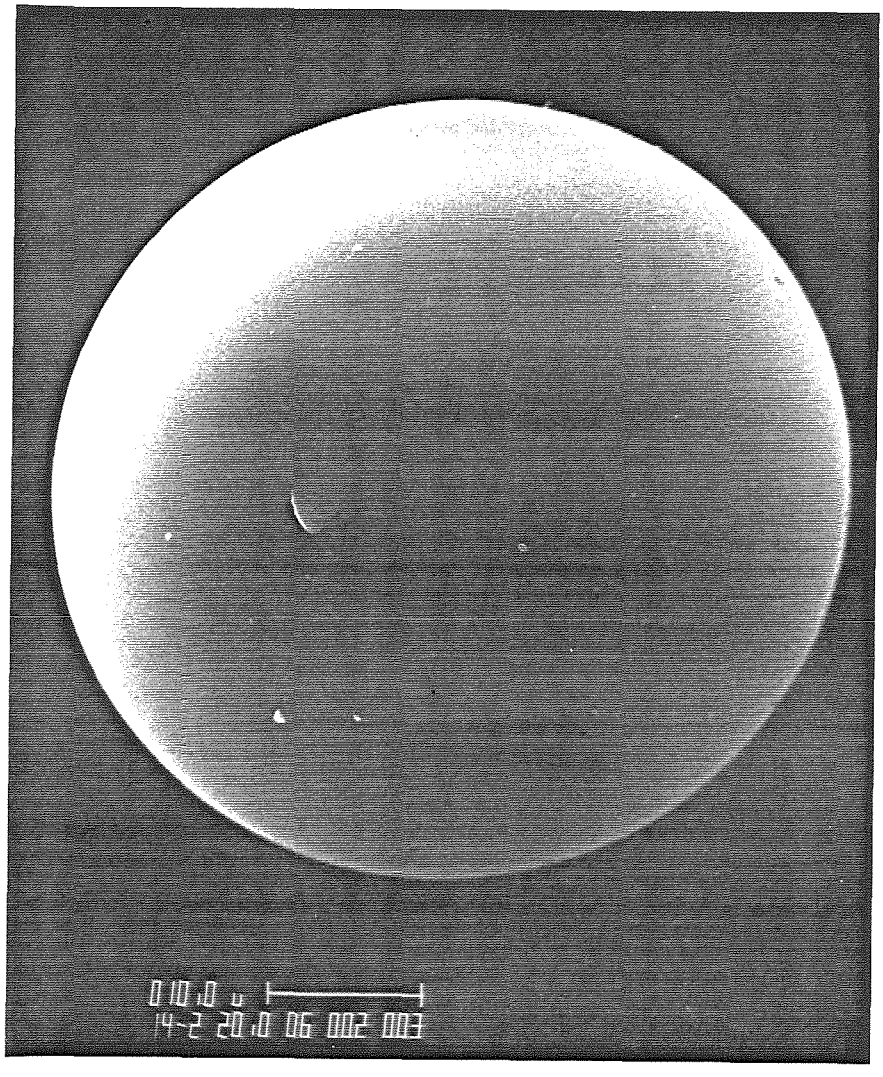

Figure 3 (b) SEM photograph of a plain polymer particle.

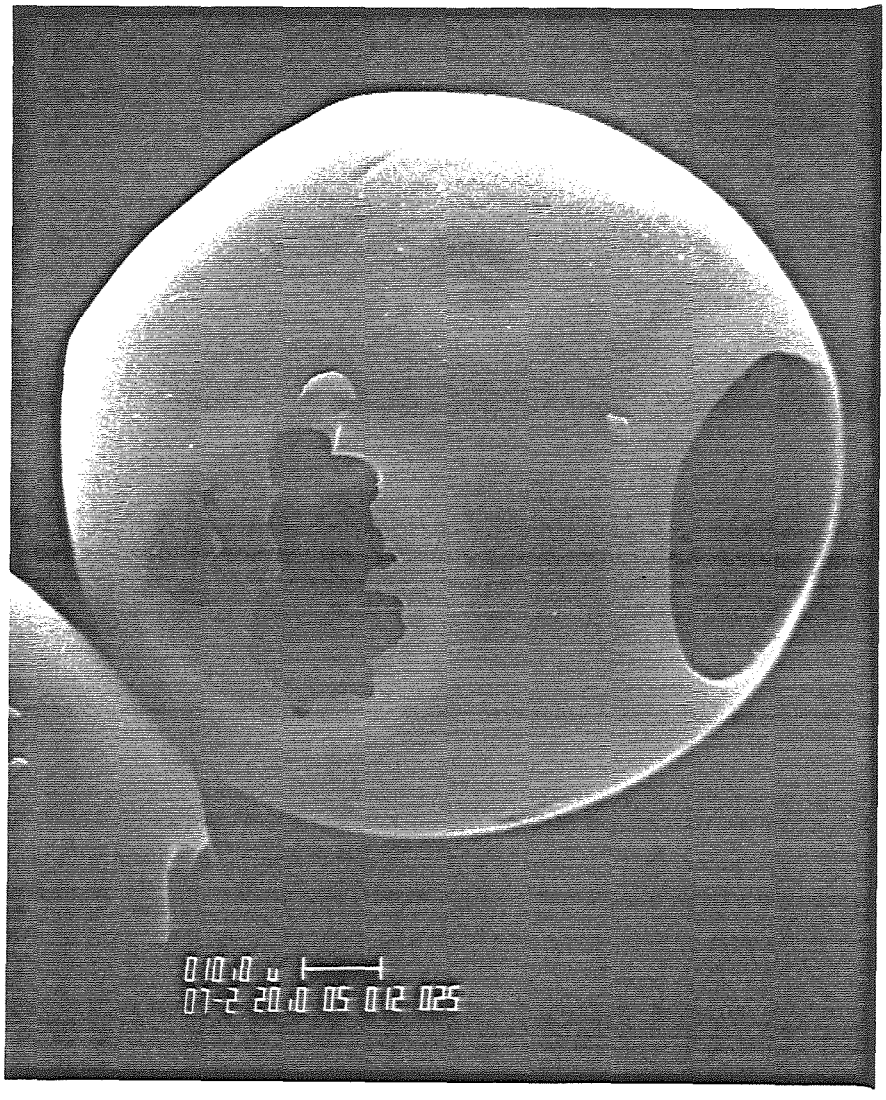

Figure 4: (a) SEM photograph of a cenosphere made from 18% tannic acid and PFA

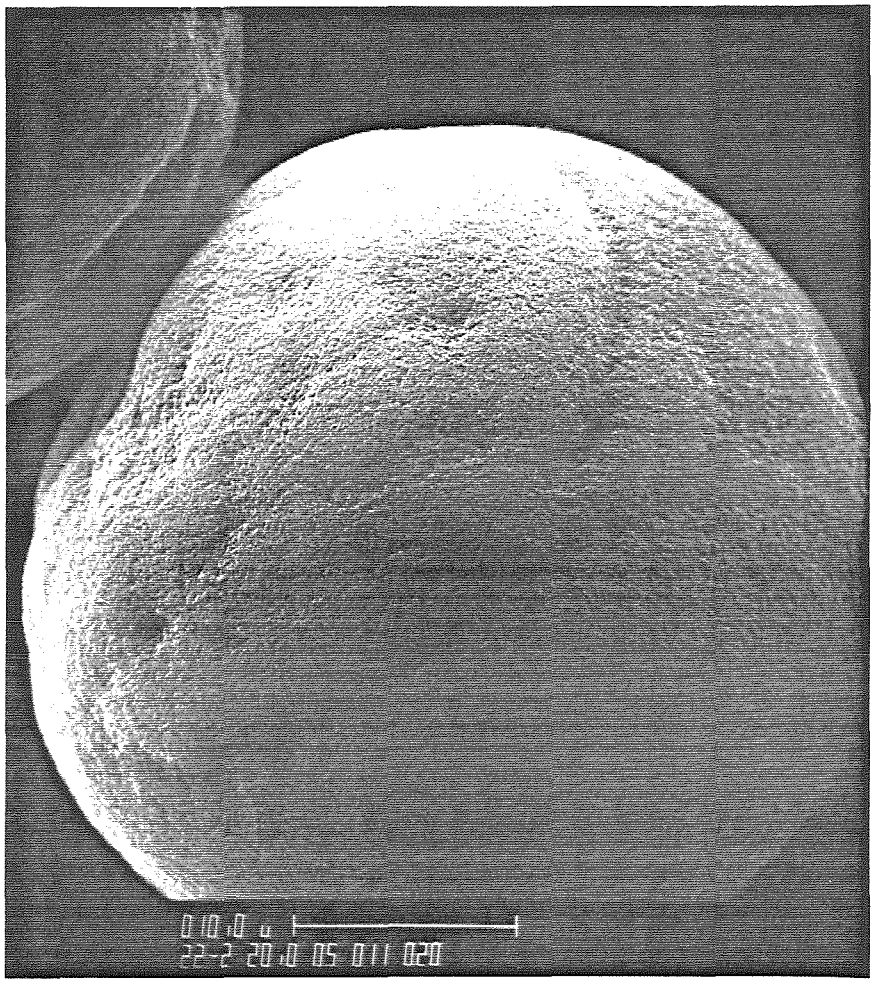

Figure 4 (b)a particle made from 25% carbon black and PFA.

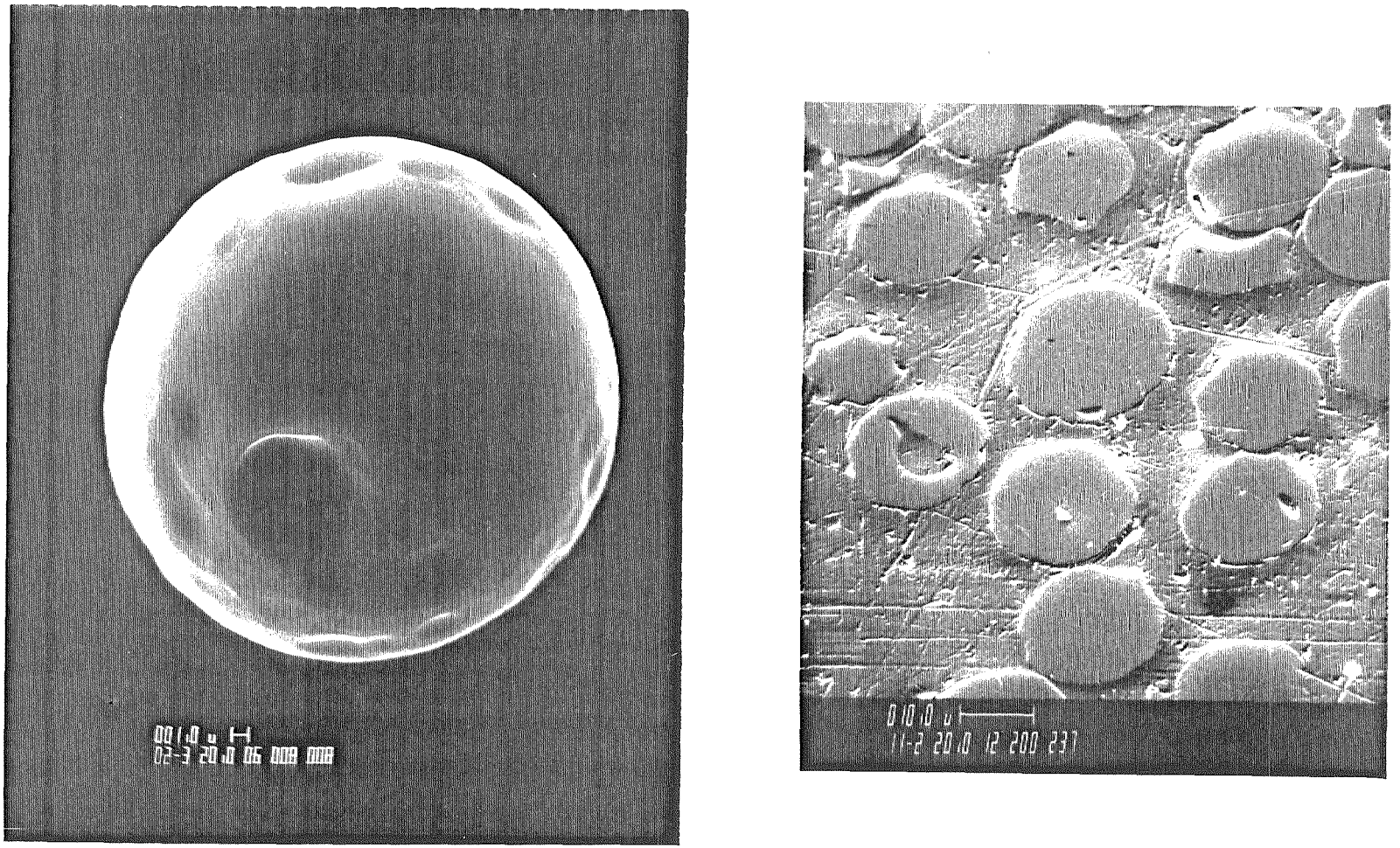

Figure 5: SEM photographs of partially burned plain polymer (PFA) particles at 1500 K for 2 sec in air (a) surface, (b) section.

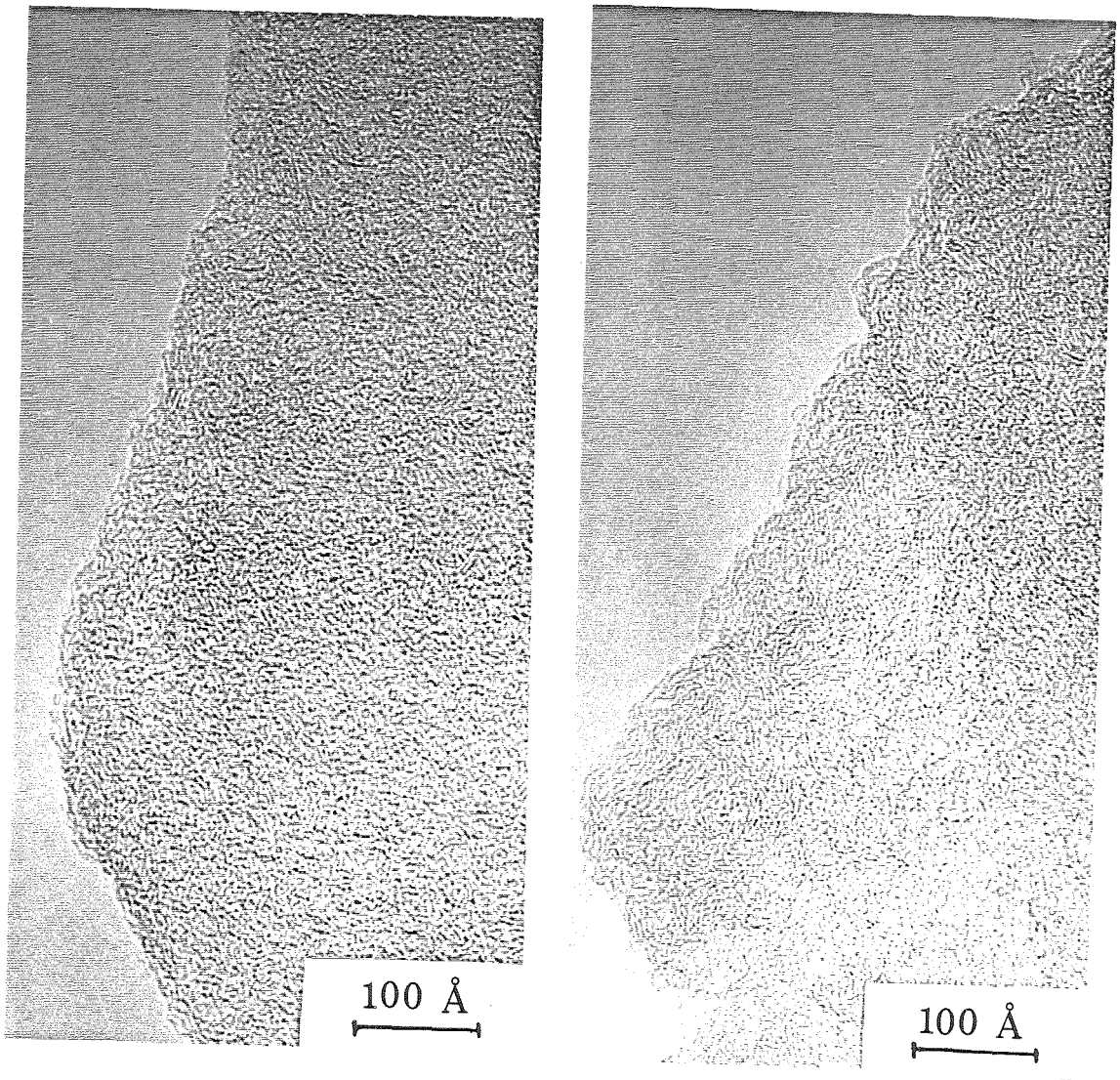

Figure 6: TEM photographs of plain polymer chars (PFA) (a) carbonized at a particle temperature of $\approx$ 1500 K in N_2 for 2 sec. and (b) partially burned in air at a particle temperature of $\approx$ 1500 K for 2 sec.

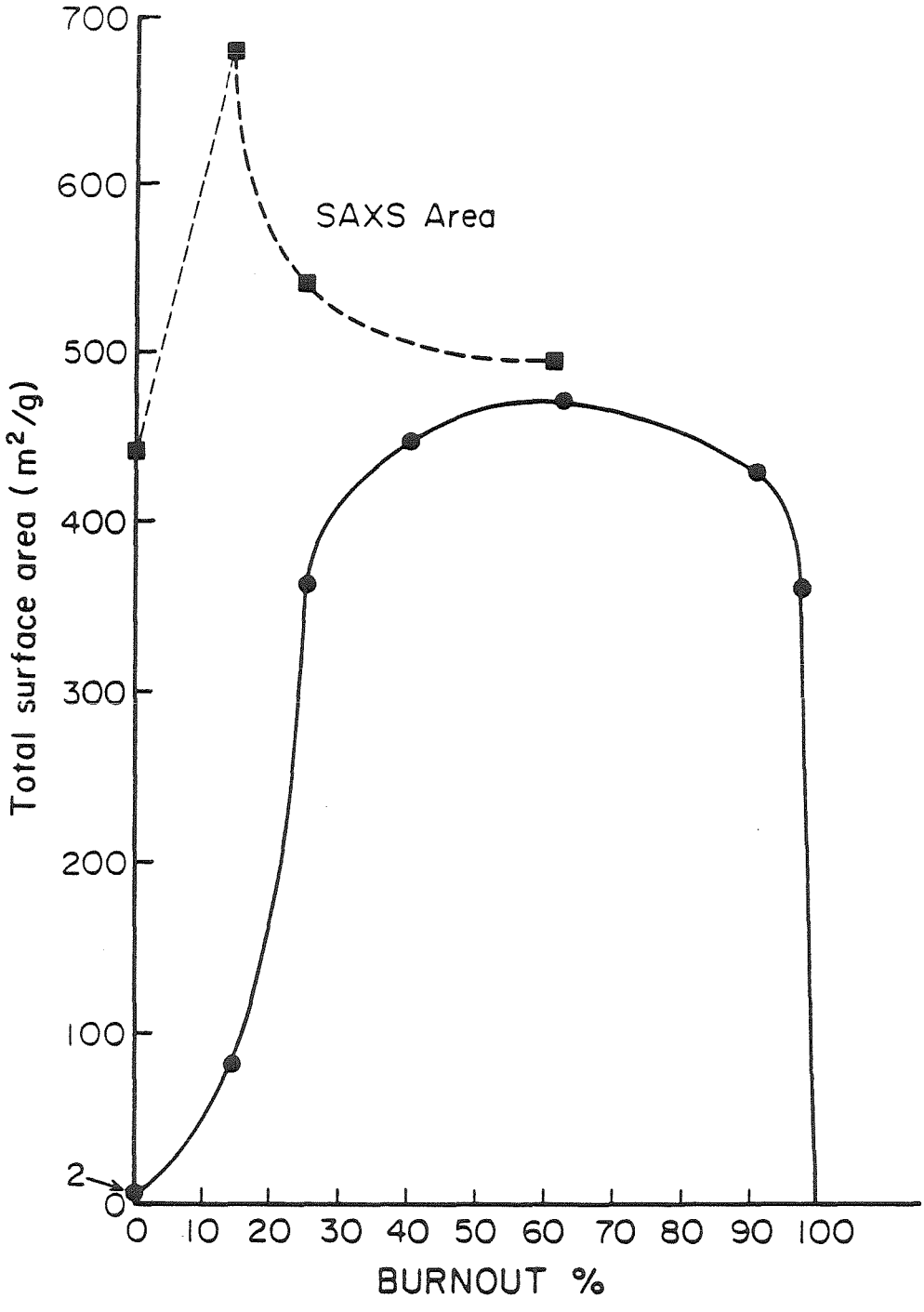

Figure 7: BET and SAXS surface area versus burn-off for plain polymer chars.

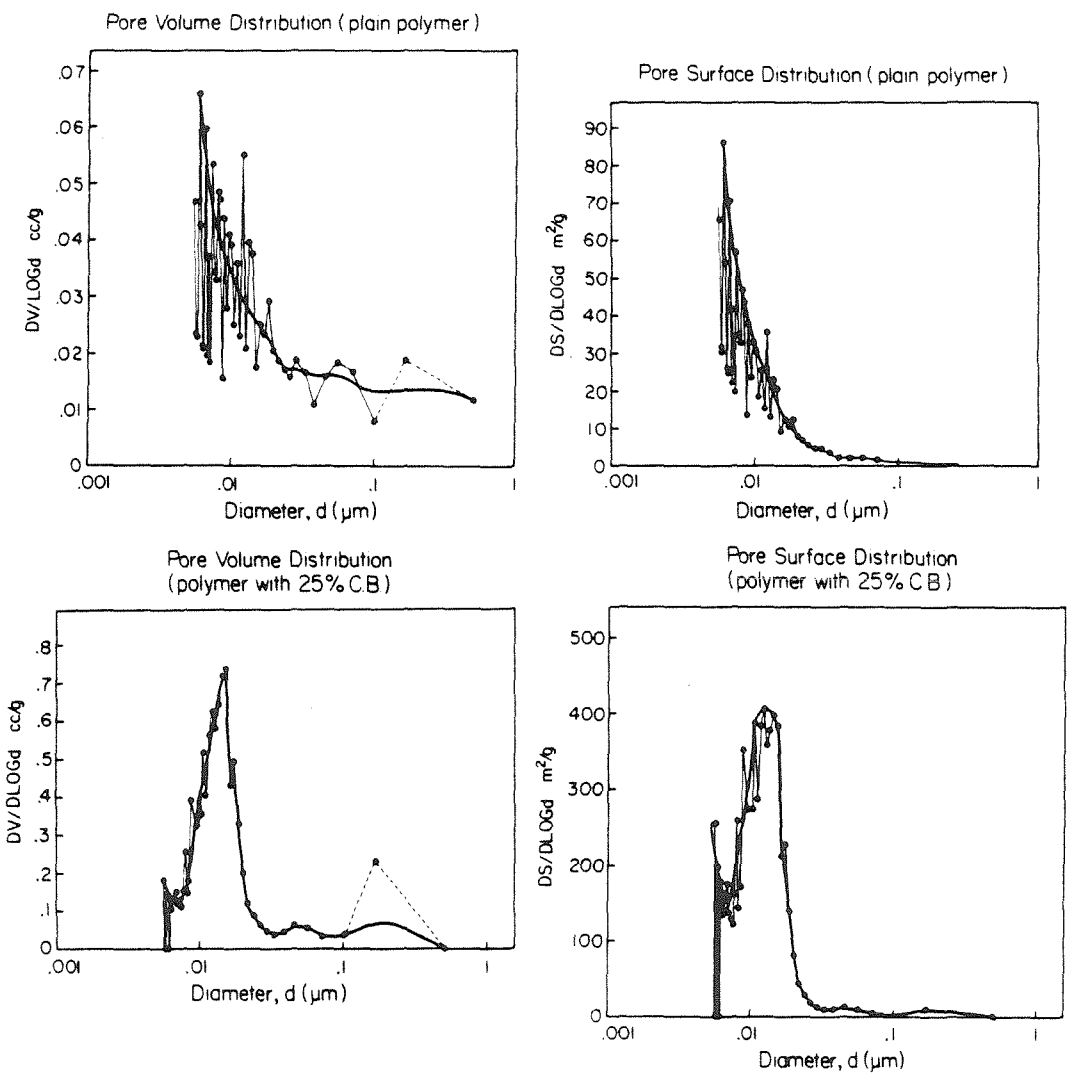

Figure 8: Mercury porosimetry pore size distribution.

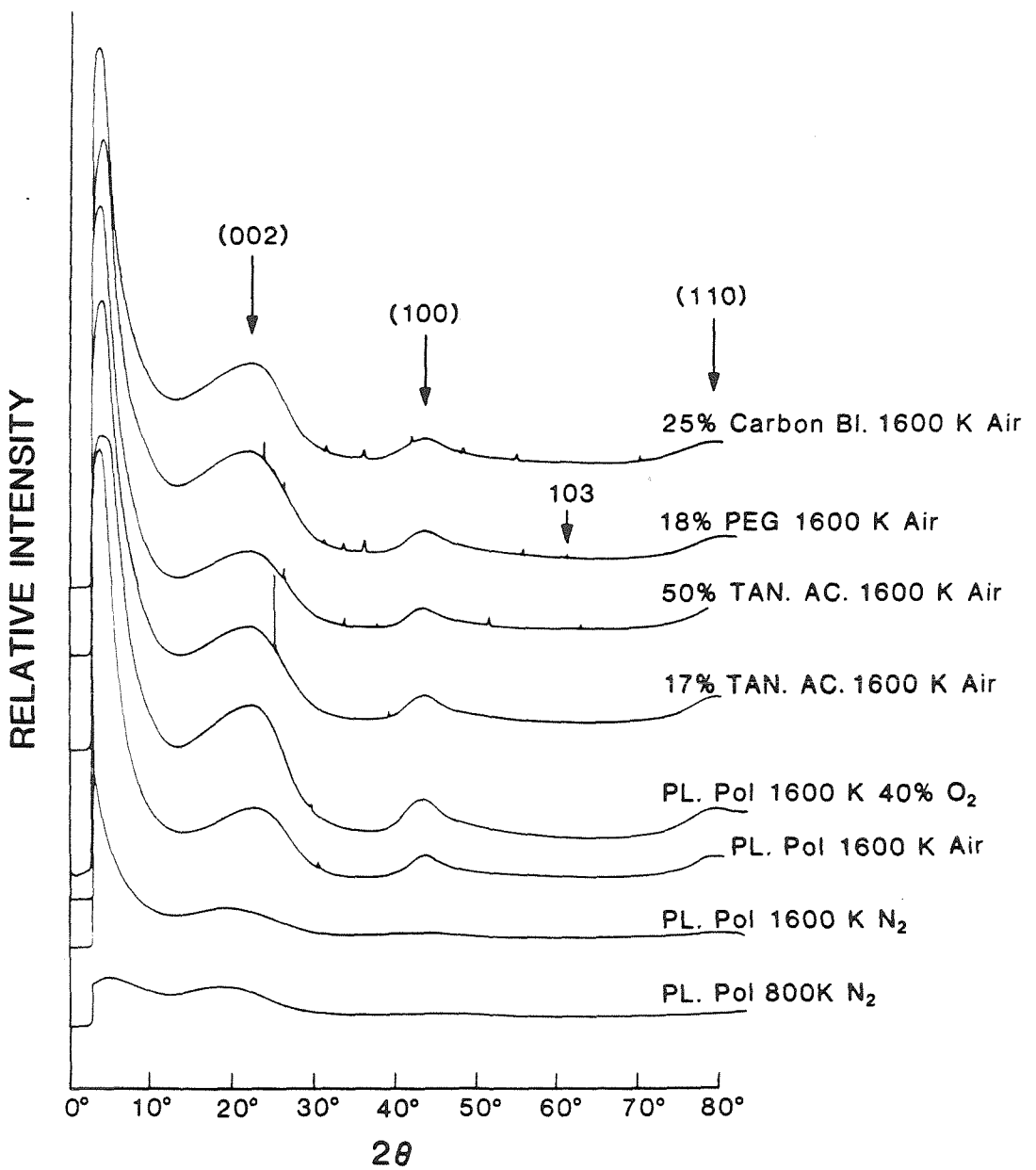

Figure 9: Wide-angle x-ray diffraction profiles of carbonized and partially combusted glassy carbons.

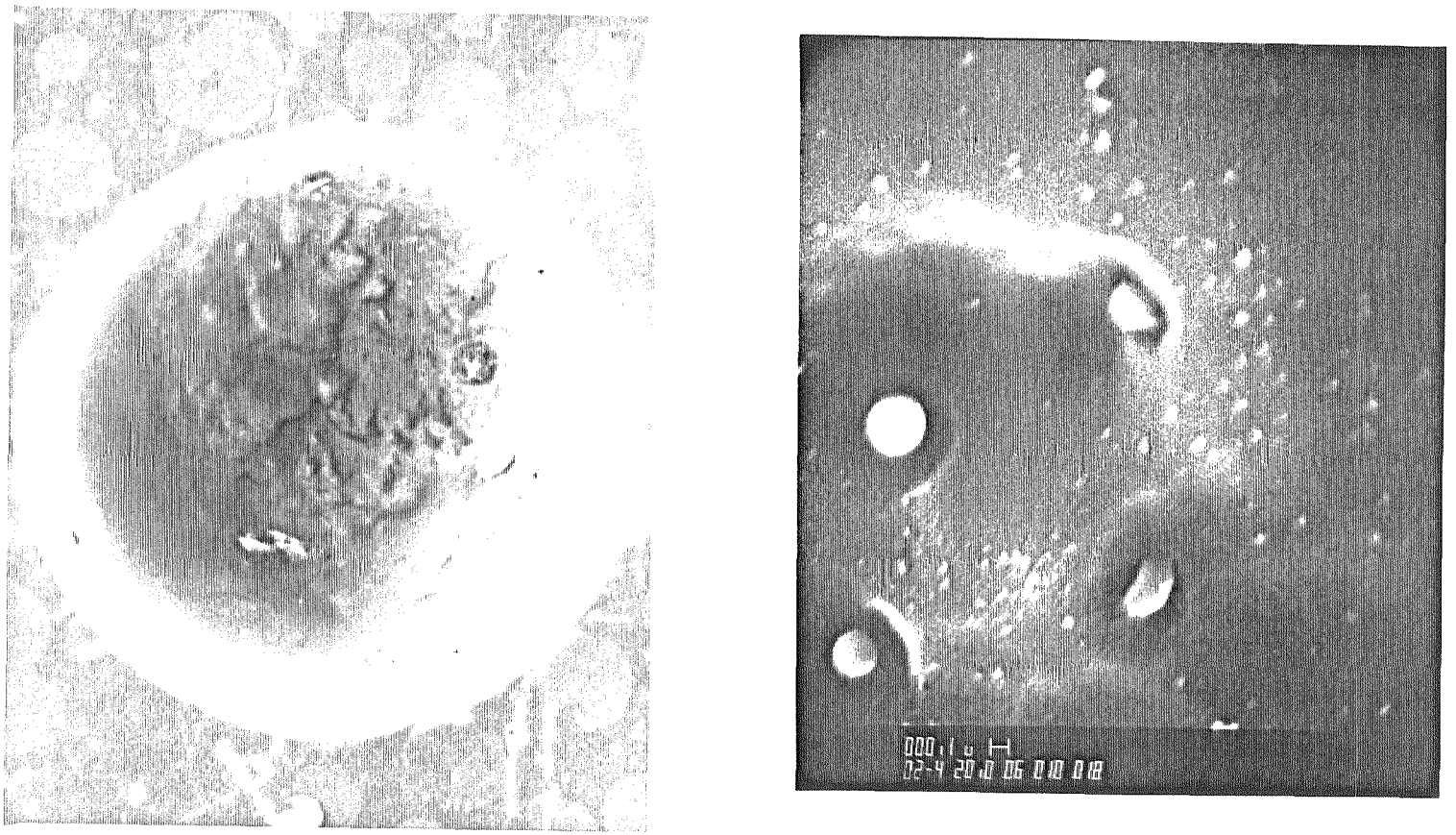

Figure 10: SEM photographs of particles made from 18% tannic acid and PFA a)section of unoxidized particle, b)detail of partially burned particle.

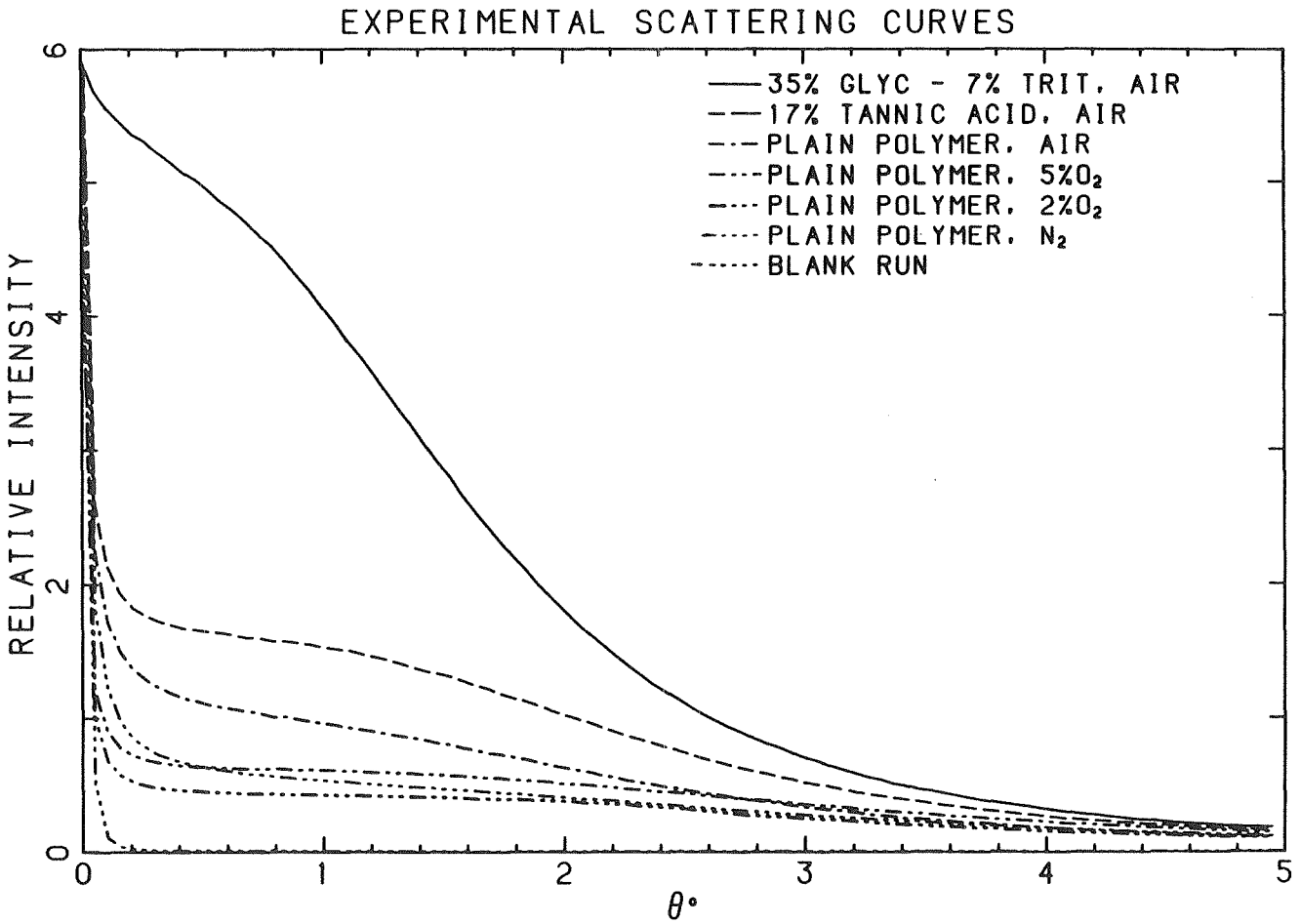

Figure 11: Experimental SAXS intensity profiles for carbonized and partially burned glassy carbons.(apperture of slits: 0.1°, 0.1°, 0.1° and 0.018°)

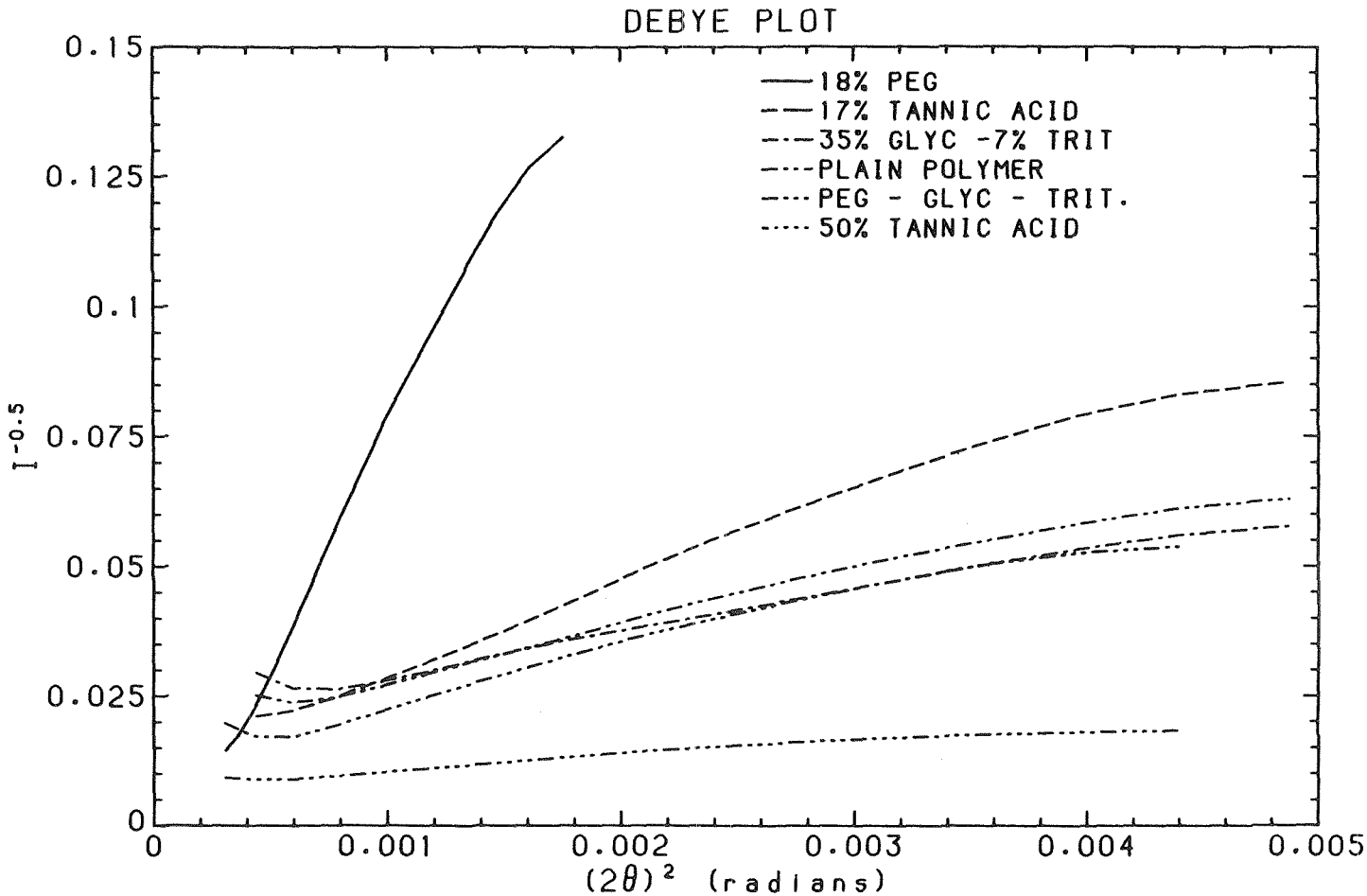

Figure 12: Debye plot for glassy carbons.

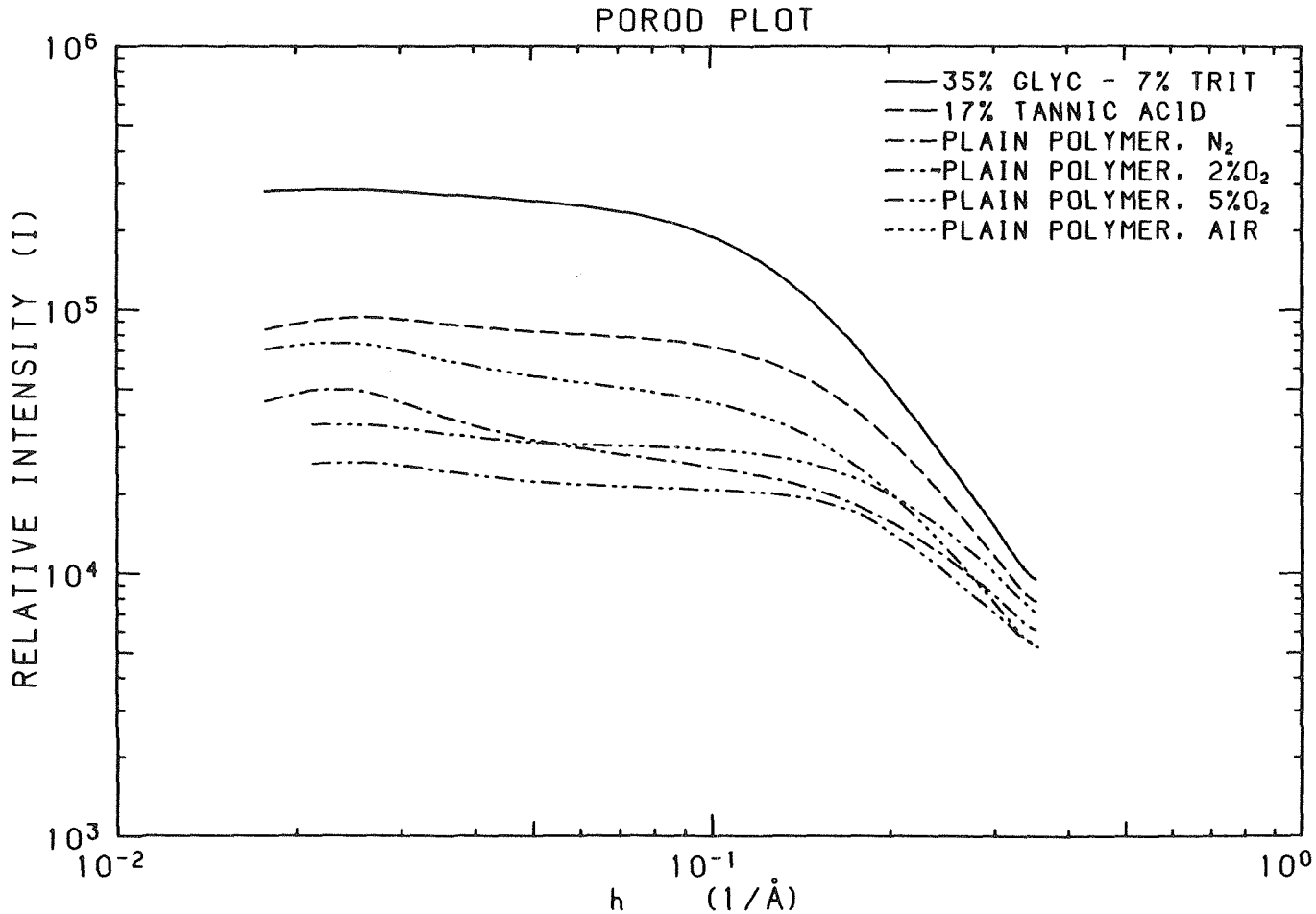

Figure 13: Porod plot for heat-treated and activated glassy carbons.

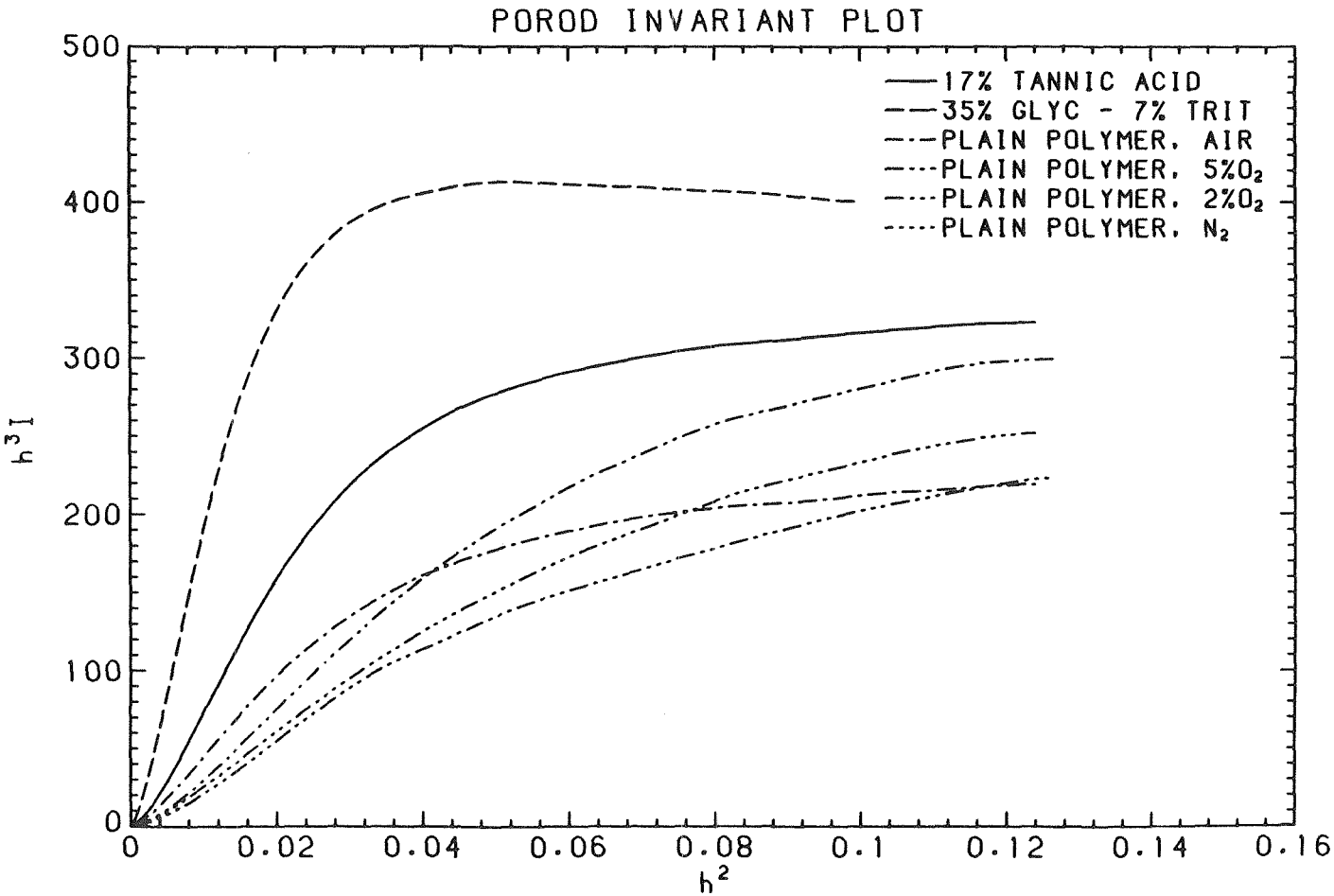

Figure 14: Porod invariant plot for heat-treated and activated glassy carbons.

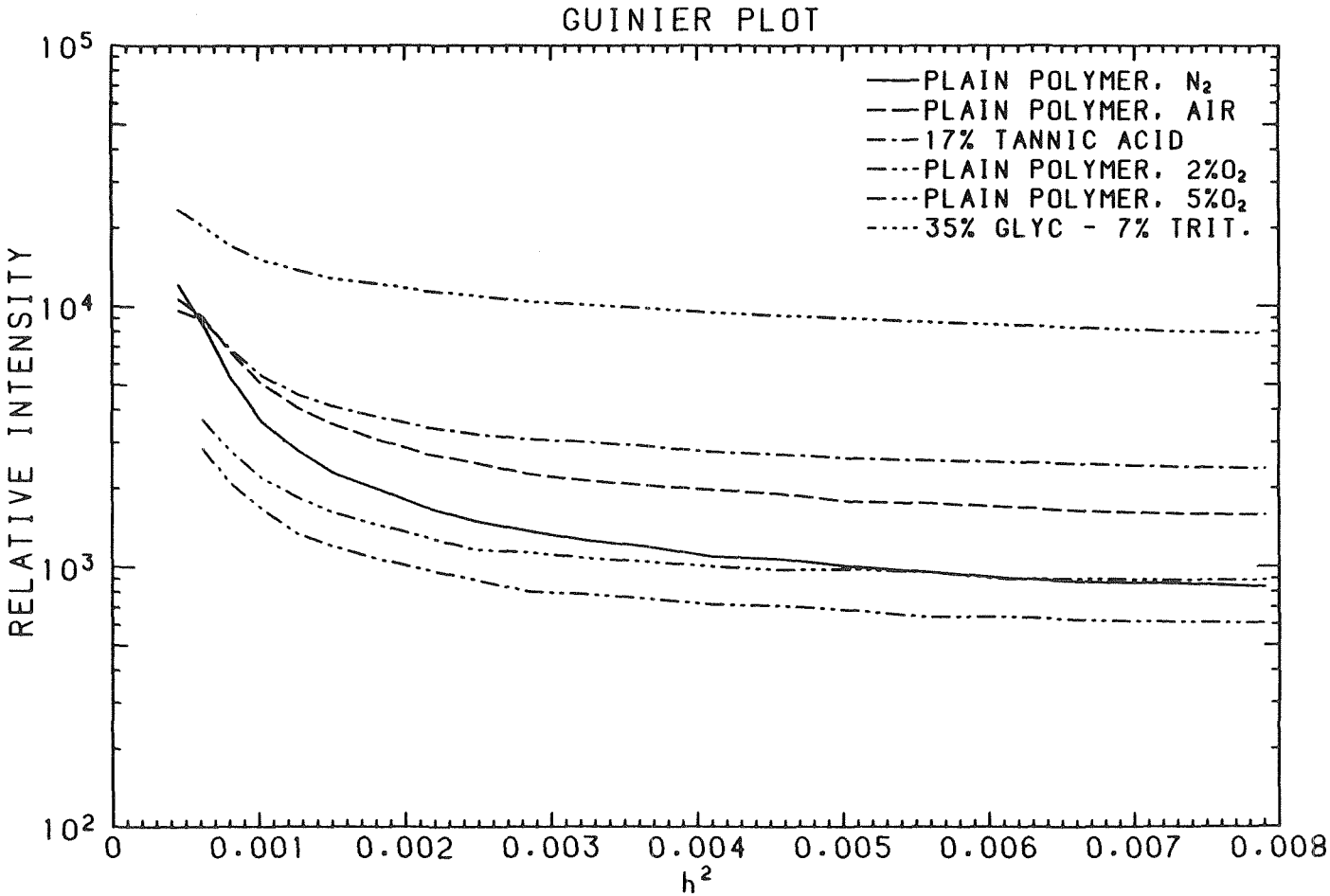

Figure 15: Guinier plot for heat-treated and activated glassy carbons.

CHAPTER 4

Submitted to the *Journal of Physical Chemistry*

Glassy Carbons from poly-Furfuryl Alcohol Copolymers: Structural Studies by High Resolution Solid State NMR Techniques

Hellmut Eckert† Yiannis A. Levendis*
Richard C. Flagan*
† Department of Chemistry,
University of California at Santa Barbara, Goleta California 93106
* Department of Environmental Engineering Science
California Institute of Technology
Pasadena, California 91125

Abstract

The chemical structure of glassy carbon particles produced from polyfurfuryl alcohol (PFA) copolymers is studied by ^{13}C cross-polarization/magic angle spinning (CP-MAS) NMR and high-speed ^{1}H MAS NMR. In agreement with earlier proposals, ^{13}C NMR spectra confirm the buildup of a highly unsaturated system at the expense of furan rings and aliphatic carbon atoms, and upon heating to 800 K this conversion is essentially complete. Successive carbonization by air oxidation or pyrolysis at temperatures up to 1600 K is reflected in a gradual decrease of the ^{13}C chemical shift from ca. 130 to 115 ppm vs. tetramethylsilane. ^{1}H MAS NMR is used to detect and quantitate the amount of residual C– bonded hydrogen species at various stages of the carbonization process. In addition, these spectra show intense, narrow resonances due to sorbed H_2O molecules which resonate over a wide range of chemical shifts (between 2.5 and −8 ppm vs. tetramethylsilane). In analogy with effects observed by Tabony and coworkers for molecules adsorbed above the basal plane of graphite, the upfield shifts observed for water sorbed in the glassy carbons of the present study are attributed to the large susceptibility anisotropy

of submicroscopically ordered, turbostratic or partially graphitized regions of the samples. The extent of this ordering is inversely correlated with the absolute content of residual C– bonded hydrogen species and depends mainly on the temperature of pyrolysis, whereas the oxygen content of the heating atmosphere and the composition of the initial polymeric material are of secondary importance. The results suggest that sorbed H_2O molecules can function as sensitive NMR chemical shift probes for the initial stages of crystallization processes in glassy carbons.

1 Introduction

Glassy carbon materials are produced by pyrolysis of a variety of highly crosslinked polymers[1]. As the result of their extensive network of micropores, these materials possess molecular sieve properties[2]. Their physical and chemical characteristics are largely independent of the chemical nature of the precursor materials, although the degree of porosity can be controlled by mixing certain pore forming agents with the initial polymer, by varying the duration and temperature of the heat treatment and by activation processes through partial oxidation[3]. Polyfurfuryl alcohol (PFA) has been used extensively as a starting material for the production of glassy carbons, because of its high carbon yield[4] and the utility of the resulting materials to function as model systems for studying the combustion of pulverized coal[4,5]. In view of this interest, knowledge of the structural properties and their change during pyrolysis, oxidation and changes of composition is essential. A variety of techniques have been employed including infrared spectroscopy[1,6,7], differential thermal analysis[8,9], dilatometry[8], thermogravimetric analysis[1,6,9], mass spectrometry[10], gas chromatography[11], and traditional solid state nuclear magnetic resonance (NMR) methods[12]. The mechanism of carbonization is thought to involve rupture of the methylene bridges between 400 and 720 K, leading to furan ring-opening, CH_4 elimination, and builtup of condensed aromatic ring systems. Above 720 K elimination of carbon monoxide takes place and at even higher temperatures significant amounts of hydrogen are released, resulting in a highly unsaturated hydrocarbon residue[6,12]. The above mechanism is supported by gas chromatography studies, in which the same order in the evolution of gaseous products is retraced[13].

Important information on the molecular mobility of polyfurfuryl alcohol-based materials carbonized at temperatures between 330 and 1130 K was obtained from NMR lineshape and spin-lattice relaxation studies[12]. Heating at temperatures up to 590 K was found to increase the molecular weight and the degree of crosslinking

to the point where the structural rigidity suppresses any segmental motion of the polymer backbone. Significant hydrogen release was inferred to take place at temperatures above 860 K. However, due to limitations inherent to the techniques used in that study, no structural information could be obtained on a molecular level. In the present study we have applied modern solid state high-resolution NMR techniques to obtain further insight into the process of graphitization. We present here the results of both ^{13}C CP-MAS and ^{1}H high-speed MAS NMR studies on the pyrolysis (650-1600 K) and oxidation (1300-1600 K) of polyfurfuryl alcohol (PFA) and several copolymer materials.

2 Principles of NMR

2.1 *Pulsed Magnetic Resonance Spectroscopy*

NMR spectroscopy involves the absorption of electromagnetic radiation in the radiofrequency portion of the spectrum. It arises from the interaction of the magnetic component of the electromagnetic radiation with the small magnetic moments possessed by atomic nuclei of isotopes with a non-zero spin quantum number I, in an external magnetic field.

Some atomic nuclei, including the most abundant isotopes of carbon (^{12}C), oxygen (^{16}O) and sulfur (^{32}S) have no magnetic properties. For these nuclei, both atomic number and weight are even and thence, the spin quantum number, I, is zero. Such nuclei do not exhibit NMR properties since they possess zero nuclear angular momentum and therefore zero associated magnetic dipole moment. Nuclei for which I is non-zero, like hydrogen (^{1}H), fluorine (^{19}F), phosphorous (^{31}P) and carbon (^{13}C) appear to behave as magnets. When inserted in a magnetic field, they have a preferred lowest energy orientation. Furthermore, for $I = 1/2$, which is the case for the above nuclei, two orientations are possible, one along the external

magnetic field (lowest energy) and one against it (highest energy). Discrete nuclear magnetic moment orientation levels have an energy separation, ΔE, and thence, a resonance frequency, proportional to the magnetic field $\mathbf{B}_0$ applied:

$$\Delta E = \frac{h}{2\pi}\gamma B_0, \tag{1}$$

where h is Planck's constant and γ is the gyromagnetic ratio. Resonance frequencies are usually in the radio-frequency range, 10 to 300 MHz. Since:

$$h\nu_0 = \Delta E, \tag{2}$$

it follows that:

$$\nu_0 = \frac{\gamma B_0}{2\pi} \qquad \text{and} \qquad \omega_0 = \gamma B_0, \tag{3}$$

where $\omega_0 = 2\pi\nu_0$ is called "Larmor frequency." Hence, it is obvious that the Larmor frequency depends on the species of the nucleus, which determine γ, and on the applied magnetic field B_0. The above situation is better illustrated in the schematic below:

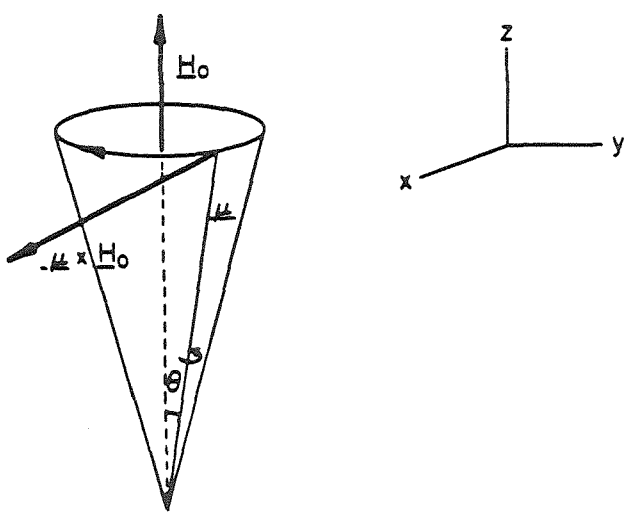

An isolated spinning magnetic moment μ, inclined at an angle θ to the static magnetic field $\mathbf{B}_0$, assumed to be in the z direction, will be subject to a torque $\mu \times \mathbf{B}_0$ in a direction perpendicular to the plane containing μ and $\mathbf{B}_0$. This torque will cause μ to precess about $\mathbf{B}_0$ with angular velocity $\omega_0 = \gamma B_0$. Now, if a small additional field $\mathbf{B}_1$ is applied, rotating in the $x - y$ plane perpendicular to the

direction of the main large field $\mathbf{B}_0$, it will create a torque $\mu \times \mathbf{B}_1$, which will tip μ away from $\mathbf{B}_0$ and increase the angle θ. This is a nuclear magnetic resonance since there is no effect unless $\omega = \omega_0$.

The same physical picture can be applied to an assembly of identical magnetic nuclei with a net magnetic moment $\mathbf{M}$. Application of an $\mathbf{B}_1$ radio-frequency, (*rf*), field tips $\mathbf{M}$ away from $\mathbf{B}_0$ and generates transverse magnetic components M_x and M_y, which decay to zero exponentially with a characteristic time T_2 called the *spin-spin relaxation time.* This decay has the form of an exponentially-decaying sine wave and is called *Free Induction Decay (FID).* The angle through which $\mathbf{M}$ is tipped determines the size of M_y and, therefore, the intensity of the signal detected by the receiver. This angle is called the flip angle, α, and is related to $\mathbf{B}_1$ γ, and t_p, the length of the time period that B_1 is applied, by the following equation:

$$\alpha = \gamma B_1 t_p \tag{4}$$

The longitudinal component M_z is restored to its equilibrium value with characteristic time T_1 the *spin lattice relaxation time.* Generally the measured *FID* consists of many superimposed exponentially-decaying sine waves that originate from different nuclear environments. The frequency spectrum is obtained by taking the Fourier Transform of the *FID*:

$$J(\omega) = \int_{-\infty}^{\infty} K(t) \exp(-i\omega t) dt. \tag{5}$$

2.2 *The Chemical Shift*

It has been shown above that when a sample containing magnetically active nuclei is placed in a magnetic field, energy will be absorbed when the frequency of the radiation of an applied *rf* field corresponds to the difference between energy levels. In NMR experiments, either the magnetic field $\mathbf{B}_0$ is kept constant and the *rf* field is varied or vice-versa. For any particular kind of magnetic nucleus, the strength

of the external magnetic field, $\mathbf{B}_0$, required to provide a field at the nucleus, $\mathbf{B}_{0,n}$, enough to cause resonance, varies slightly with the structural environment of the nucleus. This small variation in the magnetic field is called the *Chemical Shift*. By denoting as $\mathbf{B}_{0,s}$, the small amount by which the external field is diminished because of the influence of the electrons in the environment of the nucleus, then:

$$\mathbf{B}_{0,n} = \mathbf{B}_0 - \mathbf{B}_{0,s}$$

$$\text{or} \qquad 2\pi\nu_0 = \gamma B_0(1-\sigma), \tag{6}$$

where σ is the screening constant or shielding parameter. Thus, the actual frequency ν_0 depends both on the amount of screening (the chemical surroundings of the nucleus) and on the magnetic field under which the measurement is made. The chemical shift, δ, of a given peak is usually given with reference to a standard signal, such as the proton or carbon signal of tetramethyl silane (TMS) and is defined by the relationship:

$$\delta = \frac{\nu_{peak} - \nu_{TMS}}{\nu_0}, \tag{7}$$

where ν_0 is the operating frequency in MHz. This fractional type of unit has the advantage of being independent of the magnitude of $\mathbf{B}_0$, even though shielding depends on the strength of the external field. Therefore, the use of this relative unit enables direct comparison of spectra obtained from instruments employing different magnitude external fields and thence different *rf* fields.

Even if the quality of energy, absorbed by various magnetically active nuclei is different, the quantity of energy absorbed is proportional to the number of nuclei responsible for the absorption. Therefore, the total area under the peak gives information about the relative number of nuclei for which resonamce occurs at different chemical shifts. With appropriate calibration of the apparatus and for the case of pure compounds, it may be possible to estimate the absolute number of nuclei responsible for the peak.

Magnetic resonance experiments usually involve several nuclei that are magnetically coupling each other. This creates multiplicity of resonance peaks (splitting pattern) or broadening of peaks, is independent of the size of the external field and can be eliminated by various decoupling techniques. In the case of ^{13}C NMR, heteronuclear decoupling of protons and ^{13}C nuclei eliminates dipolar broadening. This method employs a second radio-frequency field, which is at or near the Larmor frequency of the protons, thereby inducing rapid transitions between the proton energy levels so that the ^{13}C nuclei see an averaged proton field. Because of the low abundance of the ^{13}C isotope, carbon-13 homonuclear interactions are relatively small, and homonuclear decoupling is not necessary.

2.3 *Basic principles of high resolution ^{13}C and ^{1}H NMR in the solid state.*

In contrast to the high resolution achievable in liquid-state NMR, polycrystalline and amorphous solid samples produce NMR spectra that are severely broadened by direct dipole-dipole interactions as well as the anisotropy (i.e. the orientational dependence) of the chemical shift. For an isolated pair of spins the internuclear dipole-diople interaction will cause a splitting into two lines, the separation of which allows determination of the internuclear distance[14]. In the more general case, however, larger ensembles of nuclear dipoles interact, resulting in a structureless broadening of the spectrum, and a concomitant loss of structural information. However, the effect of the magnetic dipole-dipole interactions (as well as the chemical shift anisotropy) can be removed by rapid spinning of the sample at the angle of 54.7° with respect to the static field direction[15]. This technique ("magic-angle-spinning (MAS) - NMR") forms the basis of most high-resolution NMR studies in solids. Spinning speeds required depend on the strength of the dipolar interactions to be time-averaged; in the case of ^{1}H MAS-NMR, speeds of 5-8 kHz are not untypical,

but frequently insufficient[16].

For solid state ^{13}C high-resolution NMR studies the MAS-NMR technique is usually combined with crosspolarization and high-power decoupling from neighboring ^{1}H nuclear spins[17]. The cross-polarization technique takes advantage of the large nuclear polarization of the abundant proton spin system, if the effective precession frequencies in the rotating frame of both types of nuclei are matched. This is achieved by spin- locking the ^{1}H magnetization in a radio-frequency field $B_{1,H}$ and applying a radio-frequency field $B_{1,C}$ at the ^{13}C frequency such that the Hartmann-Hahn condition[18]:

$$\gamma_C B_{1,C} = \gamma_H B_{1,H} \tag{8}$$

is fulfilled, where γ_H and γ_C are the gyromagnetic ratios of ^{1}H and ^{13}C respectively. At the end of this "contact period" (typically 1-5 ms), the proton radio-frequency field is left on in order to provide high power decoupling during the period in which the ^{13}C free induction decay is acquired.

A modification of the above technique can be employed to discriminate between protonated and non-protonated carbon atoms by taking advantage of the different strengths of their $^{1}H-^{13}C$ dipolar interactions. The addition of a delay time of 60-100 μs after the cross polarization period but before the decoupling and acquisition period results in a dephasing of all signals arising from protonated carbon atoms and, therefore, facilitates the selective observation of non-protonated carbon atoms.[19] Protonated carbons can also be selectively identified by measurements employing short contact times (100 μs or less), since the proton-carbon cross-relaxation times are greatly reduced due to the stronger dipolar coupling for these carbon nuclei.

3 Experimental

3.1 *Sample Preparation and Characterization*

The glassy carbon materials under investigation were synthesized from three basic ingredients consisting of a carbon yielding binder, a mixing agent and a pore forming agent. The binder was furfuryl alcohol partially polymerized with the aid of para-toluenesulfonic acid catalyst. Acetone was added to the polymer in the ratio of 2 to 1 by volume to lower the viscosity of the polymer and to facilitate mixing and subsequent atomization. Finally various organic liquids or solids were dissolved or suspended in the polymer-acetone mixture to serve as pore forming agents. The mixtures were fed through a syringe pump to an acoustically excited aerosol generator and were susequently sprayed inside an externally heated thermal reactor. The full description of this system and the thermal reactor is given elsewhere[5]. Following this procedure equal sized droplets were generated, heated to a maximum temperature of 650 K in an inert atmosphere to evaporate the solvent and form solid particles, and collected by sedimentation at the bottom of the reactor. The total residence time in the reactor was approximately 4 s. Pores, in addition to those of the polymer matrix, were generated by evaporation or decomposition of the liquid pore former during the heat treatment and/or by thermally induced stresses and cracks for the case of the solid pore formers. To eliminate sticking of the collected spherical particles all materials underwent a second stage pyrolysis treatment at 800 K in a horizontal muffle furnace in N_2 for 1 hr. Some samples were carbonized further in N_2 or partially combusted in O_2-N_2 mixtures at temperatures up to 1600 K in an externally heated, laminar flow, drop tube furnace. The residence times in this last furnace varied between 2 and 3.5 s. The particle temperature was monitored by optical pyrometry[5]. A typical Scanning Electron micrograph of monodisperse particles cured at 800 K is shown in Fig. 1.

The materials used in the present study were particles formed from PFA alone as well as particles formed from mixtures of PFA with various amounts of the following pore formers: *tannic acid, polyethylene glycol (PEG), glycerol*, and *Triton-X 100.*

Elemental analysis of the materials at various degrees of carbonization and oxidation was performed by oxidizing samples at 1100 K in O_2 and monitoring the products of combustion with the aid of a *Perkin Elmer* analyzer. Tables I-III give an overview of the samples studied, their carbon and hydrogen contents, and (where appropriate) their amount of "burnout", corresponding to the weight loss on high temperature oxidation. X-ray diffraction patterns were recorded on film with a *Guinier* powder camera using monocromatic CuKα radiation[20]. Typical spectra traced by an *Ultrascan XL* laser densitometer are shown in Figure 2. Representative TGA results, obtained on a *Dupont model 920* electrodynamic balance, are shown in Figure 3. Typically, substantial weight loss occurs in the temperature range 50-60 °C; as discussed below, most of this weight loss arises from desorption of inclusion water. Total surface areas, measured by N_2 BET at 77 K, were found to be a few m^2/g for the pristine materials (cured at 800 K), increasing to a few hundred m^2/g for the partially oxidized (activated) carbons.[20]

3.2 *NMR Techniques*

Both Proton and ^{13}C CP-MAS NMR data were obtained at room temperature on a home-built double resonance high power spectrometer[21], controlled by a *Nicolet 1280* data system, and a 293B pulse programmer.

^{13}C CP-MAS NMR experiments were carried out 50.36 MHz, in a probe from Doty Scientific Inc., using sapphire sample spinners of 7 mm o.d. Hartmann-Hahn matching was obtained at a radio-frequency field strength of 1.2 mT (90° pulse lengths 5 μs). Measurements of signal areas versus cross-polarization contact times established that no significant changes in the relative peak intensities occur for

contact times between 2 and 5 ms. Consequently, all measurements were carried out using contact times within this range. The Hartmann-Hahn matching condition was set on an adamantane standard, whose methylene peak also provided a secondary chemical shift reference at 38.56 ppm from TMS[22]. High power decoupling was applied during the acquisition period of 20 ms. The cross polarization pulse program incorporated spin temperature inversion[23] to suppress artifacts, and '*flipback*' of the ^{1}H magnetization into the z-direction by an additional 90°_{-x} pulse at the end of the acquisition period. Dipolar dephasing experiments[19], using a 70 μs delay time prior to data acquisition, as well as short contact time experiments (50 μs), were carried out to distinguish between protonated and non-protonated carbon atoms, as described in the previous section. Serious probe detuning problems arose for the case of the oxidized samples due to their enhanced electrical conductivity. Since no satisfactory Hartmann-Hahn matching conditions could be obtained for those samples, their resonances were detected by ^{13}C-MAS NMR with high power proton decoupling. The spectra were usually baseline-corrected by either using the Nicolet software or by left shifting the free induction decay by 100 μs. The FID's were then multiplied by an exponential filter function equivalent to a Lorentzian line broadening of 10-20 Hz and zero filled from 1K to 4K data points prior to Fourier transformation.

^{1}H MAS-NMR experiments were carried out at 200.27 MHz in a high-speed probe from Doty Scientific, at spinning speeds between 5 and 8 kHz, using sapphire spinners of 5 mm o.d. Additional variable temperature measurements were performed on a General Electric GN 300 system, using a Chem-Magnetics probe (spinning speed ca. 3.5 kHz). Free induction decays were accumulated by regular single-pulse acquisition (90° pulse length 1.8-2 μs). Spin lattice relaxation times, measured by the inversion recovery method, were generally found to be 1 sec or less. Thus, quantitative spectra were readily obtained under non-saturating condi-

tions. The free induction decays were multiplied by an exponential filter function, equivalent to a Lorentzian line broadening of 10-20 Hz, and were zero-filled from 4K to 16K data points, prior to Fourier transformation. A spinning sample of hydroxyapatite was used as a secondary reference material, which resonates 0.2 ppm downfield of tetramethylsilane[24].

4 Results and Assignments

4.1 *Structural Studies by ^{13}C CP-MAS NMR*

. Figure 4a shows the ^{13}C CP-MAS NMR spectra obtained for the plain PFA material as collected in the thermal reactor after exposure to a maximum temperature of 650 K. Assignments of the resonances were made in accord with delayed decoupling and short contact time experiments (see Figs. 4b and c) and are in agreement with the chemical shifts measured in solution for model compounds based on the furan unit. The ratio of the aromatic carbon to the total carbon in the char, as obtained by peak integration, was found to be 0.75, which is within experimental error from 0.8, the value expected from the structural formula. The NMR spectra thus indicate that the material has retained most of the features of the polymer precursor.

The spectrum acquired with a short contact time (Figure 4b) exhibits several additional weak peaks. We ascribe these peaks to thermal decomposition processes, which have been reported to occur for PFA polymer at temperatures as low as 650 K.[6] Specifically, we assign the small peak on the downfield side of the aliphatic peak around 45 ppm to CH_2-OH groups that may form during breakage of the furan rings.

The effect of pyrolysis at 800 K for 1 hr in N_2 is shown in Fig. 5a. The resonances arising from the starting polymer have diminished to $\approx$ 10% of the total area and are hardly discerned from a broad new peak at 130 ppm, which dominates the

spectrum. The chemical shift of this resonance is typical of unsaturated C−atoms, either of olefinic nature or arising from aromatic rings. The spectra obtained for other copolymer chars heat treated under the same conditions exhibit very similar features as the PFA char or glassy carbons made from resocinol-formaldehyde resins[25]. It is worth noting that the chemical structure of the chars after this stage of heat treatment resembles the structure of coal chars inasmuch as methylene bridges between aromatic rings are not present anymore[25−27]. These observations are consistent with the earlier proposal[6] that at this range of temperatures the furan rings open and eliminate water to form new highly unsaturated structures. The results of this study show that ^{13}C CP-MAS NMR could be used to monitor this conversion in a quantitative manner.

^{13}C CP-MAS NMR studies of the effects of heat treatment and oxidation at temperatures above 800 K proved difficult due to probe tuning problems arising from the high conductivity of these materials, as noted elsewhere for graphites[28]. Furthermore, as discussed by Resing et al. in a similar study on charcoals[29], ^{13}C CP-MAS NMR spectra are not necessarily representative of the entire carbon contents of these highly carbonized materials. This problem arises because the proton-bearing species required for the cross-polarization process are either too dilute or too mobile to function as an efficient spin-bath in these systems. Direct ^{13}C NMR detection with high power proton decoupling and magic angle spinning yielded very broad spectra whose center of gravity shifts from ca 130 ppm to ca. 115 ppm with increasing temperature of thermal treatment. While these data are in good agreement with the approximate values measured in charcoals[29], we cannot rule out that some ^{13}C spins with long spin-lattice relaxation times may have remained undetected. While ^{13}C CP-MAS NMR is the method of choice for studying the transformations that take place in the chemical structure of PFA-polymer during pyrolysis up to ca. 800 K, it appears overall less suitable to study the processes that occur during

carbonization at higher temperatures.

4.2 *^1H MAS-NMR Experiments*

Results of ^1H MAS-NMR experiments on PFA and copolymer materials pyrolyzed in N_2 in the range of 650-800 K are summarized in Table I and Fig. 6. The spectrum of the PFA char (collected after heating at 650 K), Fig. 6a, shows a broad centerband, flanked by a wide spinning sideband pattern, which reflects the strong homonuclear dipolar interactions among the protons in this material. MAS-NMR at 5 kHz is not sufficient to remove these interactions fully; for this reason, no clear distinction between aromatic and aliphatic hydrogen atoms is possible. The spectra of materials pyrolyzed at 800 K (Figure 6b) are still dominated by this hydrogen type, although in view of the ^{13}C CP-MAS results described earlier, these protons must be chemically different from those of the initial starting material. However, ^1H MAS NMR is not able to resolve any chemical differences between the initial PFA structure and the thermally converted product, since in both cases the resolution is limited by strong homonuclear dipole-dipole interactions. For the purpose of distinction between the various types of hydrogen atoms observed in the present study, these C-bonded protons, occurring as part of a largely intact unsaturated hydrocarbon structure, are labeled "type I". Inspection of Fig. 6 shows that upon pyrolysis at 800 K an additional sharp resonance at ca. 2 ppm, "hydrogen type II", appears. Among the various polymer compositions studied, the chemical shift of this additional peak varies very little (2 to 2.8 ppm), and its fractional area, listed in Table I, is comparable for all the samples pyrolyzed at 800 K, amounting to 12-19% of the total area. Heating the sample to 60° C in an open atmosphere causes the sharp line to disappear; exposure to laboratory atmosphere for 3 hrs results in its re-appearance with the same spectroscopic parameters and comparable integrated area. These experiments establish that the sharp line is due to water molecules

sorbed by the material from the atmosphere. Its room temperature spectroscopic characteristics meet all of the criteria that are typical of a species experiencing motionally averaged chemical environments[16]. The sharpness of the centerband, down to very low spinning speeds, the weak intensities of the spinning sidebands, as well as the narrow linewidth (ca. 2 kHz) observed for this component in non-spinning samples reveal a substantial reduction of the internuclear dipole-dipole couplings and chemical shift anisotropies by molecular motion.

^{1}H MAS NMR spectra of plain PFA polymer chars pyrolyzed or oxidized at temperatures ranging between 1300 and 1600 K are shown in Fig. 7; their features are summarized in Table II. Spectra and properties of chars made from tannic acid (18 and 50%) and PFA are shown in Figure 8 and included in Table III. The higher the temperature of oxidation, the weaker the "type-I" signals become, reflecting the progress of carbonization at elevated temperatures. Even in the most highly carbonized glassy carbons, MAS at 3-5 kHz does not result in appreciable line-narrowing for this component. This observation reveals that these glassy carbons (like most glasses) are best characterized as microheterogeneous systems, where regions rich in type-I hydrogens coexist with highly carbonized domains.

In addition to the type-I species all samples combusted at temperatures above 800 K show two new sharp resonances with variable, pronounced upfield shifts. As in the case of the pyrolyzed samples discussed above, both new peaks can be assigned to sorbed water, since they disappear upon heating to 60° C in an open atmosphere for 1h, and re-appear with their original chemical shifts after re-exposure to laboratory atmosphere. This assignment is also consistent with the observed TGA behavior (Fig. 3). For the purpose of identification, the smaller downfield peaks, shown in Fig. 7 and 8, are labeled type IIa and the (dominant) upfield peaks are labeled type IIb (Tables II and III). As for the type-II species discussed above, the room-temperature MAS-NMR chemical shifts represent values that are averaged over a

range of possible environments by rapid molecular motion. Figure 9 shows that this motion is gradually frozen out on the NMR timescale at temperatures below −60°C. In contrast to the well resolved spinning sideband patterns frequently observed in the slow-motion regime for isolated water molecules present in crystal hydrates, hydrous minerals, and silicate glasses[16,24,30], the low-temperature ^{1}H MAS-NMR spectra of the glassy carbons (heat treated to 1600 K) are broad and structureless. This result indicates that the water molecules are clustered within the pores (whose diameters typically range about 10-25$\AA$ for the carbonized and oxidized samples at 1300-1600 K [20]).

5 Discussion

5.1 *Chemical shifts and Ordering States in Glassy Carbons*

The strongly negative shifts observed especially for the sample combusted at the highest temperatures and the unusually wide range (2.4 to −8 ppm) over which the chemical shifts of the sorbed water species (type II, IIa and IIb) can vary, belong to the most striking features observed in the present materials. Effects of this kind have been observed for adsorbates on other carbonaceous materials, such as water on cokes[31], xenon on grafoil[32], and a variety of molecules adsorbed on the basal plane of graphitic carbon black[33–35]. We also note that, to date, no significant upfield shifts have been observed for glassy carbons, although an "anomalous" resonance at 0.8 ppm has been noticed for a glassy carbon derived from carbonized resorcinol-formaldehyde resin.[36] Previous discussions[31,33–35] have attributed such effects to the fact that the molecules are adsorbed on the basal plane of the graphite surface where they experience a strongly diamagnetic component of the highly anisotropic magnetic susceptibility[37] of the graphitic lattice. Thus, the resonance of water was reported to shift upfield by ca.15 ppm upon adsorption on crystalline graphite,

whereas no significant shift was observed for water adsorbed on amorphous carbon black[33]. Following the above interpretation, we suggest that the upfield shifts observed for the samples of the present study reflect the degree to which the interior pore surfaces resemble the "honeycomb"- like graphite surface. The NMR chemical shifts thus appear to be sensitive indicators of submicroscopic ordering processes that might eventually lead to partial crystallization. Indeed, the samples that have the most negative chemical shifts (below -5 ppm) and a clearly discernible shoulder at -8 ppm, are the only ones that exhibit some sharp reflections characteristic of either turbostratic or graphitic ordering in x-ray powder diffraction studies (see Figure 2) [20]. Highly upfield shifts are, however, also observed in the absence of any sharp diffraction peaks. Assuming a correlation between submicroscopic ordering and the extent to which carbonization (and graphitization) has occurred, it is expected that the magnitude of these shifts be inversely correlated with the amount of residual C− bonded, type-I hydrogen atoms of the material. The amount of residual C− bonded hydrogen is easily obtained from the total hydrogen contents determined by chemical analysis, and the NMR speciation listed in Tables I-III. Figure 10 reveals that the upfield shielding of the sorbed water species (weighted average of type-II, type-IIa, and type-IIb species) shows indeed a distinct inverse correlation with the absolute type-I hydrogen content. This correlation clearly illustrates that the sorbed water molecules are very sensitive chemical shift probes for the submicroscopic ordering processes in the microporous glassy carbon material at different stages of heat treatment. The qualitative form of the dependency observed corresponds well with physical intuition: In the initial stages of carbonization where graphitic ordering is absent, very little change in the shielding parameters of the sorbed water molecules is expected (and seen), whereas below a certain 'critical' concentration of C-bonded hydrogen the onset of turbostratic and graphitic structural ordering and the associated increase of the domain sizes produce the largest changes. We thus

conclude that ^{1}H MAS NMR of the sorbed water molecules in these glassy carbon atoms can be used to probe and (to some extent) quantify submicroscopic ordering during the intermediate stages of the graphitization process, where the samples still appear totally x-ray amorphous. Figures 7 and 8 illustrate that the degree of submicroscopic ordering increases strongly with the heat treatment temperature. Geschke found a similar dependence in cokes, although the chemical shift effects in his study were much smaller[31]. Similar trends, dependent on heat treatment temperature, have been observed for the bulk diamagnetic susceptibility of glassy carbons[38]. We note, however, that the changes in bulk susceptibility alone cannot be responsible for chemical shift trends observed in the present study, because their effect is removed by magic angle spinning[39]. Rather, the effect is attributed to a specific interaction between the H_2O molecules and the partially ordered internal surfaces of these materials.

Figure 11 indicates a similar correlation of the chemical shift with burnout (percentage of mass lost by oxidation). However, even though changes in O_2 partial pressure *at constant combustion temperature* dramatically affect the burnout, they cause only small chemical shift changes (component IIb). This shows that the degree of submicroscopic ordering is mainly affected by the temperature of pyrolysis, whereas the oxygen partial pressure of the pyrolysis atmosphere exhibits only a secondary effect, as noted previously.[20,40] In addition, Figs. 10 and 11 show that the influence of the starting polymer mixture composition on the degree of ordering on the average is minor.

5.2 *Bimodal Distribution of Sorbed Water Species in Glassy Carbons*

In addition to the dominant type-IIb resonance observed in all samples pyrolyzed above 800 K, Figures 5 and 6 show a weaker downfield signal ("type IIa") at a

somewhat variable shift (2 to −1 ppm) adjacent to the range usually observed for the type-II signals in the samples pyrolyzed at 800 K. Thus, in all of these samples at least two well-defined water sites are present. The NMR results indicate that at room temperature both water species are highly mobile, resulting in the measurement of a chemical shift that is the dynamic average over a (possibly wide) range of environments. On the other hand the observation of two distinct resonances indicates that dynamic exchange of the sorbate *between* these sites is slow on the NMR timescale. This might suggest that they occur within very distinct regions in the sample, characterized by very different degrees of ordering. Such an interpretation seems plausible, because the IIa species concentration tends to decrease with increasing heating temperature. On the other hand, we note that type IIa peaks are absent or greatly diminished in materials pyrolyzed, under otherwise identical conditions, in inert atmospheres or at reduced O_2 partial pressures (2 and 5 wt.%, see Fig. 12). This suggests that the type-IIa peaks are directly associated with the presence of oxygen during high-temperature treatment, which possibly results in some carbon-oxygen bonds on the internal surface of the glassy carbon.[41] Thus the type-IIa resonances may represent water molecules in the vicinity of such sites. This explanation could also account for the smaller upfield shifts observed for this species, since the presence of such sites would impede graphitic ordering.

6 Conclusions

The structure of polyfurfuryl alcohol (PFA) copolymer chars was investigated by ^{13}C CP-MAS NMR and ^{1}H MAS NMR. The ^{13}C NMR spectra confirm that the particles collected after heat treatment of partially polymerized PFA aerosols in N_2 for 4 s at temperatures up to 650 K retain their chemical identity while pyrolysis of this material at 800 K leads to almost complete conversion to a highly unsaturated structure. Upon carbonization at higher temperatures the ^{13}C NMR

resonance shifts upfield; however, the quantitative nature of the experiment becomes questionable.

^{1}H MAS NMR spectra of water molecules sorbed by the extensive pore structure of these glassy carbons show strong upfield shifts, suggesting the presence of submicroscopic ordering processes in these materials. The extent of this ordering is correlated with the degree of carbonization, as monitored by the absolute content of residual C– bonded hydrogen. For materials exhibiting two- and three phase graphitization as indicated by x-ray diffraction studies chemical shifts as low as −8 ppm are recorded. The present results suggest the utility of ^{1}H MAS-NMR of sorbed water molecules in probing the intermediate stages of graphitization of glassy carbon materials. The recent successes of using sorbed xenon as a sensitive NMR probe of site discernment in zeolites[42,43] suggest this technique as an obvious means of a finer shift discrimination and possibly resolution of more distinct sites in glassy carbons as well. Such studies are presently under consideration.

7 Acknowledgments

The NMR data were obtained at the Southern California Regional NMR Facility, supported by NSF Grant CHE84-40137. The materials preparation and characterization was supported by U.S. Department of Energy University Coal Programs Grant Number DE-FG22-84PC70775. The authors are grateful to Larry Henling for performing the elemental analysis of the materials.

8 References

1. Fitzer, E., Schafer, W.; Yamada, S.; *Carbon* **1969**, 7, 643.

2. Schmitt,Jr. J. L. and Walker,Jr. P. L. **1972**, 10, 87.

3. Walker, Jr. P. L.; Oya, A.; Mahajan, O. P. *Carbon* **1980**, *18*, 377.

4. Senior, C. L.; Flagan, R. C.; 20th Int. Symp. on Combustion, The Combustion Institute **1984**, 921.

5. Levendis, Y. A.; Flagan, R. C. *Combust. Sci. and Tech.* **1987**, *53*, 117.

6. Fitzer, E.; Schäfer, W. *Carbon* **1970**, *8*, 353.

7. R. T. Conley and I. Metil, *J. Applied Polymer Sci.* **1963**, *7*, 37.

8. Nakamura, H. H.; Atlas, L. M. *Proc. Fourth Conference on Carbon*, **1960**, 625.

9. Dollimore, D; Heal, G. R. *Carbon* **1967**, *5*, 65.

10. Saxena, R. R.; Bragg, R. H. *Carbon* **1978**, *16*, 373.

11. Lewis, I.C. *Carbon* **1982**, *20*, 519; Greinke, R. A.; Lewis, I.C. *Anal. Chem.* **1975**, *47*, 2151.

12. Glowinkowski, S.; Pająk, Z. *Carbon* **1982**, *20*, 13.

13. O'Neil, H. J.; Putscher, R. E.; Dynako, A.; Boquist, C. *J. Gas Chromatography* **1963**, *1*, 28.

14. Pake, G. E. *J. Chem. Phys.* **1948**, *16*, 327.

15. Andrew, E. R.; Bradbury, A; Eades, R. G. *Nature* **1959**, *183*, 1802; Lowe, I. *Phys. Rev. Lett.* **1959**, *2*, 285.

16. Yesinowski, J. P.; Eckert, H.; Rossman, G. R. *J. Am. Chem. Soc.* **1988**, in press.

17. Schäfer, J.; Stejskal, E. O.; Buchdahl, R. *Macromolecules* **1975**, *8*, 291.

18. Hartmann, S. R.; Hahn, E. L. *Phys. Rev.* **1962** *128*, 2042.

19. Alla, M; Lippmaa, E. *Chem. Phys. Lett.* **1976**, *37*, 260

20. Levendis, Y. A.; Flagan, R. C., submitted for publication.

21. Yesinowski, J. P.; Eckert, H.; Sandman, D. J.; Velazquez, C. S. *ACS Symposium Series*, **1987**, *337*, 230.

22. Earl, W. L; VanderHart, D. L. *J. Magn. Reson.* **1982**, *48*, 35.

23. Stejskal, E. O.; Schaefer, J. *J. Magn. Reson.* **1975**, *18*, 560.

24. Yesinowski, J. P.; Eckert, H. *J. Am. Chem. Soc.* **1987**, *109*, 6244.

25. Schmiers, H.; Schröter, B. *Z. Chem.* **1982**, *22*, 393.

26. Brown, J. K.; Ladner, W. R.; Sheppard, N. *Fuel* **1960**, *39*, 79.

27. Brown, J. K.; Ladner, W. R. *Fuel* **1960** *39*, 87.

28. Retcofsky, H. L.; Friedel, R. A. *J. Phys. Chem.* **1973**, *77*, 68.

29. Resing, H. A.; Hodgeman, D. K. C.; Baker, J. A.; Poziomek, E. J. *Carbon* **1985**, *23*, 395.

30. Eckert, H.; Yesinowski, J. P.; Silver, L. A.; Stolper, E. M. *J. Phys. Chem.* **1988**, in press

31. Geschke, D.; *Z. Phys. Chem.* **1968**, *239*, 138.

32. Shibanuma, T.; Asada, H.; Ishi, S.; Matsui, T. *Japan. J. Appl. Phys.* **1983**, *22*, 1656.

33. Tabony, J., *Prog. NMR Spectrosc.* **1980**, *14*, 1.

34. Tabony, J.; Bomchil, G.; Harris, N.; Leslie, M.; White, J. W.; Gamlen, P.; Thomas, R. K.; Trewern, T. D. *J. Chem. Soc. Faraday Trans.* I **1979**, *75*, 1570.

35. Tabony, J.; White, J. W.; Delachaume, J. C.; Coulon, M. *Surf. Sci. Lett.* **1980**, *95*, L282.

36. Schmiers, H.; Rosenberger, H.; Scheler, G. *Z. Chem.* **1982**, *22*, 424.

37. Myers, K. J. *Molecular Magnetism and Magnetic Resonance Spectroscopy*, Prentice Hall, 1973.

38. Fischbach, D. B.; Rorabaugh, M. E. *Carbon* **1983**, *21*, 429.

39. Garroway, A. N. *J. Magn. Reson.* **1982**, *49*, 168.

40. Noda T.; Inagaki, M. *Carbon* **1964**, *2*, 127.

41. Yousseff, A. M.; Ghazy, T. M.; El-Nabarawy, Th. *Carbon* **1982**, *20*, 113.

42. Ripmeester, J. A. *J. Magn. Reson.* **1984**, *56*, 247.

43. Ripmeester, J. A. *J. Am. Chem. Soc.* **1982**, *104*, 289.

9 Figure Captions

1. Electron micrograph of glassy carbon particles made from 18% polyethylene glycol and PFA cured at 800 K for 1 hr (space bar denotes 10μm).

2. X-ray powder diffraction traces of representative samples. The *(002)* diffraction peak profiles result from stacks of parallel layer planes; the *(100), (110)* peaks result from regular structure within the individual layer plane segments; and the *(103)* peak indicates three dimensional ordering. Broad peaks correspond to the disordered phase; sharp peaks correspond to the crystalline phases.

3. Thermal Gravimetric Analyses of

   (a) PFA polymer pyrolyzed in N_2 for 3.5s at 1600 K

   (b) PFA polymer oxidized in air for 3s at 1600 K

4. ^{13}C CP-MAS NMR spectra of PFA chars cured at 650 K. Peak assignments are indicated.

   (a) spectrum obtained with a 2 ms contact time,

   (b) spectrum obtained with a 50 μs contact time for selective observation of protonated carbons

   (c) spectrum obtained with a contact time of 2 ms and acquisition delayed for 70 μs, for selective observation of unprotonated carbons.

5. ^{13}C NMR spectra of PFA carbons. The features upfield and downfield of the main resonances are spinning sidebands. (a) ^{13}C CP-MAS NMR spectrum of PFA pyrolyzed at 800 K,

   (b) ^{13}C CP-MAS NMR spectrum of PFA partially oxidized at 1500 K at 10% O_2 for 2 sec.

(c) ^{13}C MAS NMR spectrum with ^{1}H decoupling of PFA partially oxidized at 1600 K in air for 2 s. Spectrum not-baseline corrected.

6. ^{1}H MAS NMR spectra of plain PFA chars. The features upfield and downfield of the dominant central peaks are spinning sidebands.

   (a) PFA polymer "as collected" after heat treatment at 650 K,

   (b) PFA polymer after pyrolyzing the initial product at 800 K for 1 h,

   (c) PFA copolymer with 18 wt.% polyethylene glycole (PEG) pyrolyzed at 800 K for 1 h.

7. Effect of oxidation temperature upon the ^{1}H MAS NMR spectra of PFA polymer chars oxidized in in air for 2 s. The temperatures of treatment are indicated in the figure.

8. Effect of pyrolysis or oxidation temperature upon the ^{1}H MAS-NMR spectra of chars based on PFA copolymers with tannic acid. The conditions of treatment are indicated in the figure,

   (a) PFA copolymer chars made from 17 wt.% tannic acid and PFA,

   (b) PFA copolymer chars made from 50 wt.% tannic acid and PFA.

9. 300 MHz variable temperature ^{1}H MAS NMR spectra of PFA polymer heat-treated at 1600 K for 2 s in nitrogen. Table IV (inset) shows the chemical shifts corresponding to various temperatures during NMR.

10. Dependence of the ^{1}H MAS NMR chemical shifts (vs. tetramethylsilane) of sorbed water in all of the glassy carbon chars investigated on the residual content (in wt.%) of C– bonded hydrogen in the char (see text).

11. Dependence of the ^{1}H MAS NMR chemical shifts on particle burnout in all of the glassy carbon chars investigated. Solid line: constant oxygen partial

pressure (0.21) and variable temperature (——). Dashed line: constant temperature (1500 K) and variable oxygen partial pressure (- - -). For the latter comparison, respective samples are indicated by arrow.

12. Effect of the heat treatment atmosphere on the ^{1}H MAS-NMR spectra of PFA chars at constant temperature (1500 K).

TABLE I

Properties of Glassy Carbon Materials

MATERIAL	Hydrogen Species (NMR)[a]	δ_{iso} (ppm) ±0.1	BURNOUT	Chemical Analysis	
				$\%H_2$ [b]	%C
PFA[c] cured at 650 K	100% Type I	5.9	0%	5.0	73.7
PFA cured at 800 K	12.8% Type II 87.2% Type I	2.1 *	0%	3.45 (3.01)	85.8
PFA + 18% tan.ac.[d] cured at 650 K	100% Type I	5.5	0%	*	*
PFA + 17% tan.ac. cured at 800 K	15.9% Type II 84.1% Type I	2.2 *	0%	3.0 (2.51)	87.2
PFA + 50% tan.ac. cured at 800 K	15.9% Type II 84.1% Type I	2.5 *	0%	3.08 (2.59)	82.6
PFA + 8% tan.ac. cured at 800 K	14.0% Type IIb 15.3% Type II 70.7% Type I	−3.1 2.0[h] *	0%	1.92 (1.36)	91.02
PFA + 9% PEG[e] cured at 800 K	17.2% Type II 82.8% Type I	2.0 *	0%	3.25 (2.69)	87.5
PFA + 18% PEG cured at 800 K	19.3% Type II 80.7% Type I	2.4 *	0%	3.36 (2.71)	87.26
PFA + 20% Glyc.[f] cured at 800 K	18.7% Type II 81.3% Type I	2.1 *	0%	3.20 (2.60)	87.2
PFA + 20% Glyc.+ 3% PEG + 3% Triton cured at 800 K	19.1% Type II 80.9% Type I	2.2 *	0%	3.41 (2.76)	84.6

* not determined

[a] determined by NMR peak integration

[b] C – bonded hydrogen (in wt.%) in parentheses

[c] poly-furfuryl alcohol

[d] tannic acid

[e] polyethylene glycol

[f] glycerol

[h] weighted average of types II and IIb = [−0.44]

TABLE II

Properties of Partially Burned PFA Glassy Carbons[U]

MATERIAL	Hydrogen Species (NMR)[a]	δ_{iso} (ppm)	δ_{iso} [†] (ppm) ±0.1	BURNOUT	Chemical Analysis % H_2 [b]	% C
PFA [c] part.burned	12.2% Type IIb	1.1		36%	2.12	87.7
21% O_2	8.0% Type IIa	2.5	[1.6]		(1.69)	
1300 K, 2s.	79.8% Type I	*				
PFA part.burned	23.1% Type IIb	0.2		42%	1.51	88.5
21% O_2	14.0% Type IIa	1.5	[0.7]		(0.95)	
1400 K, 2s.	62.9% Type I	*				
PFA part.burned	56.3% Type IIb	−4.0		62%	1.0	88.3
21% O_2	10.4% Type IIa	1.7	[−3.3]		(0.33)	
1500 K, 2s.	33.3% Type I	*				
PFA part.burned	60.3% Type IIb	−5.3		75%	0.78	93.12
21% O_2	18.5% Type IIa	−0.7	[−4.2]		(0.17)	
1600 K, 2s.	21.2% Type I	*				
PFA part.burned	49.5% Type IIb	−5.4		74%	0.79	91.30
21% O_2	16.7% Type IIa	−0.6	[−4.2]		(0.27)	
1600 K, 3s.	33.8% Type I	*				
PFA part.burned	34.7% Type IIb	−1.5	[−1.5]	40%	1.05	93.35
10% O_2	65.3% Type I	*			(0.66)	
PFA part.burned	63.0% Type IIb	−3.9		24%	1.11	85.8
5% O_2	7.0% Type IIa	2.0	[−3.3]		(0.33)	
1500 K, 2s.	30.0% Type I	*				
PFA part.burned	66.0% Type IIb	−3.8		17%	1.33	85.4
2% O_2	5.0% Type IIa	2.0	[−3.4]		(0.39)	
1500 K, 2s.	29.0% Type I	*				
PFA heated	69.4% Type IIb	−3.5		0%	0.97	88.6
N_2			[−3.5]		(0.30)	
1600 K, 2s.	30.6% Type I	*				
PFA heated	79.7% Type IIb	−5.4		0%	0.93	85.14
N_2			[−5.4]		(0.19)	
1600 K, 3.5s.[‡]	20.3% Type I	*				

[U] see legend for Table I for explanation of notation

[†] weighted average of types IIa and IIb in sq. brackets [ ]

[‡] this case is possibly indicative of the influence of *time* on the kinetics of graphitization.

TABLE III

Properties of Partially Burned PFA Copolymer Glassy Carbons[U]

MATERIAL	Hydrogen Species (NMR)[a]	δ_{iso} (ppm)	δ_{iso} [†] (ppm) ±0.1	BURNOUT	Chemical Analysis % H_2 [b]	% C
PFA [c] + 50% tan.ac.[d]	30.2% Type IIb	0.7		52%	1.83	83.58
part.burned 21% O_2	17.2% Type IIa	2.8	[1.4]		(0.96)	
1300 K, 2s.	52.6% Type I	*				
PFA + 50% tan.ac.	31.2% Type IIb	−1.1		65%	1.15	91.1
part.burned 21% O_2	11.5% Type IIa	0.7	[−0.6]		(0.66)	
1400 K, 2s.	57.3% Type I	*				
PFA + 50% tan.ac.	47.4% Type IIb	−5.0		85%	0.75	84.7
part.burned 21% O_2	12.9% Type IIc	−8.2	[−5.0]		(0.14)	
1500 K, 2s.	20.6% Type IIa	0.1				
	19.1% Type I	*				
PFA + 17% tan.ac.	13.7% Type IIb	1.2		45%	2.26	84.7
part.burned 21% O_2	10.2% Type IIa	2.8	[1.9]		(1.72)	
1300 K, 2s.	76.1% Type I	*				
PFA + 17% tan.ac.	52.2% Type IIb	−1.3		51%	1.54	90.3
part.burned 21% O_2	11.1% Type IIa	2.5	[−0.7]		(0.57)	
1400 K, 2s.	36.7% Type I	*				
PFA + 17% tan.ac.	63.4% Type IIb	−4.2		67%	1.09	85.6
part.burned 21% O_2	8.6% Type IIa	1.5	[−3.5]		(0.31)	
1500 K, 2s.	28.0% Type I	*				
PFA + 9% tan.ac.	41.7% Type IIb	−3.8		67%	1.07	85.8
part.burned 21% O_2	11.5% Type IIa	1.1	[−2.8]		(0.50)	
1500 K, 2s.	46.8% Type I	*				
PFA + 9%PEG[e]	68.5% Type IIb	−4.5		58%	0.85	84.2
part.burned 21% O_2	11.8% Type IIa	1.1	[−3.7]		(0.17)	
1500 K, 2s.	19.7% Type I	*				
PFA + 18%PEG	65.0% Type IIb	−4.7		85%	0.80	83.6
part.burned 21% O_2	19.5% Type IIa	1.4	[−3.3]		(0.13)	
1500 K, 2s.	15.5% Type I	*				
PFA + 20%Glyc.[f]	64.1% Type IIb	−4.6		61%		
part.burned 21% O_2	13.4% Type IIa	1.6	[−3.5]		*	*
1500 K, 2s.	22.5% Type I	*				
PFA + 35%Glyc.	64.7% Type IIb	−3.4		71%		
+ 7%Triton	11.5% Type IIa	0.9	[−2.8]		*	*
part.burned 21% O_2	23.8% Type I	*				
1500 K, 2s.						

[U] see legend for Table I for explanation of notation

[†] weighted average of types IIa, IIb and IIc in sq. brackets [ ]

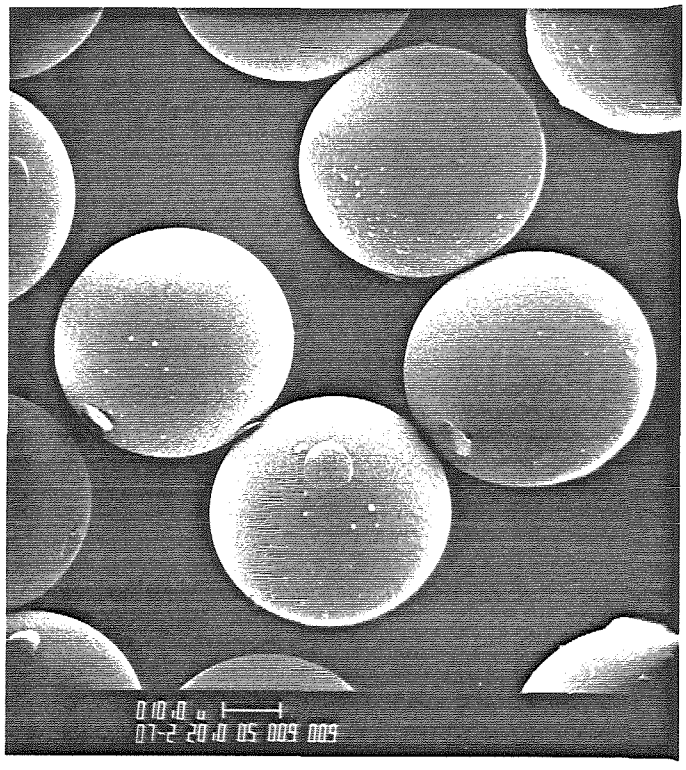

Figure 1: Electron micrograph of glassy carbon particles made from 18% polyethylene glycol and PFA cured at 800 K for 1 hr (space bar denotes 10μm).

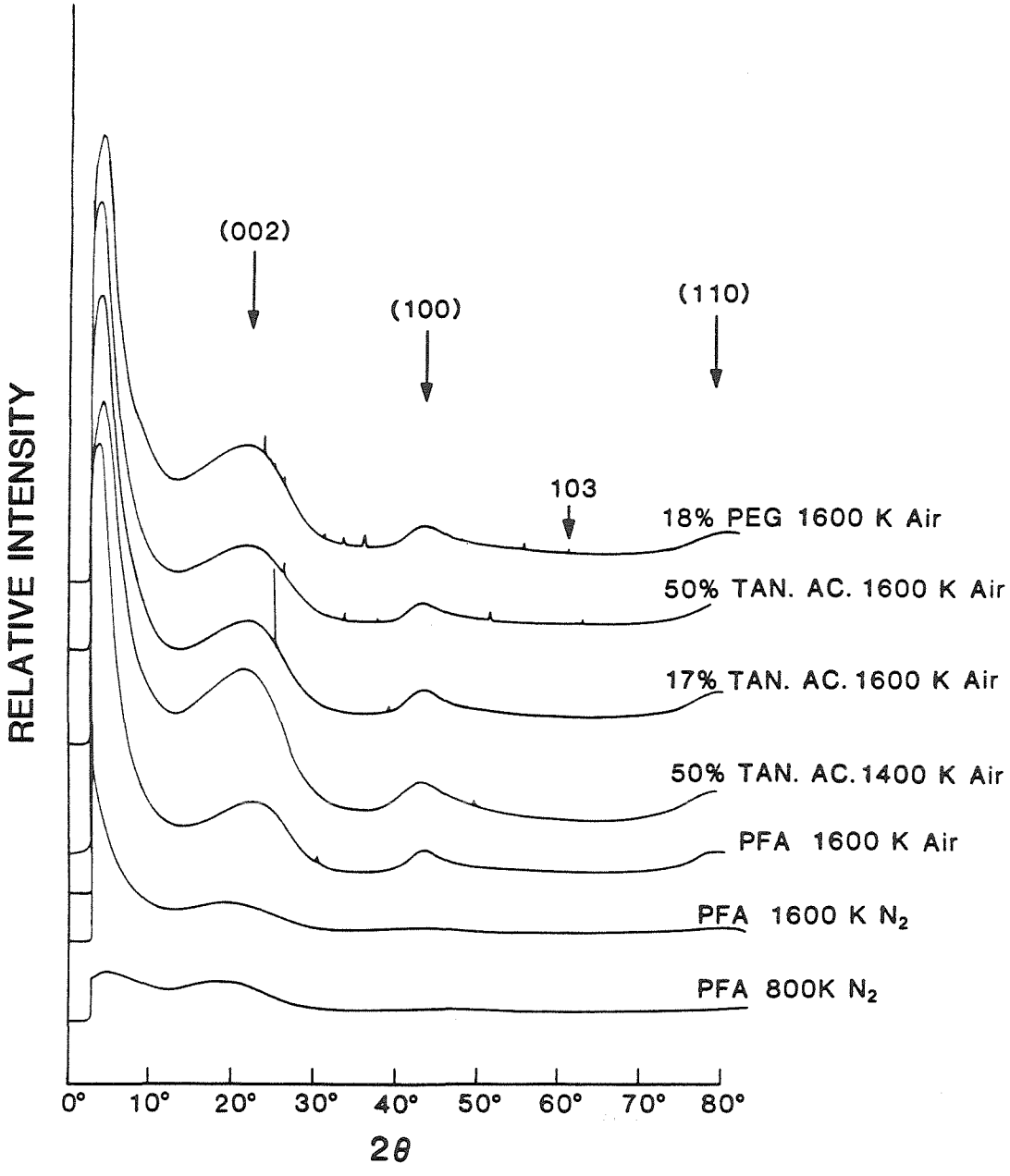

Figure 2: X-ray powder diffraction traces of representative samples. The *(002)* diffraction peak profiles result from stacks of parallel layer planes; the *(100)*, *(110)* peaks result from regular structure within the individual layer plane segments: and the *(103)* peak indicates three dimentional ordering. Broad peaks correspond to the disordered phase; sharp peaks correspond to the crystalline phase.

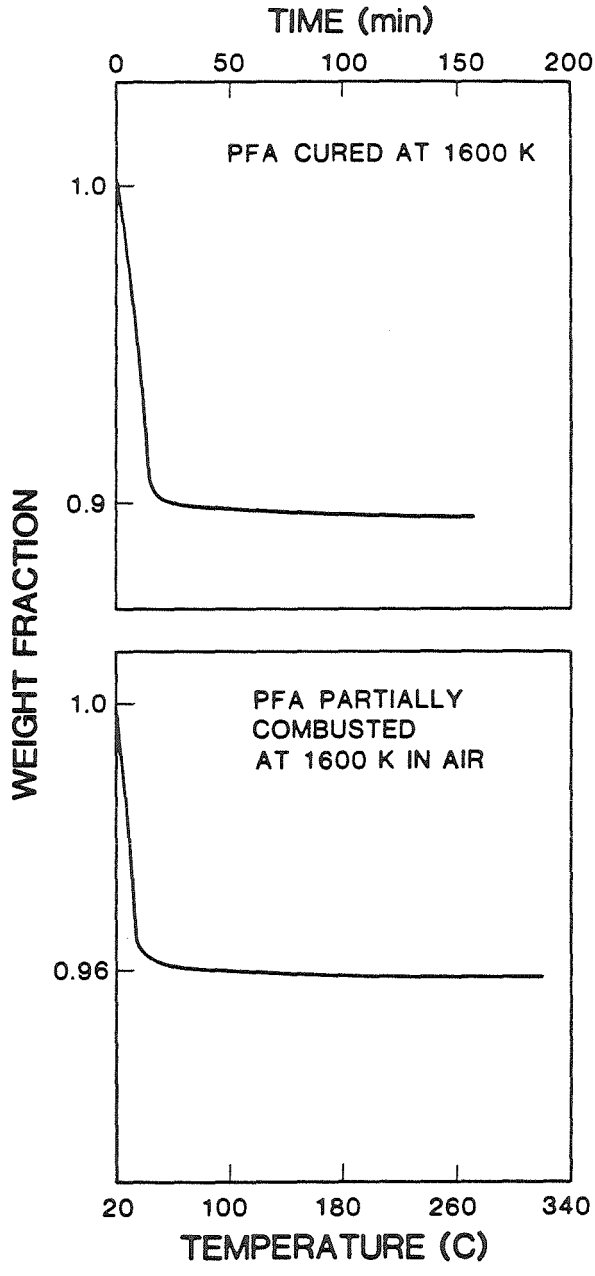

Figure 3: Thermal Gravimetric Analyses of (a) PFA polymer pyrolyzed in N_2 for 3.5s at 1600 K (b) PFA polymer oxidized in air for 3s at 1600 K.

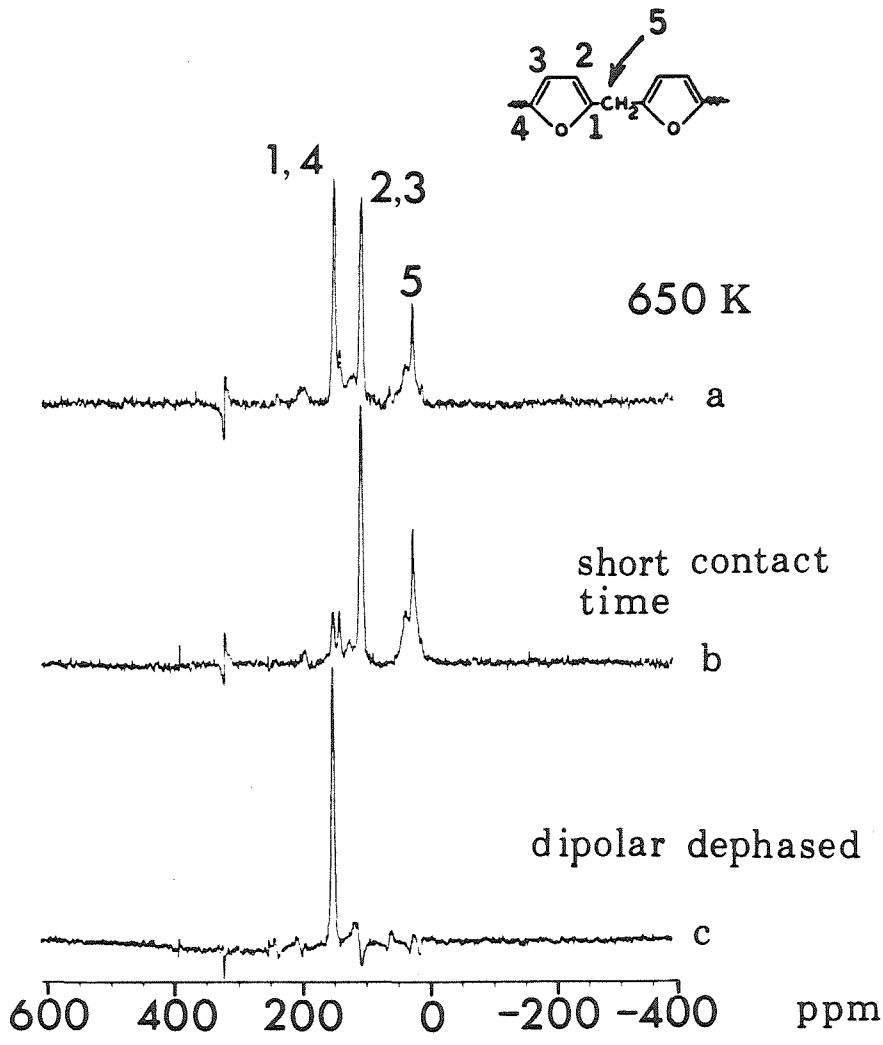

Figure 4: ^{13}C CP-MAS NMR spectra of PFA chars cured at 650 K. Peak assignments are indicated. (a) spectrum obtained with a 2 ms contact time, (b) spectrum obtained with a 50 μs contact time for selective observation of protonated carbons (c) spectrum obtained with a contact time of 2 ms and acquisition delayed for 70 μs, for selective observation of unprotonated carbons.

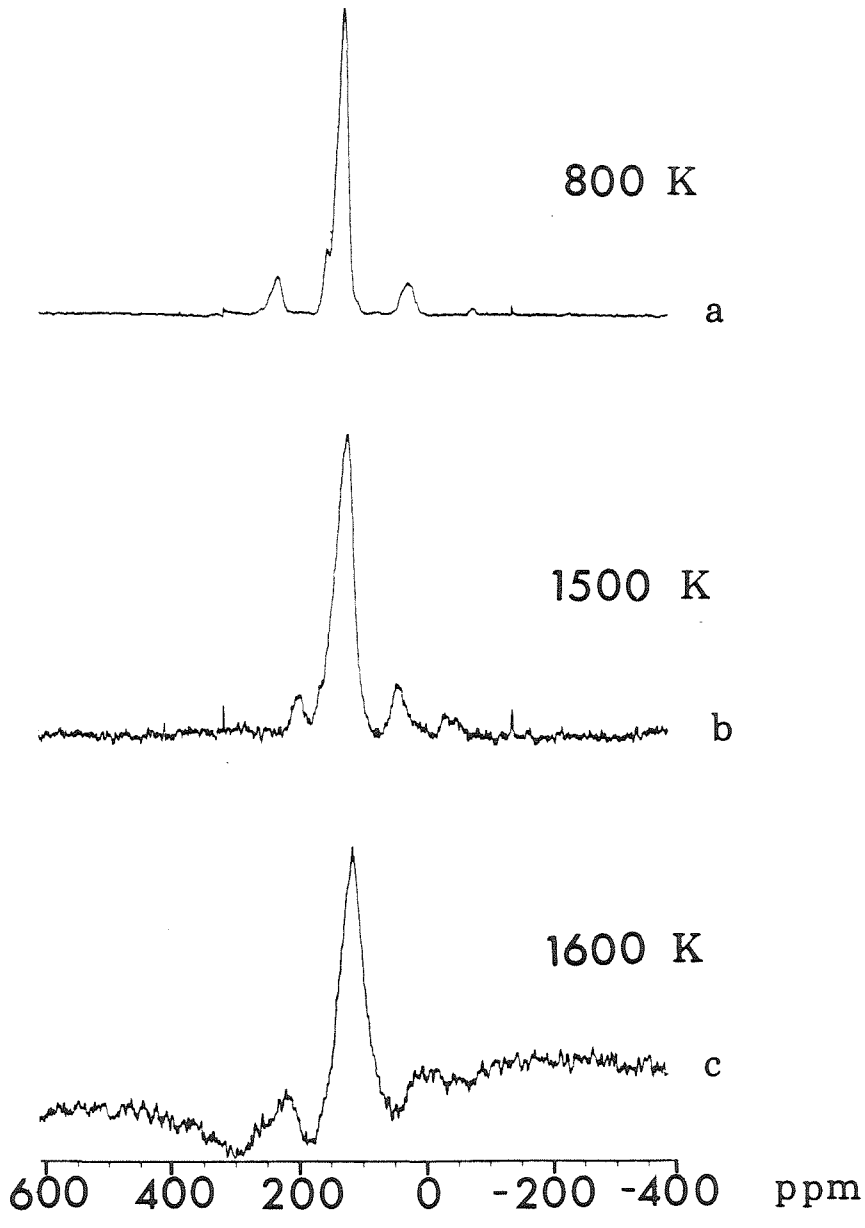

Figure 5: (a) ^{13}C CP-MAS NMR spectrum of PFA pyrolyzed at 800 K, (b) ^{13}C CP-MAS NMR spectrum of PFA partially oxidized at 1500 K at 10% O_2 for 2 sec. (c) ^{13}C MAS NMR spectrum with ^{1}H decoupling of PFA partially oxidized at 1600 K in air for 2 s.

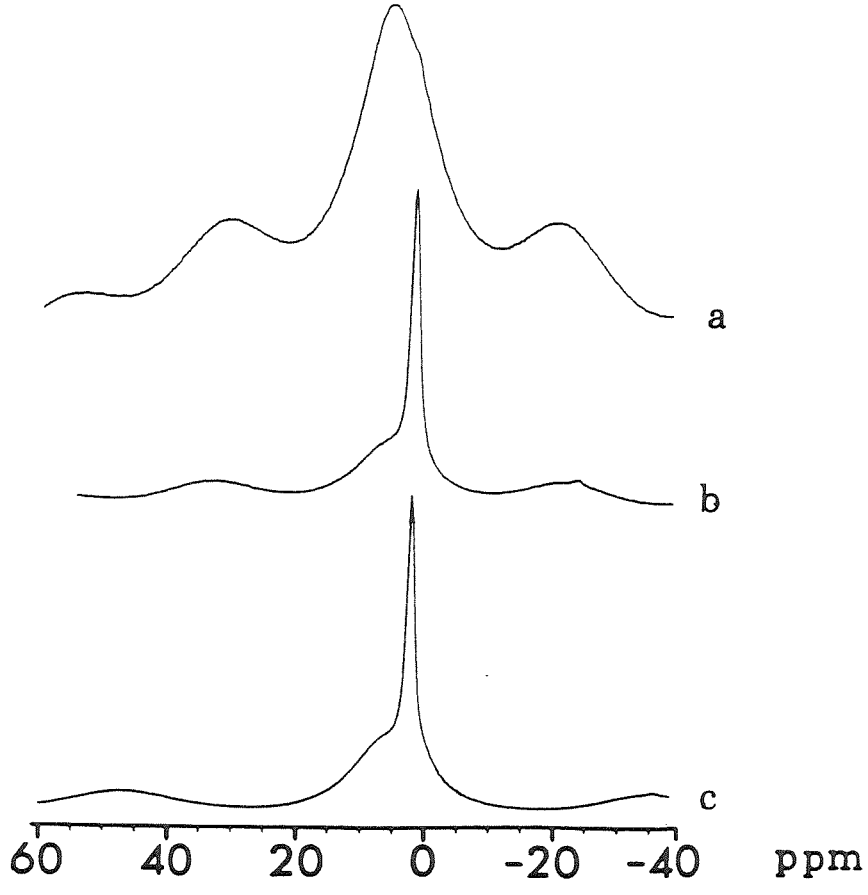

Figure 6: ^{1}H MAS NMR spectra of plain PFA chars (a) PFA polymer "as collected" after heat treatment at 650 K, (b) PFA polymer after pyrolyzing the initial product at 800 K for 1 h, (c) PFA copolymer with 18 wt.% polyethylene glycole (PEG) pyrolyzed at 800 K for 1 h.

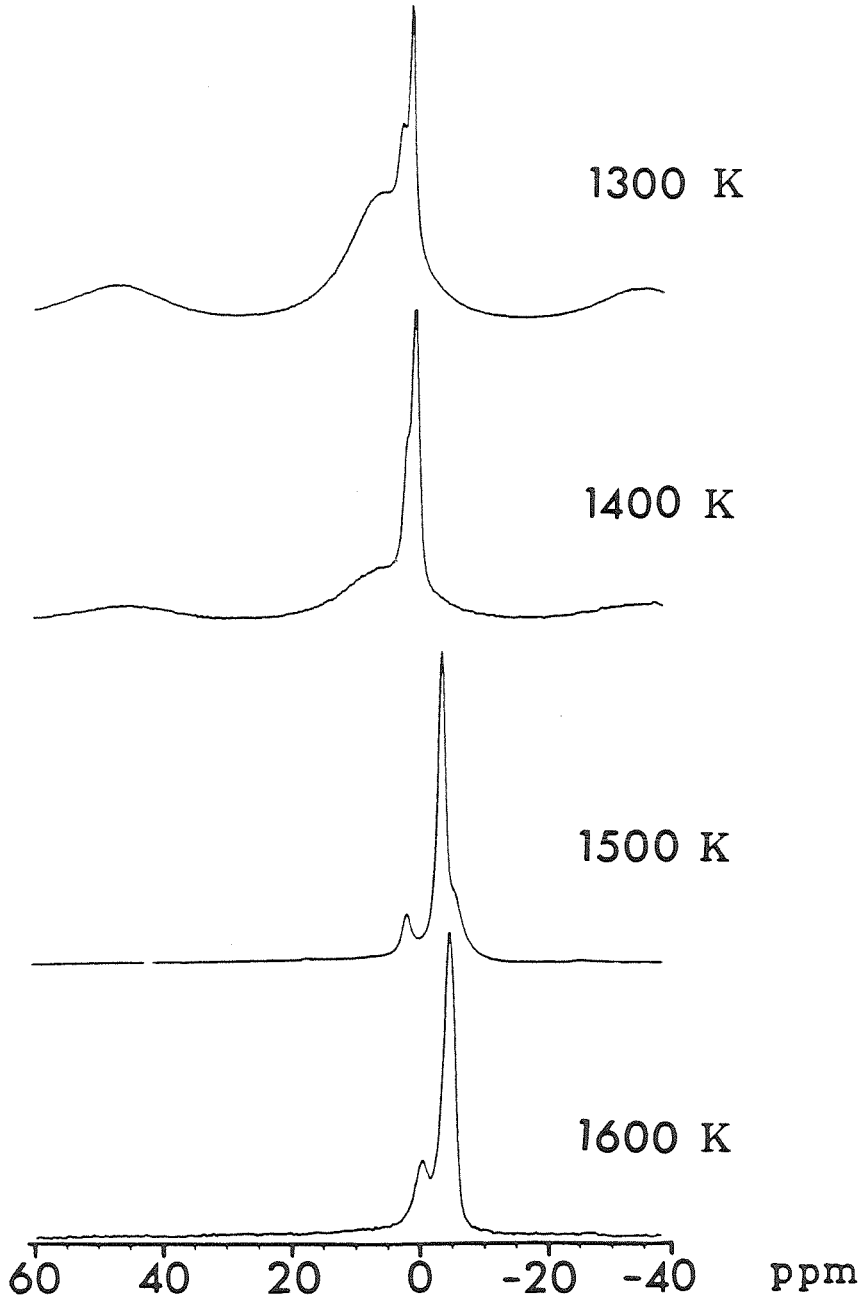

Figure 7: Effect of oxidation temperature upon the ^{1}H MAS NMR spectra of PFA polymer chars oxidized in in air for 2 s. The temperatures of treatment are indicated in the figure.

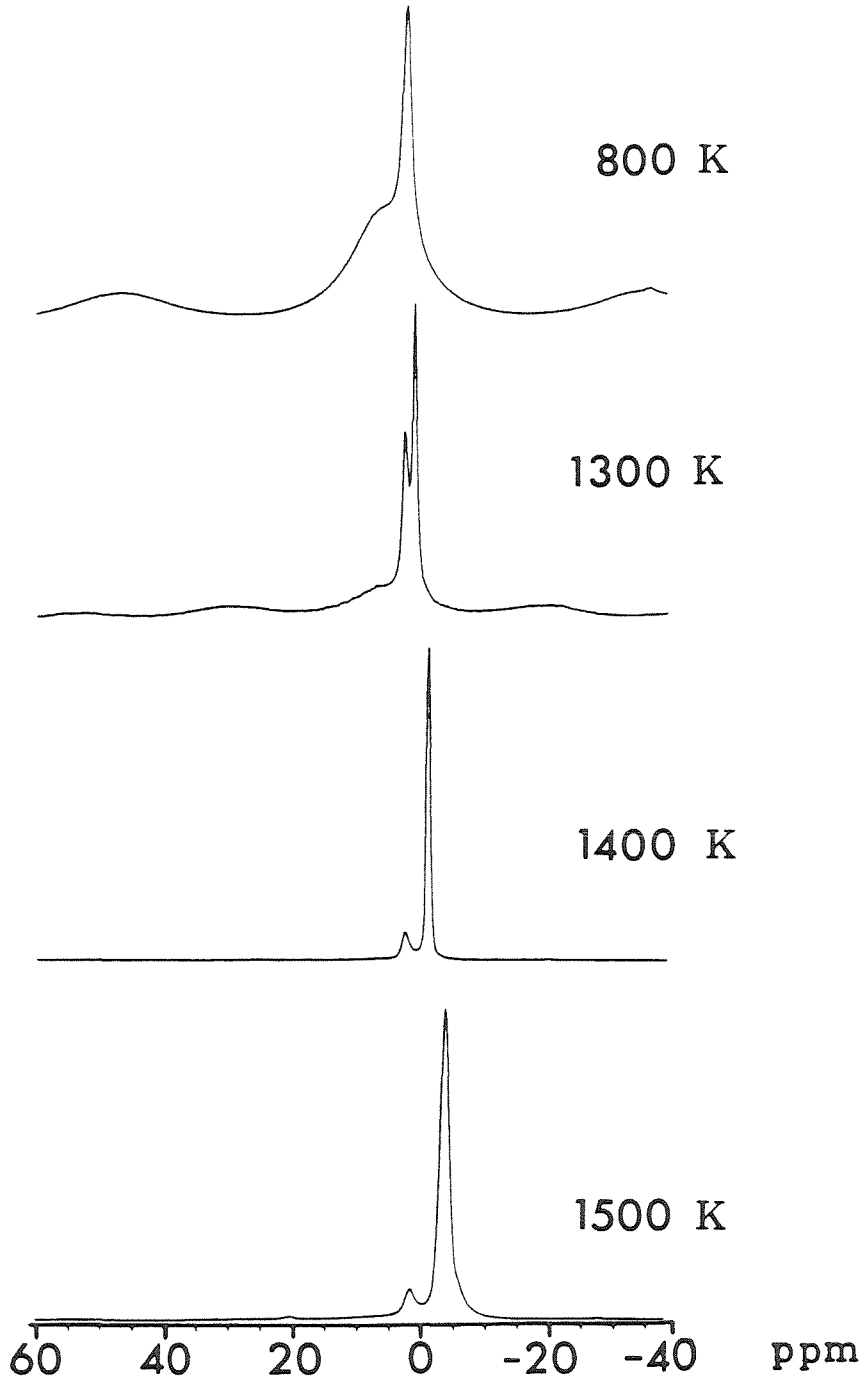

Figure 8: Effect of pyrolysis or oxidation temperature upon the ^{1}H MAS-NMR spectra of chars based on PFA copolymers with tannic acid. The conditions of treatment are indicated in the figure, (a) PFA copolymer chars made from 17 wt.% tannic acid and PFA.

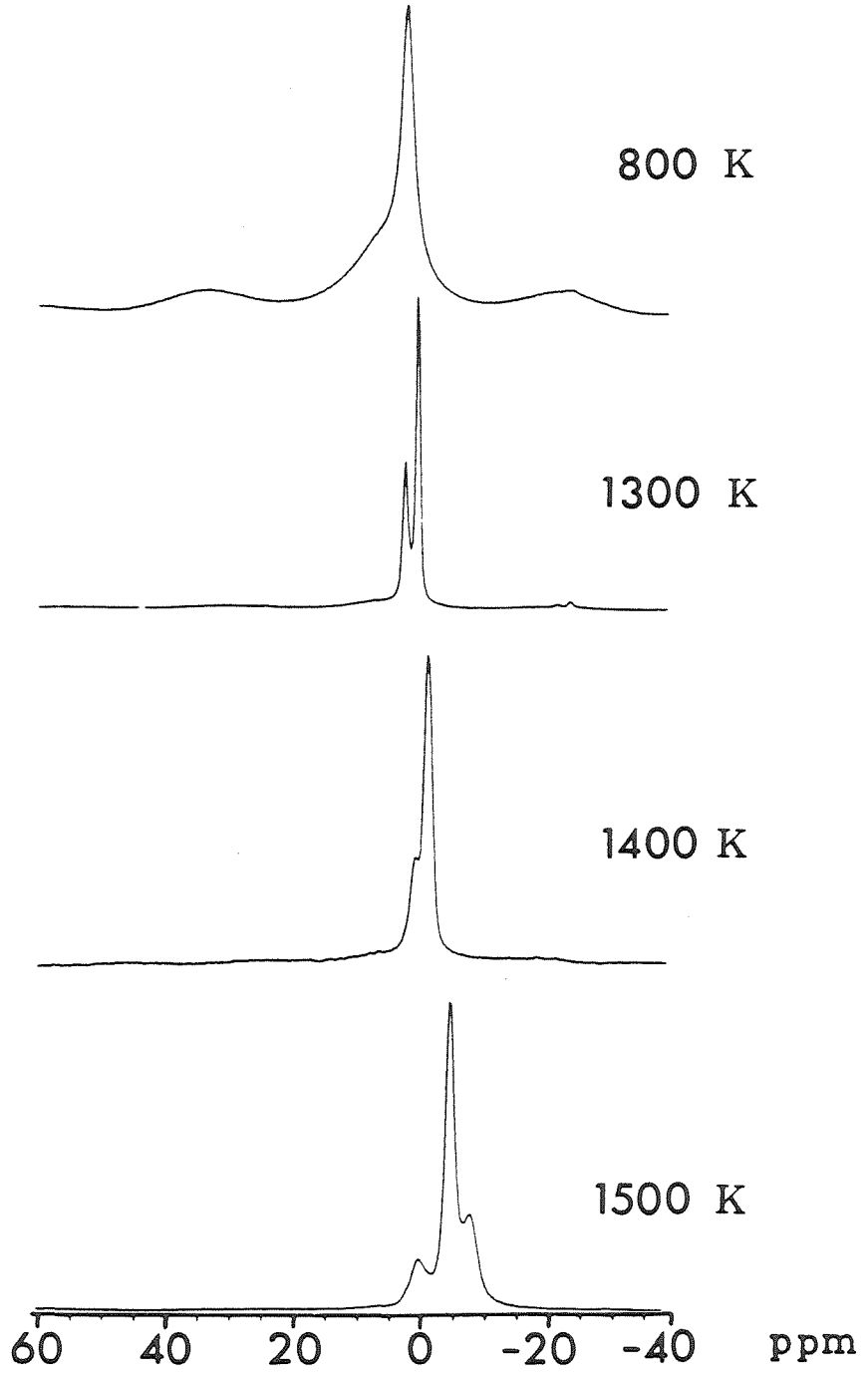

Figure 8b (b) PFA copolymer chars made from 50 wt.% tannic acid and PFA.

TABLE IV

Temperature (°C)	δ_{iso} (ppm)
25	−3.6
−40	−3.0
−60	−2.8
−80	−2.6
−97	−2.5
−110	−2.5
−120	−2.4
−130	−2.2

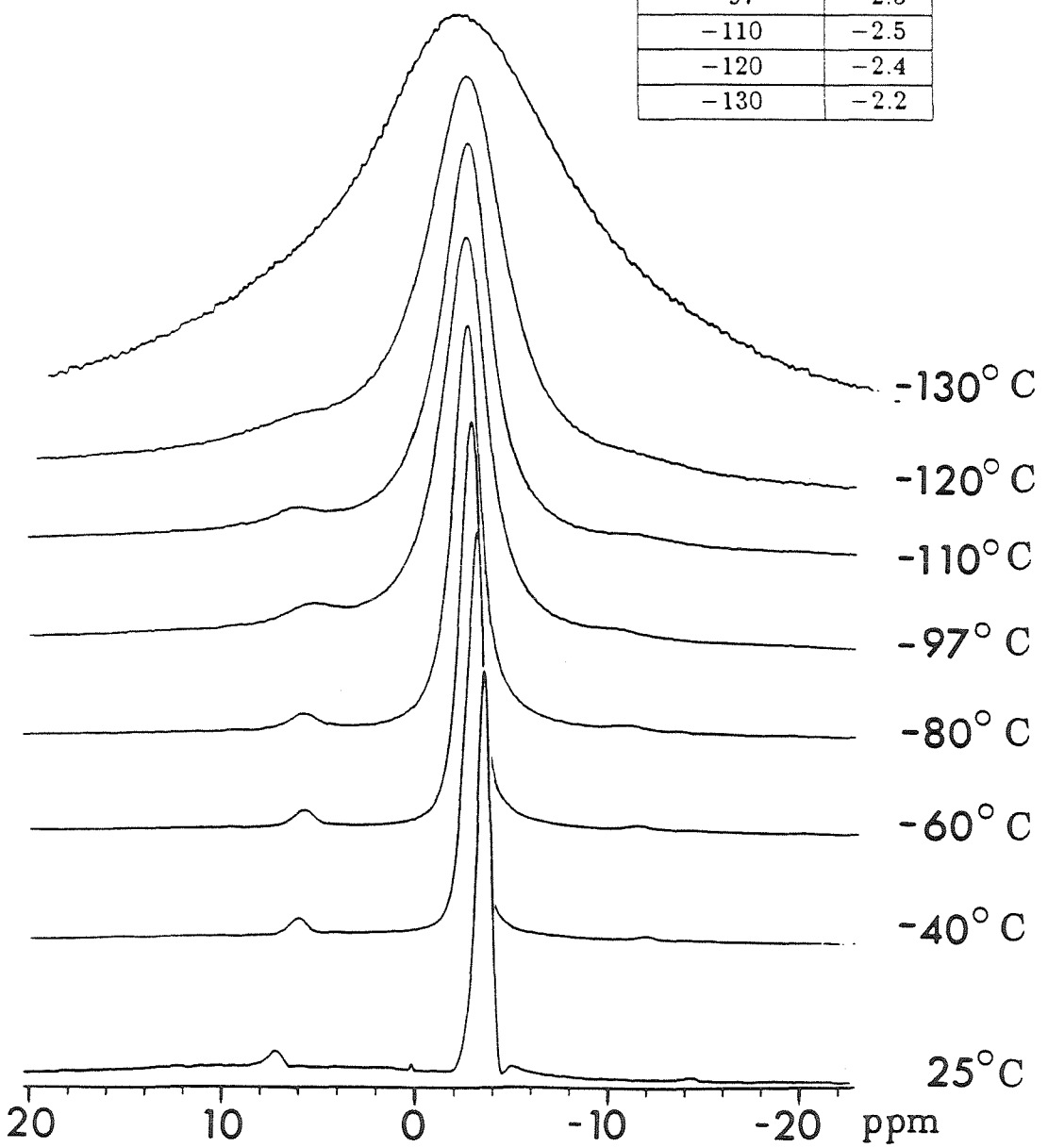

Figure 9: 300 MHz variable temperature ^{1}H MAS NMR spectra of PFA polymer heat-treated at 1600 K for 2 s in nitrogen. Table IV (inset) shows the chemical shifts corresponding to various temperatures during NMR.

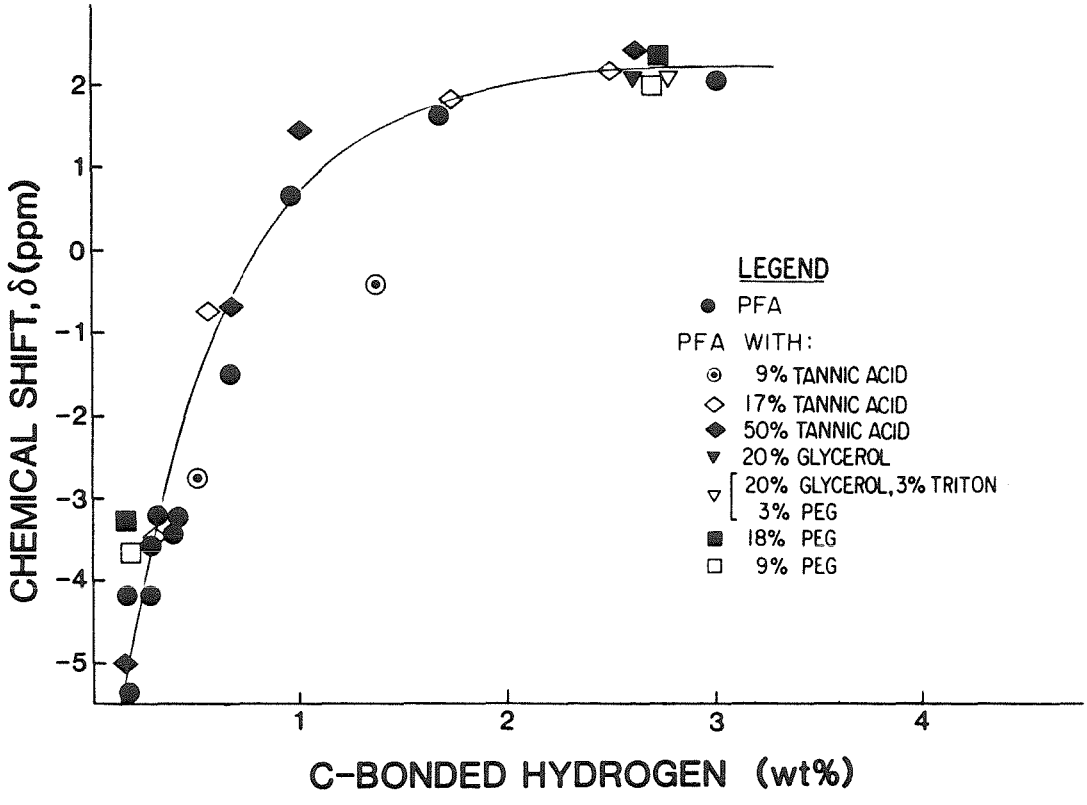

Figure 10: Dependence of the ^{1}H MAS NMR chemical shifts (vs. tetramethylsilane) of sorbed water in all of the glassy carbon chars investigated on the residual content (in wt.%) of C– bonded hydrogen in the char (see text).

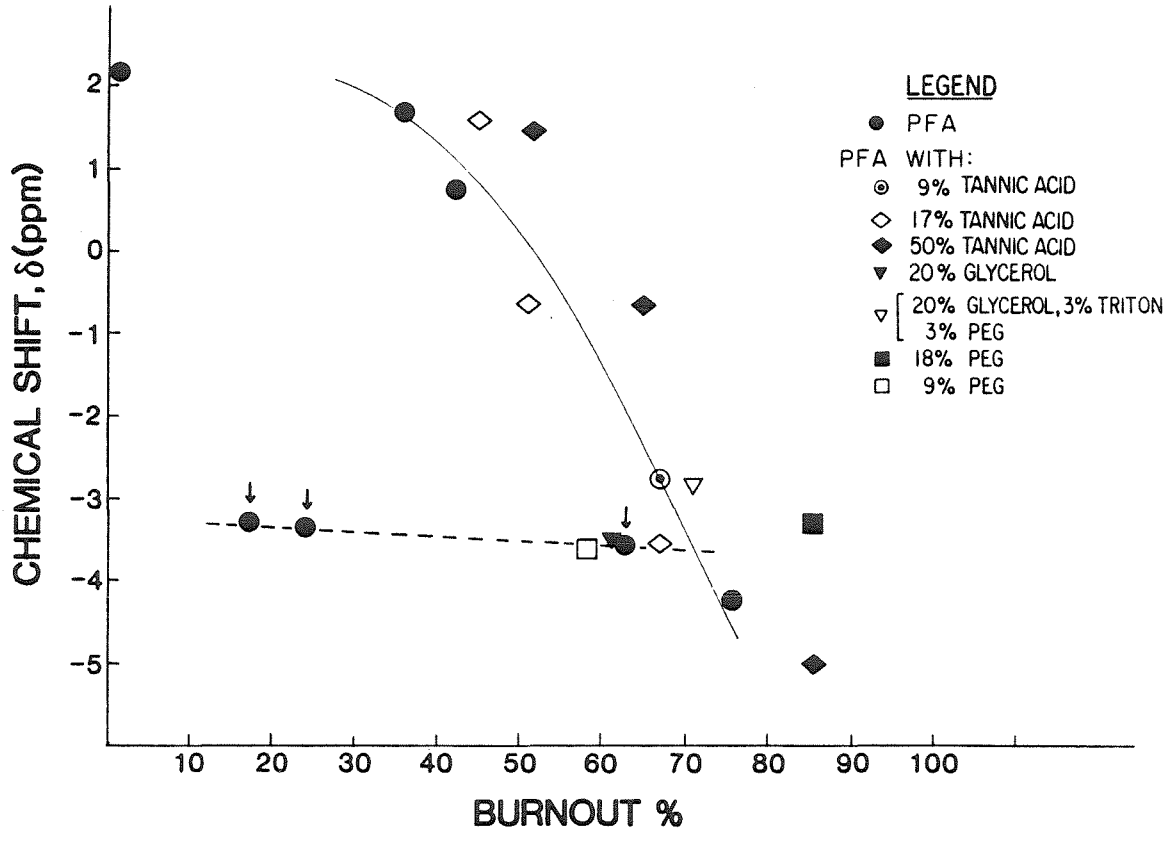

Figure 11: Dependence of the ^{1}H MAS NMR chemical shifts on particle burnout in all of the glassy carbon chars investigated. Solid line: constant oxygen partial pressure (0.21) and variable temperature (—-). Dashed line: constant temperature (1500 K) and variable oxygen partial pressure (- - -), corresponding data points are denoted by arrow.

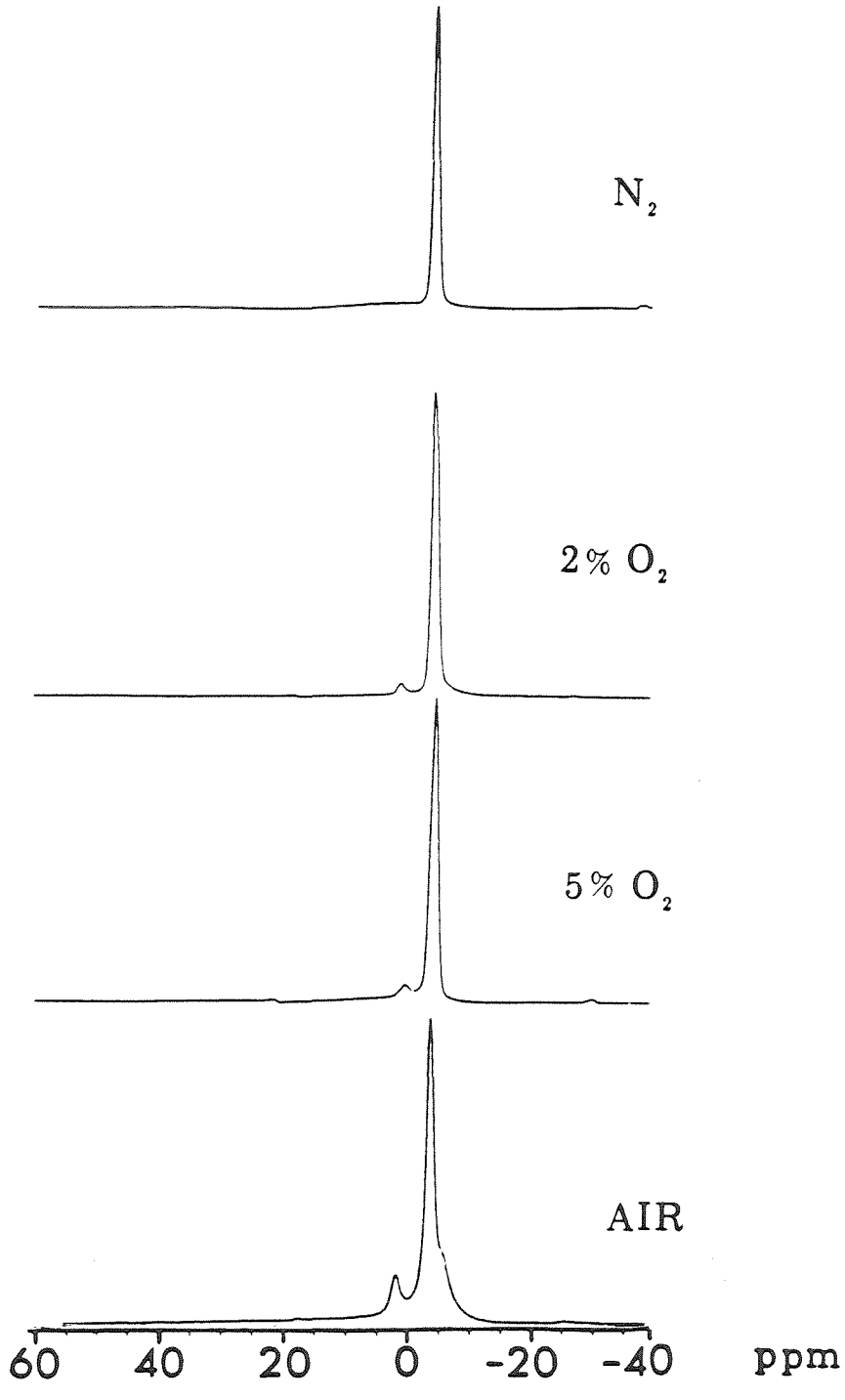

Figure 12: Effect of the pyrolysis atmosphere on the ^{1}H MAS-NMR spectra of PFA chars.

CHAPTER 5

Theory of Operation, Construction and Evaluation of a Near-Infrared Pyrometer.

Y. A. Levendis and R. C. Flagan
Environmental Engineering Science
California Institute of Technology
Pasadena, California 91125

1 Introduction

In studies of coal combustion the temperature of a burning coal particle is a parameter of utmost importance since it determines the rate at which a particle burns and thereby influences the performance and efficiency of the utility coal boilers. Particles that burn hotter enhance the radiant heat transfer to the combustion chamber walls, consequently improving the energy utilization. The nature and quantity of the gaseous and particulate pollutants emitted, however, depend strongly on temperature (Neville et al.,1981; Quann and Sarofim, 1982), and at elevated temperatures can be unfavorable from an environmental quality standpoint. According to Ayling and Smith (1972) pulverized coal particles, because of their highly exothermic nature, burn at temperatures a few hundred degrees above the local gas temperature. This temperature difference determines the combustion rate of the particles.

The only method that can be employed to measure the surface temperature of a single burning coal particle in motion is optical radiation pyrometry, since it offers

the opportunity of monitoring the temperature of a body without physical contact. Radiometers do not measure temperature directly. The irradiance in a limited spectral band at the sensing element, is directly measured and from this the temperature may be derived if the spectral emissivity of the body and the spectral response of the sensing element are known. However, accurate emissivity data for each coal particle is difficult to obtain, especially since the chemical composition varies for different coals and even from particle to particle of the same coal. Consequently, a two-wavelength pyrometer would be more appropriate because, at least with the assumption of gray body radiation, the ratio of relative intensities of radiation at two different wavelengths is independent of emissivity.

2 Theory

The monocromatic intensity of radiation emitted by a burning fuel particle depends strongly on the surface temperature, T, the wavelength of observation, λ, and the emissivity, ϵ_λ, at that wavelength. The response of the instrument is given by application of the Planck radiation distribution law as the ratio of two terms each of the form:

$$J_\lambda = \int_{\Delta\lambda} \epsilon_\lambda a_\lambda C_1 \lambda^{-5} \left(\exp \frac{C_2}{\lambda T} - 1\right)^{-1} d\lambda \qquad (1)$$

where J_λ is the energy contained in the wavelength band $\Delta\lambda$ transmitted by the interference filter with transmittance a_λ. The first radiation constant, C_1, is equal to $2\pi c^2 h$, where c is the speed of light and h is Planck's constant, and the second radiation constant, C_2, is equal to ch/k, where k is Boltzmann's constant. In the current work, $\exp(C_2/\lambda T)$ is always much greater than unity and Wien's approximation applies:

$$J_\lambda = \int_{\Delta\lambda} \epsilon_\lambda a_\lambda C_1 \lambda^{-5} \exp\left(-\frac{C_2}{\lambda T}\right) d\lambda. \qquad (2)$$

For a sufficiently narrow bandwidth to represent constant transmission over the band and for a detector efficiency, η_D, and for the efficiency of light transport to the detectors, η_L, the response R becomes:

$$R = \frac{J_{\lambda_1}}{J_{\lambda_2}} = \frac{\eta_{D,1}\eta_{L,1}\epsilon_{\lambda_1}\Delta\lambda_1}{\eta_{D,2}\eta_{L,2}\epsilon_{\lambda_2}\Delta\lambda_2}\left(\frac{\lambda_2}{\lambda_1}\right)\exp\left[\frac{C_2}{T}\left(\frac{1}{\lambda_2}-\frac{1}{\lambda_1}\right)\right]. \tag{3}$$

For graybody objects or for the constant ratio of emissivities over the wavelength interval chosen, the ratio response becomes independent of emissivity and assumes the form:

$$R = C_3 \exp\left[\frac{C_2}{T}\left(\frac{1}{\lambda_2}-\frac{1}{\lambda_1}\right)\right] \tag{4}$$

The above equation can be solved for the temperature for an experimentally measured signal ratio, R, and for an experimentally determined calibration constant, C_3:

$$\ln(C) = \ln\left(\frac{J_1}{J_2}\right) + \frac{C_2}{T_c}\left(\frac{1}{\lambda_1}-\frac{1}{\lambda_2}\right), \tag{5}$$

where T_c corresponds to the value of a known temperature source. For enhanced bandwidth filters, the integral of Equation (2) can be approximated by integrated *bands* (Dictor, 1979), as follows:

$$\frac{J_1}{J_2} = C_4 \frac{\int_{\lambda_1-\Delta\lambda_1/2}^{\lambda_1+\Delta\lambda_1/2}\eta_{L,1}(\lambda)\eta_{D,1}(\lambda)\lambda^{-5}\exp\left[\frac{-C_2}{\lambda_1 T}\right]\Delta\lambda_1}{\int_{\lambda_2-\Delta\lambda_2/2}^{\lambda_2+\Delta\lambda_2/2}\eta_{L,2}(\lambda)\eta_{D,2}(\lambda)\lambda^{-5}\exp\left[\frac{-C_2}{\lambda_2 T}\right]\Delta\lambda_2}. \tag{6}$$

The efficiency curves for the filters and the detector are usually supplied by the manufacturer. The constant C_4 reflects only the geometry of the system.

3 Experimental

3.1 *Optical System*

A laminar flow, electrically heated furnace described by Senior, (1984) was extensively modified to facilitate pyrometric observations. The new design incorporated a wide bore (1 cm, i.d) water-cooled, stainless steel injector. The width of the injector was a compromise between radiation-gathering capabilities on one hand and on the other hand, prevention of direct furmace wall radiation from reaching the top of the injector where the pyrometer optics were placed. Further features of the injector design included minimization of buoyancy effects of the hot furnace gases inside the cold environment of the injector, allowance of undisturbed furnace air flow around the outside insulation of the injector and adequate, unrestricted water flow in the cooling jacket to prevent overheating (shown in Chapter 6, Fig.1). At the top of the injector a low absorbence quartz window was press-fit with "*O-ring*" seals to keep the furnace airtight. A collimating lens was placed above the quartz window to focus any incident radiation on one end of an optical fiber bundle. An aperture (200 μm in diameter) has been inserted between the collimating lens and the fiber bundle. The purpose of this pinhole was to define a view volume in the center of the reactor and to prevent background furnace radiation, which ascends the inside injector wall through multiple reflections, from reaching the optical fiber. The length of the injector is a very important design parameter as well; it has to be optimized to preclude viewing direct background radiation in order to avoid saturating the detectors. To ensure that the background radiation will be eliminated, the index of refraction of the hot gases inside the combustion temperature must be taken into account in the design of the injector. On the other hand the longer the injector is the farther away from the burning particles the observation is taking place, with detrimental effects on the light collection efficiency of the system.

Therefore, the length should be kept to a minimum, consistent with the elimination of the background radiation. The particle feeder was inserted in the upper part of the injector below the quartz window. The small size of the feeder tube did not block the radiation from most events in the combustion chamber. With this system, viewing along the axis of the furnace can be achieved, and the temperature-time history of any burning particles can be monitored in a manner similar to the one used by Dictor (1979) and Timothy et al. (1982).

The fiber optic bundle used (*Oriel*) is bifurcated and contains randomly oriented fibers inside to ensure uniform light distribution to the two detectors. Each channel of the pyrometer consists of two focusing lenses, a band filter and a detector with the appropriate amplification circuits, shown in Fig. 1. The design of the filter-lens arrangement proved to be rather challenging inasmuch as it involved the following requirements as pictured in Fig. 2.

- The diameter of the optical fiber bundle is $d_f = 3.2$ mm; meanwhile the dimensions of the detector are 2.4×2.5 mm. Therefore, the image has to be reduced by a factor of $2.4/3.2 = 0.75$ to ensure that all of the light will be collected by the detector. For a reduction of 0.75 to be acheived, then f_2/f_1 has to equal 0.75, as readily calculated from the Lensmaker's formula. Here, f_1 and f_2 are the focal lengths of the two lenses.

- The radiation acceptance solid angle of the fiber bundle is $\beta = 68°$, meaning that for the first lens to be placed away from the fiber at a distance equal to its focal length then $d_{l,1}/f_1$ must be equal to $2\tan(\beta/2) = 1.34$, as shown in Fig. 2, for all of the light to be collected by the first lens. Here $d_{l,1}$ is the diameter of the first lens and f_1 its focal length.

- The first lens collimates the light; therefore, the diameter of the second lens, $d_{l,2}$, has to be larger or equal to the diameter of the first lens, $d_{l,1}$. The filter

will be placed between the lenses; therefore, its diameter has to be larger or equal to the diameter of the first lens for all the light to go through the filter.

The last two requirements are imposed by the necessity to collect the light emitted from the weak radiation source of a single burning particle as efficiently as possible. To satisfy all of the above constraints, aspheric lenses were chosen. Aspheric lenses are designed to have a much shorter focal length than is possible with a spherical lens of equal diameter and equal spherical aberration. A pair of *Rolyn* lenses was the only one found to comply with these requirements.

The selection of the filters was dictated by the typical particle temperatures expected. Simple heat balance calculations showed that the particles should burn between 2000 and 3000 K for most furnace conditions used in the current study. Consequently, to maximize transmission of radiation, the filters should be selected in the vicinity of the maximum in Plank's radiation energy curves, for the particular temperatures, as shown in Fig. 3. Furthermore, the slope of Plank's curves is steeper to the left of the peak; thence, the filters were selected in this region to maximize sensitivity to temperature variations. The filters were centered at 800 an 1000 nm, respectively. A rather wide bandpass at full width at half-maximum ($FWHM$) of 70 nm was chosen to maximize the signal and compensate for the unfavorable long distance between the combustion event and the observation lens as well as for the small solid angle of viewing. The peak transmittance of the filters (*Oriel*) was 69%. The optical bench, rails and lens holders were designed and constructed in such a way that three-dimensional motion, as well as rotation of all the components in respect to each other, was totally unobstructed.

3.2 *Electronics*

The detectors selected were *Hamamatsu S1336-5BK* silicon photodiodes because of their high radiant sensitivity (0.5 A/W), the flat sensitivity profile over the wave-

length range of interest (800 to 1000 nm) and their excellent rise time (0.2 μs). A preamplifier and three subsequent amplification stages were used, all employing type 3140 operational amplifiers, and capable of a gain of 10^6. Power to the amplification circuit was provided by a $\pm 15V\,DC$ power supply. An offset circuit was also inserted, as shown in Fig. 4, to provide freedom of adjustment of the baseline signal. This provision is particularly useful in cases where background (furnace wall) radiation is present and obscures the observation of combustion effects. To avoid extraneous low-frequency noise (drift) from getting transmitted through the offset circuit, a voltage regulator (*UA723*) was inserted before the offset. The regulator supplied a steady output of $+10V$. To provide the negative voltage component to the offset and eliminate "crosstalk" between the two channels (one gets affected by the other's offset) a quadruple operational amplifier (*LF347*) was incorporated. The individual gains of the four sections of this last amplifier were set equal to unity.

Numerical integration of equation (4) above, under the reasonable assumption of constant detector efficiency, η_D, over the wavelength range chosen, and using the manufacturer-supplied filter transmissivity curves, gives results that are in good agreement (within 2%) with the narrow band assumption (Eq. 2).

3.3 *Calibration*

The two color-pyrometer was calibrated against heat sources of known temperature. Given the constraints of the present furnace design, the calibration devices were placed outside the furnace, at the very bottom, opposite to the observation port. This way the source could be better defined, easily adjusted, and spurious radiation arising from furnace wall reflections on the source could be avoided. Sources capable of reaching temperatures in the range of those expected for coal combustion and well above the combustor wall temperatures were selected. Hence, any nonlinearities in the system and background radiation were prevented from influencing the

calibration accuracy. Although various calibration sources were used, encompassing a (*Pt - Pt 10%Rd*) thermocouple heated with a non-luminous flame and a quartz tungsten-halogen filament lamp, the most accurate source seemed to be a melting platinum wire. The melting point of platinum is known to be 2043 K, which is in the desired range of temperatures for the present study. Therefore, by choosing a calibration source temperature close to the expected particle temperatures, the temperature functionality of the particle emissivity does not need to be assumed constant over a broad range of temperatures. Thus the accuracy of the pyrometer is enhanced. Furthermore, the radiance temperatures of metals at their melting points are very reliable calibration sources (Cezairliyan et al. 1982), since constancy and reproducibility are exhibited irrespective of the surface conditions of the specimen and operational conditions. Platinum was preferred because, being a noble metal, it does not oxidize when exposed to atmospheric conditions. A slender platinum wire was mounted below the furnace, clamped between two leads connected to a large capacitor. A capacitance discharge at an optimized voltage setting causes a large current ($i = Cdi/dt$) to flow through the wire that overheats and melts. Two-color intensity signals vs time profiles are shown in Fig. 5. The flat (constant intensity) portions of the profiles correspond to the phase change that takes place at constant temperature when platinum transforms from solid to liquid.

Intensity-time data was acquired using a *DEC PDP-11* microcomputer. An automatic peak-finding routine (shown in Appendix 6) was developed and implemented to record the time history of events inside the combustion chamber.

The design of the pyrometer is rather uninvolved, but the alignment of the optical components and detectors is of utmost importance. This is due to the fact that the resulting image of the burning particle mapped on the detector is roughly the same size as the active area of the detector. Therefore, the slightest misalignment could cause erroneous temperature readings.

4 Error Analysis

Errors in the two-color pyrometry may arrise from many sources. Emittance errors may arrise because char particles are neither blackbodies nor graybodies. The temperature extracted from two-color pyrometry, T_r, is related to the true temperature, T, as follows, (Ackerman, 1960):

$$\frac{1}{T_r} = \frac{1}{T} - \frac{1}{n} \ln \epsilon_r \tag{7}$$

where,

$$n = C_2 \left(\frac{1}{\lambda_1} - \frac{1}{\lambda_2} \right), \tag{8}$$

and ϵ_r is the ratio of the surface spectral emittances at the two effective wavelengths, λ_1 and λ_2, respectively ($\epsilon_r = \epsilon_1/\epsilon_2$). The apparent temperature measured by the two color pyrometer is the same as the true temperature only if $\epsilon_1 = \epsilon_2$ and $\epsilon_r = 1$. For most opaque objects, however ϵ_r is not equal to unity. Differentiation of equation (7) above yields an expression showing the error caused by an uncertainty in ϵ_r:

$$dT = \frac{T^2}{n} \frac{d\epsilon_r}{\epsilon_r} = \frac{T^2}{n} \left(\frac{d\epsilon_1}{\epsilon_1} - \frac{d\epsilon_2}{\epsilon_2} \right). \tag{9}$$

Equations (7) and (9) are indicative of the advantage of a two-color pyrometer in applications where ϵ_r is close to unity and the uncertainties in ϵ_1 and ϵ_2 are in the same direction and, hence, tend to cancel. This, however, is not true for all radiating materials, and the apparent and true temperature may differ substantially.

The next topic to be examined concerns the importance of the value of n regarding its effect on the apparent temperature, as measured with a two color pyrometer, when $\epsilon_r \neq 1$. If the value of n is important, then pyrometers utilizing different effective wavelengths would produce different results under this condition. It turns out that the effect of n on the apparent temperature is minimal whenever the spectral emittance of a material varies linearly with wavelength, which assumption is reasonable for most opaque materials in the range of temperatures between 1000-3000 K.

Assuming that:

$$\epsilon_1 = a - b\lambda_1$$

$$\epsilon_2 = a - b\lambda_2,$$

where a and b are constants,

$$\text{then} \qquad \epsilon_r = \frac{a - b\lambda_1}{a - b\lambda_2} \qquad \text{and} \qquad \ln \epsilon_r = \ln \frac{a - b\lambda_1}{a - b\lambda_2} \tag{10}$$

for ϵ_r close to unity and applying Taylor's expansion :

$$\ln \epsilon_r = \ln(1 - \delta) = -\sum_{k=1}^{\infty} \frac{\delta^k}{k} \approx -\delta - \frac{\delta^2}{2} \; ; \tag{11}$$

therefore, for small values of δ, it holds that $\ln \epsilon_r = -\delta$, and

$$\ln \epsilon_r = \epsilon_r - 1 = \frac{a - b\lambda_1}{a - b\lambda_2} - \frac{a - b\lambda_2}{a - b\lambda_2} \qquad \Rightarrow \qquad \ln \epsilon_r = \frac{b(\lambda_2 - \lambda_1)}{a - b\lambda_2}$$

Thence, for two different pairs of wavelengths it can be obtained:

$$\frac{1}{T_r} - \frac{1}{T_{r'}} = \frac{1}{C_2} \left[\frac{\lambda_1' \lambda_2'}{\lambda_2' - \lambda_1'} \ln \epsilon_{r'} - \frac{\lambda_1 \lambda_2}{\lambda_2 - \lambda_1} \ln \epsilon_r \right] \quad \Rightarrow$$

$$\frac{1}{T_r} - \frac{1}{T_{r'}} = \frac{b}{C_2} \left[\frac{\lambda_1' \lambda_2'}{a - b\lambda_2'} - \frac{\lambda_1 \lambda_2}{a - b\lambda_2} \right], \tag{12}$$

with appropriate choice of constants for opaque materials, $b \geq 0.2$, usually and $D \approx 10^{-4}$; evaluation of equation (13) shows that the apparent temperature is not sensitive to variations in effective wavelengths.

The range of operation and the detectability limit of the pyrometer are also affected by statistical uncertainties in the directly measurable parameters. In the two-color pyrometry technique, the ratio of the intensities at the two wavelengths is of primary interest but the magnitude of the intensity has its merit also. The ability to determine the magnitude of surface areas, as will be explained below, and the capacity of resolving qualitative features of combustion, as will be shown in a different chapter, are based on determinations of the absolute intensity. Therefore,

it is of interest to examine the sources of errors affecting the absolute intensities. The detector's output signal at a given wavelength λ is a function of two independent parameters, the temperature and the area of the particle. The energy per unit area of the emitting source can be expressed from Wien's approximation as follows:

$$\frac{J_\lambda}{A} = \frac{\epsilon_\lambda C_1}{\lambda^5} \exp\left[-\frac{C_2}{\lambda T}\right] \quad \Rightarrow T = \frac{C_2}{\lambda} \frac{1}{\ln\left[\frac{A\epsilon_\lambda C_1}{J_\lambda \lambda^5}\right]}/.$$

Hence, the temperature has been expressed as a function of the radiating area and intensity of radiation, $T = T(A, T_\lambda)$. The standard deviation of the experimental uncertainty in temperature can be given as:

$$\sigma_T^2 = \left(\frac{\partial T}{\partial J_\lambda}\sigma_J\right)_A^2 + \left(\frac{\partial T}{\partial A}\sigma_A\right)_J^2$$

$$\Rightarrow \sigma_T^2 = \left[\left(-\frac{C_2}{\lambda}\left(\ln\frac{A\epsilon_\lambda C_1}{J\lambda^5}\right)^{-2} \frac{J\lambda^5}{A\ \epsilon_\lambda C_1} \frac{A\epsilon_\lambda C_1}{J^2\lambda^5}\right)\sigma_J\right]^2 + \left[\left(-\frac{C_2}{\lambda}\left(\ln\frac{A\epsilon_\lambda C_1}{J\lambda^5}\right)^{-2} \frac{J\lambda^5}{A\ \epsilon_\lambda C_1} \frac{\epsilon_\lambda C_1}{J\lambda^5}\right)\sigma_A\right]^2. \tag{13}$$

The standard deviations of the intensities and radiating areas should be deduced from experimental results. A complexity arises, occasionally, because of the difficulty in defining radiating areas as will be demonstrated in a later chapter, concerning combustion of coal. Errors may also arise in the calibration procedure; therefore, the standard deviation from multiple calibration runs should be recorded. Furthermore, errors may arise as a result of the environment of the pyrometer. Dust, vapors and smoke particles in long transmission paths between the source and the instrument can affect the chroma of radiation by selective absorption or scattering; moreover, particles may reflect background radiation into the optics of a two-color pyrometer and create erroneous signals. The present design is not affected by absorption of vapors, since none of the filter windows overlaps with any of the absorption bands of CO_2 or water vapor. Besides, smoke or ash particles that arise from combustion of coal volatiles, fragmentation of the residual chars and vaporization of

ash should bear no influence on the pyrometric observations, since all experiments were excecuted in the single particle mode.

5 Area Determination

In principle, the optical pyrometry technique has the potential of enabling determination of the radiative area. The recorded radiation intensities in the two individual channels ($J_\lambda \propto \exp(-C_2/\lambda T)$) are proportional to the quantity $\epsilon_\lambda A_c/L^2$, where A_c is the projection of the radiative area of the particle and L is the distance between the source and the detector. Assuming constant emissivity, ϵ_λ, and assuming that the distance covered by the particle during burnout is negligible in comparison to the total distance, L, a relative area can be estimated:

$$\frac{A_c}{A_{c,r}} = \frac{J_\lambda}{J_{\lambda,r}} \exp \frac{C_2}{\lambda}\left(\frac{1}{T} - \frac{1}{T_r}\right), \tag{14}$$

where the subscript "r" denotes reference values. A reference value can be any point in the burnout history of the particle. The assumption about constancy of the distance, L, is very consistent with the low-velocity, laminar gas flows used in the present study. The assumption of constancy of emissivity, however, is not a reasonable one, since the emissivity of carbon is known to be strongly temperature dependent (Sparrow and Cess, 1978). The constancy of emissivity can be assumed true only for the regions of the temperature-time profiles where the temperature is constant.

6 Performance and Experimental Application

Perfomance assessment for the two-color pyrometer was conducted by comparing its temperature output with the one of an appropriately calibrated brightness (disappearing filament) pyrometer. The temperature of clouds of glassy carbon particles,

burning in air at temperatures close to the wall temperatures and in oxygen at elevated temperatures, were measured with both instruments and found to be fairly consistent. An emissivity of 0.8 was assumed for carbon, and true temperatures were derived from brightness temperatures using the method of De Vos (1954). The fact that the brightness pyrometer always registers 50-100 K lower than the two-color pyrometer only for the clouds of particles burning with luminous flames, not for the clouds burning at temperatures similar to those of the combustor walls, was attributed to an optical aberration experienced by the observer. This optical illusion could be associated with the brevity of combustion at high temperatures; thus, the intermittency of bright events results in observing the dark background of the injector entrance as well, and causes the average temperatures to appear lower.

A pair of intensity traces recorded by the pyrometer and corresponding to combustion of 8μm plain polymer particles is shown in Fig. 6a. The particles were combusted in pure O_2 at a combustion chamber wall temperature of 1500 K and a gas temperature of 1300 K. In Fig. 6b, temperature-time profiles derived from Wien's approximation, for the same particles, are depicted. Temperature-time traces of groups of particles 45μm in diameter, burning in pure O_2 at the same conditions as above, are shown in Fig. 7. Finally, in Fig. 8, the temporal combustion behavior of groups of particles containing 25%, by mass, carbon black spheres, has been recorded. The agreement of the time-temperature traces of this last group of combusting particles is fairly good, denoting the consistency of the instrument.

Further details about the theory, construction and évaluation of two and multiple color pyrometers as well as calibration procedures and applications are described in selected works included in the Reference section.

7 Conclusions

A near-infrared two-color pyrometer has been constructed and implemented to record temporally resolved temperature profiles of burning coal particles. The pyrometer was interfaced with an externally heated drop tube furnace capable of achieving temperatures in the vicinity of 1600 K. The monitoring of the combustion events takes place coaxially with the particle flow, from an observation window located at the top of the coal injector. The injector's design was a compromise between maximizing the light collection efficiency and reducing the background radiation, as well as avoiding desturbing the furnace operations. The pyrometer employed fiber cable optics to transmit and split the radiation in two channels, each containing a series of optics, a filter, a detector and electronics. The filters were wavelength-centered on 800 and 1000 nm, respectively. The detectors were silicon photocells. The design of the detector electronics employed four stages of amplification and an offset circuit to avoid interference of the background radiation with the combustion signals. The two-color pyrometer was calibrated at the temperature of melting platinum, its performance was assessed by comparison to a brightness pyrometer as well as thermocouple readings and its consistency was verified in combustion experiments employing almost identical carbon particles.

8 Aknowledgements

The authors would like to express their appreciation to Joe Fontana and Elton Daily for their continous support, advice on technical issues and craftmanship of various components of the furnace interface and the all "*handmade*" pyrometer. Thanks are also due to Leonard Montenegro and John Lee for their assistance in designing the pyrometer and furnace electronics. This research was supported by U.S. Department of Energy University Coal Programs Grant Number DE-FG22-84PC70775.

9 References

1. Ackerman, S. (1960). "A Review of Automatic Radiometric Pyrometry." *Temperature, Its Measurement and Control in Science and Industry*, American Institute of Physics, 839.

2. Ackerman, S. (1960). "Notes on the Design and Performance of a Two-Color Pyrometer." *Temperature, Its Measurement and Control in Science and Industry*, American Institute of Physics, 849.

3. Altrichter, D. M. (1981). "Optical Determination of Time-Temperature Profiles for Single Particle Coal Combustion." Master thesis, MIT.

4. Assary, M. and Graig, J. (1985). "Temperature, Concentration, and Size Measurements in Turbulent Reactive Flows."

5. Ayling, A. B. and Smith, I. W. (1972). "Measured Temperatures of Burning Pulverized Fuel Particles, and the Nature of the Primary Reaction Product." *Combustion and Flame* **18**, 173.

6. Babelot, J. F., Magill, J., Ohse, R. W. and Hoch, M. (1982). "Microsecond and Sub-Microsecond Multi-Wavelength Pyrometry for Pulsed Heating Technique Diagnostics." *Temperature, Its Measurement and Control in Science and Industry*, American Institute of Physics, 439.

7. Brenden, B. B. (1960). "An Infrared Radiation Ratio Pyrometer" *Temperature, Its Measurement and Control in Science and Industry*, American Institute of Physics, p.429.

8. Cashdollar, K. L. and Hertzberg, M. 1982). "Infrared Temperature Measurements of Gas and Dust Explosions." *Temperature, Its Measurement and Control in Science and Industry*, American Institute of Physics. 453.

9. Cezairliyan, A., Miller, A. P., Righini, F. and Rosso, A. (1982). "Radiance Temperature of Metals at their Melting Points as Possible High Temperature Secondary Reference Points." *Temperature, Its Measurement and Control in Science and Industry*, American Institute of Physics, 379.

10. De Vos, J. C. (1954). "A New Determination of the Emissivity of Tungsten Ribbon" *Physica* **XX**, 690.

11. Dictor, A. R. (1979). "Determination of Complete Temperature Profiles of Singly Burning Pulverized Fuel Particles." Master thesis MIT.

12. Foley, G. M., Morse, M. S. and Cezairliyan, A. (1982). "Two Color Microsecond Pyrometer for 2000 to 6000 K." *Temperature, Its Measurement and Control in Science and Industry*, American Institute of Physics, 447.

13. Gardner, J. L., Jones, T. P. and Davies, M. R. (1982). "A Broadband Ratio Pyrometer" *Temperature. Its Measurement and Control in Science and Industry*, American Institute of Physics, 409.

14. Gat, N., Cohen, L. M. and Witte, A. B. (1985). "Three-Color Pyrometer for Burning Particle Temperature Measurement."

15. Heght, G. J. (1960). "A Two-Wavelength Near Infrared Pyrometer." *Temperature, Its Measurement and Control in Science and Industry*, American Institute of Physics, 407.

16. Hill, W. E. (1960). "Two-color Pyrometry." *Temperature. Its Measurement and Control in Science and Industry*, American Institute of Physics, 419.

17. Le Chetelier, H. L. and Boudouard, O., (1901). "High Temperature Measurements." John Wiley New York.

18. Mackowski, W., Altenkirch, R. A., Peck, R. E., and Tong, T. W. (1982). "A Method for Particle and Gas Temperature Measurement in Laboratory Scale, Pulverized-Coal Flames." *Combustion Science and Technology* **31**, 139.

19. Millikan, R. C. (1960). "Sizes, Optical Properties, an Temperatures of Soot Particles." *Temperature, Its Measurement and Control in Science and Industry*, American Institute of Physics, 497.

20. Mitchell, R. E. and McLean, W. J. (1982). ""On the Temperature and Reaction of Burning Pulverized Fuels." *Nineteenth Symposium (Intrnational) on Combustion*, The Combustion Institute, 1113.

21. Neville, M., Quann, R. J., Hayes, B. S. and Sarofim, A. F. (1981). "Vaporization and Condensation of Mineral Matter During Pulverized Coal Combustion." *Eighteenth Symposium (International) on Combustion*, The Combustion Institute, 1267.

22. Niksa, S. and Mitchell, R. E. (1983). "Interpreting Spacially-Resolved Mass Conversions and Two-Color, Single-Particle Temperatures for Burning Polydisperse Pulverized Fuel Streams." *Presented at the International Conference on Coal Science, August 15-19, 1983, Pittsburg, PA, Sandia Report 83-8707.*

23. Nguyen, Ke and Branch, M. C. (1985). "Near-Infrared Two-Color Pyrometer for Determining Ignition Temperatures of Metals and Metal Alloys." *Review of Scientific Instruments* **56** (9), 1780.

24. Nutter, G. D. (1972). "A High-Precision Automatic Optical Pyrometer." *Temperature, Its Measurement and Control in Science and Industry*, American Institute of Physics, 519.

25. Quann, R. J. and Sarofim, A. F. (1982). "Vaporization of Refractory Oxides During Pulverized Coal Combustion." *Nineteenth Symposium (International)*

on Combustion, The Combustion Institute, p.1429.

26. Ruffino, G., Righini, F. and Rosso, A. (1972). "A Photoelectric Pyrometer with Effective Wavelength in the Near Infrared." *Temperature, Its Measurement and Control in Science and Industry*, American Institute of Physics, 531.

27. Senior, C. L. and Flagan, R. C. (1986). "Synthetic Chars for the Study of Ash Vaporization." *Twentieth Symposium (International) on Combustion*, The Combustion Institute, Pittsburg, PA., 921.

28. Sparrow, E. M. and Cess, R. D. (1978). *Radiation Heat Transfer* Augmented Edition, McGraw-Hill, London.

29. Timothy, L. D., Sarofim, A. F. and Bèer, J. M. (1982). "Characteristics of Single Particle Coal Combustion." *Nineteenth International Symposium on Combustion*, The Combustion Institute, 1123.

30. Warnke, G. F. (1972). "Commercial Pyrometers." *Temperature. Its Measurement and Control in Science and Industry*, American Institute of Physics, 503.

10 Notation

SYMBOL	DESCRIPTION	UNITS
A	total radiating area	m^2
C	various constants	
J_λ	intensity of radiation	W/m^2
L	distance	
T	temperature	K
α_λ	radiation amplitude	
ϵ_λ	emissivity	
η	efficiency	
λ	wavelength	nm
σ	standard deviation	

11 List of Figures

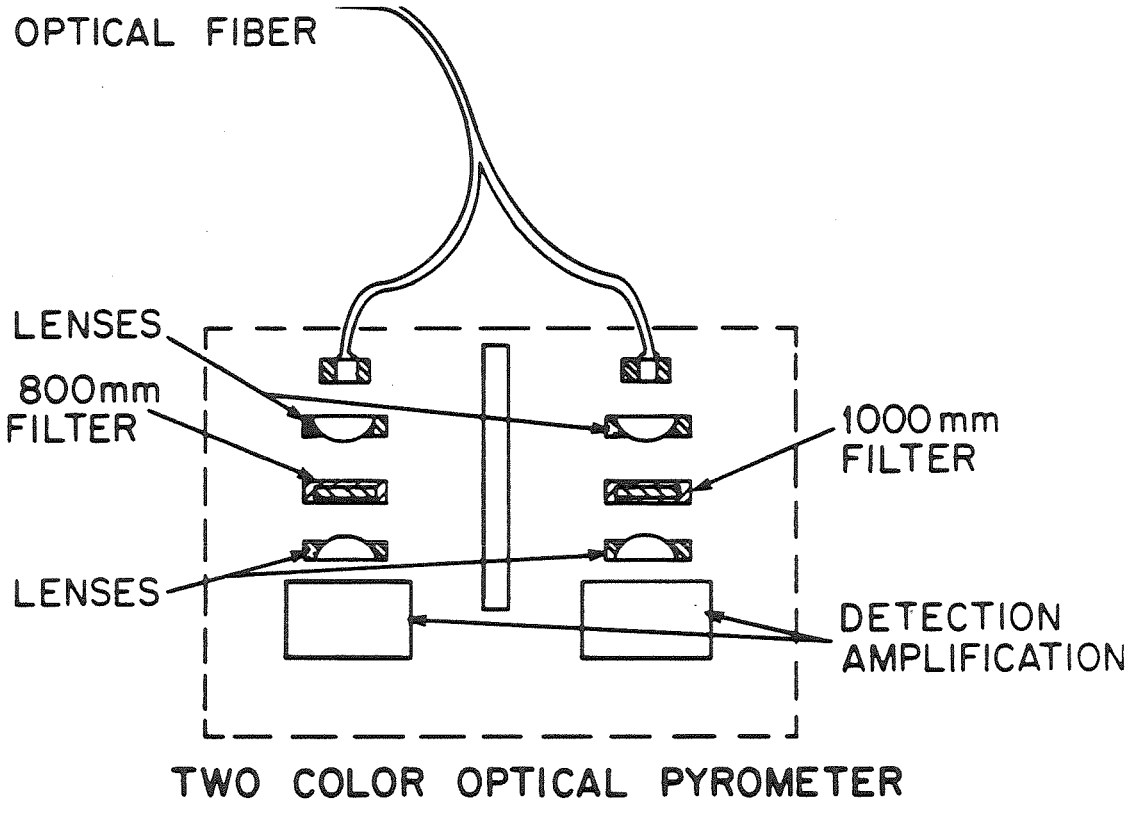

Figure 1: Schematic of the near infrared two-color pyrometer.

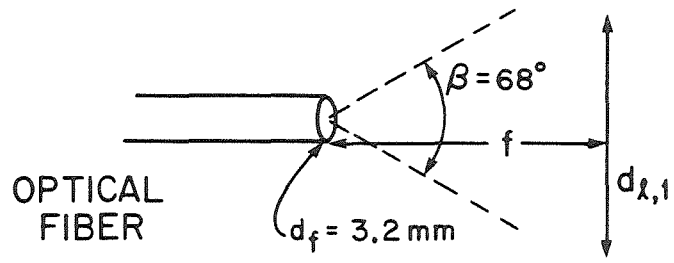

$$2 \tan(\beta/2) = 1.34$$

$$d_{\ell,1} / f_1 = 1.34$$

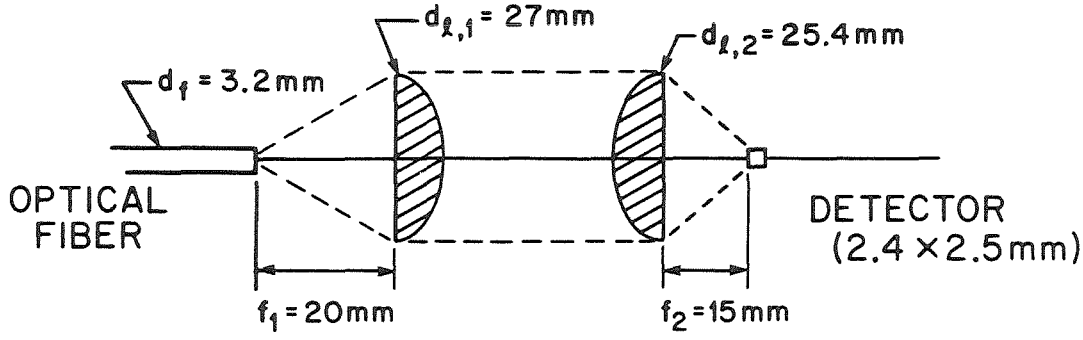

REQUIREMENTS

$$d_{\ell,1} = d_{\ell,2}$$

$$d_{\ell,1} / f_1 > 1.34$$

$$f_2 / f_1 = 0.75$$

Figure 2: Arrangement of lenses to maximize radiation collection efficiency.

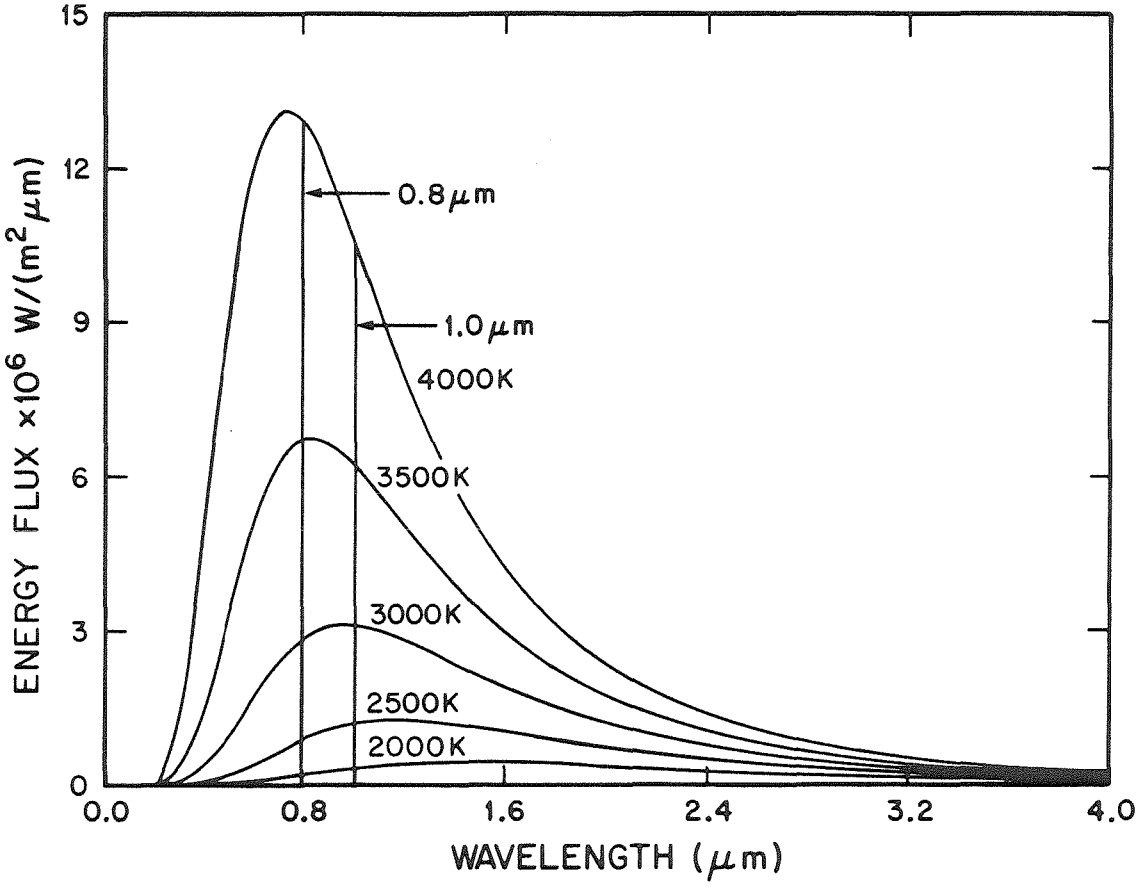

Figure 3: Planck's radiation flux vs. wavelength curves; selection of wavelengths.

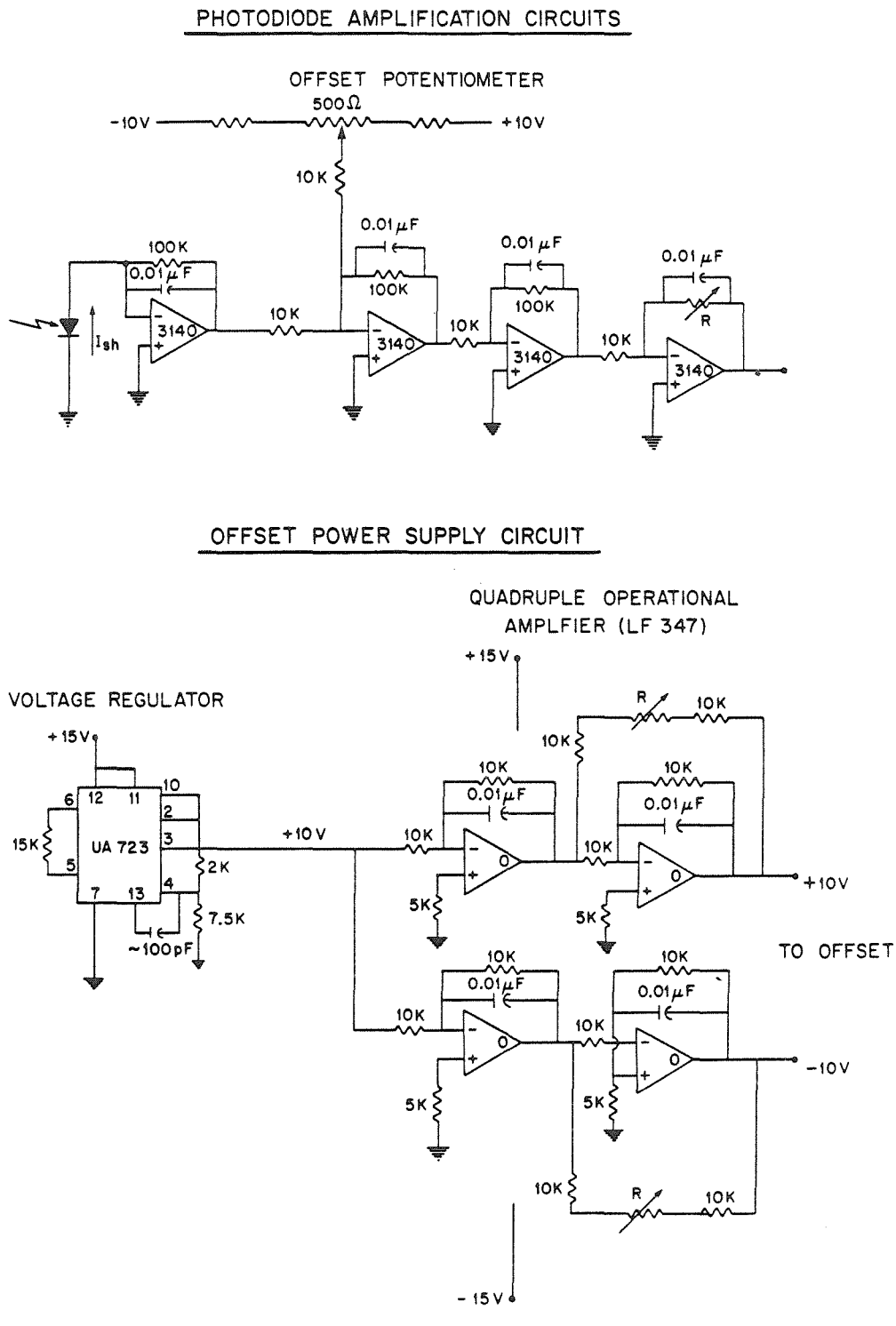

Figure 4: Schematic of the pyrometer amplification circuits.

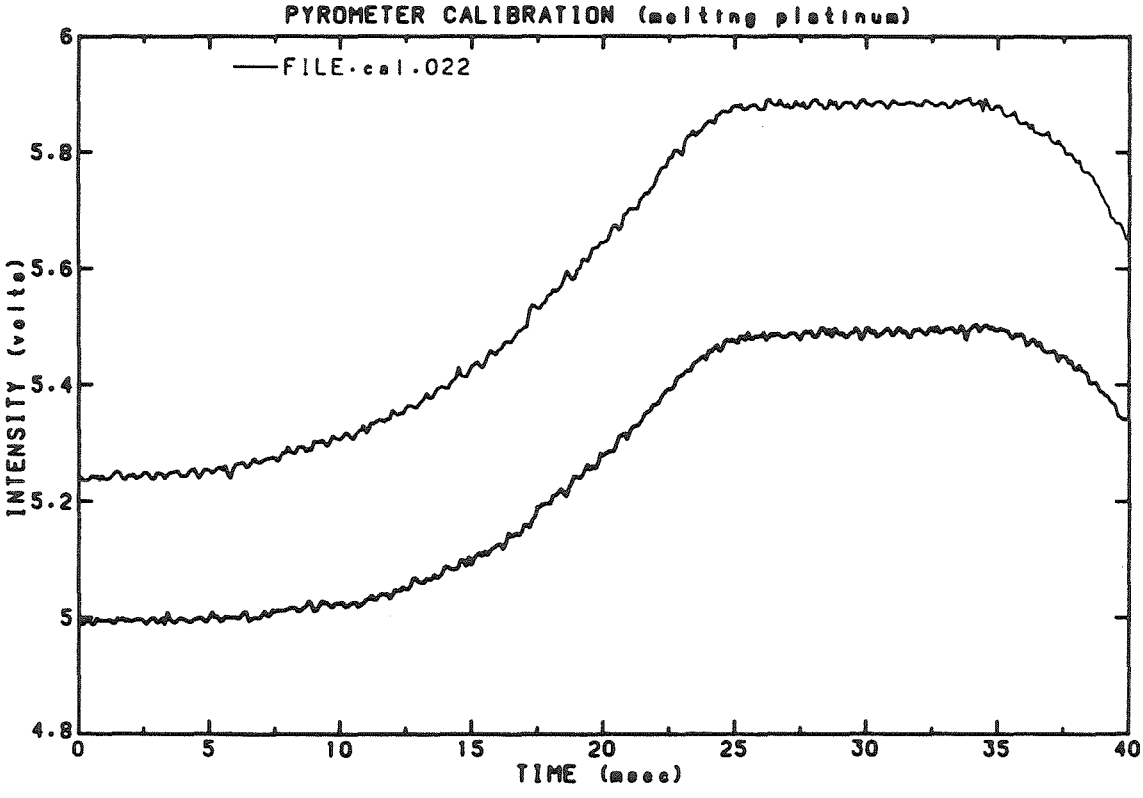

Figure 5: Calibration of the pyrometer. Two channel intensity traces generated by melting of a platinum wire.

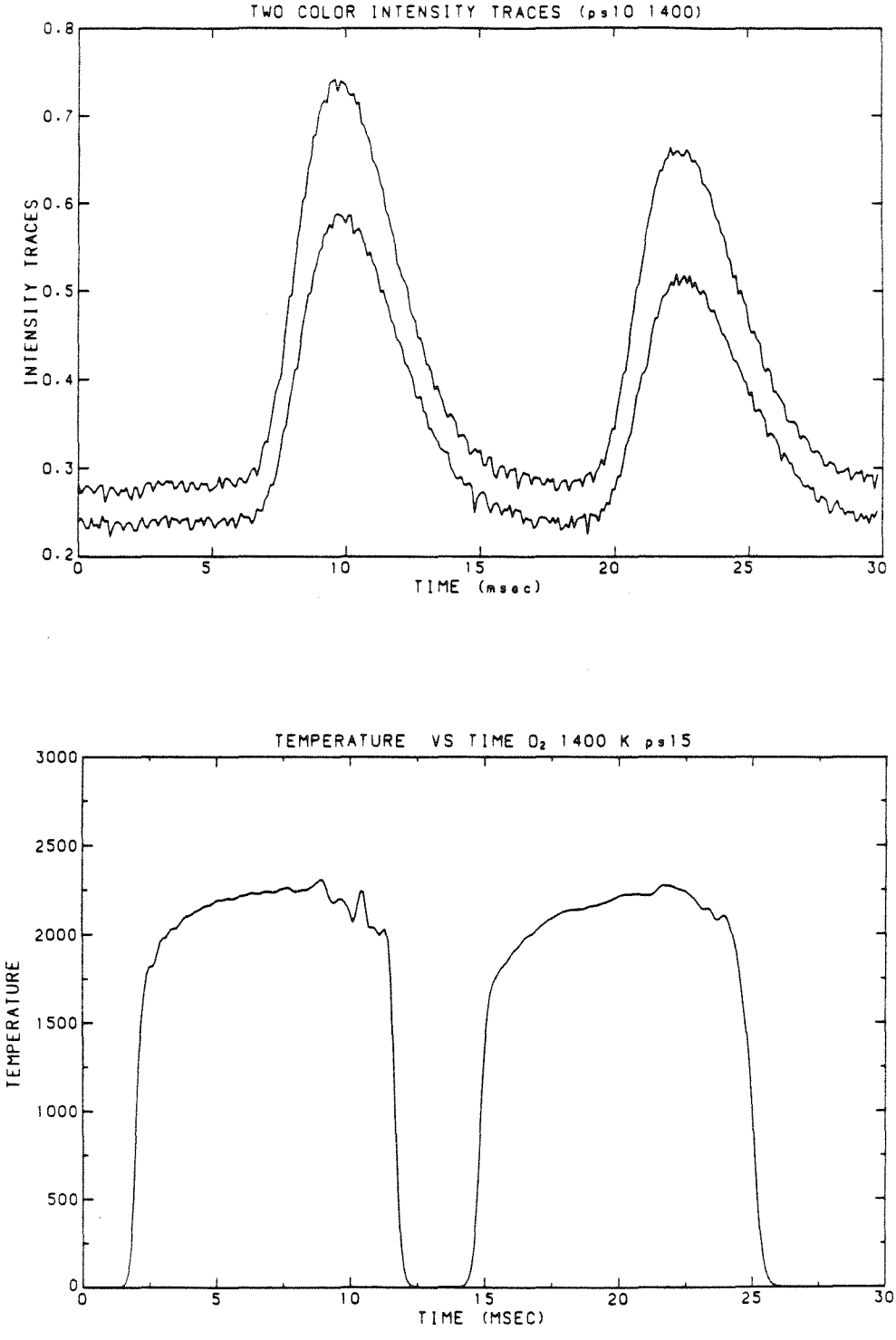

Figure 6: Combustion of 8μm, diameter, plain polymer glassy carbon particles. (a) two color intensity traces, (b) associated temperature-time profiles.

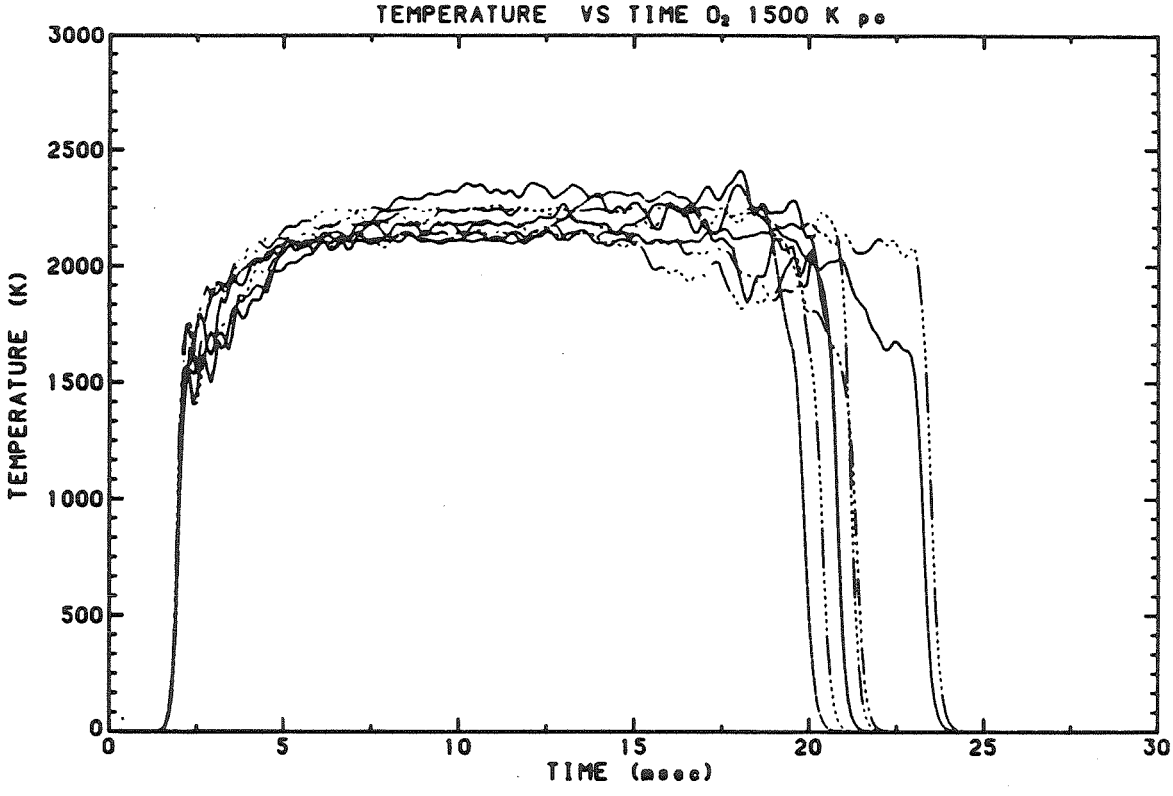

Figure 7: Superimposed temperature-time profiles of 45 μm, diameter, plain polymer glassy carbon particles burning in pure O_2.

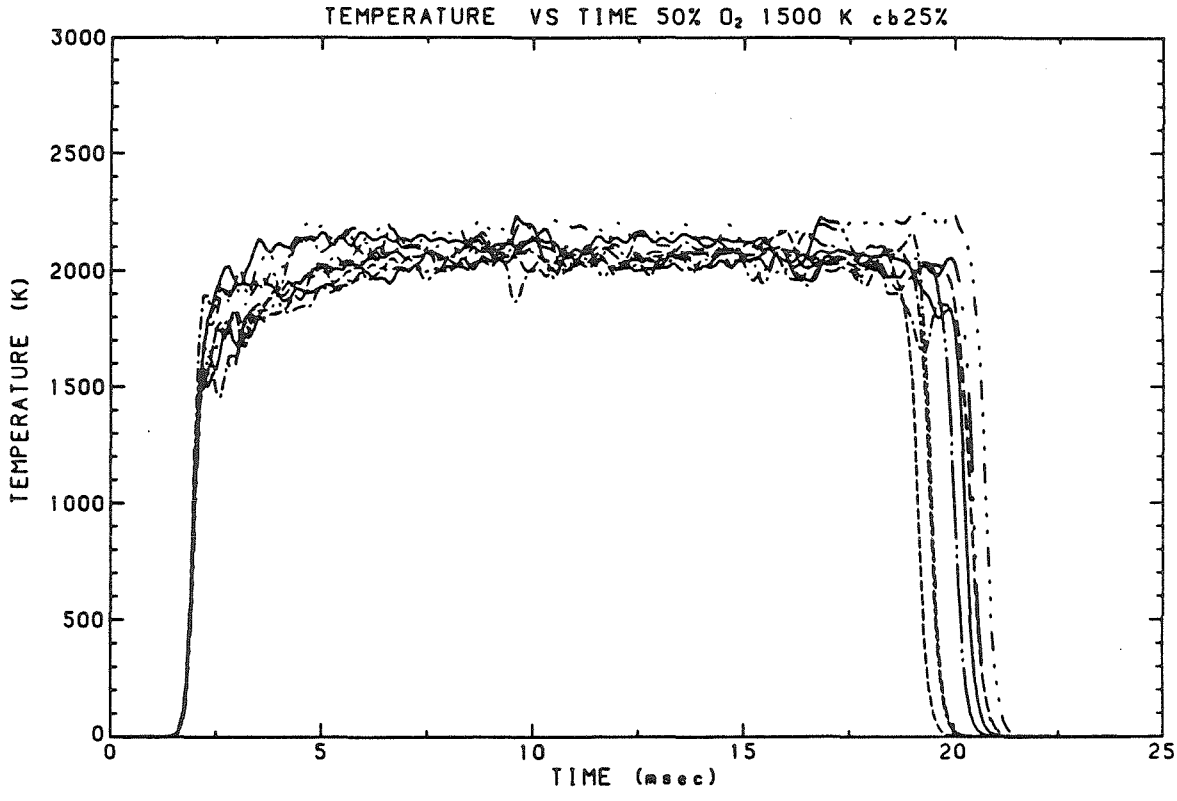

Figure 8: Superimposed temperature-time profiles of 45 μm, diameter, of 25% carbon black containing glassy carbon particles burning in a mixture of 50% O_2 - 50% N_2.

CHAPTER 6

Submitted to *Combustion and Flame*

Oxidation Kinetics of Monodisperse Spherical Carbonaceous Particles of Variable Properties

Yiannis A. Levendis Richard C. Flagan
George R. Gavalas*
Environmental Engineering Science and *Chemical Engineering
California Institute of Technology

Abstract

Synthetic chars of variable physical and chemical properties have been developed as surrogates for coal char in the study of char oxidation mechanisms and rates. The char particles were spherical and monodisperse, with sizes ranging from a few microns to several tens of microns. The particles were made from a carbon-yielding polymer and pore forming additives. The surface areas of the chars made from different additives varied by more than two orders of magnitude and the porosities varied by a factor of five. The pore size distributions included both micro and transitional pores.

X-ray studies revealed that all chars were amorphous when heat-treated to temperatures up to 1600 K in an inert atmosphere. However, upon oxidation at 1600 K, the carbon matrix underwent partial graphitization. This transformation was particularly pronounced for some of the copolymer chars.

Combustion experiments showed that the total surface area of the chars increased dramatically with conversion, revealing the existence of a vast network of micropores. Apparent oxidation rates were higher for the chars that contained transitional pores in a microporous matrix. When compared with the rates reported in the literature for coal derived chars, the calculated intrinsic rates were lower at intermediate particle temperatures (800 - 1600 K) but comparable at elevated temperatures (1800 - 2300 K). As the temperature was increased further, the intrinsic rates decreased as predicted by the Nagle and Strickland-Constable kinetic mechanism[1].

1 Introduction

Reported variations in the intrinsic oxidation rate of carbonaceous materials are large, even when burned under similar conditions. Smith[2,3] reported that the intrinsic reactivities of carbons derived from different sources vary by as much as four orders of magnitude at the same particle temperature. The intrinsic reactivity has been defined as the reaction rate per unit area of pore surface after having corrected for any mass transfer limitations[4]. Ideally, any variations in the intrinsic reactivities should reflect only differences in the atomic and chemical structure of the materials and, possibly, catalytic effects of impurities. In many studies, however, the physical structure of chars has been ill-characterized because of the extreme complexity of the materials, incomplete data, and the difficulty of decoupling the effects of existing impurities[5]. The temperature of the burning char particles and that of the surrounding gas have, in many cases, been estimated from energy balances and, therefore, are uncertain. Even after careful fractionation the sizes and shapes of char particles vary. As a result, nominally similar particles may burn at substantially different rates and temperatures[6].

Some of these difficulties in the study of char combustion phenomena can be overcome by using model materials. A synthetic char based on glassy carbons was impregnated with minerals for the study of ash vaporization by Senior and Flagan[7]. Levendis and Flagan[8] produced monodisperse spherical particles of similar glassy carbons for the study of char oxidation kinetics, eliminating uncertainties in the combustion kinetics associated with: a) *size*, since all particles have equal size; b) *shape*, since all particles are spherical; and c) *impurities*, since the particles contained no minerals and were produced from high purity materials.

The present study focusses on the influence of physical and chemical properties of chars on carbon oxidation rates through the use of spherical char particles with controlled characteristics. The physical properties examined include the particle

size, porosity, pore size distribution, the total surface area, and the density. The chemical properties include the elemental composition, the enthalpy of combustion and the degree of crystallinity.

2 Experimental Methods

The methods of char synthesis are based on previous studies of glassy carbons[9 - 11]. The methods of production and characterization of the uniformly sized char particles used in the present study have been described in detail elsewhere[12], and will be described only briefly here. All of the chars produced for this work had a common glassy carbon matrix. They were formed from a partially polymerized carbon-yielding binder and a pore-forming agent, with acetone added to facilitate mixing and atomization. The binder was poly-furfuryl alcohol. The pore formers were organic materials that dissolve in the acetone-polymer mixture: *decalin, glycerol, polyethylene glycol, tannic acid, benzoic acid, isopropyl alcohol* and *Triton X-100 (isoctyl phenoxy polyethoxy ethanol).* Submicron-sized carbon black particles were also added to the polymer/acetone mixture as pore formers[7,10]. The resulting mixtures were sprayed by means of a acoustically excited aerosol generator into a thermal reactor, where the droplets solidified and the polymer was cured in an inert atmosphere (N_2) at 600 K. The aerosol generation conditions were optimized for monodisperse particle production. The particles were collected at the bottom of the reactor by sedimentation. A secondary heat treatment at 800 K in nitrogen for 1 hr was perfomed in a muffle furnace. Subsequent sieving in a mechanical shaker eliminated any doublets or triplets that were generated by coagulation during the aerosol generation, and resulted in monodisperse spherical particles.

2.1 *Particle Characterization*

Total surface areas were measured by both small angle scattering (SAXS) techniques and gas adsorption. The method used for the adsorption studies has been described in[13]. Apparent densities, porosities, pore volume, and pore surface distributions, for pore openings larger than 5.5 nm, were determined by mercury intrusion using a *Quantachrome Autoscan* porosimeter. Distributions of pores, in the size range 5 to 30 nm, were also determined from multilayer adsorption and capillary condensation of nitrogen. The average size of the smaller pores was determined by SAXS measurements. True densities were determined by helium pycnometry at room temperature and, where applicable, by wide-angle x-ray scattering.

Optical and scanning electron microscopy (SEM) were used to examine the morphology of particles before and after oxidation. SEM studies employed an *ETEC Autoscan* microscope having a resolution of 70Å at an operating voltage of 20 kV. Elemental analysis was performed by a *Perkin Elmer* analyzer and sulfur content determination by the *Leco* method. Heating values of the chars were determined using a *Parr* calorimeter.

Wide-angle x-ray diffraction profiles were obtained using a *Guinier* camera which employed CuKα radiation at 40 kV and 25 mA. The camera used the focussing action of a bent quartz crystal monocromator to record all background-free (*hkl*) reflections on a high resolution photographic film. Small-angle scattering profilies were acquired by means of a *Siemens D500/501* Diffractometer employing Kβ Nickel filtered CuKα radiation at 40 kV 30 mA. The detector was a scintillation counter. Appropriate corrections were made.

2.2 *Combustion Experiments*

The particles were burned in a laminar-flow, drop-tube furnace that was externally heated by *Kanthal Super 33* molybdenum disilicide heating elements, shown in Fig.1.

The particles were injected on the centerline of the 50 mm i.d. alumina tube at the top of the 200 mm long hot zone. A water-cooled gas dilution sampling probe was mounted at the bottom of the hot zone to collect partially oxidized particles in experiments where combustion was not complete. The injector was water-cooled and had a wide bore (1 cm i.d.) to facilitate viewing down from the top of the furnace.

The furnace wall temperature profile was measured on the outer surface of the alumina tube by permanently installed type *S* thermocouples and on the inside surfaces by a disappearing filament optical pyrometer. These readings have an uncertainty of ± 15 K and were used for subsequent determination of the combustion environment of the particle. Gas temperatures were measured with a suction pyrometer and a bare thermocouple. After correcting the thermocouple measurements for radiation the two methods were in good agreement. The estimated uncertainty in the gas temperature is ± 20 K. Uncertainties in temperature reflect on the magnitude of the absolute values of the kinetic parameters reported; however, an effort was made in the present study to maintain similar reaction conditions for of all chars to minimize the ambiguities in the relative values.

Particle combustion temperatures were measured by a two-color optical pyrometer following the approach of Timothy et al.[14]. A lens mounted at the top of the injector focussed the radiation emitted from the burning particles onto the end of a bifurcated optical fiber bundle. The viewing was done against the cold background provided by the sample collection probe at the bottom of the furnace. A 200 μm pinhole placed between the lens and the optical fiber helped define the view volume and minimized radiation emitted from the hot combustion walls. Two broad-band filters (bandwidth 70 nm) in the near infrared (800 and 1000 nm, respectively) were used to maximize intensities collected from small particles burning at large distances. Solid state detectors (*Hamamatsu S1336-5BQ* silicon detectors) were

used for both wavelengths. The associated preamplifiers were close to the detectors and were enclosed in metallic boxes to minimize electrical noise interference. The pyrometer was calibrated at the temperature of melting platinum. The current generated from a capacitor discharge was conducted through a small platinum wire, causing its temperature to be elevated to the point of melting. The portion of the resulting intensity-time profile in which the ratio of the two-color intensity signals was constant with time is where the solid-to-liquid phase change takes place. This intensity ratio was used for calibration since it corresponds to the melting temperature of platinum (2046 K). A complete description of the pyrometer and the interpretation of results is given in [15].

Particle feed rates on the order of 1 g/hr were acheived with a syringe pump feeder[16] for experiments where clouds of particles were burned and mass and size reduction was monitored. Pyrometry measurements were conducted in a single particle mode and, therefore, the feeding system was modified to ensure that only one particle was present in the view volume during measurement. To feed particles at this low rate, a small boat containing a small amount of char was inserted at the injector line and single particles could be entrained by lightly vibrating the boat (shown in Fig.1).

3 Results and Discussion

3.1 *Physical Structure of Particles*

Physical properties of the chars that influence their combustion behavior include the pore size distribution, i.e., the pore volume in each pore size range, the shape and the connectivity of the pores, as well as the total surface area of pore walls accessible to the oxidizer gas. A complete physical and chemical characterization of the chars is given in[12]. The size of particles produced was varied from a few microns to 100 μm. Within each production run, the particle size was constant, within 1μm. The particle size is very important in combustion, since it influences the rate of diffusion of the oxidizer and energy to and inside the particle. Chars, carbonized at 800 K, were used as starting materials for all combustion experiments except where mentioned otherwise. SEM photographs of plain polyfurfuryl alcohol (PFA) particles of 45 and 8 μm, in diameter, are shown in Fig. 2 (a and b). Particles formed from 18% polyethylene glycol (PEG) and PFA [1]; and 25% tannic acid and PFA are shown in Fig. 3a and 3b, respectively. Surface structure consisting of micron sized bubbles can be seen in some of the particles and is indicative of volatiles that attempted to escape while the particle was still in the plastic state. The chars produced in this study contain only micropores that are not detectable with the scanning electron microscope (apart from the few surface macropores mentioned above). The only exception is the material which contained carbon black, added to create transitional porosity in amounts proportional to the carbon black concentration. These particles appear very porous with rough surfaces as shown in Fig. 4, where the surface of a particle containing 25% carbon black is contrasted, at high magnification, with the surface of a plain polymer particle.

[1] The composition of the synthetic chars refers to the mass percentages of additives in the initial pore-former/polymer mixture, the rest being polyfurfuryl alcohol (PFA).

The pore size distribution of carbon black containing materials, as estimated by applying the Washburn equation[17] to the porosimetry results and the Yan-Zhang model[18] to nitrogen capillary condensation results, exhibited an intense maximum corresponding to pore diameters of 150Å. All the other materials possessed only micropores that were below the detection limit of both the above techniques (60 and 30Å in diameter respectively). The average micropore dimension of the chars was measured by small-angle x-ray scattering and was found to be around 10Å, depending on the pore former used[12] as shown in Table I. Furthermore, it was concluded that the mouths of these micropores were closed, restricting outside gas penetration. Finally, the SAXS studies indicated that the shape of these pores was rather irregular[12].

The apparent densities of the materials were measured by atmospheric mercury intrusion, and the helium or skeletal density were measured by helium penetration at atmospheric conditions. The results are also shown in Table I, along with the total porosity of the chars, which includes all pores smaller than 7μm in radius. The total surface areas of the materials were measured by the BET method, employing nitrogen adsorption at 77 K. The results indicate that the areas accessible to N_2 vary from 2 m^2/g for plain polymer char, to 79 m^2/g for the material containing 18%PEG, to 185 m^2/g for the material containing 25% carbon black, as shown in Fig. 5. For the plain polymer (PFA) char, the total area was determined to be 59 m^2/g by CO_2 adsorption at room temperature applying Medek's method[19] to the resulting Dubinin's equation parameters[20,21]; showing the CO_2's ability to penetrate small pore openings (theoretically its lower limit is pore openings of 3Å). The total pore area of all the chars is actually bigger than the above values, being on the order of a few hundred square meters per gram, as shown by SAXS, but the additional area is in pores that appear to be inaccessible to gases during adsorption experiments.

Oxidation at elevated temperatures alters the physical properties of the chars dramatically. SAXS studies indicate that the pores enlarge and assume more regular shapes because of the combined effects of high temperature annealing and oxidation, and that the pore entrances open because of the effect of oxidation alone. The pores become available to outside gas penetration and as a result the surface areas measured by gas adsorption increase with the degree of burnout. The N_2 BET areas increase by two orders of magnitude, as shown in Fig. 5, and the CO_2 areas by one order of magnitude. At the same time the SAXS area, which is a better approximation to the true total (closed and open) surface area, decreases because of pore coarsening. Therefore, as burnout proceeds, the surface areas measured by the different methods tend to similar values, indicating the formation of a fully accessible interconected network of micropores[12].

An average pore radius can also be calculated from the adsorption experiments data, using the average value of surface area and average porosity and density after partial combustion with Wheeler's equation[22]:

$$\bar{r}_p = \frac{2\epsilon}{A_G \sigma_a}(r.f.)(1-\epsilon), \qquad (1)$$

where ϵ is the total porosity and $(r.f.)$ is a roughness factor, here taken as 2 after Wheeler. From this calculation an average pore radius of 13 Å for the plain polymer was estimated, which is in good agreement with the SAXS data. Physical properties for some of the partially burned chars are listed in Table Ib.

3.2 *Chemical Properties of the particles*

3.2.1 *Elemental analysis and calorimetry*

Heating values, carbon and hydrogen contents, and carbon-to-hydrogen ratios for the chars are given in Table II. Apart from the carbon and the hydrogen the particles contain oxygen and nitrogen. The nitrogen content was measured to be less than

0.25%. Therefore, the glassy carbons contain considerable oxygen which, however, was not measured directly in this study. The heating values of the chars containing tannic acid are lower than that of the the plain polymer char, and decrease with increasing tannic acid content. The carbon content of the copolymer also decreases with increasing tannic acid concentration because of the low carbon content of pure tannic acid. The oxygen content of the heat-treated tannic acid, however, appears to be very large (≈20%), which is also suggested by its chemical formula (C_{76} H_{52} O_{46}). The heating value of the char containing 40% glycerol 7% Triton X-100 is the highest, probably because of its higher hydrogen content. The materials containing carbon black exhibit the lowest heating values, due to their low hydrogen content, the extreme being the heating value of pure carbon black alone. Values for plain polymer char that had undergone high temperature treatment and partial combustion are also included. The heating value of the char decreases, as expected, during combustion due, again, to hydrogen loss (see Table II). Sulfur was introduced in the particles by the consolidation agent (p-toluene sulfonic acid). Leco analysis indicated that sulfur levels were quite low (0.08%).

3.2.2 *Atomic Structure*

All of the chars used for the combustion studies had been pyrolyzed at 800 K. According to Fitzer et.al.[23], in this first region of carbonization volatile components leave the polymer precursor in the form of gases and tars and at the same time condensation reactions produce polynuclear aromatic compounds. X-ray diffraction spectra indicate that the various copolymer chars are completely amorphous after this first stage of heat treatment. In the second stage of carbonization at temperatures between 800 to 1300 K, aliphatic side-chains and hydrogen atoms are eliminated, resulting in the evolution of methane and hydrogen gas, and a carbon residue is left behind[23]. Oxygen also evolves as oxides of carbon. After treatment

to 1600 K, the materials are still amorphous but there is some evidence that two-dimensional ordering takes place[12]. In partially burned samples, enhanced two-dimensional ordering is suggested by the appearance of the (*100*) and (*110*) peaks. The interlayer spacing $\bar{d}_{(002)}$ also decreases, approaching 3.95Å for all the copolymer materials. Jenkins *et al.*[5] suggest that the amorphous regions in glassy carbons are randomly distorted graphitic layers in intertwined ribbonlike arrays. Some partially burned copolymer chars in the present study contained both graphitic and/or turbostratic components in a disordered matrix. The diffraction spectrum of the material formed from 17% tannic acid and PFA is shown in Fig. 6 as an example of two-phase graphitization since a very intense narrow peak, corresponding to $\bar{d}_{(002)}$ = 3.49Å and indicative of turbostratic structure, is superimposed on the disordered phase component. A possible explanation for the existence of the crystalline phases is that they originated from the decomposition and melting of the pore-former materials that are less cross-linked than the polymer binder. Hence, it appears that the pore-forming agents alter both the physical and chemical structural properties of the chars.

3.3 *Combustion Behavior*

In a previous study of the combustion of monosized glassy carbon spheres, considerable particle-to-particle variation in the ignition was observed[11]. Modifications were made to the particle drying tower (reactor) to ensure that all particles were subjected to similar environments during this critical part of their evolution. The chars produced in the present study showed substantially less particle-to-particle variation than previously observed. For all furnace temperatures, the particles burned slowly at approximately the wall temperature when the oxidizing gas was air. Upon enriching the gas with oxygen a fraction of the particles burned fast emitting luminous radiation. The fraction of particles igniting increased with increased

oxygen content. Beyond a certain value of oxygen concentration, around 35-45% depending on the kind of the char, all particles ignited and burned with bright flashes. At even higher oxygen partial pressures the combustion got increasingly fast and bright.

3.3.1 *Partial Combustion*

Partial combustion experiments were conducted in air at furnace wall temperatures ranging from 1300 to 1600 K. The residence time in the hot zone was set to 2 s for all temperatures. The gas flows in the furnace and the injector were tuned to be approximately isokinetic. Particle residence time calculations took into account sedimentation (slip).

Microscopic observations in conjunction with density measurements indicate that the particles were burning in a shrinking core mode. Two SEM micrographs, one depicting a partially burned particle of plain polymer (PFA) char and the other partially burned particles formed from 17% tannic acid and PFA are shown in Fig. 7. The copolymer particles appear to have suffered the highest weight loss. Since the oxidizing conditions in the two cases were similar, the particles containing tannic acid seem to be more reactive.

Apparent oxidation rates for the partially burned particles were inferred from two different methods: (a) mass reduction measurements, and (b) particle size reduction and density changes. The mass reduction measurements were performed by monitoring the loss in mass of a known quantity of char as it passed through the combustion chamber and by correcting for the small losses in the injection lines. The particle size reduction was observed by optical and SEM microscopy. An average density was used. Additional data points, corresponding to lower temperatures, were obtained from thermogravimetric experiments (*DuPont* model 920 thermogravimetric analyzer) on plain polymer at an oxygen partial pressure of 0.17 atm.

3.3.2 *Pyrometry*

Particles burning to completion in pure oxygen and 50% O_2-N_2 mixtures at wall temperatures ranging from 1300 to 1500 K were monitored by the two-color optical pyrometer. The ratios of the two intensity signals were substituted in Wien's approximation of Planck's law, assuming gray body emission. Particle temperature-time histories were thus obtained for the entire combustion period. The uncertainty in these measurements is estimated to be ± 40 K. The observed temperatures ranged from 1600 to 2850 K. The combustion times varied between 7 and 35 msec. In most cases the temperature increased in the first few milliseconds of combustion and then remained approximately constant to the end of burn-off. In general, the particle temperatures increased with both gas and wall furnace temperatures. Three groups of traces of particles containing 25% carbon black burning in pure oxygen are shown in Fig. 8. The associated furnace wall temperatures ranged between 1350 and 1500 K and the gas temperatures between 1150 and 1300 K, since the particles burn to extinction only a few millimeters below the tip of the injector where the gas temperatures are generally lower than the average furnace temperatures. The average measured particle temperatures for this material ranged from 1900 to 2850 K and were higher than the temperatures exhibited by the other chars. The high combustion temperatures of the carbon black containing chars are attributed to the external surface area roughness, as well as to the large total pore volume of these chars and the availability of a large network of transitional pores. These pores serve as *feeder* pores[5] for the micropore matrix, thereby enhancing reaction by allowing oxygen to penetrate into the char volume. Close observation of Fig. 8 reveals that, while the particle temperature increased from 2000 K (case a, 1300 K wall temperature) to 2600 K (case b, 1450 K wall temperature), the reaction time decreased from 20 to 14 ms. However, further increase of particle temperature to 2850 K (case c, 1500 K wall temperature) caused the reaction time to increase from 14 to

16 ms. Thus, the trend of the reaction rate increasing with temperature ceases once a certain temperature region is reached beyond which the rate decreases with temperature. The existence of this inversion region in carbon kinetics has been observed by Nagle and Strickland-Constable[1] as well as Walls and Strickland-Constable[24] for oxidation of pyrolytic graphite rods. Park and Appleton[25], also observed this behavior in the oxidation of submicron carbon black particles in a shock tube. The similarity of the the results obtained with graphite rods and particles, however, cannot be quantified because of the different time scales involved in the two types of experiments.

4 Oxidation Kinetics

Before analyzing the data to obtain the intrinsic oxidation rates of the synthetic chars it was necessary to verify that the combustion rate was not strongly controlled by film diffusion. A comparison of the experimentally observed, burnout times to the times required for combustion under film diffusion control will assess the importance of the role of the chemical kinetics. The burning time under diffusion control can be estimated using an analysis similar to that of Field et al.[26], assuming first order kinetics. Including the convective flow away from the char surface (Stefan flow), the oxygen conservation equation can be written:

$$\dot{m}_{O_2} = -\sigma_g D_b \frac{dY_{O_2}}{dr} + Y_{O_2}\dot{m}_{tot} \ , \tag{2}$$

where $\dot{m}_{O_2}$ is the flux of oxygen (g/cm^{2}s), $\dot{m}_{tot}$ is the net mass flux (g/cm^2 s), D_b is the bulk diffusion coefficient, σ_g is the average gas density in the film, r is the distance from the center of the particle (cm) and Y_{O_2} is the oxygen mass fraction. Assuming the product of combustion to be only CO, the following mass balance holds:

$$\dot{m}_{O_2} = -16/12\dot{m}_{tot} \ , \tag{3}$$

Integrating between the particle surface, $r = a$ and infinity, $r = \infty$ and making use of the mass balance at the particle surface:

$$\sigma_a \left(\frac{dr}{dt}\right)_a = -\dot{m}_{tot,s} \ . \tag{4}$$

the following equation is obtained:

$$a\frac{da}{dt} = -\frac{\sigma_g D_b}{\sigma_a} \ln\left(\frac{1 + 3/4Y_{O_2\infty}}{1 + 3/4Y_{O_2s}}\right) . \tag{5}$$

Integrating between the initial and final radii and setting the particle surface oxygen concentration Y_{O_2s} equal to zero, the diffusion-limited combustion time t_B can be obtained:

$$t_B = \frac{\sigma_a(a_i^2 - a_f^2)}{56} \frac{RT_m}{D_b} \frac{1}{\ln(1 + 3/4Y_{O_2\infty})} \ , \tag{6}$$

where a_i and a_f are the initial and final particle radii, R is the universal gas constant, and T_m is the mean temperature in the film in (K). The experimentally observed combustion times were about 3 times longer than t_B for the largest particles burning in pure O_2 at elevated temperatures, over 2000 K (worst case), and 2 orders of magnitude longer for the medium temperature experiments in air. Therefore, the combustion of the synthetic char particles was not controlled by external mass transfer.

As another estimate of diffusion limitations, oxygen concentrations at the particle surface $Y_{O_{2s}}$ for the initial radius ($r = a_0$) were calculated from the integral of Eq. (5) by substituting for the observed combustion time $t_{B,obs}$. This corresponds to the worse-case calculation since diffusional resistance is proportional to the particle size. The resulting $Y_{O_{2s}}$ values never fell below 50% of the free stream values.

Using the diffusion equation to calculate the oxygen concentration at the particle surface, thereby correcting for the external diffusion resistance, the observed combustion rate can be related to the apparent reaction rate constant. Combining Eq. (2) and (3):

$$\dot{m}_{tot,s} = \sigma_g \frac{D_b}{a} \ln\left(\frac{1 + 3/4 Y_{O_{2\infty}}}{1 + 3/4 Y_{O_{2s}}}\right) = R_c Y_{O_{2s}} \sigma_g \qquad \mathrm{g/m^2 s}, \tag{7}$$

where R_c is the chemical rate coefficient and the reaction order has been assumed to be equal to unity. $Y_{O_{2s}}$ can be eliminated for the above equation by substituting: $Y_{O_{2s}} = Y_{O_{2\infty}}(1 - \psi)$ and approximating the logarithmic term as

$$\ln\left(\frac{1 + 3/4 Y_{O_{2\infty}}}{1 + 3/4 Y_{O_{2s}}}\right) \approx 3/4 \ \psi \frac{Y_{O_{2\infty}}}{1 + 3/4 Y_{O_{2\infty}}}. \tag{8}$$

Substituting this expression in Equation (7), expressions for ψ and $\dot{m}_{tot,s}$ as a function of R_c can be obtained. The expression for $\dot{m}_{tot,s}$ is then used to integrate Eq. (4) and obtain an expression for R_c. From this expression of R_c an average integrated value (between the initial and final radii) of $\dot{m}_{tot,s}$ can be obtained from Equation (7) again. We call this average value the apparent rate ρ_a. An Arrhenius

plot of the apparent rate vs temperature is shown in Fig. 9. In general the reaction rate increases with temperature. The material containing carbon black appears to be the most reactive. Since this char is the only one that contains a transitional pore network superimposed on the microporous matrix, the higher reactivity can be attributed to enhanced oxygen diffusion inside the particles. In addition, the micropores themselves seem to be open to the oxidizer from the very beginning of combustion as suggested from the high initial total area of this material. The combustion rates differ from one char to another by as much as a factor of four. Among the microporous chars the most reactive appear to be those formed from high percentages of tannic acid, the one formed from 18% PEG and the one formed from 35% glycerol and 7% triton X-100. The differences in reactivity between the chars could result from differences in the porous microstructure or from chemical composition and structure differences.

The intrinsic rate is the rate per unit total surface area that would be observed if there were no diffusional resistances. However, because of the diffusional resistances, not all of the internal surface area is equally available for reaction. A model describing the coupled diffusion and reaction of oxygen is needed if the intrinsic reaction rate is to be deduced from experiments in which there are appreciable diffusional resistances. An effectiveness factor η can be defined as the ratio of the apparent rate (that has been corrected for external diffusion resistance) to the rate which would be attained if there were no resistance to diffusion in the pores[4]. The effectiveness factor is a function of the Thiele modulus ϕ and the effective diffusivity

D_e, [3][2]

$$\eta\phi^2(m+1)/2 = \frac{\gamma\rho_a(m+1)}{2D_eC_s}, \tag{9}$$

where C_s is the oxygen concentration at the surface, m is the true reaction order related to the apparent reaction order, n, by the relation: $n = (m+1)/2$, and γ is the characteristic dimension of the particle defined as the ratio of the particle volume to the external area[32]. The Thiele modulus is given by

$$\phi = \gamma(A_G\sigma_a R_i C_s^{m-1} D_e^{-1})^{1/2} , \tag{10}$$

where A_G is the specific total surface area of the char. Previous workers have used the area determined prior to combustion[4], or the area measured after the completion of a test run[33] to characterize the char. Since the surface area varies dramatically during combustion, as shown in Fig. 5, we used the specific BET surface area determined by averaging over the combustion process, from the beginning to the point of the final burnoff. The right hand side of Eq. (9) is a function of the reaction order and known quantities and, therefore, can be evaluated explicitly. Mehta and Aris[34] present a theoretical analysis of the relationship between the effectiveness factor η and the group $\eta\phi^2(m+1)/2$. Following the approach of Smith and Tyler[4] with the major modification of using the average surface area, we use the plot of these variables presented by Mehta and Aris to determine η.

If the pore diffusion coefficient is D_p the effective diffusivity is[27],

$$D_e = D_p\epsilon/\tau , \tag{11}$$

[2]This equation incorporates Jamaludin's correction to Smith's Equation 15 of Ref.[3], (see p.1050 footnote). The correct implementation of this correction results in a factor of 2 in the denominator of Eq. 12 above as suggested in [50] not a factor of 4 that appeared in our previous paper[8]. Smith had used a factor of 8 therefore his reported values are lower than what should be, by up to a factor of 4 when pore diffusion has a strong effect. This difference should be kept in mind when examining Fig. 10 of the present work.

where ϵ is the porosity and τ is the tortuosity. With the exception of the carbon black containing char, all the chars under consideration are microporous, so the pore sizes are small compared to the mean-free-path of the gas molecules. Hence, the pore diffusion coefficient is that for Knudsen diffusion, i.e.,

$$D_p = D_K = 9700\bar{r}_p(T_m/M)^{0.5} \qquad \text{cm}^2/\text{s}, \tag{12}$$

where T_m is the mean temperature (K) in the film, and M is the molecular weight of the diffusing gas (oxygen), and $\bar{r}_p$ is the mean pore radius (cm). SAXS measurements were used to determine $\bar{r}_p$ when such data were available. The carbon black containing chars have a bimodal pore size distribution and, therefore, require a special treatment. Making the smooth field approximation, the effective diffusivity for a network of micro- and transitional pores is[30]

$$D_e = D_{K,micro}\frac{\epsilon_{micro}}{\tau} + \left(\frac{1}{D_b} + \frac{1}{D_{K,trans}}\right)^{-1}\frac{\epsilon_{trans}}{\tau} \qquad \text{cm}^2/\text{sec}, \tag{13}$$

where the pore size and volume for the two pore classes was determined from porosymetry data. Finally, the intrinsic rate can be written as:

$$\rho_i = \frac{\rho_a}{\eta\gamma A_G \sigma_a} \qquad \text{g/cm}^2\text{s}, \tag{14}$$

Average areas and densities were used. The apparent order n was measured to be around 0.85 from partial combustion experiments of plain polymer char at 1500 K and oxygen partial pressures ranging from 0.05 to 0.3 atm. In this range of O_2 concentrations, the measured particle temperatures were between the gas and the combustor wall temperatures.

The intrinsic rates plotted in Arrhenius form are shown in Fig. 10. All of the data presented are converted to an oxygen pressure of 101 kPa using the relationship:

$$\rho_i = R_i p_{O_2}^m \qquad \text{g/cm}^2\text{s}, \tag{15}$$

where R_i is a chemical rate coefficient. The intrinsic oxidation rates fall the best-fit line derived for a variety of coal chars[3]. The average activation energy for the chars at temperatures below 2000 K is 40 kcal/mole.

This difference in rates is most pronounced (up to an order of magnitude) at the low and medium particle temperatures (800-1700 K). Purified carbons have been reported to exhibit lower reaction rates than coal chars in the temperature region (400-800 K)[3]. The fact that purified chars exhibit lower reactivities suggests that the oxidation of carbon at low temperatures is very sensitive to catalysis by mineral impurities[5,35].

The discrepancy between the present rates and Smith's best-fit line decreases as the temperature is increased, the accord becoming fair at about 2000 K.[3] This behavior suggests that the chars tend to a common chemical structure at high temperatures and that the importance of impurities diminishes. Previous experimental studies confirm that the catalytic effects become less pronounced with increasing temperature[35,36].

The reaction rates of the glassy carbon chars are, on average, one order of magnitude smaller than the *N-S-C* kinetics for pyrolytic graphite at medium-to-low temperatures. The agreement between the reactivities of the two materials improves as the temperature increases. At temperatures around 1800 to 2000 K the agreement is very good indicating that the present chars approach a common graphitic structure at elevated temperatures. Partial graphitization has been observed in x-ray diffraction measurements of glassy carbons that have undergone partial oxidation at medium temperatures (see Fig. 6 and TEM micrographs in Ref. 12). If O_2-catalyzed contraction of the interlayer spacing and two dimensional ordering of the amorphous glassy carbon matrix occured in the temperature range of 1300-1600 K, these changes would be accelerated with increasing temperature. This behavior is further enhanced by the availability of the oxidizer, since all high-temperature experiments were conducted in pure oxygen. It has been shown[37] that graphitiza-

[3]The reader should be reminded that Smith's best fit line would have shifted to higher values of rate by up to a factor of four had it been determined similarly to the present work. Therefore, the difference between the rates obtained herein and Smith's line would have been more pronounced.

tion proceeds at a finite rate. The activation energy for the graphitization reaction is large, 215 - 250 kcal/mole [38,37], so the rate increases rapidly with temperature. Current experiments employing copolymer chars that exhibit multiphase graphitization at intermediate temperatures, have shown that a small increase in particle temperature (50 K) causes the crystalline components to grow appreciably at the expense of the disordered component. At the temperatures acheived in combustion at high O_2 levels, 2000 -3000 K these materials may be expected to be higly crystalline.

The relative reactivities of the amorphous and crystalline phases are still unresolved in the literature. It has been determined that reactivity of carbons is structure-dependent[39] and that oxygen attack occurs at the edges of graphitic and amorphous regions rather than on the basal planes. Several comparative thermogravimetric studies of the oxidation of glassy carbon and graphite at 500-1000 K have been performed [1,8,35,31]. Lewis[40] reported that pure vitreous (glassy) carbons prepared from phenolic resins exhibit a rate of oxidation lower than that of pyrolytic graphites. The apparent overall activation energy of the reaction of the phenolic resins in this temperature range was 43 kcal/mole. Tingey[41] contrasted the reactivity of a whole variety of glasslike carbons (including a carbon produced from polyfurfuryl alcohol and a porous carbon produced by the method of Hucke[9]) to the reactivity of a relatively pure polycrystalline graphite. All types of glassy carbon, heat-treated to 3200 K, exhibited reaction rates 3 to 30 times lower than those of the graphite sample. The activation energy for graphite was found to be 42.7 kcal/mole and the one for glassy carbon to be 35 Kcal/mole. Das and Hucke[42] found that glasslike carbons are more stable than graphite and estimated the free energy of the process $C_{graphite} \rightarrow C_{glassy}$ to be around -4 kcal/g-mole. Jenkins et al.[5], based on TEM studies, attributed the chemical "inertness" of glassy carbons to the lack of "loose ends," in the structure which possibly means deficiency of active

sites. Rodriguez-Reinoso and Walker,Jr.[43] studied the reaction of glassy carbon plates with oxygen and compared it with the reactivity of pyrolytic graphite[44]. Both materials were heat-treated to 3273 K. Their results show that the surface recession rates of the glassy carbon both parallel and perpendicular to the plate surface are bracketed by recession rates for the highly oriented graphite sample. The oxidation rate of pyrolytic graphite was found to be anisotropic, with that parallel to the basal plane much higher than that perpendicular to the basal plane.

This anisotropy might possibly explain the appearance of pits and craters on the surface of the synthetic chars of the present investigation after partial combustion. Randomly oriented crystallites might lead to regions of enhanced reactivity where those crystallites are exposed perpendicular to the surface. Pits and channels could also be caused by nonuniform pore distribution or by regions rich in the residual hydrogen that is found in the carbonaceous matrix by NMR techniques[45].

The scatter of the reactivity values among the different chars at fixed temperature is within a factor of two. The intrinsic rates, shown in Fig. 10, seem to be independent of particle size over the range of 8-70 μm, as would be expected if the physical situation were properly taken into account. Some of the copolymer chars contain more residual oxygen and hydrogen than others, as shown by the elemental analysis results. Oxygen is evolved as oxides of carbon at temperatures below 1500 K[39], but hydrogen is very difficult to completely remove even at temperatures well above 1500 K. Residual amounts of hydrogen are expected to enhance reactivity. This and other chemical factors may account for some of the differences in reactivities of the various chars. Copolymer chars that exhibit multiphase graphitization appear to be the most reactive.

The carbon black containing char is intrinsically the least reactive, even if apparently the most reactive, its lower intrinsic reactivity being partly due to the added carbon black that have previously been heat treated at high temperatures.

Elemental analysis of the carbon black containing material shows that the hydrogen and oxygen content of the material is low. The enthalpy of combustion of the material was also measured to be rather low (7800 cal/g), neighboring the enthalpy of pure carbon.

At very high temperatures, above 2300 K, the measured reaction rates start decreasing with temperature. This behavior was exhibited by two of the hottest burning chars, the 17% tannic acid char and that containing 25% carbon black. Maxima in the rate of reaction with CO_2 have previously been observed at a temperature of 2200 K vitreous carbon, and 1900 K for pyrolytic graphite[46]. Nagle and Strickland-Constable[1] and Walls and Strickland-Constable[24], also observed rate maxima at 1900 K for the O_2 reaction with pyrolytic graphite. To account for this phenomenon, Nagle and Strickland-Constable[1] proposed a mechanism that postulates the existence of two types of carbon sites. One (type A) is more reactive than the other (type B). As the temperature increases, the concentration of type B sites increases by thermal rearangement and annealing of type A sites and hence the reactivity falls. The dashed curve in Fig. 10 is this semiempirical model[1]. Duval[47,39] proposed that the reaction with an oxidizer produces active sites on the surface of a carbon. As the temperature increases, the active sites become deactivated by closure of microcleavages in the graphitic planes. At high temperatures the lifetime of generated active sites is shorter than the rate of removal of the active sites by oxidation, and the reaction rate decreases.

4.1 *Alternative Calculation of Intrinsic Reaction Rate*

An alternative approach to calculating reaction rates for "shrinking core" type of combustion was developed by Gavalas[48,49]. According to this approach, the intrinsic rate coefficient, R_i, is given by the following expression:

$$R_i = \frac{\rho_a^2 b J (m+1)}{C_s^{m+1}(1-\epsilon_0)^2}, \tag{16}$$

where b is a stoichiometric coefficient ($= 1/24$), ϵ_0 is the initial porosity and J is the quadrature of the physical factors given as:

$$J = \int_{\epsilon_0}^{\epsilon^*} \frac{(\epsilon - \epsilon_0)d\epsilon}{\delta_e(\epsilon)S(\epsilon)}. \tag{17}$$

here, ϵ^* is a limiting value of the porosity corresponding to a point where the particle starts disintegrating. For this calculation, ϵ^* was taken equal to 0.9. The total surface area, S, and the effective diffusivity, δ_e, are both functions of conversion. These functions could, in principle, be measured but if such measurements are not available one can estimate them by some pore model. For the case of the particularly simple capillary model these functions are given by:

$$S = S_0 \frac{(1-\epsilon)\left(\ln \frac{1}{1-\epsilon}\right)^{1/2}}{(1-\epsilon_0)\left(\ln \frac{1}{1-\epsilon_0}\right)^{1/2}} \tag{18}$$

$$\delta_e = \epsilon \frac{A_K}{\tau} \left(\frac{2(1-\epsilon_0)\left(\ln \frac{1}{1-\epsilon_0}\right)^{1/2}\left(\ln \frac{1}{1-\epsilon}\right)^{1/2}}{S_0} \right), \tag{19}$$

where S_0 is the initial area, τ is the tortuosity of the pores, A_K is the coefficient of the Knudsen diffusivity defined as $A_K = 9700(T_p/M)^{1/2}$, T_p is the particle temperature and M is the molecular weight of oxygen.

Application of the above equations to the high-temperature (T_w =1500 K) combustion of plain polymer particles in pure O_2 results in an intrinsic rate ρ_i of 1.2×10^2 g/cm^{2}s which is higher by a factor of two than the value calculated with the previous method. This descrepancy is due to the fact that the random capillary geometry, although it accounts for the enlargement of pores, it cannot describe the opening of closed pores which seem to be prevalent in the synthetic char materials. The opening of closed porosity and the enlargement of all pores by thermal contraction of the carbon matrix have already been shown to result in an increase of the surface area by two orders of magnitude (Fig. 5). Since the random capillary model does not incorporate the experimentally measured surface area vs. conversion curve, it tends to underestimate the extent of the area and thereby to overpredict the rate.

5 Conclusions

Monodisperse spherical synthetic char particles were used for kinetic studies of the oxidation of carbonaceous materials. Several mineral-free chars with different physical and chemical properties were studied. Some of the chars had pore size distributions that were unimodal (micropore) or bimodal (micropore and transitional). During combustion, micropores that were initially closed opened and enlarged, resulting in an increase of the total surface area by as much as two orders of magnitude by 50% burnout. The initial areas of the chars varied by two orders of magnitude and the maximum areas by a factor of two. Densities varied by up to 40%. The carbon, hydrogen and oxygen contents of the chars also varied. X-ray diffraction studies indicated that the carbon approached a crystalline structure as the particle temperature increased. This graphitization was also found to be much faster in the presence of oxygen. Some of the copolymer chars were subjected to two and three-phase graphitization.

The combustion behavior of the chars was monitored in a laminar flow furnace. Mass-loss measurements and temperature-time profiles obtained by optical pyrometry were used to deduce combustion kinetics. Additional data was obtained by thermogravimetric measurements of combustion rates. The chars possessing the bimodal pore distribution exhibited the fastest apparent rates and, therefore, burned at the highest temperatures. In these chars, the transitional pores enhance the oxygen transport to the interior of the particles. The intrinsic combustion rates of the chars were an order of magnitude lower than the corresponding rates of coal-derived chars at medium particle temperatures (800-1600 K). As the temperature increased, however, the intrinsic rates of the synthetic and coal chars approached similar values. Above particle temperatures of 2300 K, the carbon reactivity decreased. A twofold variation of the intrinsic reactivity of the synthetic chars was observed. This variation is much smaller than that commonly observed with chars

derived from natural fuels. When compared to pyrolytic graphite, the glassy carbons of the present study were found to be less reactive at low temperatures but comparable at high temperatures.

6 Acknowledgements

This research was supported by the U.S. Department of Energy University Coal Programs Grant Number DE-FG22-84PC70775. The authors gratefully acknowledge technical assistance from Paul Scott Northrop, Patric Kohen, Sten Samson, Bob Johnson and Bob Hously.

7 Notation

SYMBOL	DESCRIPTION	UNITS
a	particle radius	cm
A_G	specific total area	m^2/g
A_K	Knudsen coefficient of diffusivity	
b	stoichiometric coefficient (=1/24)	
C_∞	ambient oxygen concentration	g/cm^3
C_s	oxygen concentration at particle surface	g/cm^3
d	particle diameter	cm
$\bar{d}$	interlayer spacing	Å
D_{eff}	effective diffusivity	cm^2/sec
D_b	molecular bulk diffusivity	cm^2/sec
D_K	Knudsen diffusivity	cm^2/sec
D_p	pore diffusivity	cm^2/sec
J	physical factor quadrature	
m	true order of reaction	
$\dot{m}$	mass flux	g/cm^2sec
M	molecular weight	g/g-mole
n	apparent order of reaction	
N	mass flux	g/cm_2s
p_{O_2}	ambient partial pressure of oxygen	
P	pressure	atm
r	radial distance	cm
r_p	pore radius	cm
R	universal gas constant	atm cm^3/mole K
R_c	apparent rate coefficient	$g/(cm^2sec(atm)^n)$
R_i	intrinsic rate coefficient	$g/(cm^2sec(atm)^m)$

S	instantaneous total surface area	m^2/g
T_g	ambient temperature	K
T_m	boundary layer temperature	K
T_p	particle temperature	K
V_{Hg}	specific Mercury pore volume	cm^3/g
Y	mass fraction	
α	contact angle	
γ	characteristic particle dimension	cm
δ_e	instantaneous effective diffusivity	cm^2/s
ϵ	porosity	
η	effectiveness factor	
ρ_a	apparent reaction rate	g/g-sec
ρ_i	intrinsic reaction rate	g/cm^2-sec
σ	surface tension of mercury	dyne/cm
σ_a	apparent density	g/cm^3
σ_{Hg}	Mercury density	g/cm^3
σ_{He}	true(Helium) density	g/cm^3
σ_g	ambient gas density	g/cm^3
τ	tortuosity	
ϕ	Thiele modulus	

8 References

1. Nagle, J. and Strickland-Constable, R.F. *Proc. of the Fifth Carbon Conf.* 1:154, Pergamon Press, Oxford, (1961).

2. Smith, I.W. *Fuel* 57:409 (1978).

3. Smith, I.W. *Nineteenth Symp. (Int.) on Combustion*, The Combustion Institute, Pittsburgh, PA. p.1045 (1982).

4. Smith, I.W. and Tyler, R.J. *Fuel* 51:312 (1972).

5. Jenkins, R.G., Nandi, S.P., Walker Jr, P.L. *Fuel* 52:288 (1973).

6. Mitchell, R.E. and McLean, W.J. *Nineteenth Symp. (Int.) on Combustion*, The Combustion Institute, Pittsburgh, PA. p.1113 (1982).

7. Senior, C.L. and Flagan, R.C. *Twentieth Symp. (Int.) on Combustion*, The Combustion Institute, Pittsburgh, PA. p.921 (1984).

8. Levendis, Y.A and Flagan, R.C. *Comb. Sci. Tech.* 53:117 (1987).

9. Hucke, E.E. United States Patent 3,859,421 (1975).

10. Schmitt,Jr J.L., Walker,Jr P.L. and Castellion G.A. United States Patent 3,978,000 (1976).

11. Moreno-Castilla, C. Mahajan, O.P., Walker Jr, P.L. *Carbon* 18:271 (1980).

12. Levendis, Y.A and Flagan, R.C., Submitted to *Carbon* (1987).

13. Northrop, P.S., Gavalas, R.G. and Flagan, R.C. *Langmuir* (in Press). (1987).

14. Timothy, L.D., Sarofim, A.F. and Beer, J.M. *Nineteenth Symp. (Int.) on Combustion*, The Combustion Institute, Pittsburgh, PA. p.1123 (1982).

15. Levendis, Y.A. (1987). "A Fundamental Study of Char Oxidation Kinetics Using Model Materials." Ph.D Thesis, California Institute of Technology.

16. Senior, C.L. (1984). "Submicron Aerosol Formation During Combustion of Puverized Coal." Ph.D Thesis, California Institute of Technology.

17. Scholten, J. J. E., in Porous Carbon Solids (R. L. Bond Ed.), Academic Press, London, p.225., 1967.

18. Yan, J. and Zhang, Q. *Particle Characterization* 3:20 (1986).

19. Medek, J. *Fuel* 56:131 (1976).

20. Dubinin, M. M. *Chem. Rev.* 60:235 (1960).

21. Dubinin, M. M. *Carbon* 25:321 (1987).

22. Wheeler, A. *Advances in Catalysis* 3:249 (1951).

23. Fitzer, E. and Schäfer W. *Carbon* 8:353 (1970).

24. Walls, J.R. and Strickland-Constable, R.F. *Carbon* 1:333 (1964).

25. Park, C. and Appleton, J.P. *Combust. Flame* 20:369 (1973).

26. Field, M.A., Gill, D.W., Morgan, B.B., Hawksley, P.G.W. Combustion of Pulverized Coal BCURA, Leatherhead, 1967.

27. Satterfield, C.N. Mass Transfer in Heterogeneous Catalysis Massachussets Institute of Technology Press, 1970.

28. Wakao, N. and Smith, J. M. *Chem. Engin. Sci.* 17:825 (1962).

29. Wakao, N. and Smith, J. M. *Ind.Eng.Chem. Fundamentals* Vol.3 No.2:123 (1964).

30. Feng, C. and Stewart, W. E. *Ind.Eng.Chem. Fundamentals* 12:143 (1973).

31. Smith, I.W., and Tyler, R.J *Comb. Sci. and Tech.* 9:87 (1974).

32. Aris, R. *Chem. Eng. Sci.* 6:262 (1957).

33. Mehta, B.N. and Aris, R. *Chem. Engin. Sci.* 26:1699 (1971).

34. Tyler, R. J. and Smith, I. W. *Fuel* 54:90 (1975).

35. Mulcahy, M. F. R. and Smith, I. W. *Rev. Pure and Appl. Chem.* 19:81 (1969).

36. Hawtin, P. and Gibson, J. A. *Carbon* 4:473 (1966).

37. Fischbach, D. B. *Chem. and Phys. of Carbon* 7:1 (1971).

38. Saxena, R. R. and Bragg, R. H. *Carbon* 16:373 (1978).

39. McEnaney, B. and Willis M. A. in High Temperature Chemistry of Inorganic Ceramic Materials. 1977, p.102.

40. Lewis, J. C. *Second Conf. on Industrial Carbon and Graphite* Soc. of Chem. Ind., London, p.258 (1965).

41. Tingey, G. L. *Ext. Abstr., Twelveth Biennial Conf. on Carbon* p.181 (1975).

42. Das, S. K. and Hucke, E. E. *Carbon* 13:33 (1975).

43. Rodriguez-Reinoso, F., and Walker,Jr P. L. *Carbon* 13:7 (1975).

44. Rodriguez-Reinoso, F., Thrower, P. A. and Walker,Jr, P. L. *Carbon* 12:63 (1973).

45. Eckert, H., Levendis, Y. A. and Flagan, R. C. In preparation.

46. Lewis, J. C., Floyd, I. J. and Cowland, F. C. *Proc. Third Conf. on Carbon and Graphite* Soc. for Chem. Ind., London, p.282 (1971).

47. Duval, X. *Ann. de Chim.* 10:903 (1955).

48. Gavalas, G. R. *A. I. Ch.E. Jl.* 26:577 (1980).

49. Gavalas, G. R. *Comb. Sci. and Tech.* 24:197 (1981).

50. Pan, Y. S. Personal Communication.

9 List of Figures

TABLE Ia
PHYSICAL PROPERTIES OF CHARS

Polymer with Pore Former	σ Apparent solid and pores less than 7μm g/cm^3	σ Helium g/cm^3	ε Total porosity %	SAXS data	
				d_{pores} Å	d_{solid} Å
PLAIN POLYMER	1.23	1.37	11	8	65
DECALIN (21%)	1.17	1.36	14	---	----
DECALIN (37%)	1.25	1.35	8	---	---
GLYCEROL (20%)	1.24	1.39	11	---	---
GLYCEROL (20%) TRITON (3%)	1.24	1.37	10	---	---
GLYCEROL (35%) TRITON (7%)	1.26	1.33	6	5.5	87
GLYCEROL (20%) TRITON (3%) PEG (3%)	1.25	1.32	6	8.2	128
PEG (9%)	1.23	1.43	14	---	---
PEG (18%)	1.17	1.39	16	33	175
TANNIC ACID (8%)	1.31 ave.	1.38	6.0 ave.	---	---
TANNIC ACID (17%)	1.33	1.39	4	8.6	207
TANNIC ACID (50%)	1.35	1.40	----	11.5	275
PLAIN TANNIC ACID	----	1.45	----	----	----
CARBON BLACK (25%)	0.88	1.45	39	{164 8}	{580 43}
PURE CARBON BLACK	----	1.86	----	----	----

TABLE Ib
PARTIALLY BURNED MATERIALS

PEG (9%)	1.25	2.0	37	18	34
TANNIC ACID (8%)	1.21	2.1	42	—	—
TANNIC ACID (17%)	1.205	2.2	45	23	35
GLYCEROL (35%) TRITON (7%)	1.20	2.1	49	26.6	41

TABLE II
ELEMENTAL ANALYSIS AND CALORIMETRY

POLYMER WITH PORE FORMER	C%	H%	C/H	HEATING VALUE (cal/g)
PLAIN POLYMER	85.85	3.45	2.07	8160
DECALIN (25%)	87.80	3.32	2.18	8193
TANNIC ACID (8%)	91.02	1.92	3.83	8082
TANNIC ACID (17%)	87.17	2.98	2.44	7706
TANNIC ACID (50%)	82.56	3.08	2.23	7655
PURE TANNIC ACID CURED AT 800K	76.92	2.52	2.54	----
PEG (9%)	87.48	3.25	2.44	8062
PEG (18%)	87.26	3.36	2.16	8184
PURE PEG	----	----	----	6328
GLYCEROL (20%)	87.21	3.20	2.27	8109
GLYCEROL (20%) TRITON X-100 (2%)	85.8	3.52	2.03	8163
GLYCEROL (40%) TRITON X-100 (7%)	85.95	3.38	2.12	8534
GLYCEROL (20%) PEG (3%) TRITON (3%)	84.60	3.41	2.07	7950
PURE CARBON BLACK	----	----	----	7750
CARBON BLACK (25%)	92.49	1.38	----	7900
PLAIN POLYMER CURED AT 1500K IN N_2	97.0	1.1	.7.35	7890
PLAIN POLYMER PARTIALLY BURNED AT 1500K	97.05	0.82	9.86	7628

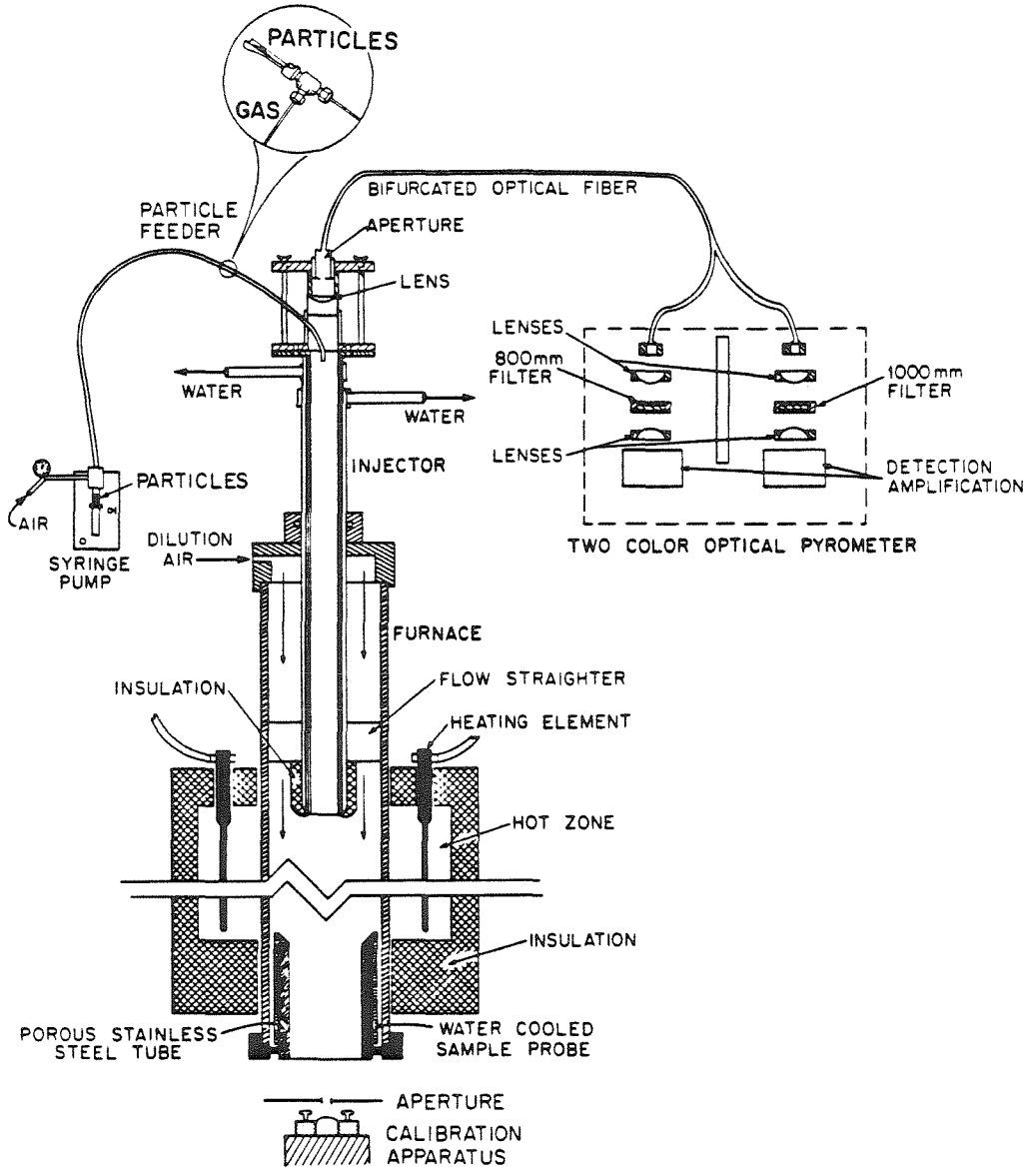

Figure 1: Schematic diagram of the combustion apparatus and two-color optical pyrometer.

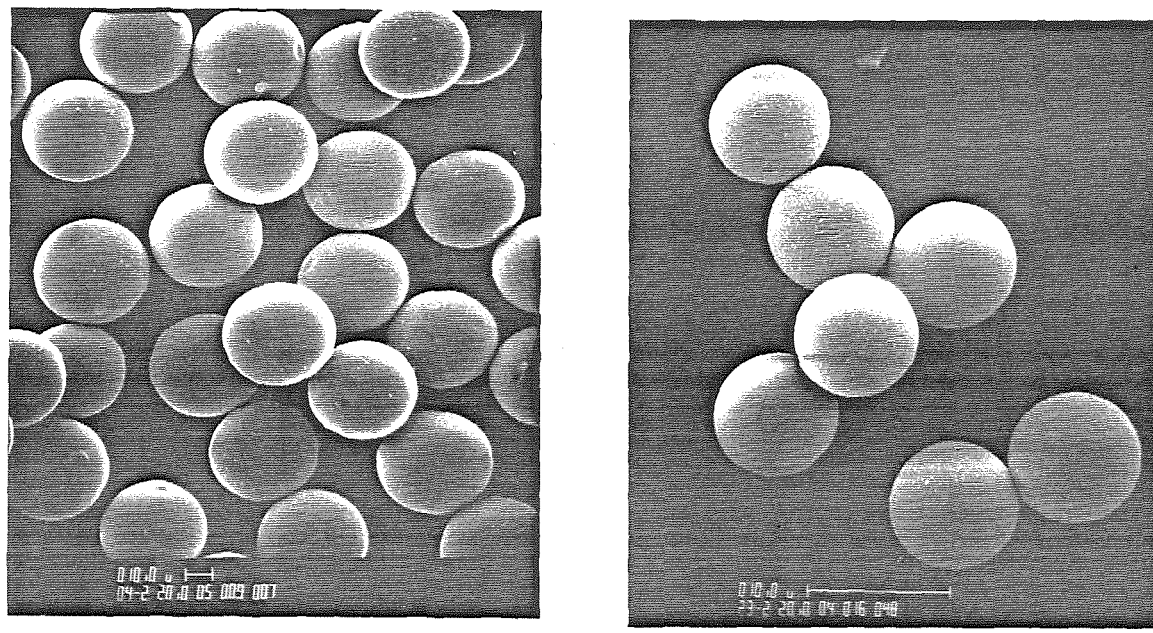

a b

Figure 2: SEM pictures of plain polymer (PFA) particles (a) 45 μm and (b) 8 μm in diameter.

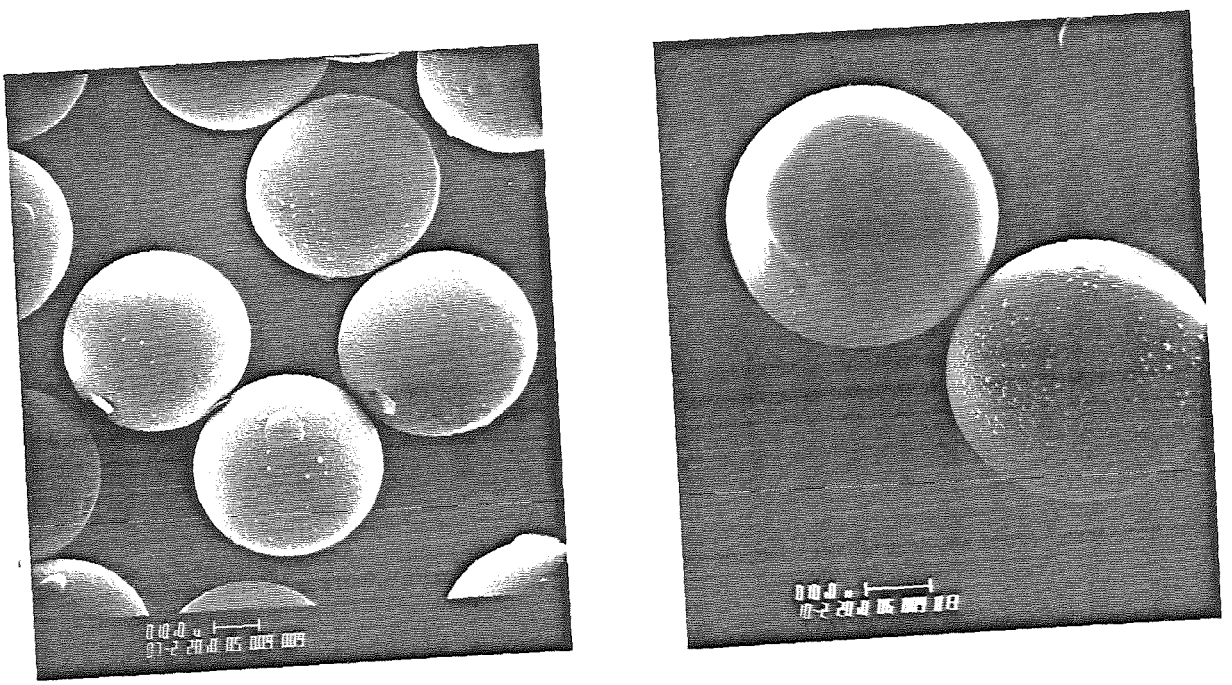

a b

Figure 3: SEM pictures of particles made from (a) 18% PEG and PFA; and (b) 17% tannic acid and PFA.

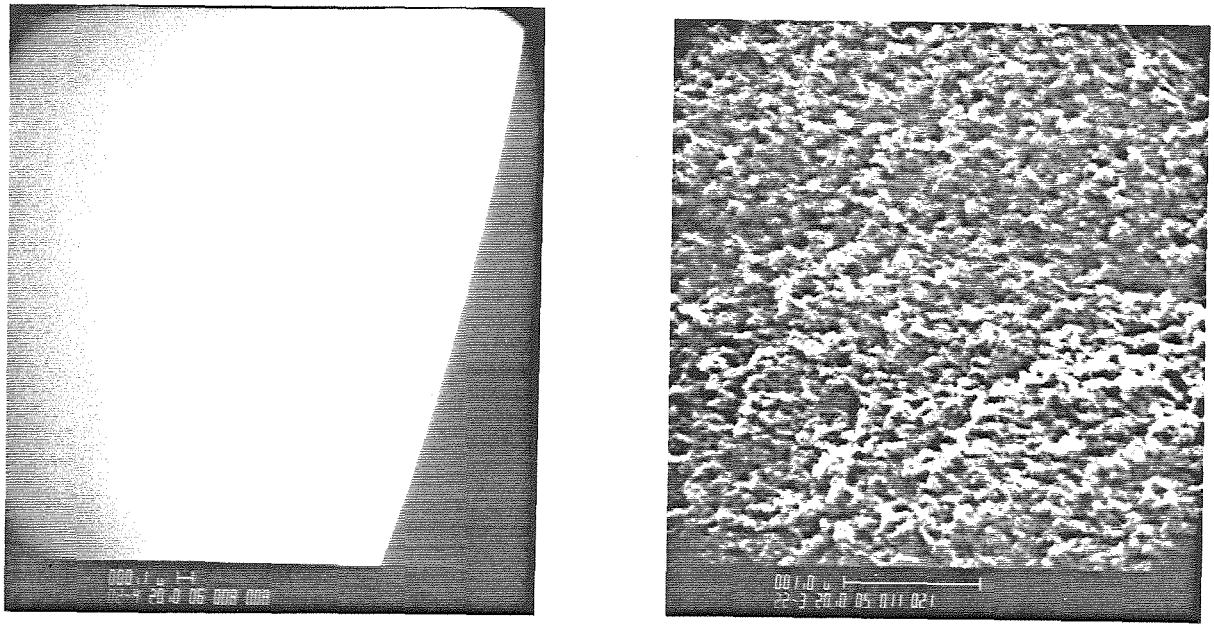

a b

Figure 4: Expanded views of SEM photography of (a) plain polymer particles and (b) particles made from 25% carbon black and PFA.

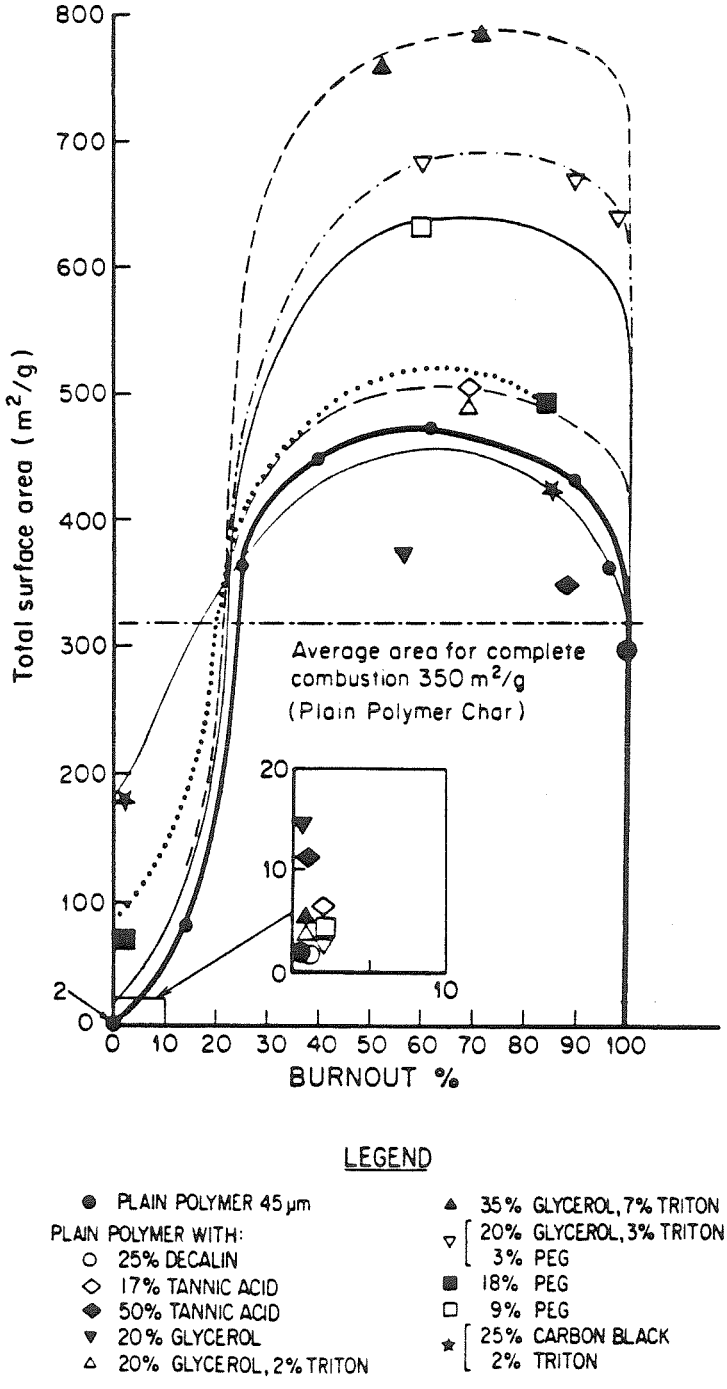

Figure 5: BET surface area vs. burnout for various glassy carbon chars.

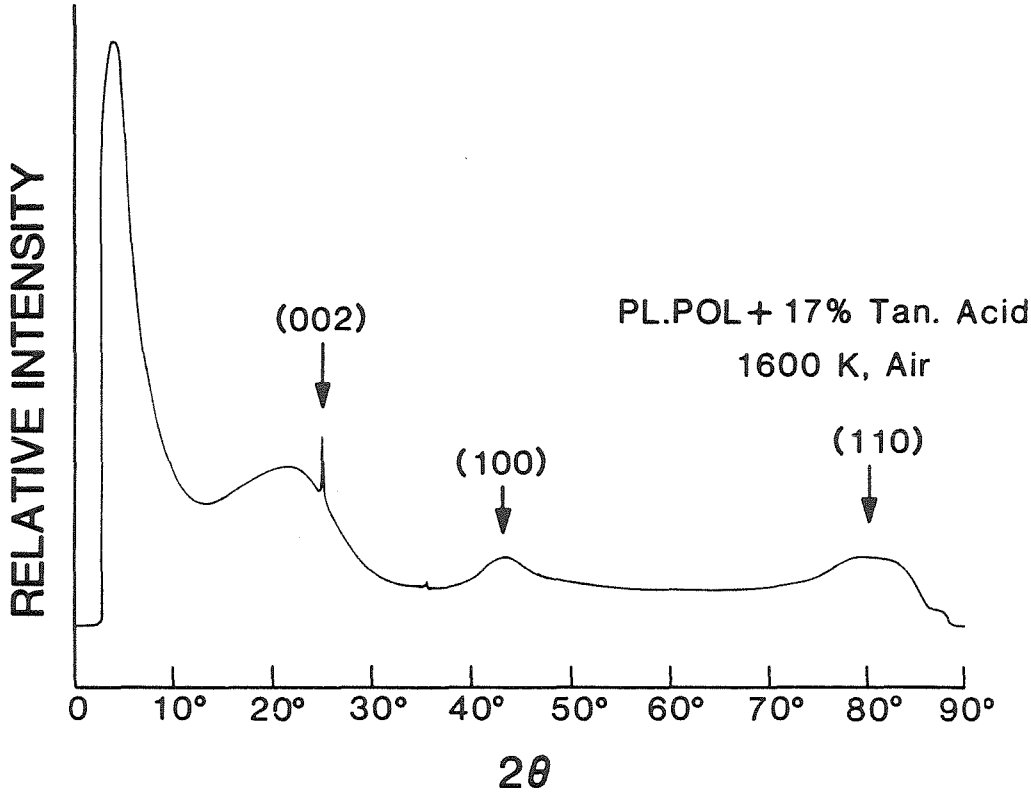

Figure 6: X-ray diffraction spectrum for particles formed from 17% tannic acid and PFA partially burned at 1600 K for 2 sec. in air.

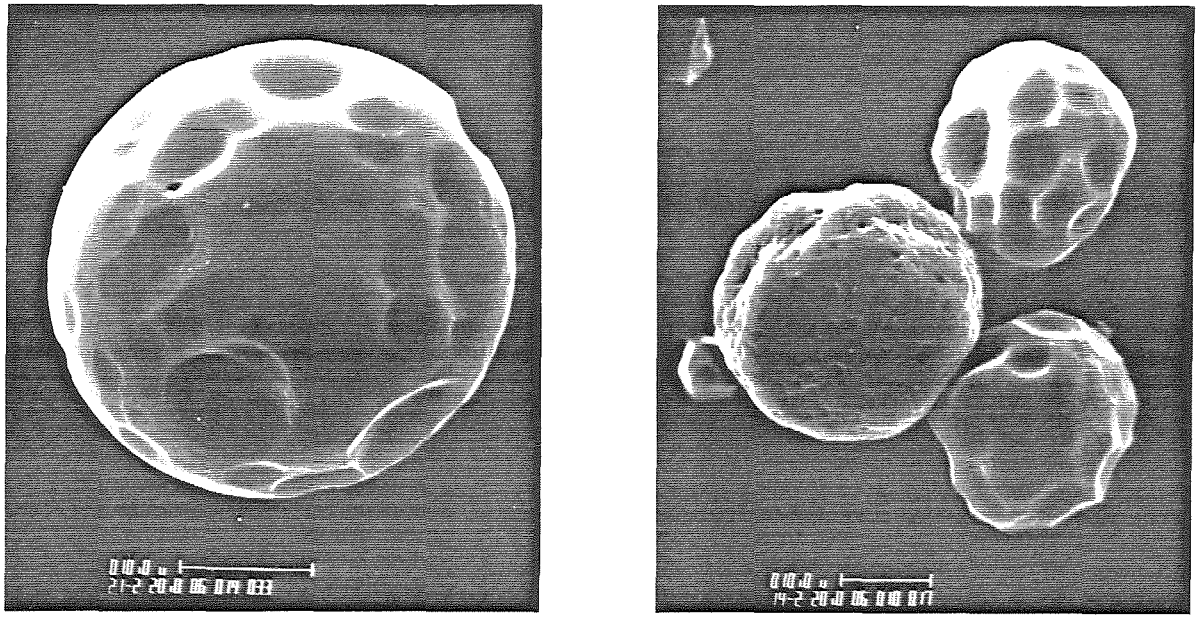

a b

Figure 7: SEM pictures of partially burned particles (a) plain polymer and (b) made from 17% tannic acid and PFA.

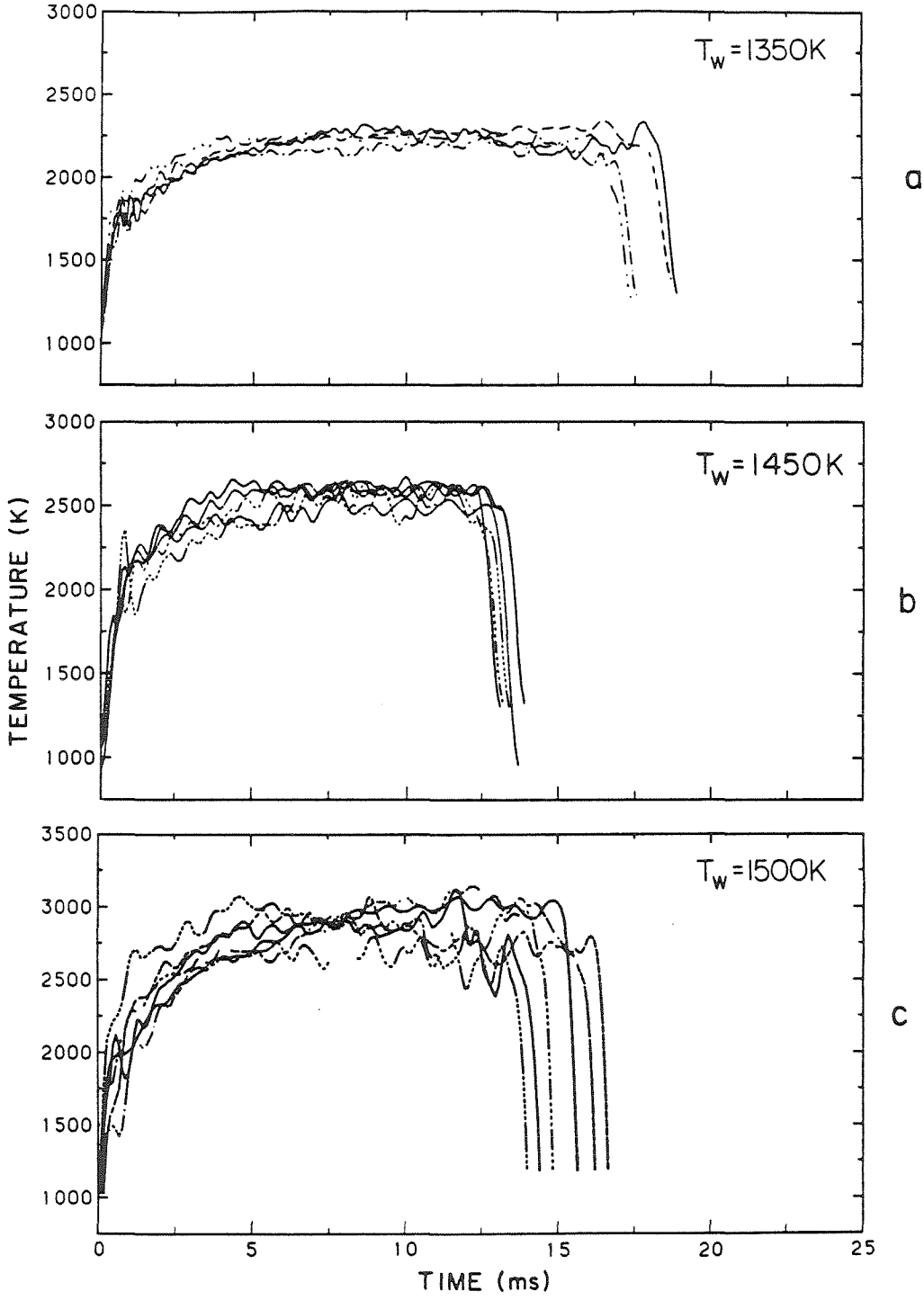

Figure 8: Pyrometry traces of particles made from 25% carbon black and PFA.

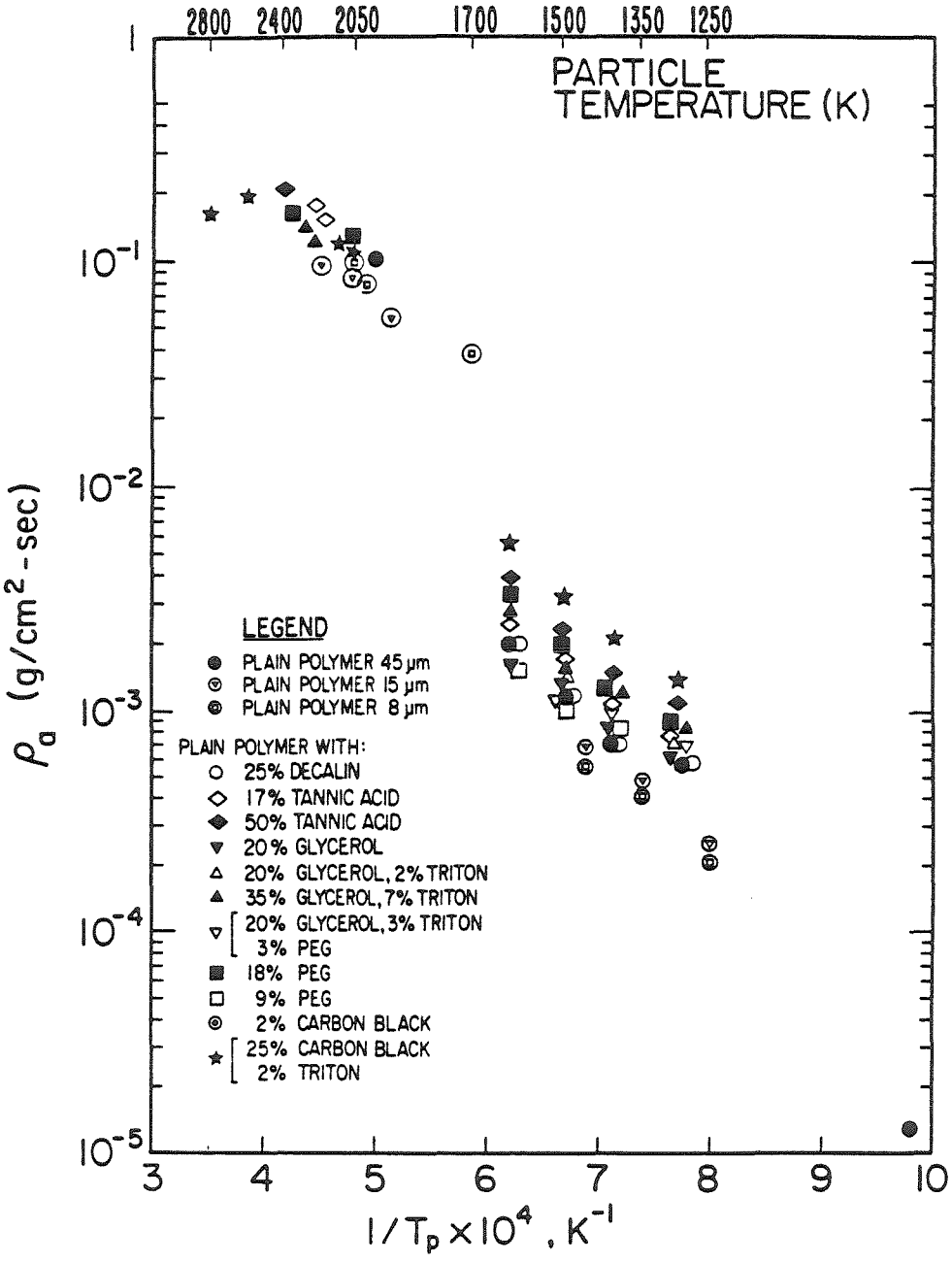

Figure 9: Apparent reaction rate with oxygen (P_{O_2} = 101 kPa.)

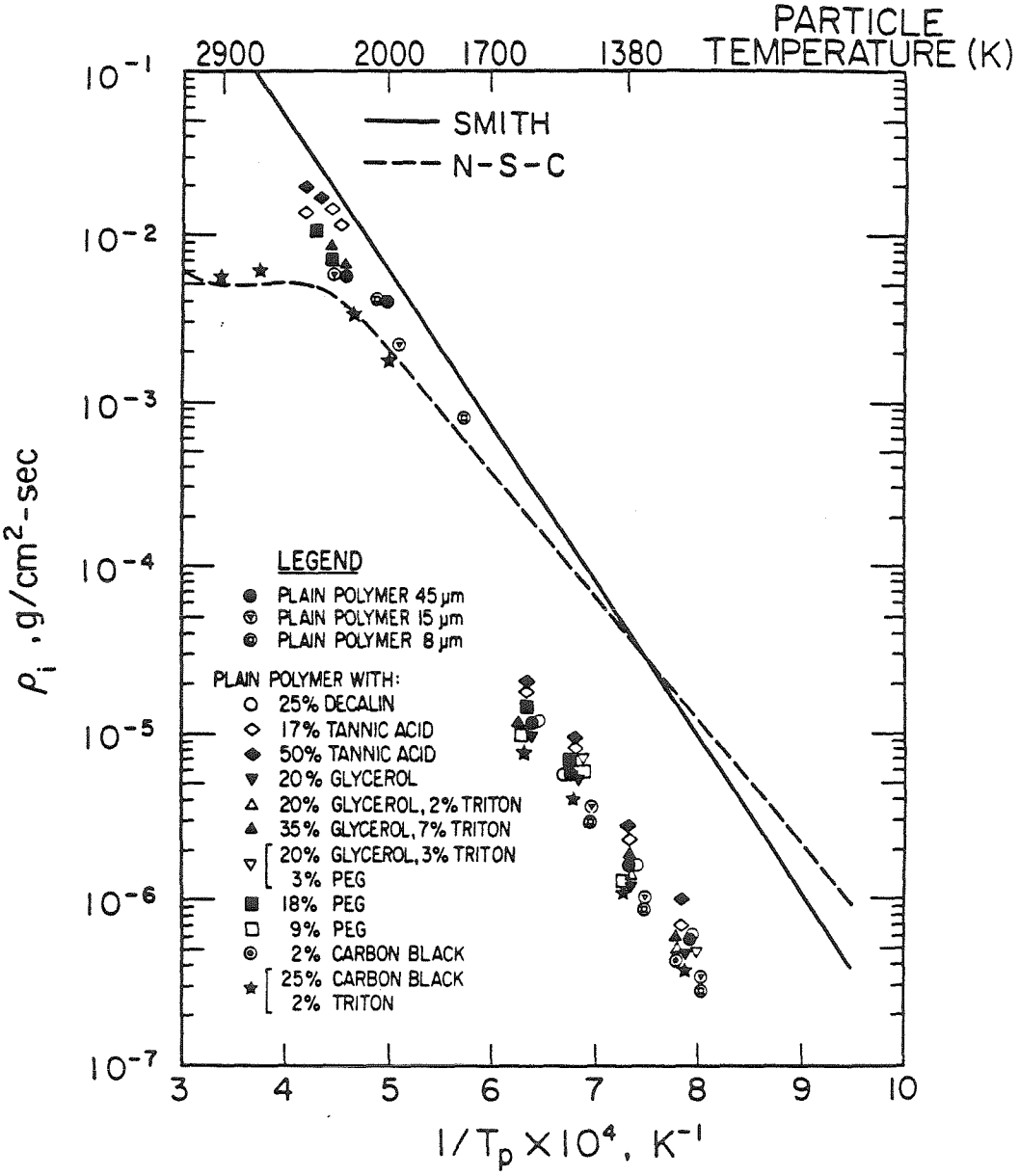

Figure 10: Intrinsic reaction rate with oxygen and comparison with rate expressions of Smith for coal chars[3] (——-); and N-S-C pyrolytic graphite[24] (- - - -). (P_{O_2} = 101 kPa.)

CHAPTER 7

A Direct Approach to Char Combustion Modelling with Application to Synthetic and Coal-derived Chars

M. Loewenberg*, Y. A. Levendis**, G. R. Gavalas*, R. C. Flagan**
* Department of Chemical Engineering 206-41
** Department of Environmental Engineering Science 138-78
California Institute of Technology
Pasadena, California 91125

Abstract

A theoretical model describing the combustion of carbonaceous particles at intermediate and high temperatures has been developed and compared with experimental results. The analysis includes the effects of pore diffusion and growth, inert mineral matter, gas-phase heat and mass transfer, and treats solid spherical and cenospheric char particles. The combustion dynamics are described by time-dependent equations for particle temperature, radius, ash layer thickness and a number of intraparticle conversion variables. These are coupled to pseudosteady equations for gas-phase transport and internal reaction and diffusion. Model predictions were contrasted with combustion measurements obtained for several synthetic chars and two coal-derived chars. The synthetic chars were glassy carbons produced in the form of solid monodisperse spheres. Cenospheric synthetic chars were also produced. All synthetic chars were mineral free. The coal-derived chars contained mineral matter and were considered spherical. In each case, apparent and intrinsic rate parameters were deduced by direct application of the combustion model to experimental data gathered under conditions of moderate to large Thiele modulus. The estimated kinetic parameters were subsequently used to generate temperature-time profiles of single burning particles. The results obtained are in good agreement with the experimentally observed behavior of the synthetic and coal-derived chars. The validity of the intrinsic rate calculation was tested by simulating the combustion behavior of particles burning in the kinetically limited (low Thiele modulus) regime.

1 Introduction

The combustion of char particles has been the subject of numerous experimental and theoretical investigations because of its obvious importance in the operation of coal combustion systems. During the last ten years experimental capabilities have been greatly expanded by the introduction of powerful optical techniques for direct measurements of temperature, size, and velocity of individual particles.[1-5] During the same period, theoretical description of particle combustion has become increasingly more sophisticated by including multicomponent diffusion and heat transfer in the gas phase and diffusion with simultaneous pore growth phenomena within the particle.[6-11]

While experimental technique and theoretical analysis have both undergone significant advance, they have evolved along somewhat independent paths. To appreciate the difficulties encountered in bringing together theory and experiment we consider the determination of intrinsic rate parameters from combustion experiments. These typically include temperature, conversion, and perhaps porosimetry measurements at a few locations along a drop tube furnace. The analysis of such data by means of a particle combustion model requires treating all particles as spherical and uniform in size and properties, and using a pore model consistent with the available porosimetry data. However, the porosimetry data will not, in general, provide adequate information to determine independently the evolution of pore structure with conversion at high temperatures. Moreover, the distributions of sizes, shapes and properties of the char particles versus the identical spherical particles postulated in the analysis introduces an uncertainty that has not been evaluated as yet. In view of these difficulties and uncertainties, it is not surprising that the analysis of experimental data has not progressed beyond the original work of Field and Smith (*eg.* 12,13).

This paper describes an attempt to bring closer experiment and theory by elim-

inating certain experimental uncertainties and comparing with calculations that include diffusion and pore growth as well as external transport processes. The experiments include combustion tests using synthetic and coal chars. The use of synthetic chars consisting of monodisperse spherical particles removes the uncertainty caused by the irregular shape and variable size and properties of individual particles. The analysis consists of three steps. In the first step the apparent rate parameters are estimated from the time-averaged combustion rate by solving the heat and mass transfer equations in the gas film surrounding the particle. In the second step intinsic parameters are estimated from the apparent parameters using a random pore model and measured physical properties. The third step consists of simulations with the complete model and a limiting form of the model appropriate to large values of the Thiele modulus. The calculated temperature-time histories are compared to the experimental histories for a broad range of particle temperatures.

2 Theory

In this section, we develop the equations describing energy and mass transport following the approach of Loewenberg *et al.*[11] Accordingly, the temperature and concentration profiles are assumed to be at steady state with respect to the dynamical quantities: particle conversion, temperature and radius. The temperature within the particle is assumed to be uniform. The only reaction considered is the direct oxidation of carbon to form carbon monoxide:

$$\mathrm{C} + \frac{1}{2}\mathrm{O_2} = \mathrm{CO} \tag{1}$$

The gas-phase oxidation of CO to CO_2 is assumed to occur in the free stream and therefore does not enter in the energy and material balance equations for the film. The char is treated as a continuum with a local diffusion coefficient $\delta_e(q)$ and surface area (per unit volume) $S(q)$, where $q(r,t)$ is the length by which the local surface

has receded by oxidation. The structure functions, $S(q)$ and $\delta_e(q)$, are determined from given pore surface area and pore size distribution by means of a random pore model. The pores may be modelled as cylindrical voids[12] and/or spherical voids[11] Pore overlap between voids of all sizes in the distribution is an implicit feature of this model.

At any given time, the state of the particle is fully defined by its temperature, T_p, radius, r_p, and radial distribution of the structural variable, $q(r)$ $(0 \leq r \leq r_p)$. The radial oxygen profile within the particle is decribed by the pseudosteady equation:

$$0 \leq r \leq r_p(t) \quad : \quad \frac{1}{r^2}\frac{\partial}{\partial r}\left(r^2 \delta_e(q) \frac{\partial C}{\partial r}\right) = bR_{in}(C, T_p)S(q), \tag{2}$$

subject to the boundary conditions:

$$r = r_p(t) \quad : \quad C = C_s, \qquad r = 0 \quad : \quad \frac{\partial C}{\partial r} = 0 \tag{3}$$

where the intrinsic rate $R_{in}(C, T_p)$ is independent of local conversion and is expressed as mass of carbon per unit surface area and time, thus, the stoichiometric factor, $b = 1/24$. Solution of the boundary value problem, (2) and (3) yields a relation for the mass flux at the particle surface caused by chemical reaction, F_p, which [1] can be expressed succinctly as:

$$F_p = G_1(C_s; T_p, r_p, q(r)) \tag{4}$$

In general, G_1 must be evaluated numerically. The radial profiles of temperature and oxygen concentration outside the particle are governed by energy and material balances[11] pseudosteady in particle temperature and radius. The solution of these equations is simplified by assuming ternary mass transfer involving O_2, CO and "inert," the latter including N_2, and CO_2. The three binary diffusion coefficients are assumed equal but temperature dependent, as are the thermal conductivity and density of the gas-phase. Fluxes induced by thermal and pressure gradients

[1] The complete set of equations is given in Appendix 7

are neglected and the gas-phase is assumed to be transparent to radiation. These assumptions permit solution of the film equations to yield the relations:

$$C_s = G_2(F_p, e_p; T_p, r_p) \tag{5}$$

$$e_p = G_3(F_p; T_p, r_p) = 0 \tag{6}$$

where the functions G_2 and G_3 are defined by simple quadratures[11] and e_p is the energy flux resulting from conduction and convection at the particle surface.

Eqs. (4)-(6) yield the mass and energy fluxes, and the oxygen concentration at the particle surface for given values of the time-dependent quantities: T_p, r_p, $q(r)$; it remains to derive their dynamical equations. The local structure variable satisfies:

$$\frac{\partial q}{\partial t} = \frac{1}{\rho_T} R_{in}(C, T_p) \tag{7}$$

with the initial condition:

$$t = 0 \quad : \quad q = 0 \tag{8}$$

which is solved on a suitable discrete set of grid points simultaneously with the equations for r_p and T_p. The pseudosteady oxygen concentration at each grid point is given by the solution of Eqs. (2) and (3). The particle radius decreases by combustion on the pore surfaces according to equations:[10,11]

$$r_p(t) = r_{p0}, \quad q < q^* \tag{9}$$

$$\frac{dr_p}{dt} = -\left(\frac{\partial q/\partial t}{\partial q/\partial r}\right)_{r=r_p}, \quad q = q^* \tag{10}$$

where q^* is the value of the local structure variable at the onset of fragmentation[13,14] and is defined by: $\epsilon(q^*) = \epsilon^*$. The apparent rate (total mass flux), F_p^T, is equal to the sum of the mass flux generated by chemical reaction, F_p, and the flux of fragmented particles which is given by:

$$F_p^* = -\rho^* \frac{dr_p}{dt} \tag{11}$$

where ρ^* is the local density at the onset of fragmentation. The detached char fragments are assumed to burn in the free stream thereby not affecting the heat and mass balances.[11] We chose ϵ^* equal to 0.8 although the combustion rate is insensitive to the precise value.[10] If fragmentation does not occur or if char fragments are retained, *eg.* by an ash layer, $\epsilon^* = 1$. The fragmentation process is not sufficiently understood to be accounted for in greater detail. The differential equation for the particle temperature is:

$$m_p c_p \frac{dT_p}{dt} = 4\pi r_p(t)^2 \left[F_p \int_{T_\infty}^{T_p} c_p dT - e_p - e_R \right] \tag{12}$$

where e_R is the radiative heat transfer which is given by the Stefan-Boltzmann law.

Mineral matter is assumed to be inert and finely distributed throughout the carbonaceous matrix and forms an ash layer as combustion progresses.[15-17] The additional diffusional resistance of this layer is neglected.[17,18] A volume balance on the mineral matter contained within the char relates the radius of the ash layer to the radius of the carbonaceous particle:

$$r_a^3 = \frac{v_a}{1 - \epsilon_a} \left(r_{p0}^3 - r_p^3 \right) + r_p^3 \tag{13}$$

where $1 - \epsilon_a$ is the solid volume fraction within the ash layer and v_a is the volume fraction of ash within the carbonaceous phase and is given by:

$$v_a = \frac{x_{a0} \bar{\rho}_0}{\rho_a} \tag{14}$$

where x_{a0} is the measured initial mass fraction of ash, and $\bar{\rho}_0$ is the initial apparent density of the char (including ash). Although, the volume fraction of ash within the particle increases with conversion, v_a is constant.

The combustion of a cenosphere that contains one or more large voids within a thin, porous shell was also modelled. Such particles are often produced by rapid devolatilization of softening coals or heavy oil droplets. In the present work, cenospheres that have a single central void can be described by a simple modification of the above equations. Two limiting cases were considered:

(I) Oxygen diffuses into the char solely through the external surface of the cenosphere shell; the central void is not directly accessible.

(II) The interior of the cenosphere shell "communicates" directly with the external surface through several large "blow-holes" in the cenosphere shell.[19] Oxygen penetrates the central void.

For cenospheric char, boundary condition (3) at $r = 0$ is replaced with the appropriate boundary condition at $r = r_i$. In case (I), the position of the inner shell surface is constant but in case (II), the inner shell radius is described by equations similar to (9) and (10).

The physical and chemical properties of the char and the ambient conditions are required for modelling. An assortment of independent experimental techniques, described below, were used to determine the particle size, density, pore structure and mineral content. The composition of the gas phase is specified by the mole (volume) fraction of oxygen; the remainder is assumed inert. The ambient conditions also include the gas and wall temperatures. The initial particle temperature, T_{p0}, is taken equal to the ambient gas temperature.

The solution procedure consists of integrating the dynamical Equations (7)-(10) and (12) for the local structural variable, particle radius and particle temperature. Evaluation of the dynamical equations requires the quantities: C_s, e_p and F_p, given by simultaneous solution of Eqs. (4)-(6).[11] An important simplification results by the choice of an intrinsic rate linear in oxygen concentration. In this case, Eq. (4) is separable and becomes:

$$F_p = C_s \, \tilde{G}_1(T_p, r_p, q(r)) \tag{15}$$

In the limiting case of high Thiele modulus, the solution can be simplified drastically by exploiting a closed-form solution of the intraparticle problem[10] which eliminates the local structural variable and the corresponding dynamical equation

at each grid point. The limiting solution is:

$$dr_p/dt = -\frac{1}{b^{1/2}\rho_T}\frac{I^{1/2}}{J^{1/2}} \tag{16}$$

where $I^{1/2}$ and $J^{1/2}$ are simple quadratures which describe kinetic and physical parameters respectively:

$$I = \int_0^{C_s} R_{in}(C, T_p)dc \tag{17}$$

$$J = \int_0^{q^*} \frac{\epsilon(q) - \epsilon_0}{\delta_e(q)}dq \tag{18}$$

Then according to Eq. (11), F_p and the apparent rate, F_p^T, become:

$$F_p = \frac{\rho_0 - \rho^*}{b^{1/2}\rho_T}\frac{I^{1/2}}{J^{1/2}} \qquad \text{and} \qquad F_p^T = \frac{\rho_0}{b^{1/2}\rho_T}\frac{I^{1/2}}{J^{1/2}} \tag{19}$$

which reflects the assumption that detached char fragments burn in the free stream. According to this procedure, Eq. (5), (6) and (19) are solved for C_s, e_p and F_p and the dynamical equations are reduced to two: Eq. (17) and (12) for the particle radius and temperature.

The results of the above semi-analytical solution have been compared with those of the full numerical solution and found in fair agreement for Thiele moduli larger than 3 and excellent agreement for Thiele moduli larger than 15 [11] (based upon characteristic length, $r_p/3$). Thus, the simplified intraparticle solution procedure can be successfully employed in the regime of strong pore diffusion resistance. This will be shown again herein by comparison with the results of the full solution of Equations (4)-(10) and (12).

3 Experimental

3.1 *Experimental Methods*

The foregoing model has been used to simulate the combustion of both synthetic (glassy carbon) and coal-derived chars. Spherical glassy carbon particles of equal

size have been produced, from polyfurfuryl alcohol (PFA) and pore forming agents.[20]. The pore formers used in conjunction with the present study were *tannic acid, glycerol, polyethylene glycol (PEG), Triton X-100* and solid *carbon black* spheres. The particles were generated by atomization of the PFA-pore former mixtures in a thermal reactor (650 K, 4s). Different particle sizes were produced ranging from 8-100 μm in diameter. The solidified particles were subsequently carbonized at 800 K for 1 hr. The two coal chars were derived by pyrolyzing a bituminus coal (PSOC-176 HVBA) at 1400 and 1600 K, respectively in N_2 for 2 seconds.

Combustion studies were conducted in an externally heated laminar flow furnace. The wall temperatures were monitored by both a thermocouple and a brightness pyrometer, the gas temperature by a suction pyrometer and the particle temperature by a near-infrared, two-color pyrometer (800 and 1000 nm).[21] Particle temperatures were calculated from the ratio of the signals of the two channels, applying Planck's law. Partial combustion experiments were also conducted under conditions where the particle temperatures were low. The extent of burnout in those experiments was monitored by measuring the change in the mass, size and density of the particles.

Char characterization included determination of particle size, morphology, density and pore structure as well as density and mass of mineral matter. The parameters required for the intrinsic rate were empirically determined, but the form of the intrinsic rate was chosen *a priori*.

3.2 *Experimental Results*

The various synthetic and coal-derived chars have widely different porosities and pore structures. While all synthetic chars contained micropores, only the chars containing carbon black had transitional pores. The coal-derived chars contained a broad distribution of pore sizes. The pore size distribution of the transitional- and macropores was obtained by high-pressure mercury intrusion, and the results

were analyzed by means of the Washburn equation.[22] The resulting distribution was verified by application of Kelvin's equation to gas adsorption measurements. SEM microscopy was used to observe the surface morphology and the structure of the interior of the particles, by examining ground and polished sections. Plain polymer particles and particles containing 25% carbon black are shown in Fig. 1 a,b and a cenospheric particle is shown in Fig. 2a. In Fig. 2b, a section of a partially burned particle is shown. The particle appears dense, and no porosity can be detected with the SEM. The average size of the micropores in the unoxidized chars, deduced by small-angle x-ray scattering (SAXS), was around 10Å. Corresponding BET sorption experiments indicate that most of this porosity is closed and impermeable to the outside gases. High temperature heat treatment increases pore size because of the densification of the carbon matrix. Parallel oxidation further increases pore size and removes constrictions at the pore entrances. The size of the micropores for the partially oxidized chars was determined from the BET area in conjunction with the pore volume measurements, using the random capillary model. The agreement with the SAXS results was good. The enhanced pore sizes (20-30 Å) are reported in Table I. As a result of the opening and enlarging of the pores, the N_2 BET area, measured at 77 K, increases dramatically from a few square meters per gram, for the unoxidized materials, to a few hundred square meters per gram for the partially combusted materials.

Apparent densities, $\bar{\rho}$, and helium densities, ρ_T, for the synthetic chars, measured by mercury porosimetry and helium pycnometry are given in Table I. The apparent density of the synthetic chars remained almost constant (decreased slightly) in the course of combustion at mid-range temperatures (1200-1600 K), meanwhile the helium density incresed sustantially (by up to 50%). The fact that the carbon matrix becomes denser in the course of high-temperature combustion has also been verified by wide and small-angle scattering. Porosity values for particular intervals in the

transitional and macropore region can be deduced from the mercury porosimetry data, the remaining void volume being due to micropores.

In air, the synthetic char particles burned slowly, at temperatures close to that of the combustion chamber walls. Temperatures of clouds of particles burning under this condition were measured by both the two color and the brightness pyrometer, for the latter assuming a carbon emissivity of 0.8. At higher oxygen partial pressures, the particles ignited and burned with luminous flashes. At the 0.5 and 1.0 atm oxygen partial pressures selected for the present study all particles ignited and burned at high temperature.

To account for the opening of the pore restrictions at the early stages of combustion, the initial total area, true (helium) density, and pore sizes were taken as those of the partially burned chars at about 25% conversion. This procedure is justified for combustion under conditions of strong pore diffusion resistance in which the particle burns with nearly constant apparent density.

A coal char particle is shown in Fig. 2c; the particle is irregular in shape and mineral matter inclusions are obvious. The mass fraction and composition of mineral matter (for the coal-derived chars) were obtained from ashing experiments and from elemental analysis of the ash constituents. The mass fraction of ash was found to be 8.5% and 10% for the chars obtained by pyrolysis at 1400 K and 1600 K, respectively. The composition of the ash allows calculation of its heat capacity and density. The coal chars analyzed in the present study contained mineral matter with the approximate composition: SiO_2, 46%; Fe_2O_3, 20%; Al_2O_3, 30%; CaO, 4%, which yields an ash density, $\rho_a = 3.59$ gm/cm^3.

3.3 *Estimation of Kinetic Parameters*

The form of the intrinsic rate, $R_{in}(C, T_p)$, was assumed *a priori*. Particle temperatures and apparent densities were assumed constant during combustion, as observed.

The average apparent rate is related to the measured burnout time, t_b, by:

$$\overline{4\pi r_p^2 F_p^T} = \frac{4\pi r_{p0}^3 \rho_0 X}{3t_b} \tag{20}$$

where X is the extent of burnout and the overbar denotes a time average. Kinetic parameters were estimated by matching the apparent rates with theoretical predictions.

The assumption of constant particle density allows use of the simplified form of the model defined by Eqs. (16) - (19). This limiting form is valid for the high temperature conditions considered throughout most of this paper, and conveniently eliminates $q(r)$ from consideration thus, the final particle radius is given by mass balance. Then, assuming constant surface recession rate, Eqs. (19) and (20) yield:

$$F_p = \frac{\rho_0 - \rho^*}{b^{1/2}} \frac{I^{1/2}}{J^{1/2}} = \frac{r_{p0}^3 X}{3t_b r_{p,rms}^2} (\rho_0 - \rho^*) \tag{21}$$

where $r_{p,rms}$ is the root-mean-square particle radius during combustion and is given by:

$$r_{p,rms} = \frac{r_{p0}}{\sqrt{3}} \left[1 + (1-X)^{1/3} + (1-X)^{2/3}\right]^{1/2} \tag{22}$$

Similar but somewhat more complicated expressions can be derived for cenospheric chars and/or chars that contain mineral matter. Under the assumption of constant particle temperature, Eq. (12) may be written in the form:

$$G_4(T_p, e_p, F_p) = 0 \tag{23}$$

$J^{\frac{1}{2}}$ is computed from measured physical parameters and Eqs. (5), (6), (21), (22) and (23) are solved for C_s, T_p, and $I^{\frac{1}{2}}$. According to Eqs. (20) and (22), an apparent rate constant, k_a, may be identified:

$$F_p^T = k_a C_s = \frac{r_{p0}\rho_0 X}{t_b} \left[1 + (1-X)^{1/3} + (1-X)^{2/3}\right]^{-1/2} \tag{24}$$

assuming first-order oxygen concentration dependence. For a power law model,[23] $R_{in} = k_{in} C^m$,

$$I^{\frac{1}{2}} = \sqrt{k_{in}(T_p)} \frac{C_s^{\frac{m+1}{2}}}{\sqrt{m+1}} \tag{25}$$

The reaction order, m, can be determined, in principle, from rate measurements at particle temperature and different oxygen concentrations. Then, with the reaction order, m, known, an Arrhenius-type plot of $I^{\frac{1}{2}}$ divided by $C_s^{\frac{m+1}{2}}/\sqrt{m+1}$ yields estimates for the activation energy and pre-exponential factor. Although any form of intrinsic rate may be employed in principle, first-order kinetics were assumed throughout.

4 Results and Discussion

Arrhenius plots of the apparent and the intrinsic rates, calculated as outlined above, are shown in Fig. 3a and 3b, respectively, for selected synthetic chars and the two coal-derived chars. The intrinsic activation energies are in the range of 32 to 37 kcal/mol for the sythetic chars, and about 47 kcal/mol for the coal-derived chars. The solid line, in Fig. 3b, corresponds to Smith's best-fit line for a variety of coal chars.[24] The intrinsic reaction constants calculated in this study fall below Smith's curve, indicating that the materials examined are less reactive as shown previously.[21] Although, the present rates were calculated by a different method than used by Smith, the two are in fair agreement when compared for the same materials.[21] A comparison between the apparent and the intrinsic rates reveals that the coal-chars, although apparently more reactive because of their enhanced macropore network, seem to be intrinsicaly less reactive.

Using the intrinsic rate constants of Fig. 3 and properties listed in Table I, temperature-time profiles for chars oxidized under various conditions were obtained. At the high particle temperatures encountered under most conditions investigated, estimates of the Thiele modulus (based upon average pore structure and particle temperature) were high (100-130 for synthetic chars and 15-20 for coal-derived chars). Thus, application of the simplified intraparticle model (Eq. (19)) was assumed valid, except as noted, implying that particle combustion occurs with

constant apparent density and monotonically decreasing radius. Verification of this assumption was demonstrated and is discussed below.

To reproduce the observed initial sharp increase in particle temperature exhibited by the sythetic chars under oxygen rich conditions, it was necessary to take into account the combustion of residual volatile matter in these chars. Pyrolysis at 1600 K resulted in mass loss up to 10% [21] on an estimated time scale of 1 ms. Further evidence for the existence of volatile material is given by high heating values (calorimetry) in comparison to pure carbon, and the existence of H_2 and O_2 (elemental analysis). At high oxygen concentrations, the volatiles may burn near the particle surface and cause significant influence upon particle ignition by inducing rapid heatup. At lower O_2 concentrations, the residual volatile matter did not ignite. The coal chars were assumed volatile-free because of their previous high-temperature pyrolysis.

Figures 4a and 4b show the experimental (dotted) and the theoretical (solid) temperature histories for PFA particles and particles formed from 50% Tannic acid and 50% PFA, respectively. Figures 4c and 4d show the conversion and normalized values for surface oxygen concentration and particle radius versus time. The particles had a diameter of 45 μm and were burned in pure oxygen at a wall temperature, T_W, of 1500 K and a free-stream gas temperature, T_∞, of 1400 K. Inspection of Figures 4a and 4b demonstrates a successful simulation for the combustion of both kinds of particles.

The steep rise in particle temperature and decrease in surface oxygen concentration within the first 1-2 milliseconds predicted by the model reflects the assumed combustion of volatiles at the particle surface and is consistent with the observed behavior. After the initial heatup period, the theoretical temperature and surface oxygen profiles are relatively flat. Film diffusion is important but not rate-controlling. Figures 4c and 4d indicate that experimental extinction occurs at

about 85% theoretical conversion when the normalized particle radius is 53% of its initial value. Extinction seems to be caused by the increased convective heat losses accompanying the decrease in particle size.

Figures 5a and c show the combustion of 45 μm glassy carbon particles containing 25% carbon black (O_2, T_W = 1450 K, T_∞=1350 K). These particles burn more quickly and at higher temperatures, and exhibit a sharper initial temperature rise than those described above because of their lower density and the presence of transitional pores which facilitate intraparticle diffusion. The calculated and measured extinction times nearly coincide in this case.

Model predictions and experimental traces for synthetic char cenospheres are shown in Figs. 5b and d (O_2, T_W=1500 K, T_∞=1400 K). The particles have an outer diameter of $\approx$ 114 μm and wall thickness of about 3 μm. The same kinetic parameter values as obtained for the solid particles of the same composition were used to simulate combustion of the cenospheres. The solid line in Fig. 5b corresponds to case (I), explained earlier, where oxygen diffuses into the char through the external surface only, and the dashed line corresponds to case (II) where oxygen diffuses into the char through both shell surfaces. The experimental curves clearly favor case (I), suggesting that depletion by the oxidation reaction effectively shields the central void from oxygen penetration (under the particular experimental conditions).

Figure 5d displays particle conversion, as well as normalized values for surface concentration and shell thickness $(r_p - r_i)/(r_{p0} - r_{i0})$; these quantities are presented only for case (I). Particle size is essentially constant during the combustion process, hence, neither convective heat losses nor film diffusion are appreciably enhanced with burnoff thereby explaining the plateaus in particle temperature and surface oxygen concentration. This reasoning suggests that the cenospheres burn in a luminous mode throughout their history explaining the coincidence of experimental extinction and theoretical burnout.

The combustion of the coal chars PSOC-176 pyrolyzed at 1400 and 1600 K are shown in Fig. 6 (50% O_2, T_W=1500 K, T_∞=1400 K). The calculated curves were obtained by treating the particles as spherical, with 50 μm diameter. Considerable variability is observed among the measured traces as expected from variations in size, shape and properties of individual particles. The calculated curve lies within the range of the measured traces in terms of temperature and burnout time. Figures 6c and 6d include and additional curve showing the ratio of ash layer thickness to particle radius, $(r_a - r_p)/r_p$.

Synthetic chars (solid spheres) burning in air exhibit particle temperatures between the gas and wall temperatures yielding estimates for the Thiele modulus in the range 3-6 thus allowing deeper oxygen penetration than under the conditions investigated above. Therefore, decreasing particle density is expected to accompany combustion. To describe combustion behavior under these conditions and to justify the earlier use of the simplified intraparticle model, the full intraparticle solution (Eq. (5)) is implemented (solid curves) and compared with the approximate solution (dashed curves) in Figures 7a and 7b. In both cases, the surface oxygen concentration was predicted to be within 1% of the ambient value and, thence, is not shown. Film diffusion is unimportant.

Figures 7a and 7b depict the behavior of a synthetic char particle burning in air with T_∞=1450 K, T_W=1500 K; and T_∞=1350 K, T_W=1400 K, respectively. The simplified solution necessarily predicts constant density and monotonically decreasing radius while the full solution predicts decreasing density with constant radius initially followed by shrinking-core combustion. The discrepancy between the two solutions is most pronounced at lower temperatures (Fig. 7b) but both correctly predict the observed particle temperatures and conversion after 2 s, the residence time in the combustor. These results support the application of the simplified intraparticle model to simulations at higher particle temperatures. The kinks in the

particle radius and density profiles (Figs. 7a and 7b) reflect the tacit assumption in the full intraparticle model that the char fragments upon reaching a prescribed local void volume, ϵ^* exactly equal to 0.8.[11]

The combustion behavior of all chars described in Table I, burning at various combustor (wall) temperatures (1300 K - 1600 K) and different ambient oxygen concentrations (air, 50%, 100%), were predicted with qualitatively equal success by the model, although only selected cases have been shown for the sake of brevity.

The general fidelity with which apparent rates and temperature profiles were reproduced in the foregoing examples demonstrates successful determination of apparent reaction rates but not intrinsic parameters. This point is illustrated by application of the model (case (I)) to cenosphere combustion behavior. In this case, intrinsic rate parameters were determined from solid particles of the same material; however, both particles (solid and hollow) have similar pore structure and burn under conditions of high Thiele modulus. Therefore, this test cannot be used to access the method by which intrinsic rate parameters are estimated but it does provide support for the apparent rate determinations.

Comparison between experimental results and model predictions under a variety of conditions which affect intraparticle transport provides a test of estimated kinetic parameters. This demonstrates that indeed the intrinsic parameters are a chemical property of the material and, thus, are independent of pore structure and evolution. Such a test was acheived by using the intrinsic activation energy and pre-exponential factor previously determined for a particle burning under conditions of high Thiele modulus to describe the combustion of a particle with identical material and pore structure under conditions of low diffusional resistance.

Combustion parameters for 8 μm diameter PFA particles are depicted in Fig. 8. The particles burned slowly in air at particle temperatures approximately equal to the gas (T_W = 1400 K, T_∞ = 1350 K; and T_W = 1300 K, T_∞ = 1250 K). To

obtain the profiles of these parameters, the intrinsic rate previously derived from the 45 μm particles was employed. The model closely predicted the experimentally observed conversion (at the end of the 2 s. residence time in the furnace). The average Thiele modulus during combustion was small (less than unity) consistent with the model predictions of continuously decreasing apparent density and nearly constant size. The foregoing example supports the present model of intraparticle transport which is used to infer intrinsic rate parameters from apparent rate data.

5 Conclusions

The intrinsic and apparent kinetic parameters of several synthetic chars and two coal chars were deduced by a simple analysis of time-temperature traces of individual particles, measured by two-color pyrometry. Estimated intrinsic parameters were then used in a detailed particle combustion model to calculate complete temperature-time histories of burning particles. Measured and calculated temperature profiles were found in good agreement for the the synthetic char particles. The experimental temperatures of the coal char particles exhibited considerable particle-to-particle variation and could only be described approximately by the calculated temperatures corresponding to nominal particle properties.

Under most conditions employed in the experiments, the Thiele modulus was in the range of 50-200 and a limiting form of the combustion model represented the data very well. Even at values of the Thiele modulus as low as 10, the limiting calculations were in good agreement with the complete calculations and the experimental results. It is concluded that the limiting form of the model is sufficient under most conditions. At temperatures above 2000 K, the intrinsic rates of all chars examined varied by less than a factor of two. The kinetic parameters determined from experiments conducted at moderate to high Thiele modulus conditions were applied to simulate the combustion behavior of particles burning under kinetic

control. The results support the procedure by which rate parameters were deduced.

6 Acknowledgements

This work was supported by DOE Office of Energy Utilization Research, ECUT Program and by the DOE University Coal Programs Grant Number DE-FG22-84PC70775.

7 Notation

SYMBOL	DESCRIPTION	UNITS
b	stoichiometric coefficient	$(= 1/24)$
C	oxygen concentration	gmoles/cm^3
C_s	oxygen concentration at particle surface	gmoles/cm^3
c_p	average specific heat capacity of particle	cal/g K
e_R	radiative energy flux	cal/cm^{2}s
F_p^T	total mass flux at particle surface	g/cm^{2}s
F_p	mass flux due to reaction at particle surface	g/cm^2 s
k_{in}	intrinsic rate coefficient	g/cm^2 s (atm)^n
m	intrinsic reaction order	
m_p	particle mass	g
q	local structural variable	cm
q^*	value of q at critical porosity, ϵ^*	
r	radial position	cm
r_a	instantaneous ash radius	cm
r_i	instantaneous inner shell radius (cenosphere)	cm
r_p	instantaneous particle radius	cm
$r_{p,rms}$	root-mean-square particle radius	cm
R_{in}	intrinsic rate-per-unit pore surface area	g/cm^{2}s
T_p	particle temperature	K
t	time	s
t_b	burnout time	s
v_a	volume fraction of ash in carbon matrix	
X	conversion	
x_a	mass fraction of minerals	
δ_e	effective diffusion coefficient	cm^2/s

ϵ	total porosity	
ϵ_a	volume fraction of ash in carbon matrix	
ϵ^*	critical porosity	
ρ	particle density	g/cm^3
$\bar{\rho}$	average particle density	g/cm^3
ρ_a	density of ash	g/cm^3
ρ^*	particle density at critical porosity	g/cm^3
ρ_T	true carbonaceous density	g/cm^3

SUBSCRIPTS

0	initial value
∞	at ambient conditions

8 References

1. McLean, W. J., Hardesty, R. D. and Pohl, J. H. *Eighteen Symp. (Int.) on Combustion,* The Combustion Institute, Pittsburgh, PA. p.1239 (1981).

2. Mitchell, R. E., McLean, W. J. Nineteenth Symposium (International) on Combustion. The Combustion Institute, Pittsburgh, PA. p.1113 (1982).

3. Timothy, L. D., Sarofim, A. F. and Beér, J. M. *Nineteenth Symp. (Int.) on Combustion.* The Combustion Institute, Pittsburgh, PA. p.1123 (1982).

4. Jorgensen, F. R. A. and Zuiderwyk, M. J. *J. Phys. E: Sci. Instrum.* 18:486 (1985).

5. Levendis Y. A. and Flagan R. C. *Comb. Sci. Tech.* 53:117 (1987).

6. Libby, P.A., and Blake, T.R. *Comb. Flame* 36:139 (1979).

7. Sundaresan, S. and Amundson, N.R. *Ind. Eng. Chem. Fund.* 19:344 (1980).

8. Sotirchos, S.V., and Amundson, N.R. *Ind. Eng. Chem. Fund.* 23:191 (1984b).

9. Sotirchos, S.V., and Amundson, N.R. *A.I.Ch.E.Jl.* 30:549 (1984d).

10. Gavalas, G.R. *Comb. Sci. Tech.* 24:197 (1981).

11. Loewenberg, M., Bellan, J. and Gavalas, G. R. *Chem. Eng. Comm.* 58:89 (1987).

12. Gavalas, G.R. *A.I.Ch.E.Jl.* 26:577 (1980).

13. Dutta, S.,Wen, C.Y., and Belt, R.J. *Ind. Eng. Chem., Process Des. Dev.* 16:20 (1977).

14. Kerstein, A.R., and Niksa, S. *Twentieth Symp. (Int.) on Combustion.* The Combustion Institute, Pittsburgh, PA. p.941 (1984).

15. Sarofim. A. F., Howard, J. B., and Padia, A. S. *Comb. Sci. Tech.* 60:187 (1977).

16. Hamblen, D. G., Solomon, P. R., Hobbs, R. H.: *Physical and Chemical Characterization of Coal*, EPA Report No. EPA-600/7-80-106, 1980.

17. Northrop P.S.: (1987), personal communication.

18. Senior, C. Y. "Submicron Aerosol Formation During Combustion of Pulverized Coal." Ph.D. Thesis, Caltech, 1984.

19. Gavalas, G.R., Loewenberg, M.,Bellan, J. and Clayton, M. Paper presented at the annual A.I.Ch.E. meeting, Chicago, November 10-15, 1985.

20. Levendis Y. A. and Flagan R. C. Submitted to Carbon.

21. Levendis Y. A., Flagan R. C. and Gavalas G. R. submitted to Comb. and Flame.

22. Scholten, J. J.: From Porous Carbon Solids (R. L. Bond, Ed.), Academic Press, p.225, 1967.

23. Smith, I. W., and Tyler, R. J. *Comb. Sci. Tech.* 9:87 (1974).

24. Smith, I.W. *Nineteenth Symp. (Int.) on Combustion.* The Combustion Institute, Pittsburgh, PA. p.1045, 1982.

9 List of Figures

7. Combustion parameters for 45 μm solid particles formed from 50% tannic acid - 50% PFA burning in air at a T_W of (a) 1500 K and (b) 1400 K. Temperature-time profile, burnout, surface oxygen concentration, relative radius and apparent density vs. time; complete model: solid line, simplified model: dotted line.

8. Combustion parameters for 8 μm solid PFA particles burning in air at a T_W of (a) 1400 K and (b) 1300 K. Temperature-time profile, burnout, surface oxygen concentration, relative radius and apparent density vs. time.

TABLE I

Physical Properties of Synthetic Chars

CHAR	Apparent Density g/cm^3	Helium Density g/cm^3	Porosity Mic-Trans-Mac %	BET area m^2	Pore Radius Mic-Trans-Mac Å	Heating Value cal/g
Plain Polymer	1.25	1.69	26 - 1 - 1	400	11-100-1000	8160
Plain Polymer + 18% Tan.Acid	1.33	1.85	26 - 1 - 1	420	12-100-1000	7706
Plain Polymer + 50% Tan.Acid	1.37	1.96	28 - 1 - 1	320	13-100-1000	7655
Plain Polymer + 18% PEG	1.17	1.80	30 - 1 - 1	430	18-100-1000	8184
Plain Polymer + 35% Glycerol + 7% Triton	1.26	1.80	33 - 1 - 1	620	14-100-1000	8534
Plain Polymer + 25% CarbonBlack	0.88	1.70	22 - 25 - 1	360	11-75-1000	7900
Plain Polymer + 50% Tan.Acid 'Cenospheres'	0.65	2.0	26 -.5 -.5	300	12-100-1000	7690
PSOC-176 1600 K char	0.76	1.85	30 - 12 - 20	350	10-250-1000	7250 Ash free
PSOD-176 1400 K char	0.65	1.80	28 - 1 - 27	450	10-100-1000	7800 Ash free

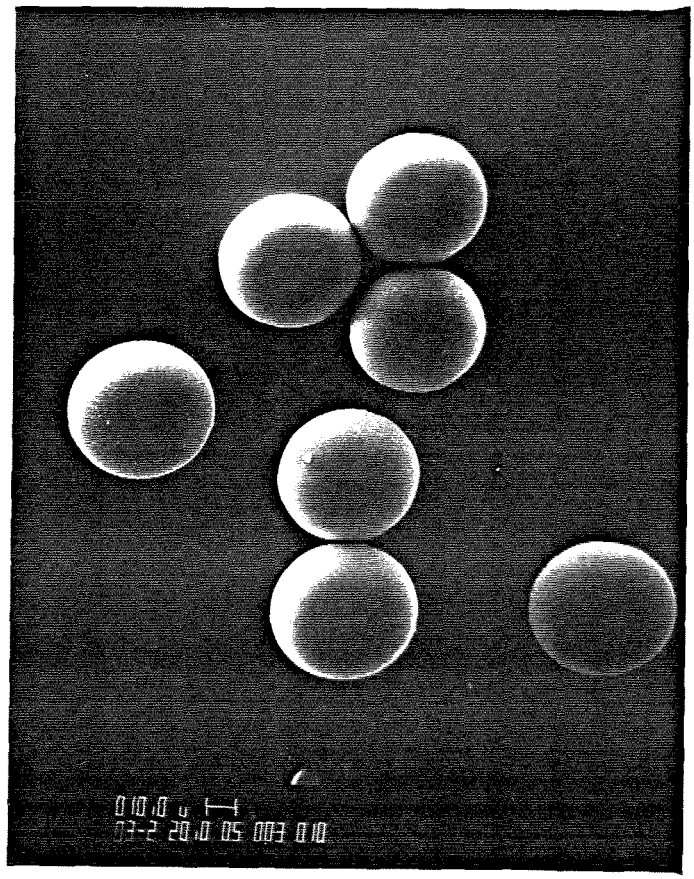

a

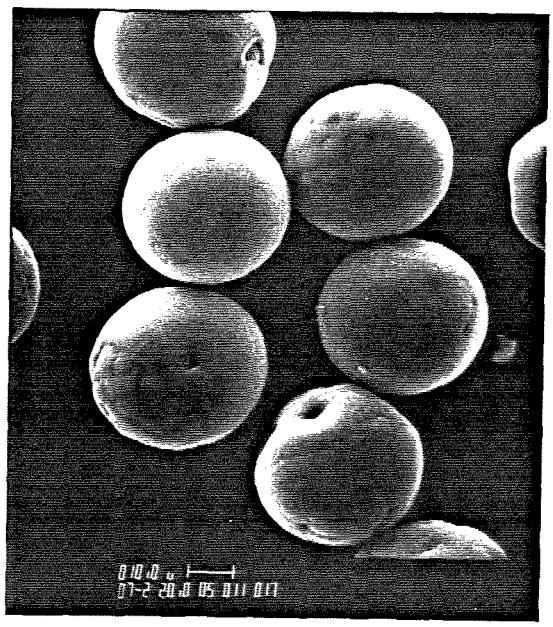

b

Figure 1: SEM micrographs of solid synthetic particles: (a) plain polymer (PFA) and (b) PFA with 25% carbon black.

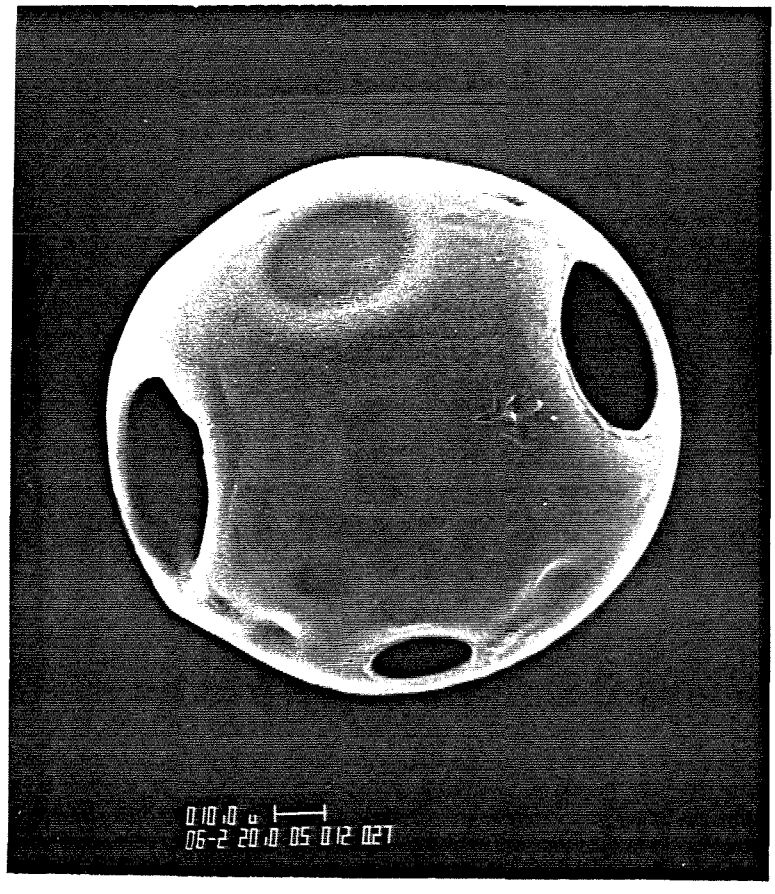

a

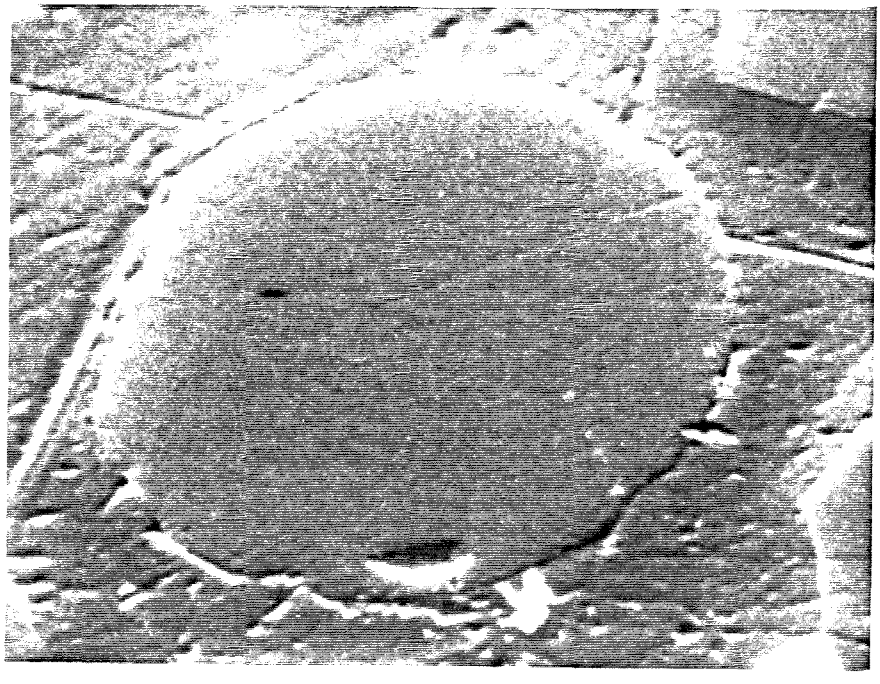

b

Figure 2: SEM micrographs of (a) a cenospheric particle (b) a section through a partially burned PFA particle and

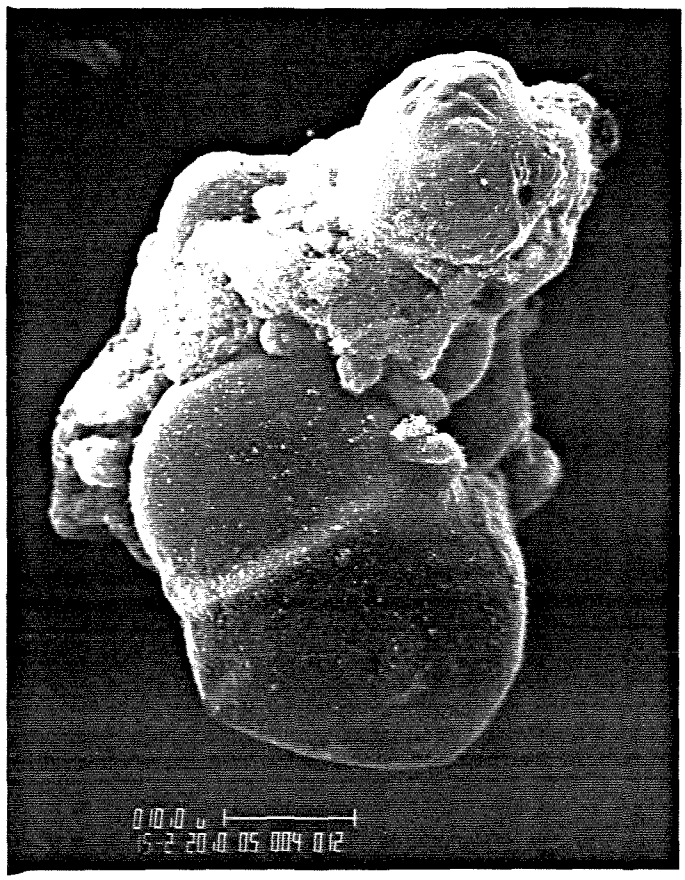

(c) a PSOC-176 coal-char particle pyrolyzed at 1600 K.

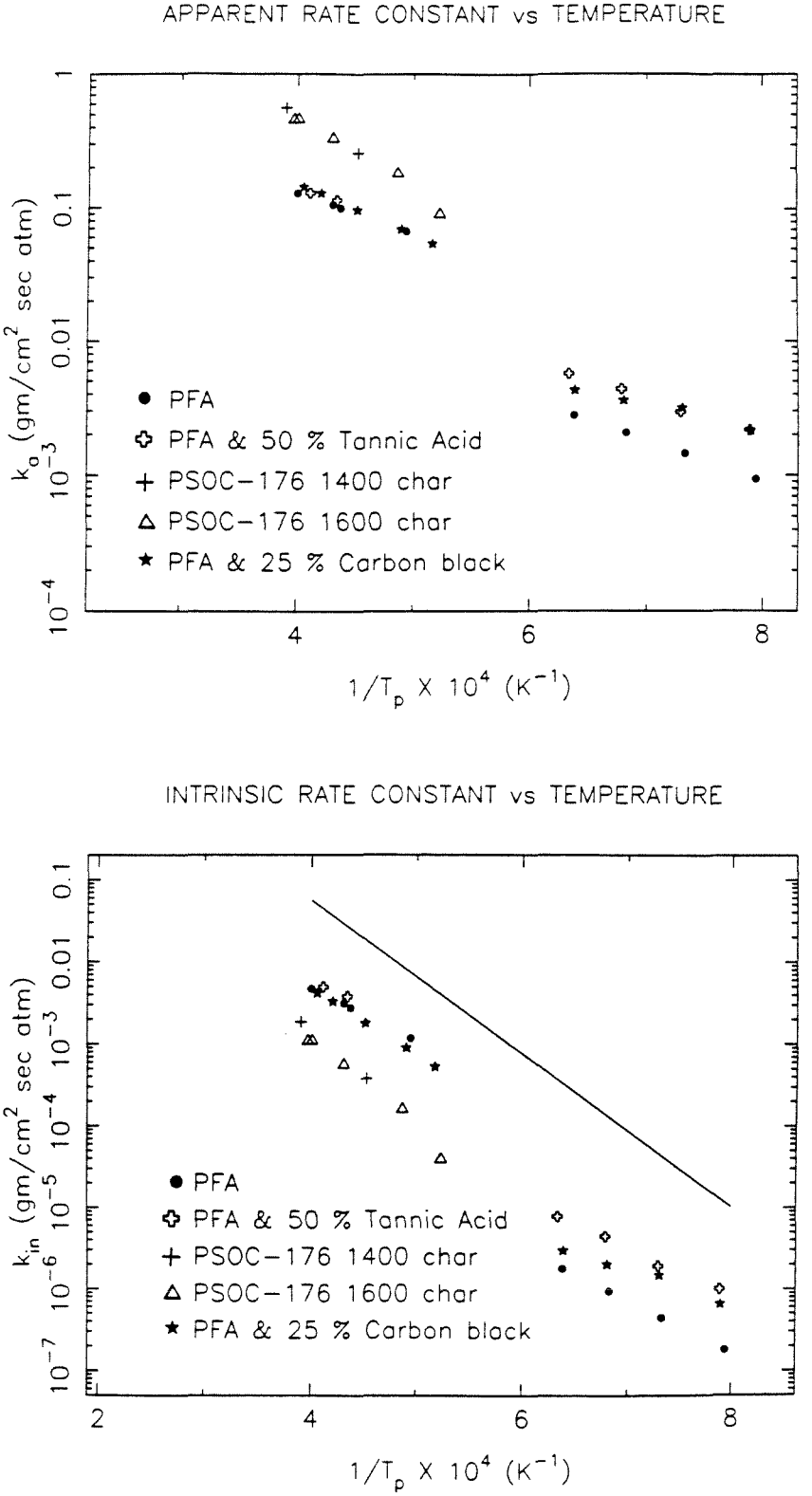

Figure 3: Arrhenius-type plot of the intrinsic reaction rate coefficient vs. the inverse of particle temperature.

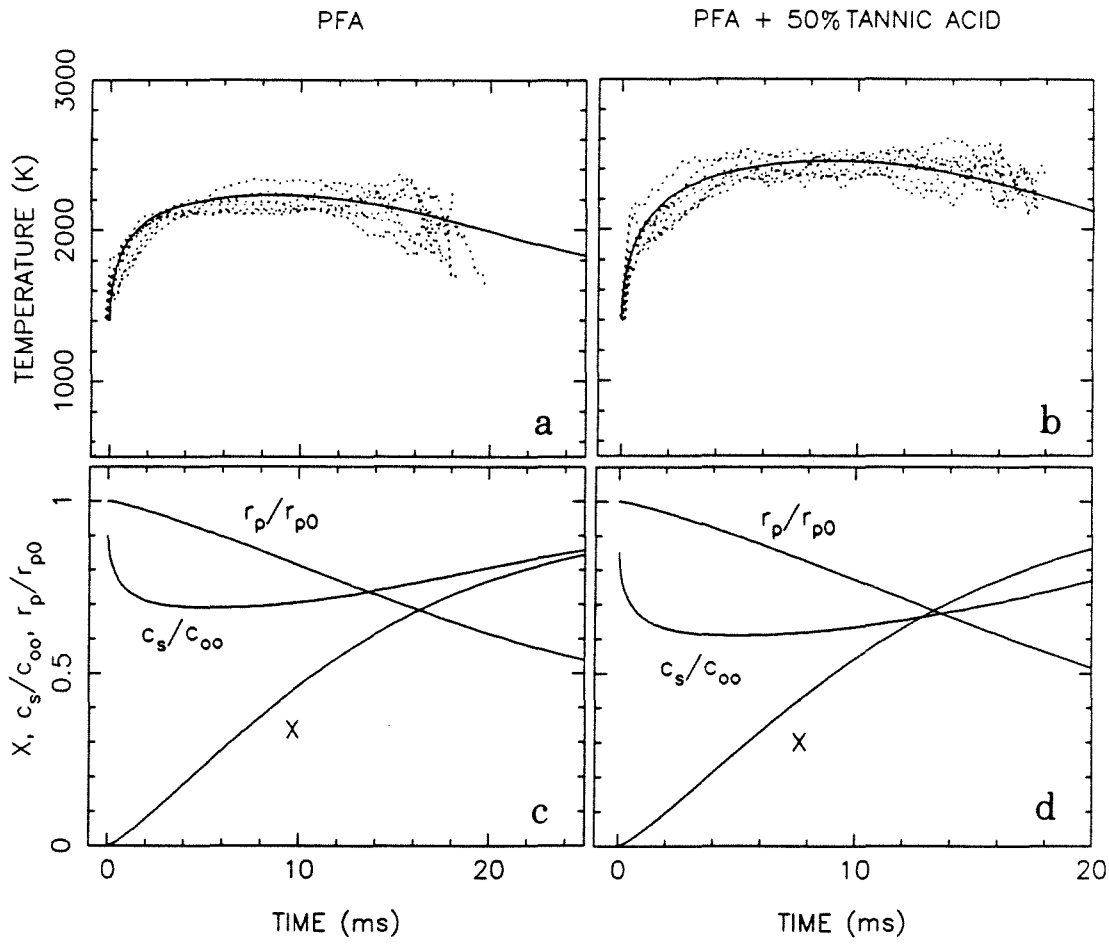

Figure 4: Combustion parameters for 45 μm (a,c) solid PFA particles and (b,d) solid PFA particles formed from 50% tannic acid - 50% PFA burning in O_2 at a T_W of 1500 K. (a,b) temperature-time profile, model: solid line, experiments: dotted line. (c,d) burnout, relative surface oxygen concentration and relative radius vs time.

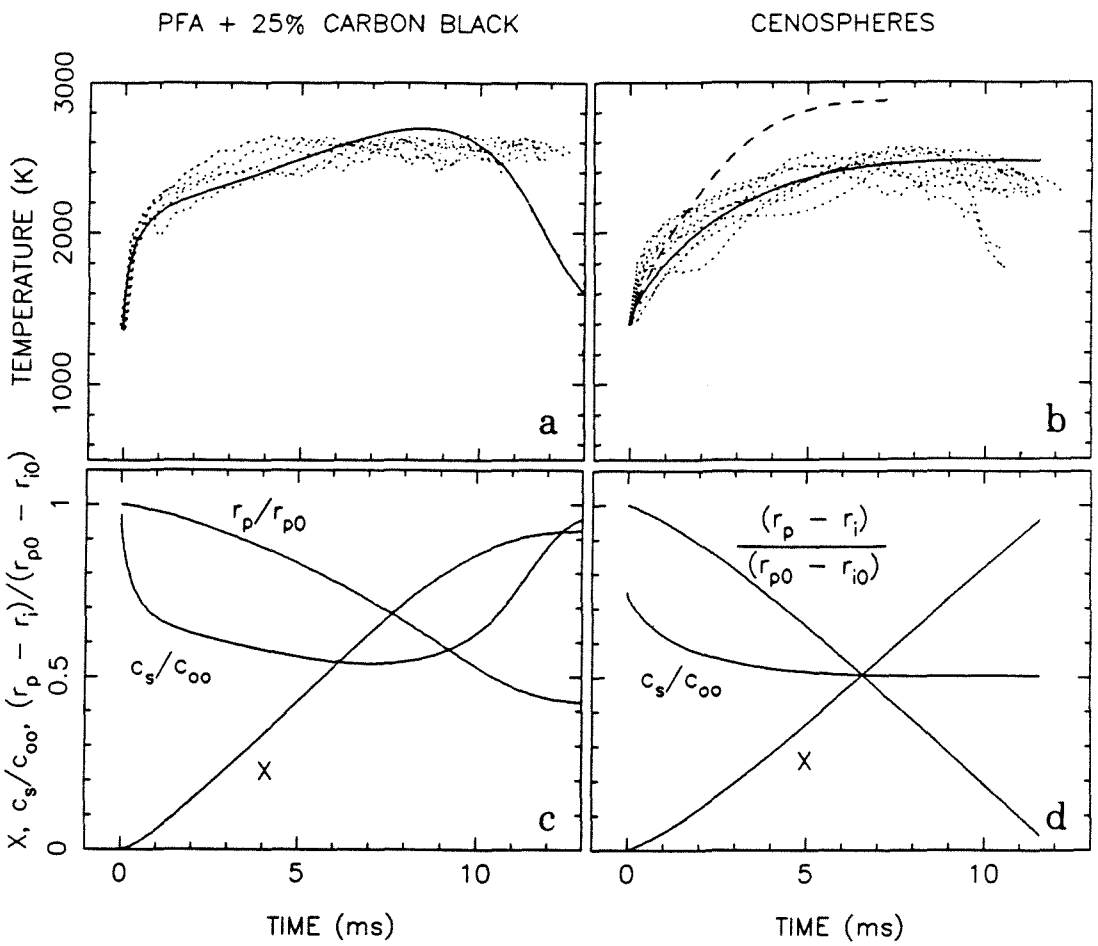

Figure 5: Combustion parameters for (a,c) 45 μm solid PFA particles containing 25% carbon black burning in O_2 at a T_W of 1450 K and (b,d) 114 μm cenospheric particles formed from 50% tannic acid and 50% PFA burning in O_2 at a T_W of 1500 K. (a,b) temperature-time profile, model: solid line, case(II) (cenospheres) dashed line; experiments: dotted line. (c,d) burnout, relative surface oxygen concentration and relative radius vs. time.

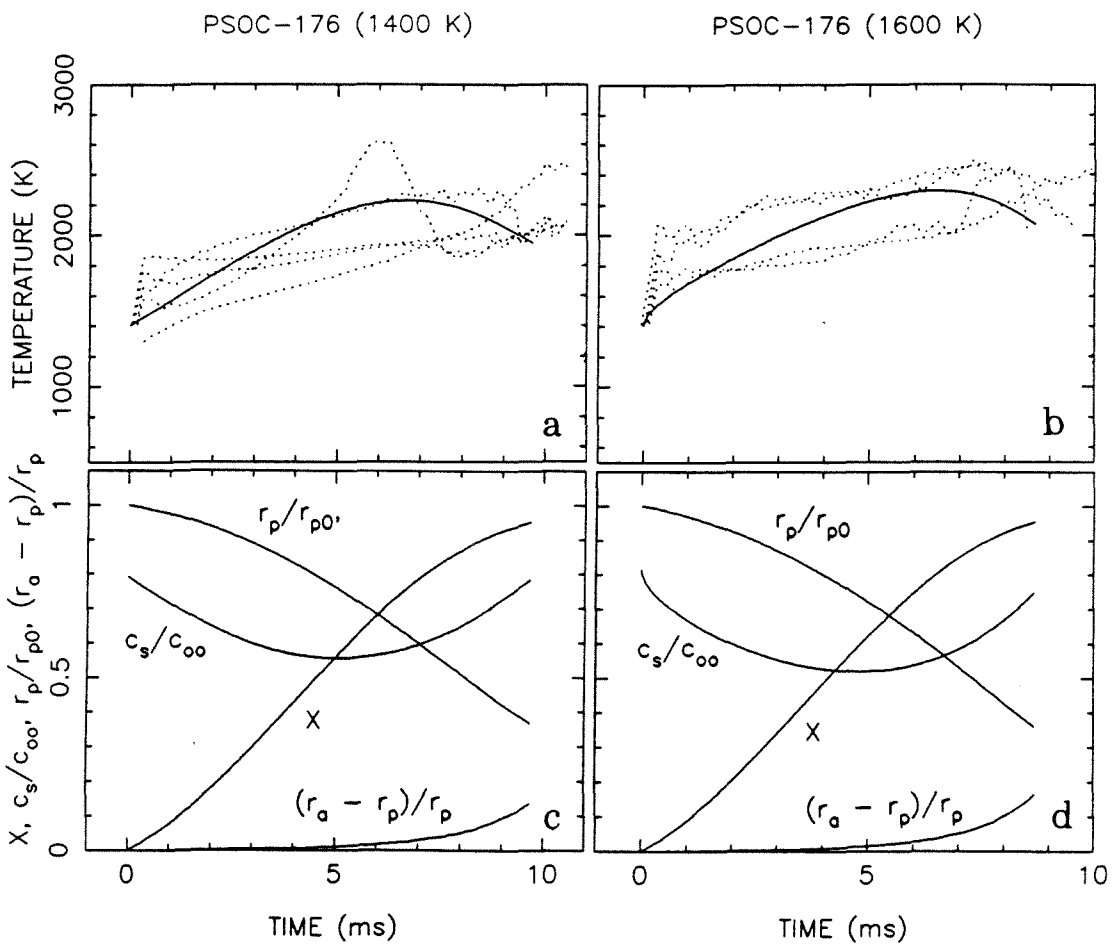

Figure 6: Combustion parameters for 50 μm PSOC-176 coal-char particles ((a,c) 1400 K and (b,d) 1600 K pyrolysis) burning in O_2 at a T_W of 1500 K. (a,b) temperature-time profile, model: solid line, experiments: dotted line. (c,d) burnout, relative surface oxygen concentration, relative particle radius and relative ash layer thickness vs. time.

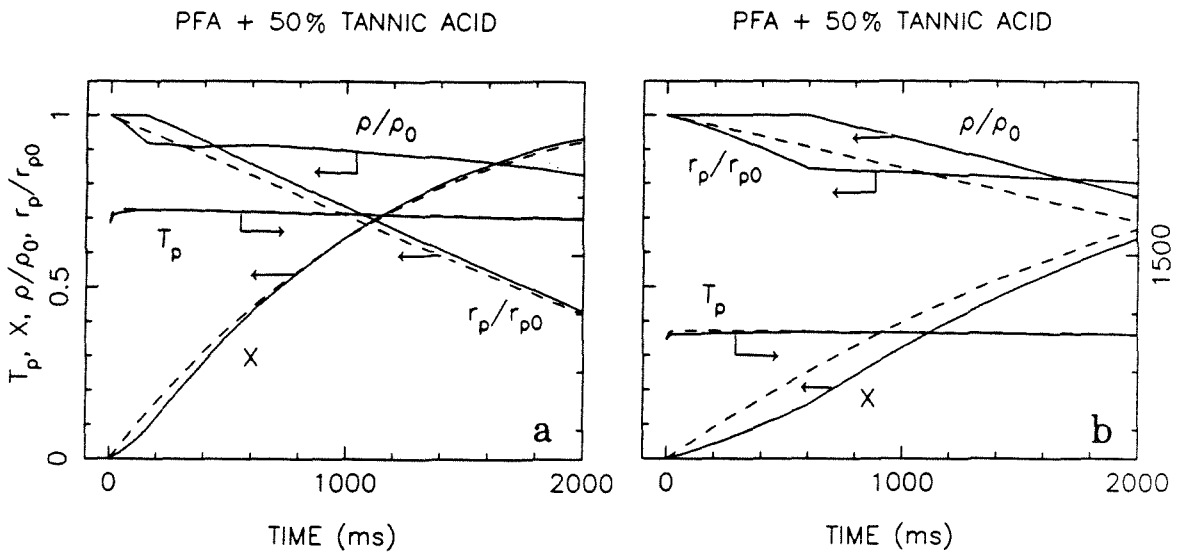

Figure 7: Combustion parameters for 45 μm solid particles formed from 50% tannic acid - 50% PFA burning in air at a T_W of (a) 1500 K and (b) 1400 K. Temperature-time profile, burnout, surface oxygen concentration, relative radius and apparent density vs. time; complete model: solid line, simplified model: dotted line.

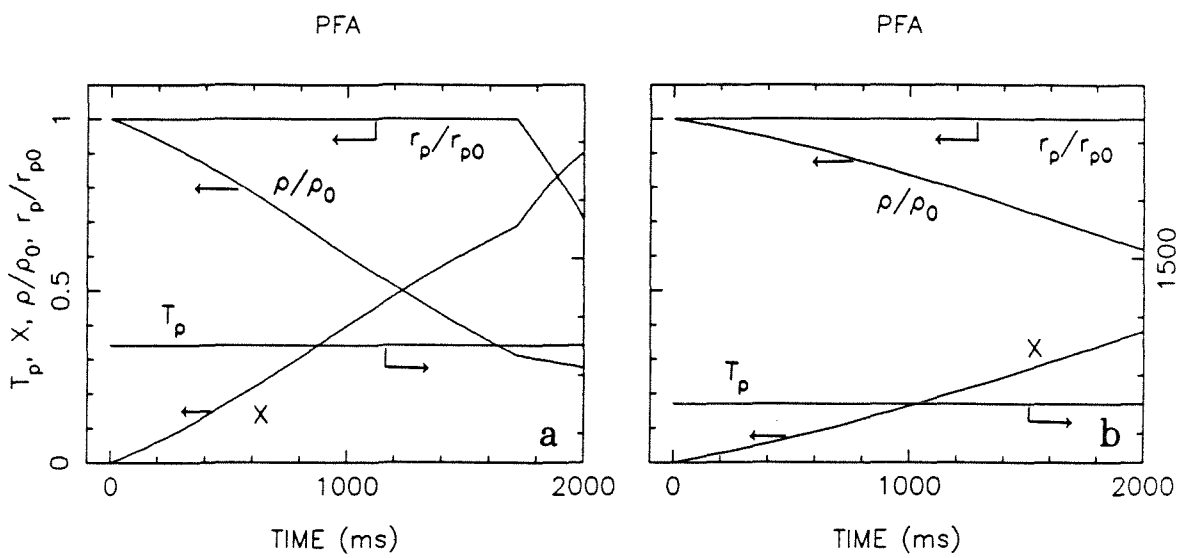

Figure 8: Combustion parameters for 8 μm solid PFA particles burning in air at a T_W of (a) 1400 K and (b) 1300 K. Temperature-time profile, burnout, surface oxygen concentration, relative radius and apparent density vs. time.

CHAPTER 8

Ignition Transients in the Combustion of Single Char Particles

[†]Yiannis A. Levendis [‡] Ranajit Sahu [† ‡] Richard C. Flagan
[*]George R. Gavalas
Departments of [†]Environmental,
[*]Chemical and [‡] Mechanical Engineering
California Institute of Technology

Abstract

The temperature-time history of single char particles burning at temperatures above 1500 K have been measured by two-color near infrared pyrometry techniques. Two coal chars and a synthetic char consisting of spherical glassy carbon particles of uniform size were used in the experiments. The results indicate that in the regime of lean combustion and low-to-medium temperatures, the char particles do not ignite over their whole external surface, but exhibit preferential ignition at specific sites. These *hot-spots* probably involve regions where the material exhibits strong inhomogeneities, either on or below the surface. Following ignition, the reaction may propagate over the particle surface. At elevated combustor temperatures and/or high oxygen partial pressures, ignition spreads quickly over the entire particle surface and the importance of the *hot-spots* diminishes. A simple model is used to estimate the rate of growth of a *hot-spot* under various experimental conditions.

Key Words – Ignition, coal-chars, combustion, pyrometry.

1 Introduction

The structural complexity of coal is well-documented. The organic components have been mixed with sedimentary strata, compacted, variably subjected to decay and chemically altered by geological processes[1]. In addition to the organic components, the coal microstructure incorporates small and large pores and a plethora of minerals. The particles produced during the grinding process have irregular shapes, and contain cracks and loosely bound material on the surface. Because of this variable surface morphology and the physical and chemical inhomogeneities, there is no reason to expect the particles to ignite and burn uniformly over their surface. In the customary mathematical analysis of char combustion the particles are assumed to have spherical shape and spatially uniform properties, density, pore structure etc. Real particles of course, have irregular shapes and gross spatial inhomogeneities (pores, cracks, minerals) but these irregularities cannot be described mathematically in any reasonable fashion. Nevertheless it is quite clear that these irregurities in char particles cause significant particle-to-particle variations in particle temperature and burnout time. Variations in ignition behavior due to these irregularities can also be expected.

Efforts to understand the ignition mechanism of coal particles date back to Semenov[2]. Thereafter studies on the ignition of clouds of particles,[3,4] and packed beds of particles[5] have been conducted but studies concerning the ignition behavior of single particles are rare. Ignition of coal particles has been assumed to be either homogeneous[6] where emitted volatiles ignite first or heterogeneous[7] where ignition occurs at the particle surface. Recent studies on ignition of single coal particles[8] suggest that ignition swiches from being homogeneous to heterogeneous as the reactor temperature increases. The ignition of char particles is heterogeneous, in view of the absence of volatiles. Ignition occurs with[9] or without[10] a temperature jump and the measured ignition temperature has been observed to increase with decreasing

particle size.[9]

Previous modelling work has utilized steady or unsteady energy balances assuming that the particle ignites uniformly over its surface.[9-12] In this paper we shall present experimental observations that suggest that ignition does not occur uniformly over the particle surface but, rather, occurs in small localized regions. Reaction fronts then propagate over the particle surface. A theoretical description of a reaction front propagation is developed.

2 Experimental

The coal chars used in the combustion experiments were derived from the two high volatile bituminous coals, listed in Table I, by devolatilization at 1600 K, for 2 s, and in nitrogen. Experiments were also conducted with glassy carbon chars for comparison purposes. These glassy carbons were synthesized from polymer materials[13] in the form of mineral-free, homogeneous, uniformly sized spheres. The char particles were sized by sieving, with the aid of a mechanical shaker. The size and surface morphology of the particles were examined by optical and scanning electron microscopy (SEM). Physical properties and chemical composition of the particles were measured as described elsewhere.[13,14]

Both coal pyrolysis and char combustion were performed in an externally heated, laminar flow, drop-tube furnace capable of reaching centerline temperatures of 1600 K. Pyrolysis was performed in a stream of pure nitrogen and combustion in O_2-N_2 mixtures at oxygen partial pressures varying between 0.21 (air) and 1.0 atm. Particle temperatures were monitored with a two-color pyrometer, with broad band filters centered in the near-infrared at 800 and 1000 nm, respectively, and employing silicon photocell detectors. Details of the combustion apparatus and the pyrometer are given elsewhere.[13] For the present experiments, only one particle at a time was introduced into the combustion chamber making it possible to record

the two-color radiation intensity traces throughout the combustion life of a single particle. Employing a Planck-law analysis, temperature-time profiles were derived from the ratio of the two intensity signals.

3 Results and Discussion

Typical intensity-time traces and the corresponding calculated temperatures for the two coal chars are shown in Figs. 1-3. The combustion atmosphere and wall temperatures were as indicated in the figures while the gas temperature was 1100 K for all cases. Since the oxidation took place at furnace temperatures (centerline and wall) lower than the temperatures used for the pyrolysis process, no devolatilization is anticipated during the char combustion experiments. In Fig. 1, the particle temperature is approximately constant throughout combustion, but the emission intensities rise through a large fraction of the burn time (region 1) and then decrease throughout the remaining time (region 2). The behavior in region 2 can be attributed to the decreasing particle cross section as the char particle shrinks during the final stages of combustion. In short, the increase in intensity in region 2 is a purely geometrical effect.

The behavior in region 1, where the intensity increases while the temperature remains approximately constant is more difficult to explain. We first ascertained that this behavior is not an artifact generated by the pyrometer electronics. This possibility can be eliminated by the following observations: (a) The silicon photocell detectors used, *Hamamatsu S1336-5BQ*, are very fast, having a nominal rise time of 0.2 μs, and exhibit a linear response. (b) The 'slew' rate of the amplifiers is very fast, 2 V/μs. (c) The response of the two channels of the pyrometer was verified to be the same, by swapping the filters. (d) Radiation intensity traces obtained by Sarofim and coworkers[15,16] exhibit similar behavior, even though a totally different system was used for data acquisition. The pyrometer used in their work employed

photomultiplier tubes (PMT) that exhibited a rise time of 15 ns. (e) The peak occured at different times for different particles and, moreover, a late peak occured only for particles burning in air, in contrast to particles burning at high O_2 partial pressures, where the intensity rise is almost instantaneous. Thus, it can be safely concluded that the intensity increase must be a characteristic of the combustion behavior of the chars.

It is proposed that the gradual increase in intensity at constant temperature is caused by the spread of the reacting region from one or more localized ignition sites at the particle surface. The intensity of the radiation that is received by the detectors depends on three parameters: (i) the *luminosity* of the light source that is directly related to its temperature; (ii) the *size* of the light source, and (iii) the *distance* between the source and the detector. The distance did not vary significantly in our experiments since, at the furnace flowrates used, a particle travels at most 2 to 4 mm during its burntime (velocity $\approx 10^{-1}$ mm/ms), which is much smaller than the distance between the particle and the detector ($\approx$ 300 mm). Hence, the detectors see a particle that is almost stationary during its entire combustion history. Further, if distance were responsible for the intensity variation at constant temperature, the intensity traces would monotonically decrease, since the particles travel away from the detector. Such behavior was not observed for any particles. The second parameter, luminosity at some fixed wavelength, is a function of temperature via the temperature dependence of Planck's law and by the temperature dependence of the emissivity. However, if the temperature of the particle remains constant, as observed, the luminosity of the particle should also remain constant. Therefore, the recorded intensity variations must be due to variations in the radiating area of the particle projected in the direction of the detector. The increase in the radiating area could be attributed to either an increase in the total area, radiating uniformly, or an increase of the radiating fraction of a roughly constant physical area. In view of

prior devolatilization, the total area could not increase by swelling. Therefore, the area of the particle that is radiating increases with time in region (1). It is proposed that a few reactive regions on the char surface ignite first, and thereafter combustion fronts propagate over the rest of the particle. Thus, the radiating area of the particle can increase without an associated increase in temperature, if the ignited regions or *hot-spots* have roughly the same temperature. Progressive ignition on the particle surface has also been observed by photographic techniques.[17]

The higher reactivity in localized regions on the particle surface could result from a number of causes. One possibility is local mineral concentrations that catalyze and accelerate reaction. Previous investigations[18] have shown that the reactivity is greatly enhanced in the presence of impurities, particularly magnesium and calcium. Reactive spots could also be due to localized macro- and transitional pores that serve as *feeders* to the micropores and enhance reactivity. In Fig. 4a the scanning electron micrograph of a char particle reveals an irregular particle shape, various surface cavities, and large pores and protrusions that usually appear (by the degree of darkness in BSE-SEM) to be rich in ash and could contribute to localized ignition.

Whatever the cause of the localized ignition, particles of the same char would be expected to become fully ignited more rapidly in oxygen-enriched atmospheres than at lower oxygen levels because the combined effect of the oxygen availability and the resulting higher temperatures accelerate the reaction. Hence, the observed delay times, i.e., the duration of region (1), should be short. This is seen by comparing Figs. 1-3. Clearly, the rate of intensity increase in region (1) increases with oxygen level. The short delay observed in the high O_2 level experiments was usually associated with the period of increasing temperature. Ignition in pure oxygen was almost instantaneous.

Combustion of spherical synthetic char particles such as that shown in Fig. 4b provides a sharp contrast to coal char combustion. These particles are highly

uniform and are mineral-free, hence catalytic effects are minimal. These particles are not expected to have important reactive sites. Instead of undergoing localized ignition, such a particle may be uniformly heated close to the ignition temperature before rapid reaction begins. Once ignited, the particle would rapidly be engulfed in flame. This was confirmed in the experiments whenever it occured. Combustion of the synthetic chars, proceeded rapidly. Any delay in reaching peak intensities was associated with rising temperatures. The temperature and intensity profiles for combustion of a typical synthetic char particle is shown in Fig. 5.

Some coal char particles exhibited another interesting phenomenon that is shown in Fig. 6. The intensities undergo roughly periodic fluctuations. In Fig. 6a, the intensity in each channel fluctuates periodically for three complete cycles while following an overall decreasing trend. The temperature of the particle is almost constant over that period of time. We attribute these oscillations to the tumbling motion of the particle that changes the projected burning area that is viewed by the detector. Another set of measurements is shown in Fig. 6b. In this case the periodically varying signal is superimposed on an increasing trend suggesting that tumbling is taking place while *hot-spots* are growing.

Pyrometry traces were also obtained for a lignite char. These are not shown here but they exhibit similar ignition delay times as those observed for the chars of the two bituminous coals. Similar pyrometry results on lignite have also been obtained by others.[15,16]

4 Analysis of the Growth of a Hot Spot

In this section we examine the growth of a single local ignited region in an attempt to explain the gradual intensity rise while the particle temperature remains constant. We postulate that a hot, burning region propagates on the comparatively cooler particle surface without delving into the reasons of how such a region was ignited in

the first place. The burning region, assumed circular and locally two-dimensional (Fig. 7), dissipates heat to the surroundings and the rest of the particle while spreading on the surface at the same time. Using a quasi-one-dimensional analysis and thermal balance arguments, we calculate the growth of the burning region and determine the time required for the ignited region to engulf a hemisphere of the entire particle. This time turns out to be larger than the experimental ignition delay time indicating that ignition involves several rather than one spot on the particle surface.

Assuming the burning region to be a spherical sector, its area A_s is given as:

$$A_s = 2\pi r_p^2 \left(1 - \sqrt{1 - (r/r_p)^2}\right) \tag{1}$$

where r and r_p are the radii of the burning region and the particle, respectively. The area of a differential element is then given by:

$$dA_s = 2\pi r \frac{r_p}{\sqrt{r_p^2 - r^2}} dr \ . \tag{2}$$

The growth of the burning region is controlled by the balance between heat generation and heat dissipation:

$$\tilde{d}\sigma_a c_p (T_s - T_p) \frac{dA_s}{dt} = Q_G - Q_D \ , \tag{3}$$

where Q_G and Q_D are the heat generation and dissipation terms, respectively, c_p the heat capacity and σ_a the apparent density. The thickness, $\tilde{d}$, and the temperature, T_s, of the burning region are assumed to be constant. The temperature T_s is taken equal to the temperature measured by pyrometry. The thickness, $\tilde{d}$, is estimated by the procedure followed in reaction-diffusion problems in the limit of large Thiele modulus. It is given by:

$$\tilde{d} = \frac{r_p}{\phi} \ , \tag{4}$$

where r_p is the particle radius and ϕ is the Thiele modulus of the particle[19] given as:

$$\phi = \frac{r_p}{3} \left[A_T \sigma_a R_i C_s^{m-1} D_e^{-1}\right]^{1/2} . \tag{5}$$

A_T is the pore surface area per unit mass, averaged over the course of combustion, obtained from BET measurements or other equivalent techniques; σ_a is the apparent density of the solid; R_i is the intrinsic reaction rate coefficient; C_s is the oxygen concentration at the particle surface; m is the true reaction order, taken as unity in the present calculations, and D_e is the effective diffusivity in the porous particle. Thus the value of ϕ can be estimated using information about the porous structure of the particle and measured combustion rates.

The heat generated by the burning region can be expressed as:

$$Q_G = A_i \exp(-E_i/\mathrm{R}T_s) C_s A_T \tilde{d} A_s \sigma_a \Delta H \ , \tag{6}$$

where E_i is the activation energy of the reaction, A_i is the pre-exponential factor, and C_s is the oxygen concentration at the particle surface. ΔH is the heat of combustion at temperature T_s assuming that the heterogeneous reaction at the surface produces CO exclusively.

Heat dissipation consists of three contributions: conduction into the core of the particle, convection to the surrounding gas, and radiation to the furnace walls. The convection to the ambient gas can be calculated from:

$$\frac{k_{gas}}{r_p}(T_s - T_{gas}) A_s \ , \tag{7}$$

where k_{gas} is the thermal conductivity of the gas at the film temperature. This assumes that the Nusselt number is 2, since the Reynolds number, based on the slip velocity between the particle and the gas is very small. The radiation to the furnace enclosure is:

$$\sigma(\epsilon_s T_s^4 - \epsilon_w T_w^4) A_s \ , \tag{8}$$

σ is the Stefan-Boltzmann constant and ϵ_s and ϵ_w are the emissivities of the *hot-spot* and the wall respectively.

Conduction from the surface layer to the interior of the particle is a complicated unsteady two-dimensional problem coupled with the overall propagation problem.

For the purpose of this analysis we assume that heat conduction occurs only perpendicular to the surface in an unsteady fashion. The heat flux from an element of the burning region is then given by:

$$\frac{k_c(T_s - T_p)}{\sqrt{\alpha_{eff}(t - \acute{t})}}, \tag{9}$$

where k_c, α_{eff} are the thermal conductivity and the effective thermal diffusivity of the particle core, t is the current time, and $\acute{t}$ is the time at which burning first reached the surface element in question. The conduction heat flux over the entire burning region is then given by:

$$(T_s - T_p) \int_0^r \frac{k_c d\acute{A}_s}{\sqrt{\alpha_{eff}(t - \acute{t})}}, \tag{10}$$

where now $\acute{A}_s$ is the area of the burning region at time $\acute{t}$ and r is the radius at time t.

Combining Eqs. (3),(6)-(8) and (10) we obtain the heat balance equation for the burning region:

$$\begin{aligned} A_i \exp(-E_i/RT_s) C_s A_T \tilde{d} A_s \sigma_a \Delta H \;=\; & \sigma_a \tilde{d} c_p (T_s - T_p) \frac{dA_s}{dt} + \\ \frac{k_{gas}}{r_p}(T_s - T_{gas}) A_s + \sigma(\epsilon_s T_s^4 - \epsilon_w T_w^4) A_s + & \frac{k_c(T_s - T_p)}{\sqrt{\alpha_{eff}}} \int_0^r \frac{d\acute{A}_s}{\sqrt{t - t_{\acute{r}}}}. \end{aligned} \tag{11}$$

In equation (11), the time t for the front to propagate to radius r is given by

$$t = \int_0^r \frac{d\hat{r}}{S(\hat{r})}, \tag{12}$$

where $S(r) = dr/dt$ is the velocity of propagation of the burning region. Similarly $t_{\acute{r}}$ is given by Eq. (12), replacing r in the upper limit of the integral with $\acute{r}$. Thus Eq. (11) is an integro-differential equation in $r(t)$ which must be solved numerically. Once $r(t)$ has been computed, the total time taken by the burning region to cover the hemispherical surface of the particle (visible to the detector) can be found as that value of t for which $r(t) = r_p$. This time, which will be denoted as t_b, should

be the upper bound of the experimentally observed delay time, t_D, that elapses before the peak in the pyrometer signals occurs. For the present calculations the temperature of the burning region was taken equal to the temperature deduced from the pyrometer traces, assumed constant, and the temperature of the rest of the particle was assumed equal to the combustor wall temperature. The total surface area of the layer was deduced from BET area measurements on partially combusted samples, assuming that the burning region had the same average surface per unit mass as that of the char after partial burning. Details of the variation of total surface area with burnout are not included in the present analysis but are given elsewhere[14]. The effective conductivity was estimated using the correlation of Butt[20], while the heat capacity by a relationship given by Kelley[21]. The intrinsic kinetics used were determined for the present chars from other experiments[22] employing the same experimental setup and analyzing the results using the capillary model of Gavalas[23] to describe the evolution of pores. For the PSOC-1451 1600 K char the activation energy, E_i was estimated to be 34000 cal/mole and the pre-exponential factor A_i was 8.6x10^5 cm/s. Smith's kinetics[24] (E_i = 42800 cal/mole and A_i = 1.46x10^6 cm/s) give similar values.

Figure 8 shows the calculated variation of t_b with oxygen partial pressure. The predicted ignition transient times are higher by a factor of almost five compared to those observed experimentally. For the case of the particle shown in Fig. 1, the experimentally observed delay time is 12 ms while the theoretically determined delay time (corresponding to an oxygen partial pressure of 0.12) is around 60 ms. This suggests that there are more than one such spots propagating over the particle surface. As expected, t_b decreases with increasing oxygen partial pressure and with decreasing particle size.

The speed of propagation of the spot increases rapidly as the radius expands, reaches a maximum and falls off as the particle radius is reached. This is shown

in Fig. 9. If several *hot-spots* are growing simultaneously as suggested by the experimental ignition delay times then only the first part of the speed versus radius curve is physically significant. The values assumed for the emissivities of both the particle and the wall had negligible effects in the calculation, indicating the minor importance of the radiation heat loss in the cases examined. Likewise, the apparent particle density does not seem to be an important factor. Finally, t_b is inversely proportional to the pore surface area of the char.

5 Conclusions

The ignition behavior of coal chars at various oxygen partial pressures and combustion chamber temperatures has been observed by means of near-infrared optical pyrometry techniques. It has been concluded that at mild combustion conditions (combustor temperatures around/or below 1300 K and oxygen partial pressures at/or below 0.21), the char particles undergo preferential ignition at localized reactive sites leading to the development of *hot-spots*. The reaction zones take a finite time to engulf and ignite the whole particle. These reactive sites can be due to of mineral matter catalysis, enhanced porosity or favorable surface morphology. At elevated combustor temperatures and/or high O_2 concentrations the ignition proceeds almost instantaneously because of temperature-dependent kinetics. A energy balance was used to estimate the time required for the spreading of a local *hot spot*. Comparision of the estimated times and measured ignition times suggest that several spots are spreading over the particle surface simultaneously.

6 Acknowledgements

This work was supported by the U.S. Department of Energy University Coal Programs Grant Number DE-FG22-84PC70775.

7 References

1. Neavel, R. C.: *Chemistry of Coal Utilization* (M. A. Elliot, Ed.) Wiley-Interscience, New York, 1981.

2. Semenov, N. N.: Chemical Kinetics and Chain Reactions, Clarendon Press, Oxford, 1935; original publication in USSR in 1934.

3. Palmer, K. W.: Dust Explosions and Fires, Chapman and Hall, London, 1973.

4. Essenhigh, R. H.: *Chemistry of Coal Utilization*, 2^{nd} suppl. vol. (M. A. Elliot, Ed.) Wiley, New York, 1981.

5. Hardman, J. S., Lawn, C. J. and Street P. J.: Fuel 62, 632 (1983).

6. Borio, R. W.: ASME Paper No. 74 WA/FU-2 (1974).

7. Howard, J. B. and Essenhigh, R. H.: *Eleventh Symposium (International) on Combustion*, p. 399, The Combustion Institute, 1967.

8. Gomez C. O. and Vastola F. J.: Fuel 64, 558 (1985).

9. Bandyopadhayay S. and Bhaduri D.: Comb. Flame 18, 411 (1972).

10. Thomas, G. R., Stevenson, A. J. and Evans, D. G.: Comb. Flame 21, 133 (1973).

11. Annamalai, K and Durbetaki P.: Comb. Flame 29, 193 (1977).

12. Libby, P. A.: Comb. Flame 38, 285 (1980).

13. Levendis, Y. A. and Flagan, R. C.: Comb. Sci. Tech. 53, p117 (1987).

14. Sahu, R., Levendis, Y. A., Flagan, R.C., and Gavalas, R. G.: Fuel, in print.

15. Altrichter, D. M.: *Optical Determination of Time-Temperature Profiles for Single Coal Particle*, Master's Thesis, MIT, 1981.

16. Timothy, L. D., Sarofim, A. F. and Béer, J. M.: *Nineteenth Symposium (International) on Combustion* p. 1123, The Combustion Institute, 1982.

17. Sarofim, A. F. and Béer. (1986), personal communication.

18. Jenkins, R. G., Nandi, S. P. and Walker, Jr. P. L.: Fuel 52, 288, (1973).

19. Hill, Jr. C. G.: An Introduction to Chemical Engineering Kinetics and Reactor Design, Wiley, New York, p. 447, 1977.

20. Butt, J. B.: A.I.Ch.E.I VII, 106 (1965).

21. Kelley, K. K.: US Bureau of Mines, Bull. 476, 1949.

22. Sahu, R., Northrop, P. S., Flagan, R. C. and Gavalas, R. G.: Presented at AIChE 1987 Annual Meeting, Nov 15-20, 1987.

23. Gavalas, G. R.: Comb. Sci. Tech. 24, 197 (1981).

24. Smith, I. W. Comb. Flame 17, 303 (1971).

8 Notation

SYMBOL	DESCRIPTION	UNITS
A_i	pre exponential factor	g/cm^2s
A_s	surface area of spherical sector	cm^2
A_T	specific total surface area	cm^2/g
c_p	heat capacity of carbon	J/g K
C_s	surface oxygen concentration	g/cm^3
$\tilde{d}$	oxygen diffusion zone	cm
$\acute{d}$	thermal diffusion zone	cm
D_e	effective diffusivity	cm^2/s
e	particle porosity	
E_i/R	reduced activation energy	K
k_p	conductivity of carbon	W/cm K
k_c	effective conductivity	W/cm K
k_{gas}	conductivity of gas	W/cm K
$p_{O_2,s}$	oxygen partial pressure at particle surface	atm
r	radial distance	cm
r_p	particle radius	cm
R_i	intrinsic reaction rate coefficient	cm/s
S	flame front velocity	cm/s
t_b	theoretical flame propagation time	ms
t_D	experimentally observed delay time	ms
T_p	particle temperature	K
T_g	ambient temperature	K
T_s	*hot-spot* temperature	K
T_w	combustor wall temperature	K
α_{eff}	effective thermal diffusivity	cm^2/s

δ	flame front propagation zone	cm
ΔH	heat release	J/g
ϵ_s	emissivity of *hot-spot*	
ϵ_w	emissivity of wall	
σ_a	apparent density	g/cm^3
σ	Stefan-Boltzmann constant	W/cm^2K^4

9 List of Figures

TABLE I: COAL DATA.

COALS	176	1451
RANK	Bit. HVB	Bit. HVA
MOISTURE (%)	0.8	2.5
ASH (%)	6.5	13.5
CARBON (%)	78.4	71.5
HYDROGEN (%)	5.4	4.7
OXYGEN (%)	5.5	7.0
NITROGEN (%)	1.3	1.3
SULFUR (%)	2.9	1.3
VOLATILE MATTER (%)	40.2	33.5
HEATING VALUE (DRY BASIS) cal/g	7910	6965

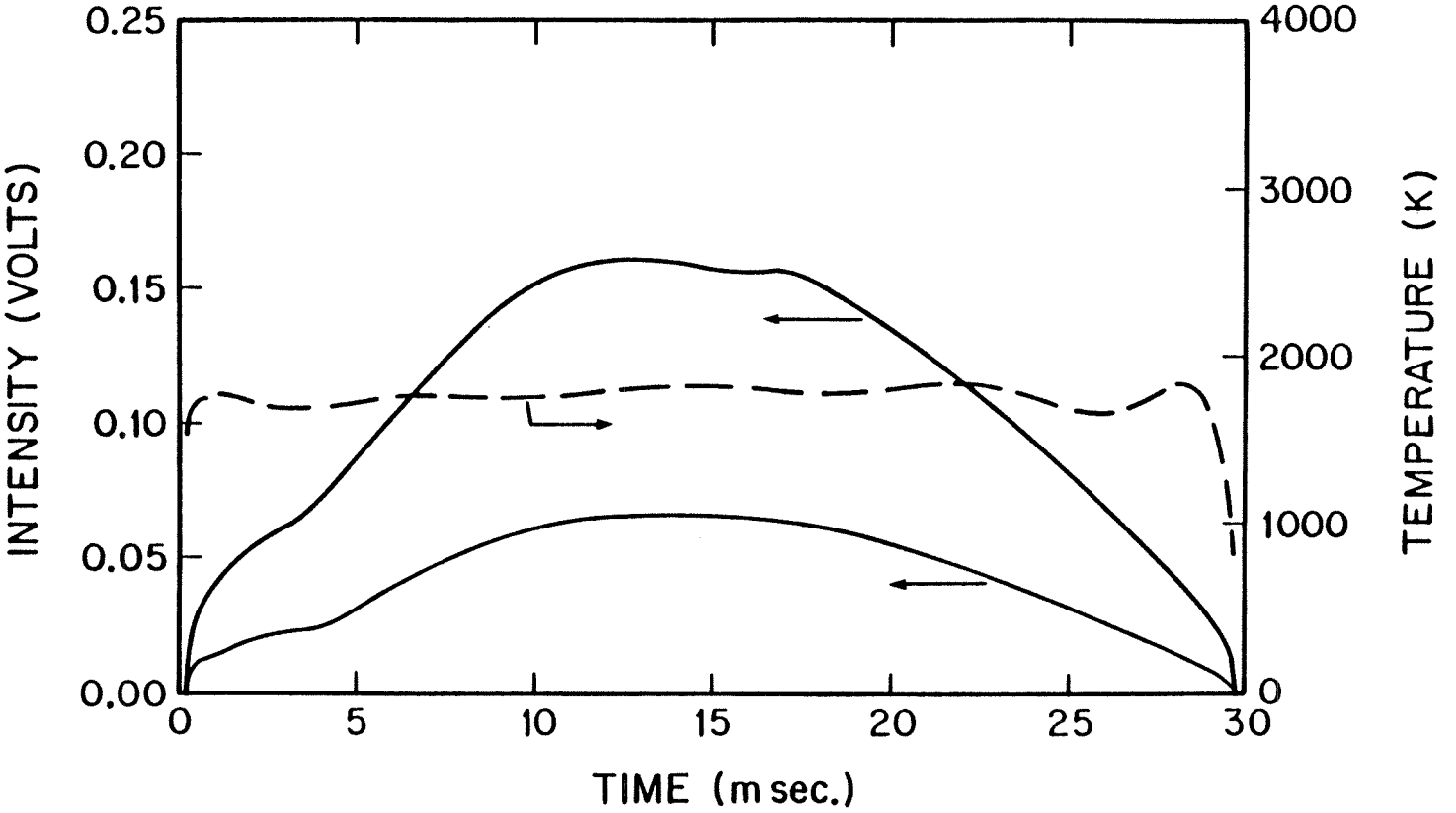

Figure 1: Intensity signals and particle temperature profiles of a PSOC-1451 100μm coal char particle burning at a combustor wall temperature of 1300 K and $p_{O_2} = 0.21$.

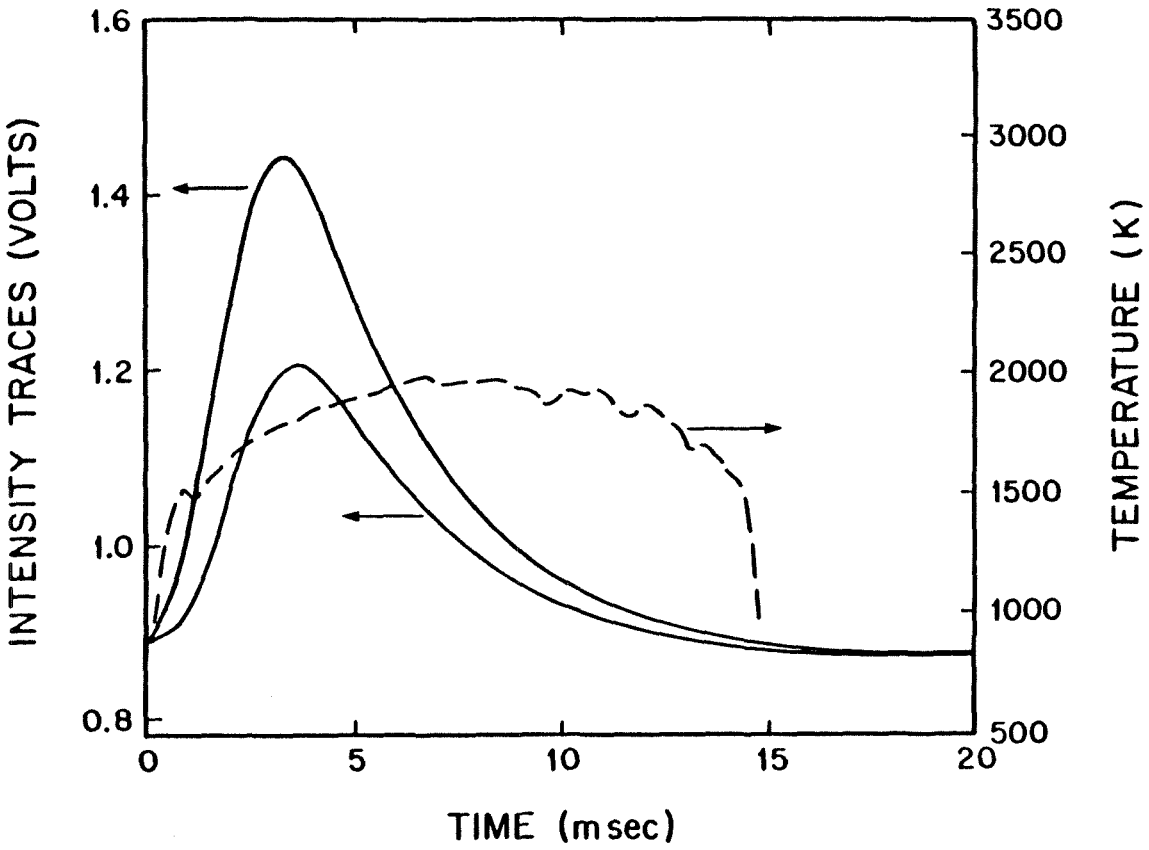

Figure 2: Intensity signals and particle temperature profiles of a PSOC-176 50μm coal char particle burning at a combustor wall temperature of 1300 K and $p_{O_2} = 0.50$.

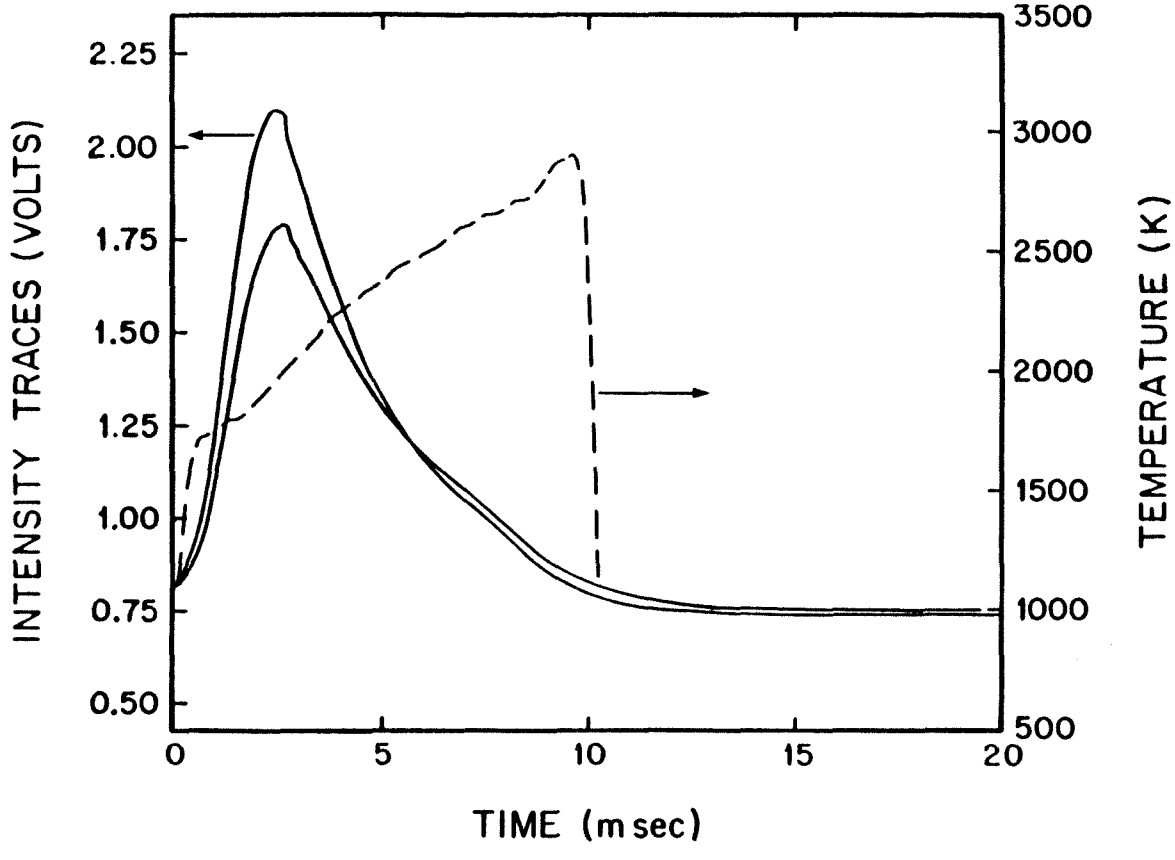

Figure 3: Intensity signals and particle temperature profiles of a PSOC-176 50μm coal char particle burning at a combustor wall temperature of 1300 K and $p_{O_2} = 1.0$.

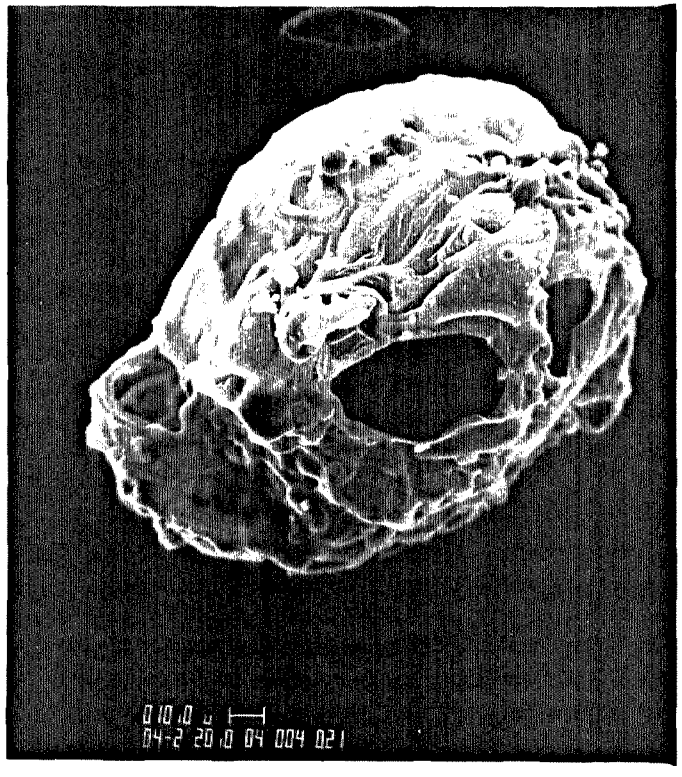

a

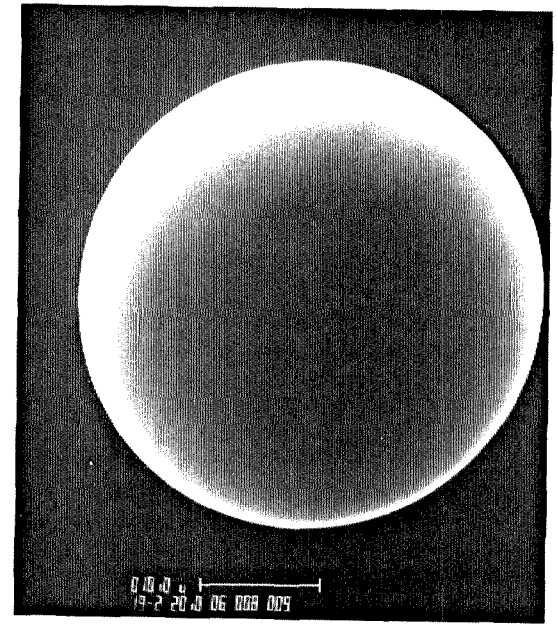

b

Figure 4: *SEM* micrographs depicting (a) a PSOC-1451 particle pyrolyzed at 1600 K. and (b) a glassy carbon particle.

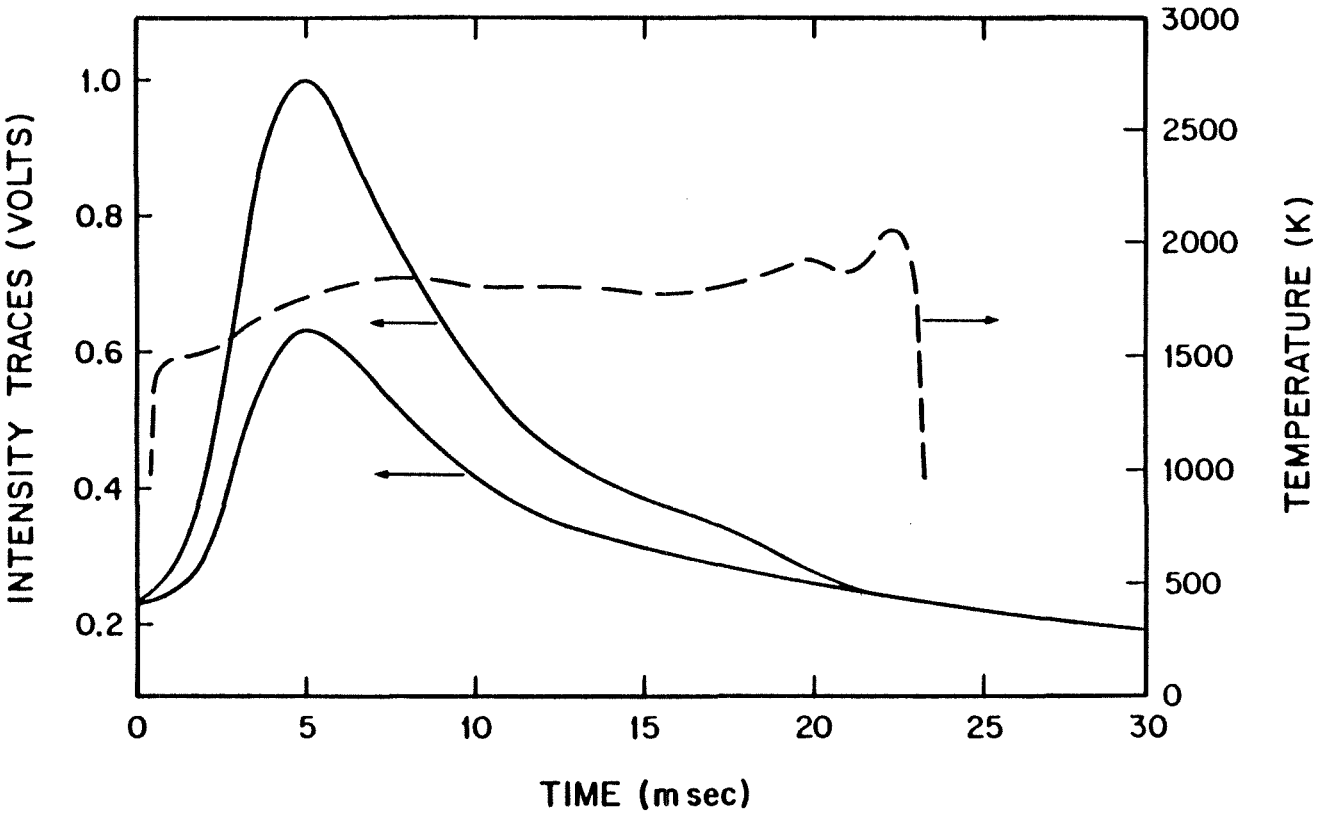

Figure 5: Intensity signals and particle temperature profiles of a 45μm glassy carbon particle burning at a combustor wall temperature of 1500 K and $p_{O_2} = 0.40$.

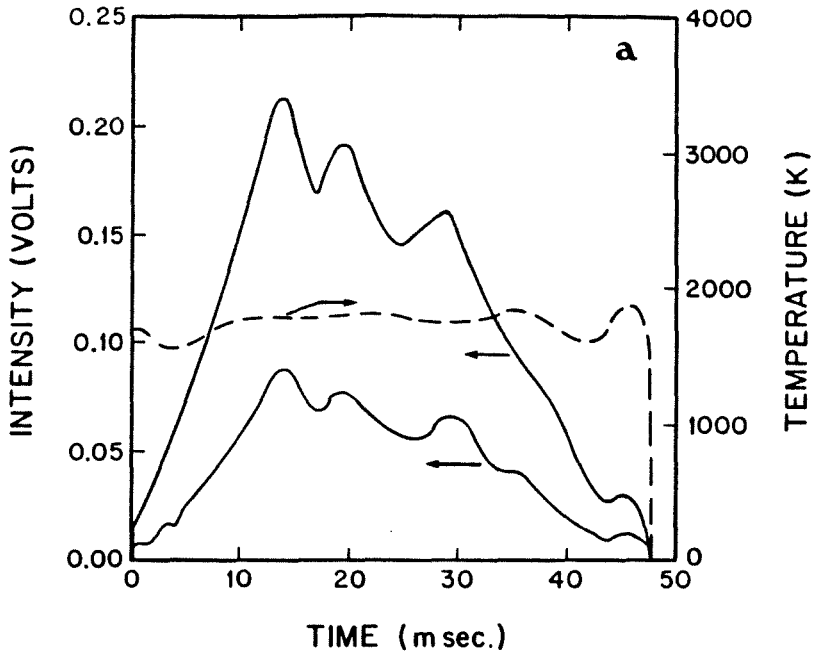

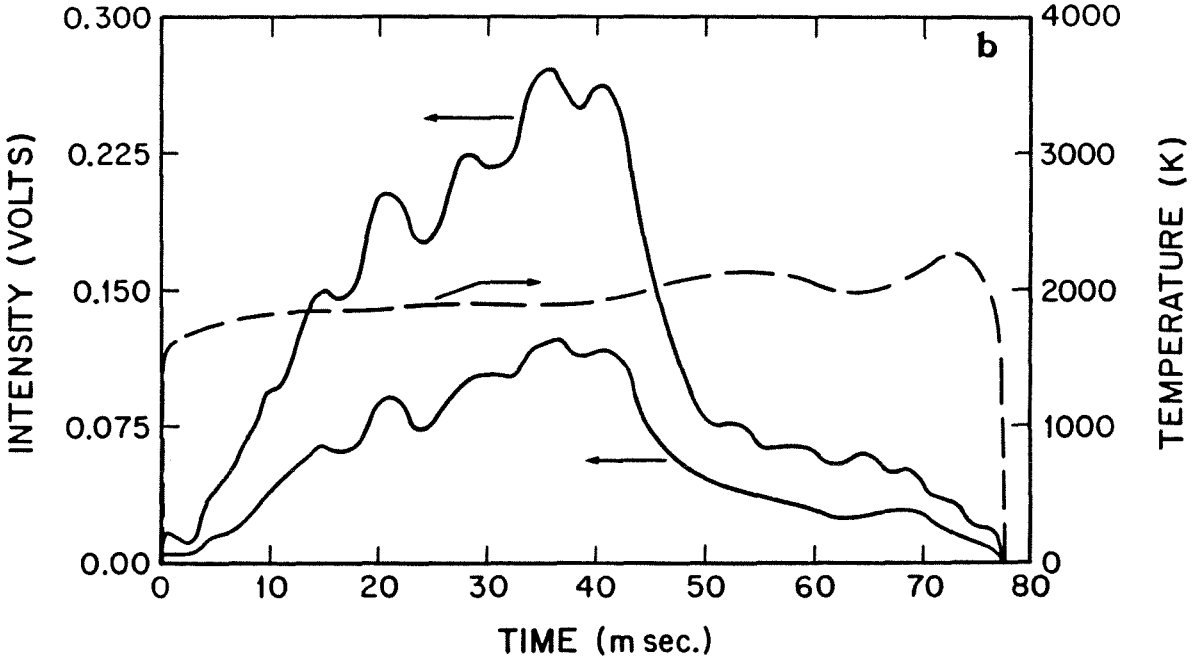

Figure 6: Intensity signals and particle temperature profiles of PSOC-1451 100μm coal char particles burning at a combustor wall temperature of 1300 K and $p_{O_2} = 0.21$. The particles exhibit tumbling behavior.

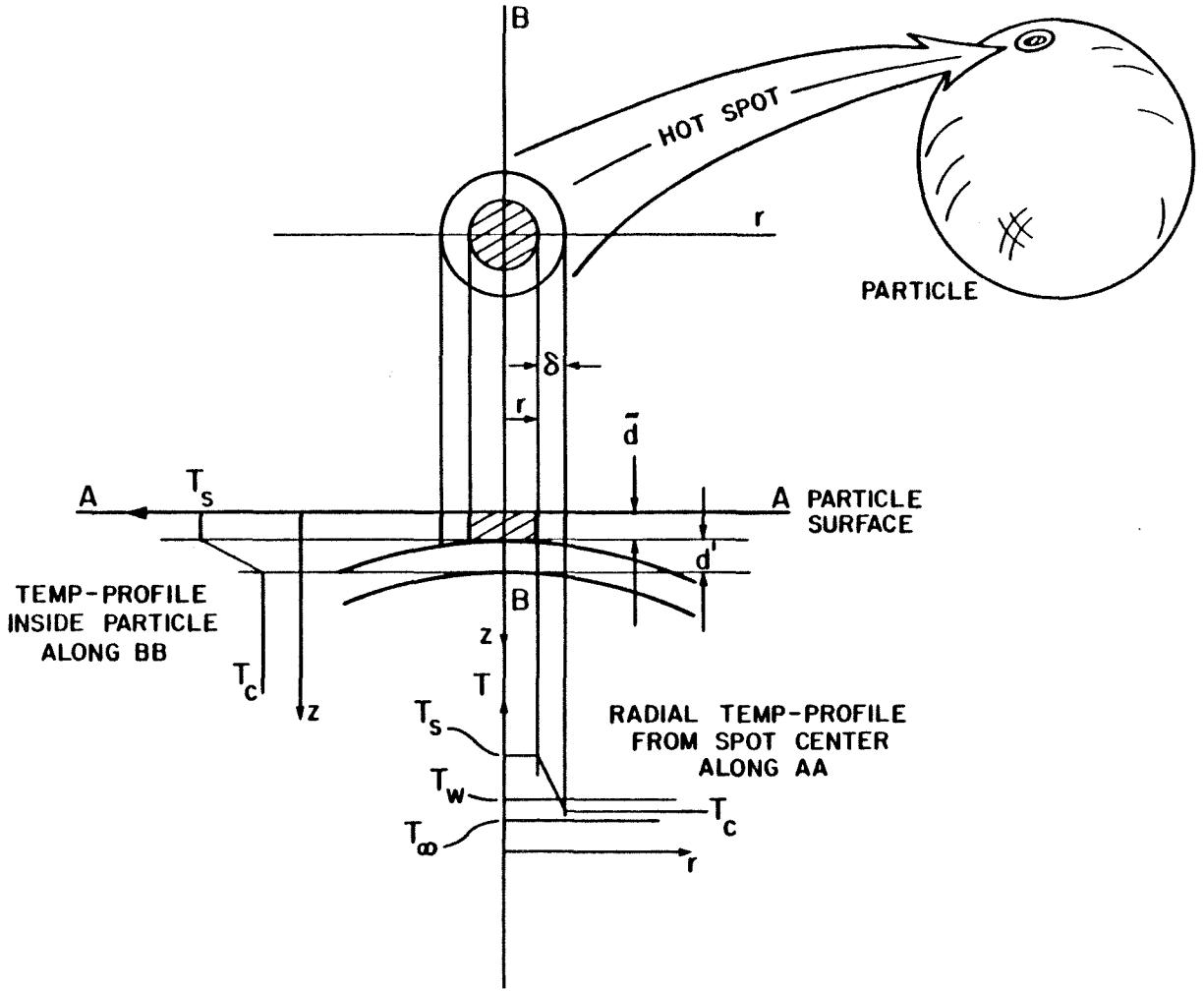

Figure 7: Schematic representation of the *hot-spot* assumed in the model.

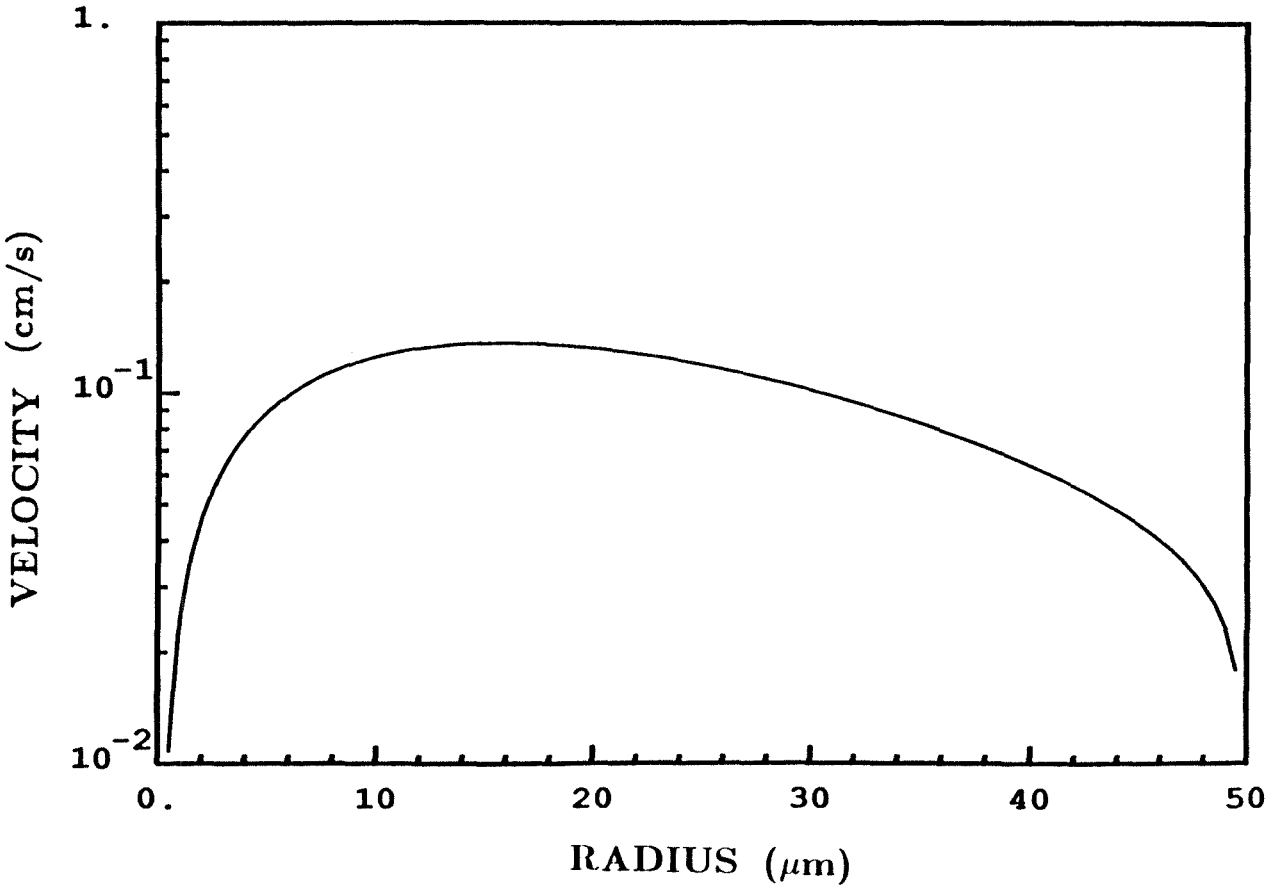

Figure 8: Results of the mathematical modelling: the effect of oxygen partial pressure on the flame spreading delay time t_b.

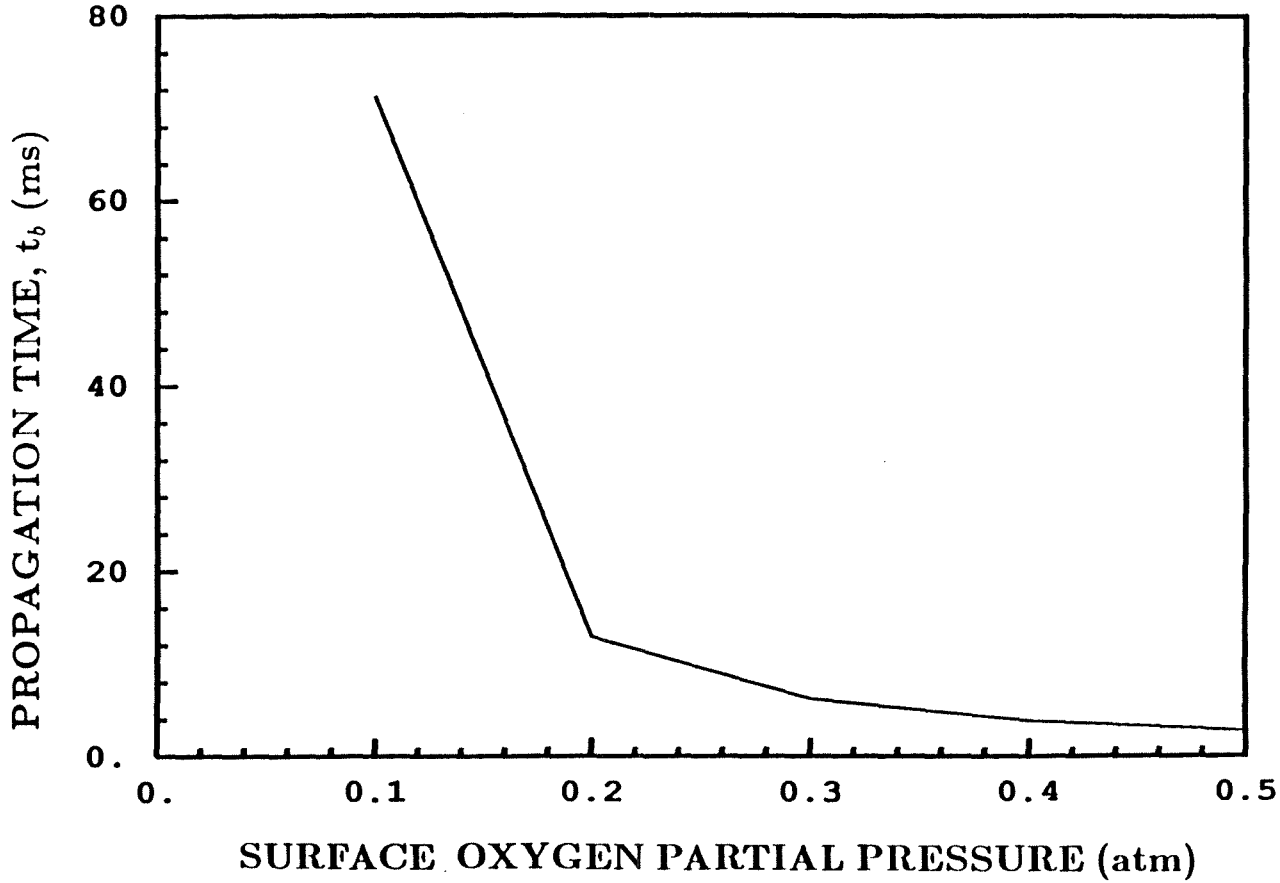

Figure 9: Results of the mathematical modelling: velocity of propagation of the burning region as a function of its radius.

CHAPTER 9

SUMMARY

1 *General Conclusions*

This work represents an effort to understand the factors that influence the reactivity of pulverized fuels. Model particles have been produced and used in combustion studies. The particles were monosized, spherical and, to a high degree, free of impurities. Various sizes of particles having different porosities, pore size distributions and other physical and chemical properties were produced. The ingredients used for synthesizing these chars were a polymer binder, pore-forming agents, a polymerization catalyst as well as a mixing and a dispersion agent. Upon partial polymerization, the mixture was sprayed through an aerosol generator into a thermal reactor, pyrolyzed and subsequently collected as solid spheres of equal size. Further pyrolysis at 800 K produced glassy carbon chars whose aromatic ring chemical structure resembles that of coal chars (as shown from NMR studies). These aromatic rings, in glassy carbons, are randomly cross-linked by carbon-carbon covalent bonds and form tangled ribbonlike molecules. It is clear that the formation of micropores between the ribbons is inevitable in such a structure. It has been indicated from gas sorption and x-ray studies that these micropores are of random and irregular shape and are closed to the outside.

Carbonization to high temperatures (1500 K) induces additional devolatilization accompanied by densification of carbon matrix and pore formation and growth. The shape of the pores becomes less irregular but they still remain closed. The presence of an oxidizer gas during partial combustion experiments causes preferential oxidation and removal of the pore restrictions, resulting in a vast internal surface area of well-connected pores. Surface areas, open to the outside gas penetration of up to 500 m^2/g for the plain polymer chars and up to 800 m^2/g for the materials containing pore formers have been achieved. Furthermore, the function of the pore

formers was to vary the size of the micropores and, for the case of using submicron carbon black spheres as pore formers, to introduce an additional network of transitional pores. Moroever, introduction of specific amounts of tannic acid as a pore former resulted in the formation of cenospheric chars.

The presence of the oxidizer also promoted structural ordering and for the case of various copolymer chars induced formation of graphite and graphitelike phases at the highest temperatures examined (1600 K).

Combustion experiments conducted at various furnace temperatures and oxygen concentrations revealed apparent reaction rates strongly dependent on the particle temperature and on the mode of oxidation (ignition or non-luminous combustion). Experiments in air revealed that the particles were oxidizing slowly at the temperature of the surroundings; meanwhile, at high oxygen concentrations the particles were igniting and burning in a luminous mode. Upon corrections for external and internal (pore) diffusional resistances were made, using either of the models of Smith (1974) or Gavalas (1981); intrinsic reaction rates, expressed per unit total surface area, were derived. It was revealed that the reaction rates of glassy carbons were slower than those observed for many coal chars and pyrolytic graphites. The comparison with coal chars might not be valid since it is uncertain to what degree their complex structures have been characterized successfully. The comparison with graphite indicates the very stable structure of glassy garbons where "loose ends" and active sites are at minimum. Combustion at high particle temperatures (1900 - 2200 K) reveals that all materials tend to comparable reaction rates, which can be explained by structuring and crystallization schemes, as well as by lessening of the importance of catalytic effects of impurities.

At the elevated temperature range (above 2200 K), the reactivity of carbon starts decreasing with temperature, in good agreement with the behavior of pyrolytic graphite. This observation extends the validity of the semi-empirical theory

proposed by Nagle and Strickland-Constable (1961) to the mode of combustion of pulverized fuel particles.

The combustion temperature-time traces obtained for the synthetic chars were used to validate the model of Gavalas (1981) and Loewenberg *et al.* (1987), which was then extended and modified to describe the behavior of cenospheric and ash-containing particles.

Utilizing the experience obtained from the combustion of synthetic chars and employing pyrometry techniques, conclusions were drawn concerning the mode of ignition of coal chars at medium temperatures (below 1300 K). It was proposed that these chars ignite by pre-ignition of "hot-spots" and subsequent spreading of the flame over the entire external surface of the particle.

An additional finding of the present study relates to the importance of the chemical structure of the char on reactivity. The phase, the degree of crystallinity, the atomic structure, the arrangement of molecular layers and the state of purity of carbon are factors of critical importance on the combustion behavior of chars. While physical properties alone are very significant factors, the chemistry and the structural properties of chars should be given appropriate attention. The results of Chapter 2 indicate that similar particles of equal size and shape exhibited widely different combustion behavior in air. Although some particles ignited and burned at temperatures exceeding 2000 K in a few milliseconds, others did not ignite and oxidized slowly, for a few seconds, at 1500 K. While the cause of this particle-to-particle variability is still not known with certainty and can be attributed to both physical and chemical factors, it is interesting to note that the plain polymer chars manufactured and discussed in Chapter 2 were more reactive than the plain polymer chars presented in Chapter 6. Some particles of the first chars ignited and combusted with a luminous flame, in air, at a furnace wall temperature of 1500 K; meanwhile none of the latter chars ignited under the same conditions. Furthermore, even those

that oxidized slowly, in the first case, were shown to be more reactive than those of the second case. This becomes obvious by comparing Figures 9 of Chapter 2 and 10 of Chapter 6, both depicting the intrinsic reactivity of chars. The reactivity varies by a factor of three at the medium to low temperatures. This observation is supported by Fig. 1 of the present chapter, where plain polymer particles of the earlier study (Fig. 1a) are contrasted with plain polymer particles of the more recent study (Fig. 1b) both partially combusted at similar conditions. The two materials were made by different batches of furfuryl alcohol, the first partially polymerized in the bottle (dark), the second, absolutely clear. Close examination of Fig. 1 reveals that the early particles were oxidized to a higher degree and contained craters, pits and tunnels on their surfaces, possible indicators of catalytic action of impurities. X-ray diffraction studies conducted in both samples reveal that the earlier chars exhibited a second highly graphitic phase superimposed on the amorphous matrix (Fig. 2). The generation of the graphitic phase is in accord with the hypothesis of the existence of catalytic impurities since previews investigations, reviewed by Fischbach (1971), have shown that metal or mineral additions can favorably influence the graphitization process. This finding also supports the conclusion drawn earlier, that graphitizing chars are more reactive than glassy carbons. Finally, it should be pointed out that even if the old chars were more reactive than the new chars at temperatures below 1700 K, they exhibited similar reactivities at elevated temperatures, as pointed out earlier.

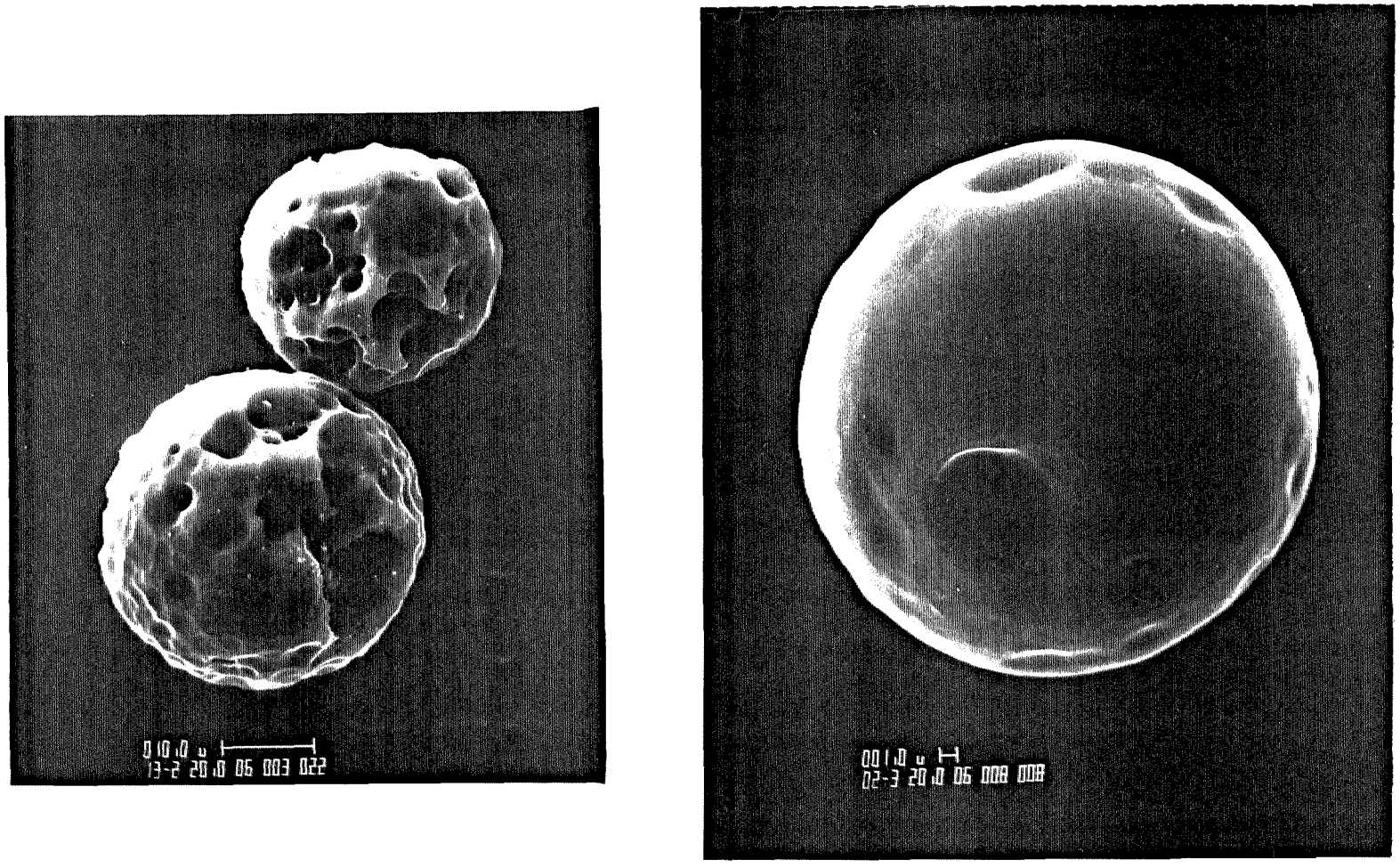

a b

Figure 1: Plain polymer particles partially combusted at 1500 K in air (a) early study (old) and (b) recent study (new).

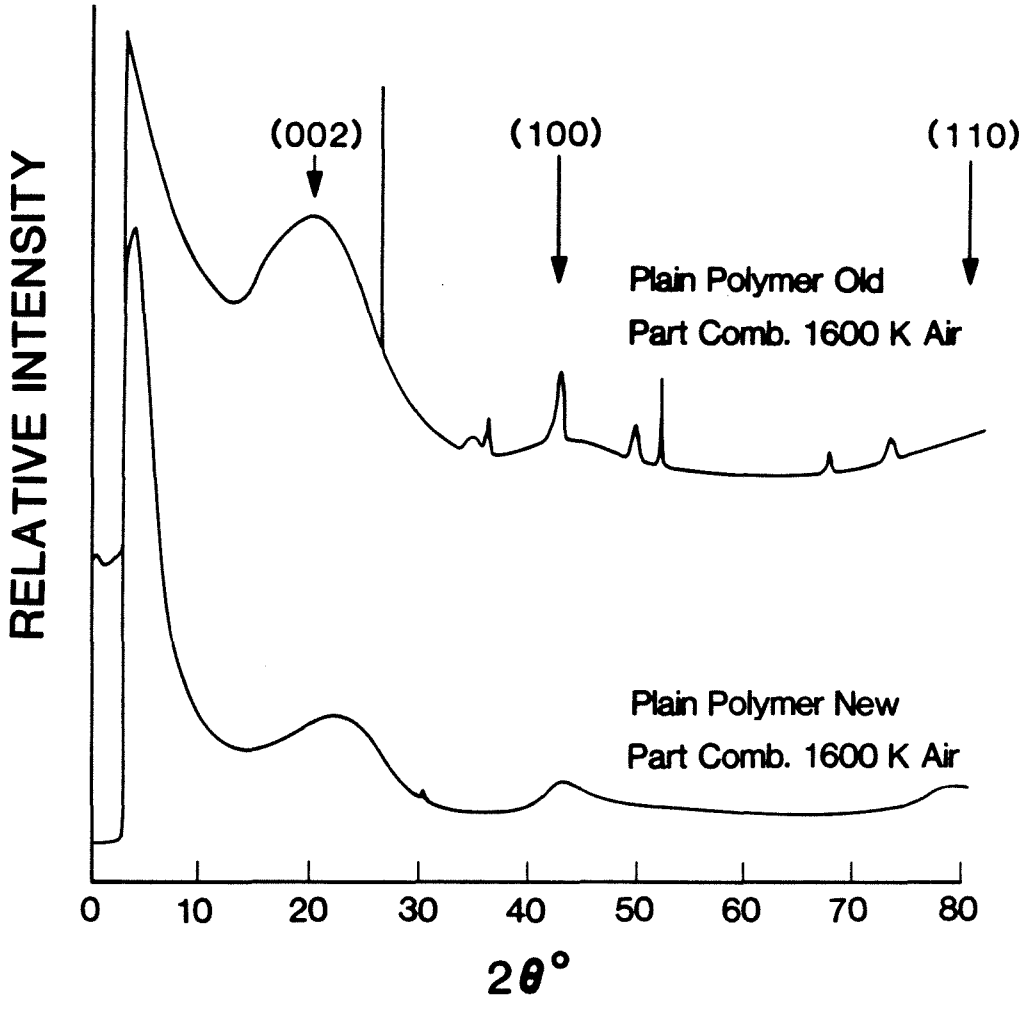

Figure 2: X-ray diffraction spectra of plain polymer particles partially combusted at 1500 K in air (a) early study (old), and (b) recent study (new). CuKα radiation used.

2 *Suggestions for future work*

There is a potential for use and applicability of the synthetic chars in many areas of scientific endeavor. These areas range from studies pertinent to the understanding and modeling of the combustion processes, like the present undertaking, to the development of optimal materials for catalyst supports, to calibration of scientific instruments and so forth. At the present time the synthetic chars are used, impregnated with calcium oxide, in a study aiming to investigate the vaporization mechanism of the oxide at high-temperature combustion. At the same time, the chars are used in an other laboratory to calibrate the temperature environment in a combustion chamber. There is also a large potential for using the synthetic chars to carry on the reactivity studies instigated by this work: to examine the effects and extent of catalysis induced by different minerals, either introduced on an individual basis or as combinations. This way the importance of catalysis at various temperatures can be assessed. The minerals can be either mixed with the binder prior to polymerization or introduced at a later stage. Fig. 3 shows the results of introducing submicron particles of elemental silicon (4% by weight) by mixing them with the monomer prior to particle production. The particle shown has been partially combusted in air at 1500 K. Prior to combustion, no silicon was evident on the particle surface.

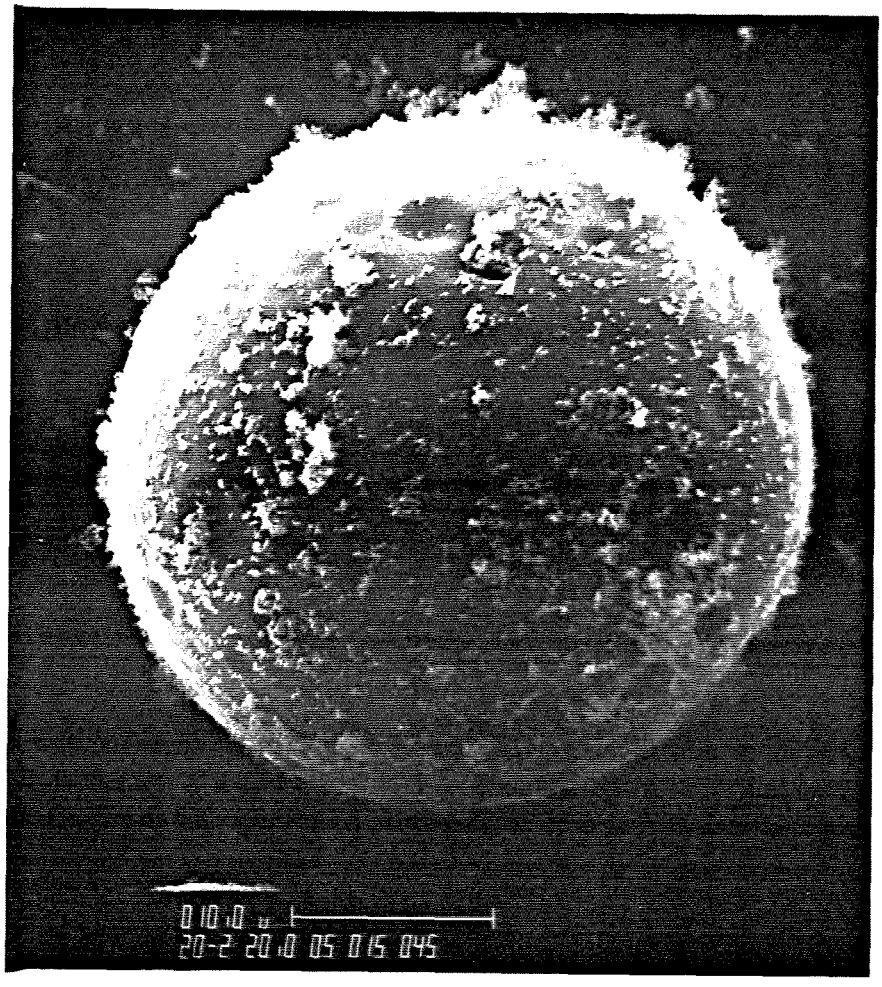

Figure 3: SEM micrograph of a plain polymer particle containing 4% elemental silicon partially combusted at 1500 K in air.

3 *References*

1. Fischbach, D. B. (1971). "The Kinetics and Mechanism of Graphitization" from *Chemistry and Physics of Carbon* **7**, edited by P. L. Walker,Jr., Marcel Dekker, New York, p.1.

2. Gavalas, G. R. (1981). "Analysis of Char Combustion Including the Effect of Pore Enlargement." *Combustion Science and Technology* **24**, 197.

3. Loewenberg, M., Bellan, J. and Gavalas, G. R. (1987). "A Simplified Description of Char Combustion." Submitted for publication.

4. Nagle, J. and Strickland-Constable, R. F. (1961). "Oxidation of Carbon between 1000 - 2000° C." *Proceedings of the Fifth Carbon Conference* **1**, p.154.

5. Smith, I. W. and Tyler, R. J. (1974). "The Reactivity of a Porous Brown Coal Char to Oxygen between 630 and 1812 K," *Combustion Science and Technology* **9**, 87.

CHAPTER 10

Epilogue

This Chapter is reporting on results of work performed mostly after the PhD oral defense.

Effects of the Catalytic Activity of Calcium in the Combustion of Carbonaceous Particles

1 Introduction

A study of the combustion behavior of calcium enriched synthetic chars has been undertaken. The chars used, were derived by pyrolysis of polyfurfuryl alcohol (PFA). The generated char particles were spheres of uniform size (45μm in diameter) and were mineral free. Since many of their physical and chemical properties are similar to those of coal derived chars they can be used as surrogates in studies of coal combustion. These synthetic chars possessed a vast network of micropores ($\approx$ 10Å in diameter). Upon high temperature heat treatment, in conjunction with partial oxidation, the pores enlarged and pore restrictions were removed. The extent and the nature of porosity in these glasslike materials was controlled by mixing certain pore forming agents with the polymer material. The synthetic chars selected for the present study were a plain PFA char containing only micropores and a high porosity (75% PFA - 25% carbon black) char containing both micro- and transitional pores. A HVA bituminous coal was also used for complementary studies. Both the synthetic char and the coal particles were treated with calcium using the following methods: (i) precipitation of $CaCO_3$ within the pores of the chars, (ii) impregnation with calcium acetate solution and (iii) calcium addition by ion exchange. The combustion behavior of the calcium treated chars, in the particle temperature range of 1200-3000 K, has been investigated.

2 Experimental

2.1 *Production of Synthetic Chars.*

The glassy carbon materials used in this study were produced from a carbon yielding binder (polyfurfuryl alcohol) and a thining and mixing agent (acetone). To produce a high porosity char, submicron (ca. 20 nm in diameter) carbon black particles were suspended in the polymer-acetone mixture to serve as pore forming agents. The mixtures were conducted through a syringe pump to an aerosol generator and were subsequently sprayed inside an externally heated thermal reactor. The full description of the atomization system and the thermal reactor is given elsewhere[1]. Following atomization the equal sized droplets were heated to a maximum temperature of 650 K, in an inert atmosphere, and were collected by sedimentation at the bottom of the reactor. The total residence time in the reactor was approximately 4 s. To eliminate sticking of the collected spherical particles all materials underwent a second stage pyrolysis treatment at 800 K in a horizontal muffle furnace in N_2, for 1 hr.

To facilitate distiguishing between the chars produced for the present study the following nomenclature will be used: (a) the plain polymer char will be labeled *low porosity* char, (b) the char containing 25% carbon black filler will be termed *high porosity* char and (c) the PSOC-680 coal will be labeled as such.

To render the pores of the low porosity char accessible to penetration of outside gases, necessary for the calcium treatment processes, the char was partially oxidized in bulk for 10 min, at 800 K, in air. This oxidation process was conducted by spreading the particles in a thin layer inside porcelain boats, to minimize bed diffusion resistance, and heating the boats in a muffle furnace.

2.2 *Calcium Treatment*

2.2.1 *Techniques*

Calcium addition to the synthetic char was achieved by $CaCO_3$ precipitation, acetate impregnation and calcium ion exchange methods.

$CaCO_3$ precipitation was carried out by the following ionic reactions:

$$Ca(CH_3COOH)_2 + H_2O + CO_2 \rightarrow CaCO_3 + 2CH_3COOH \qquad \Delta H^{298} = 3.6 kcal/mole \tag{1}$$

$$2CH_3COOH + Ca(OH)_2 \rightarrow Ca(CH_3COOH)_2 + 2H_2O \qquad \Delta H^{298} = -26.9 kcal/mole \tag{2}$$

A small amount of char or coal was evacuated in a 10 ml reactor vessel at 70°C for 1 day. Carbon dioxide was then introduced into the reactor at room temperature and a pressure of 200 mbar, and allowed to equlibrate with the char for 30 min. A slurry of calcium acetate solution in water and a predetermined amount of calcium hydroxide was introduced into the reactor which had been cooled in an ice bath for 10 min in order to prevent desorption of CO_2 by heat of the exothermic reaction (2). The char and the slurry mixture were stirred with a magnetic stirrer for 30 min. The pH of the mixture dropped from 12.0 to 6.8 indicating that all the $Ca(OH)_2$ had reacted. The char was then filtered, rinsed with distilled water and dried at 80°C for 24 hrs.

Acetate impregnation was implemented using an incipient wetness method. The char was evacuated at 70°C for 1 day. Calcium acetate solution (1 N)was then slowly added to incipient wetness while the sample was stirred vigorously. Since the synthetic char is not readily wetted, the impregnation was done under vacuum. The treated sample was dried at 80°C and the procedure was repeared 3 times. After the third impregnation the sample was washed and dried.

In the calcium ion exchange of char the reactor vessel was a 300 ml beaker

placed in a water bath maintained at 50°C. The char samples were first mixed with 10 ml of distilled water, for 10 min in the reactor, to ensure that they were wetted thoroughly. Subsequently, 100 ml of 1 N calcium acetate solution, the pH of which was adjusted to 8.5 with calcium hydroxide, were added to the reactor. The temperature was kept at 50°C. The reactor was sealed quickly and the slurry was maintained at the initial pH value with continuous addition of 0.01 N $Ca(OH)_2$ solution. A stream of N_2 was used to purge the reactor of air in order to prevent the absorption of atmospheric CO_2 in the solution. At the end of the process the slurry was filtered and washed with distilled water. The treated char was then dried at 80°C for 24 hrs.

2.3 *Characterization of Chars*

2.3.1 *Physical Properties*

The total (internal and external) initial surface area of the chars was measured by means of N_2 adsorption at 77 K and CO_2 adsorption at room temperature. The results were analyzed by applying the BET theory and the Polanyi-Dubinin potential theory, respectively. It was found that the BET area of the low porosity char was 2 m^2/g and after the partial oxidation treatment it increased to ca. 300 m^2/g. The surface area, as measured by Medek's approximation to the Polanyi-Dubinin isotherm came out to be 59 m^2/g and 560 m^2/g after partial oxidation. The above values indicate the presence of a vast network of micropores in this char which is actually very porous and its characterization as "low porosity" is a missnomer and is only used to distinguish it from the other synthetic char in this investigation. The porosity of this char after partial oxidation, as measured from CO_2 adsorption, is 27% which corresponds to a void volume of 0.22 cm^3/g. The porosity deduced from the helium and the apparent density, however, came out to be lower (17%). The apparent density, as measured by low pressure mercury intrusion, is 1.25 m^2/g and

the true density was found to be ca. 1.5 m^2/g using helium pycnometry techniques.

The high porosity char was not subjected to any partial oxidation treatment since its initial porosity was considered adequate for the calcium treatment processes. Its initial surface area was found to be 184 m^2/g the apparent density was 0.6 m^2/g, the true density 1.45 m^2/g and the porosity 0.60.

2.3.2 *Calcium Distribution*

The effectiveness of the calcium treatment method was assessed by using both electron microprobe-WDS and scanning electron microscope SEM-EDS techniques. The samples were cast in epoxy and polished in a *Buehler Minimet* automatic polisher. They were subsequently gold-spattered and sections through the center of particles (max. diameter) were examined at predetermined intervals along the diameter employing a *CamScan* SEM using either the back scattered electron beam or the electron dispersive spectroscopy (EDS) capabilities of the instrument. To detect the lower concentrations of calcium compounds existing in the interior of the particles a *Jeol Superprobe 733* electron microprobe with wavelength dispersive spectroscopy (WDS) capabilities was used. The two methods were in very good agreement at the regions where they overlapped. Figure 1 shows the amount of Ca, in CaO equivalents, as a function of the distance from the surface of the particle towards the center (which is located $\approx 25\mu m$ from the surface). These profiles are averaged for three particles in each case. The variability in calcium distribution between particle to particle was rather insignificant, indicative of both the uniformity of the particles and the repeatability of the process. It can be noticed that the calcium oxide distribution is very different in the high and the low porosity chars. In the high porosity chars, that contain both transitional- and micropores, the calcium compounds can penetrate effectively to the interior of the particles resulting in a rather uniform radial distribution. In the low porosity chars, that contain only

micropores, the penetration is not very effective and the concentration of calcium is high close to the surface and very low at the center. A comparison of the various methods indicates that for the low porosity chars the ion exchange method is the most effective; the calcium concentration is rather constant in an outside layer of 5μm, it then drops rapidly in the next 5μm by two orders of magnitude and becomes again flat all the way to the center. The calcium carbonate precipitation method differs inasmuch as (a) the resulting concentration is lower everywhere and (b) the concentration is constant only for 1-2μm below the surface, it then drops continously for about 9μm and finally assumes a constant value towards the center. The calcium acetate impregnation method resulted in a distribution similar to the $CaCO_3$ precipitation method, the difference being that the latter penetrated more effectively the region below the surface of the particle but more poorly the region close to the center.

The effectiveness of the calcium treatment as a function of the char porosity reveals that:

- In the $CaCO_3$ precipitation method the total amount of calcium deposited in the high and low porosity particles is approximately the same, the difference being in the radial distribution profile only.

- In the case of the ion exchange method, however, it can be calculated that the overall concentration of calcium in the low porosity particle is much higher than the concentration in the high porosity particle. A plausible explanation for this event, suggested by the findings of Freund and Lyon[2], might be that the ion exchange capacity of the low porosity char might have been enhanced by the the air oxidation pretreatment which this char was given prior to calcium treatment.

SEM-BSE (Back Scattered Electrons) micrographs of sections through calcium treated glassy carbon particles are shown in Fig. 2 revealing the compositional

changes in the material. Here one of the most important contrast features of BSE is utilized, i.e. the dependence of the electron backscattering coefficient on the mean atomic number $\bar{Z}$ which allows phases with differences in $\bar{Z}$ to be recognized. Examination of Fig. 2 reveals, qualitatively, the same features regarding the radial distribution of calcium as the microprobe analysis above. The bright color in the periphery of the particles is caused by the presence of calcium. The particle depicted in Fig. 2a is calcium ion exchanged, while the particle of Fig. 2b contains precipitated $CaCO_3$. It can be observed that the calcium concentration is constant over a thick layer in case (2a) but it is continously decreasing in case (2b). Figures 3a and b depict high porosity particles that have been treated by ion exchange and $CaCO_3$ precipitation respectively. The presence of calcium cannot be detected since its concentration is at levels below the resolution of the instrument.

Information about the nature of the distribution of calcium in the particles can also be obtained by burning the particles to completion and examining the ash residue. Ashing experiments were performed in air at 800 K. Optical microscope and SEM observations of the ash, revealed features that are in good agreement with the findings described before. The ash residue from the combustion of low porosity $CaCO_3$ precipitated particles consists of thin bubble-like shells while the residue of the ion exchanged low porosity particles has the form of thick rough shells. The latter are depicted in Fig. 4. Combustion of high porosity synthetic chars results in irregularly shaped small size ash residues reminiscent of coal ash.

2.4 *Combustion Experiments*

Combustion experiments were conducted in an externally heated, laminar flow furnace. Particle temperatures were measured by means of near-infrared two color pyrometry. The combustion apparatus and the pyrometer are described in[3]. All present experiments were conducted at a constant combustor wall temperature of 1470 K and at two O_2 partial pressures: 0.21 (air) and 1.0 (pure oxygen). The pyrometric observations were conducted in such a way that the whole temperature-time history of a single burning particle was observed. The obtained profiles are shown in Figures 4-9.

In Fig. 5a superimposed temperature-time traces of several single high-porosity particles burning in O_2 are shown. The average maximum temperature appears to be around 2600 K and the burnout time 14 ms. The combustion behavior of same size particles that have been treated by calcium ion exchange is shown in Fig. 5b. The profiles appear to be rather flat exhibiting maximum temperatures of about 2900 K and burnout times of 11.5 ms. The traces shown in Fig. 5c correspond to high porosity particles precipitated with $CaCO_3$. Again the profiles are rather flat, the average maximum temperatures are around 2800 K the the average burnout times 12 ms. Therefore, it can be seen that the calcium treatment causes the particles to burn faster and at higher temperatures. This is true for both kinds of treatment, i.e. ion exchange and precipitation since particles treated with both methods exhibited very similar combustion behavior.

In Fig. 6a and 6b the combustion history of high porosity particles burning in air is depicted. The behavior of particles treated by either ion exchanged calcium or precipitation is similar. The particles burn (or the flame extinguishes) within 25 to 30 ms and the average temperatures are in the vicinity of 2000 K. This combustion behavior is strikingly different from the behavior of plain PFA char (no calcium) particles. Under identical conditions the latter particles burned slowly in a non-

luminous mode at temperatures close to the combustion chamber wall temperature, for a total time of 2 sec.

Combustion of low porosity particles reveals similar features to the combustion of high porosity particles. Burnout times are shorter and temperatures are higher in the presence of calcium. Figure 7 depicts combustion of low porosity particles in O_2. The untreated particles burn at an average temperature of 2200 K and a burnout time of approximately 22 ms (Fig. 7a). Upon introduction of calcium the particles burned faster, $\approx$12.5 ms, and hotter, $\approx$2500 K (Fig. 7b and c). The combustion behavior of particles containing calcium seemed to be independent of the method of calcium treatment. Combustion in air, however, revealed large differences in the manner in which the particles burned. The untreated char particles did not ignite and burned slowly at temperatures between the gas and the wall and by the end of the 2 sec residence time in the combustion chamber they acheived 60% conversion[4]. On the contrary, all particles that had been calcium treated by acetate impregnation ignited and burned in an average of 30 ms at a temperature of 1900-2000 K (Fig. 8a). Particles that were ion exchanged or precipitated exhibited considerable variability in ignition; others ignited and burned in $\approx$25 ms and $\approx$1900 K (Fig. 8b), while others burned slowly at a lower temperature. This behavior signifies that the particles so treated were at the verge of ignition and had the oxygen concentration been a little higher they would all have ignited[4].

A few combustion experiments were conducted using the PSOC-680 coal. These experiments were excecuted in air and the combustion behavior of the untreated coal is contrasted to the behavior of $CaCO_3$ precipitated coal in Fig. 9 a and b. Examination of Fig. 9a reveals that the untreated coal particles readily ignited in air because of their enhanced reactivity caused, possibly, by their content of volatiles, heteroatoms and minerals, as well as the existence of macropores. The burnout times were in the vicinity of 35 ms and the average temperatures around 2000 K.

The particle temperatures were fairly uniform from particle to particle (all but one trace) although the burnout time changed somewhat. At the very beginning of the combustion history of the particles a distinct temperature peak lasting only 1-2 ms was observed, most probably caused by the combustion of evolving volatiles. Introduction of $CaCO_3$, by precipitation, accelerated the combustion and the resulting burnout times were $\approx$ 15 ms (Fig. 9b). The particle temperatures exhibited large scatter but on the average the temperatures were similar to those of the untreated particles.

Combustion experiments at lower particle temperatures were also conducted in the same drop tube furnace, by lowering the oxygen partial pressure. At P_{O_2} lower than $\approx$7% and at a combustor wall temperature range of 1200-1500 K the particles did not ignite, but rather burned slowly at approximately the wall temperature. Observed combustion rates were deduced from particle size reduction and/or sample mass and density change. It became evident, again, that the calcium laden chars were by far the most reactive. As an example, at T_W = 1250 K and T_{gas} = 1225 K at P_{O_2} = 0.04, and residence time t = 2 s, 50μm PFA particles exhibited 22% burnout meanwile calcium ion exchanged PFA particles exhibited 85% burnout. Under the same conditions the $CaCO_3$ precipitated particles underwent 68% burnout.

3 Conclusions

Monodisperse synthetic char and coal particles have been treated with calcium using the following methods: (i) precipitation of CaO_3 within the pores of the chars, (ii) imregnation with calcium acetate solution and (iii) calcium addition by ion exchange. The distribution of calcium inside low porosity synthetic chars was high in the vicinity of the surface and low at the center. A steep fall in concentration occurs at 2 to 6 μm depth below the surface depending on the method of calcium treatment; the ion exchange method produces the deeper penetration. The calcium concentration in the high porosity chars was rather uniform throughout the particles with the precipitation method resulting in the highest concentration. Combustion experiments revealed that the presence of calcium enhances the particle temperature and reduces the burnout time. The difference in combustion rates was more pronounced in air rather than in pure oxygen. All methods of calcium introduction enhanced the combustion rate but the calcium acetate impregnated particles appeared to be the most reactive in the examined temperature region (1200 - 3000 K).

4 References

1. Levendis, Y. A. and Flagan, R. C. (1987) "Synthesis, Formation and Characterization of Glassy Carbon Spheres of Various Properties" Submitted to *Carbon.*

2. Freund, H and Lyon, R. K. (1982) *Combustion and Flame* **45**, 191.

3. Levendis, Y. A. and Flagan, R. C. (1987) "Combustion of Uniformly Sized Glassy Carbon Particles" *Combustion Science and Technology* **53**, 117.

4. Levendis, Y. A., Flagan, R. C. and Gavalas G. R. (1987) "Oxidation Kinetics of Monodisperse Spherical Carbonaceous Particles of Various Properties" In preparation.

TABLE I

Physical Properties of Synthetic Chars before Calcium Treatment

CHAR	Low Porosity plain polymer	High Porosity polymer + 25% carbon black
Apparent Density (g/cm^3)	1.25	0.6
Helium Density (g/cm^3)	1.5	1.45
Porosity	17%	59%
Average Pore Size	$\approx$ 10Å	150Å and 10Å bimodal
BET area (m^2/g)	300	184
CO_2 area at 298 K (m^2/g)	560	-

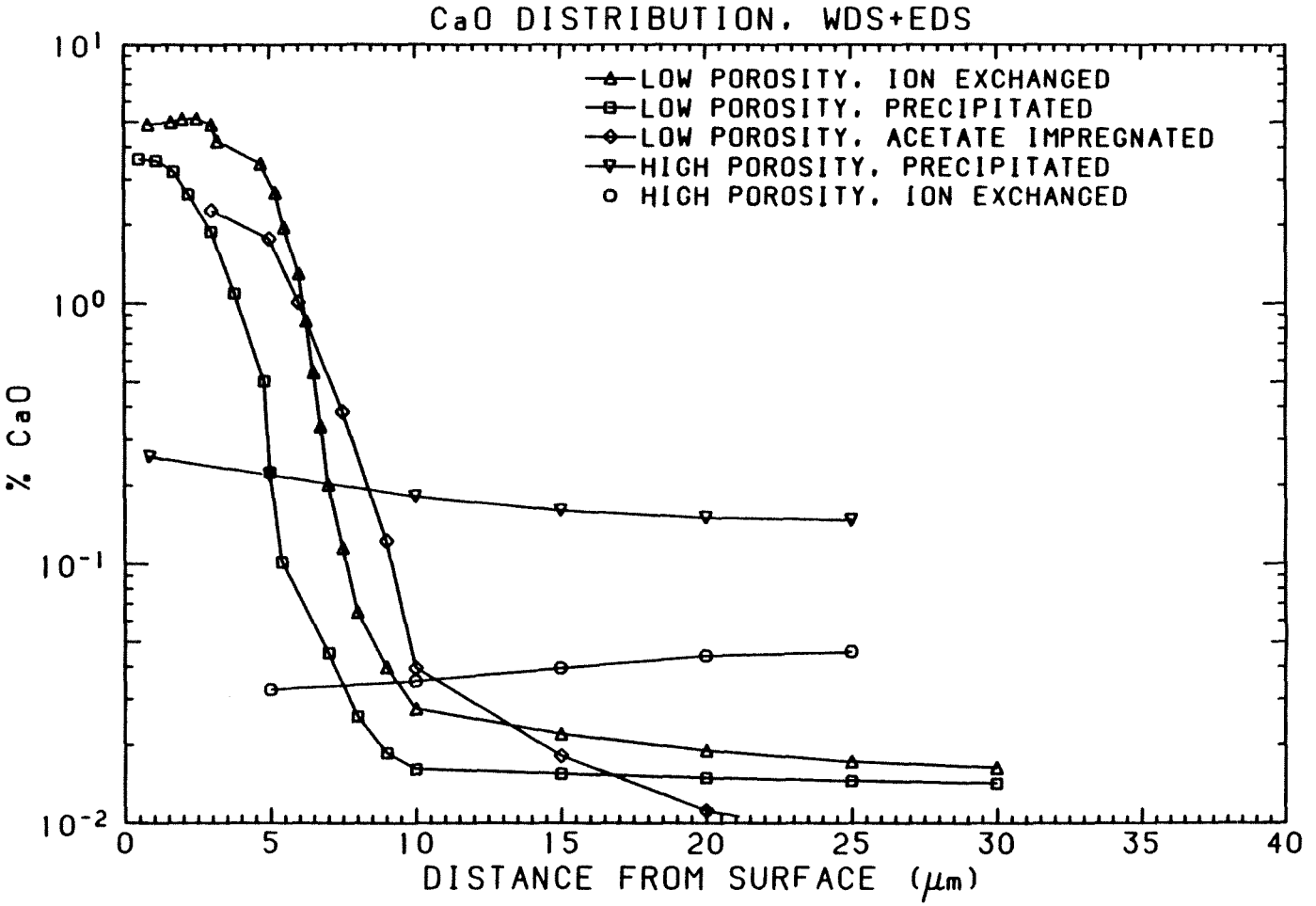

Figure 1: Distribution of calcium in CaO equivalents along the radius of calcium treated synthetic chars

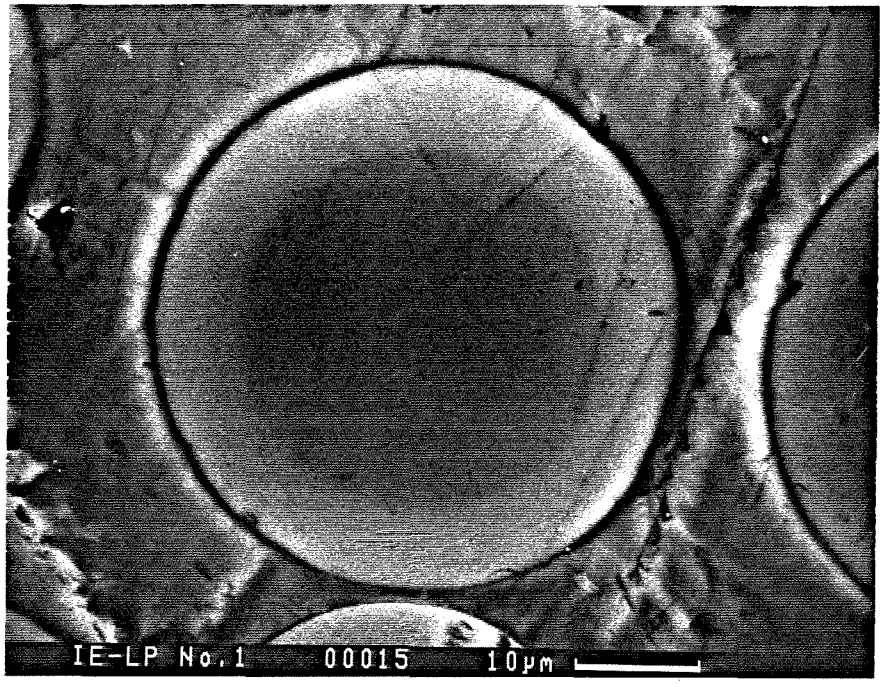

a

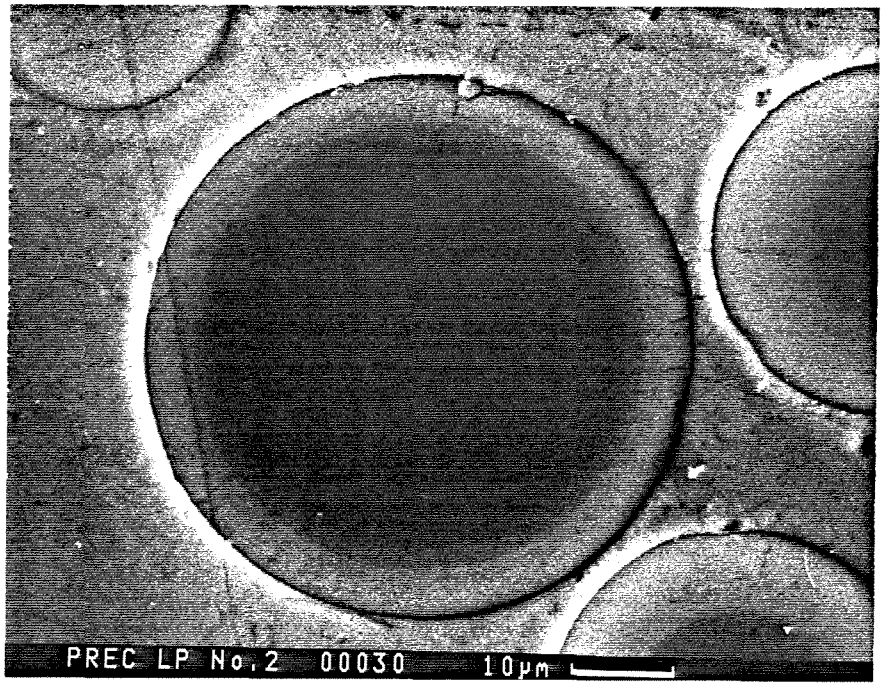

b

Figure 2: SEM-BSE micrographs of sections through calcium treated synthetic char particles (a) low porosity ion exchanged (b) low porosity $CaCO_3$ precipitated

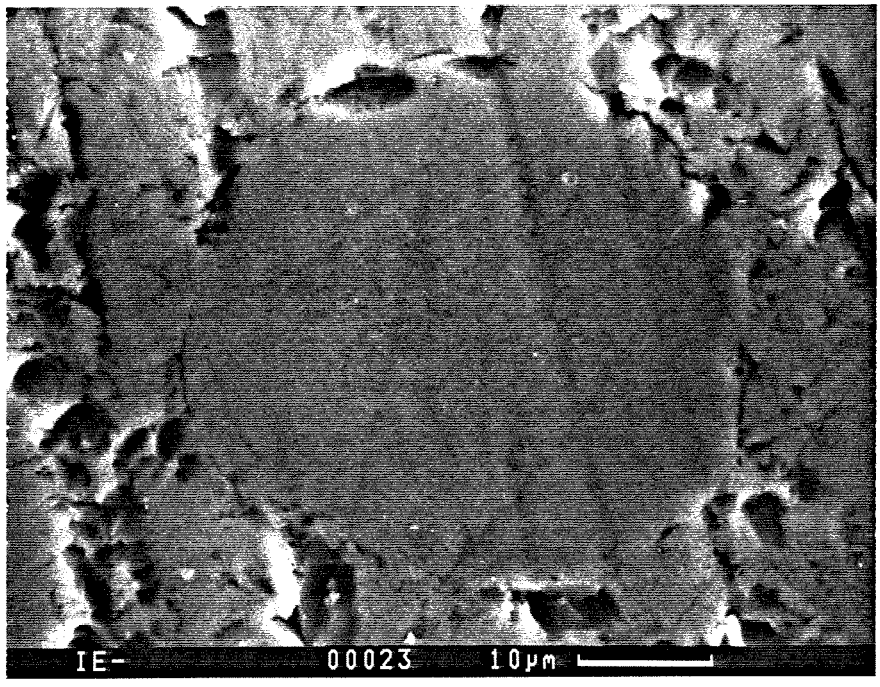

a

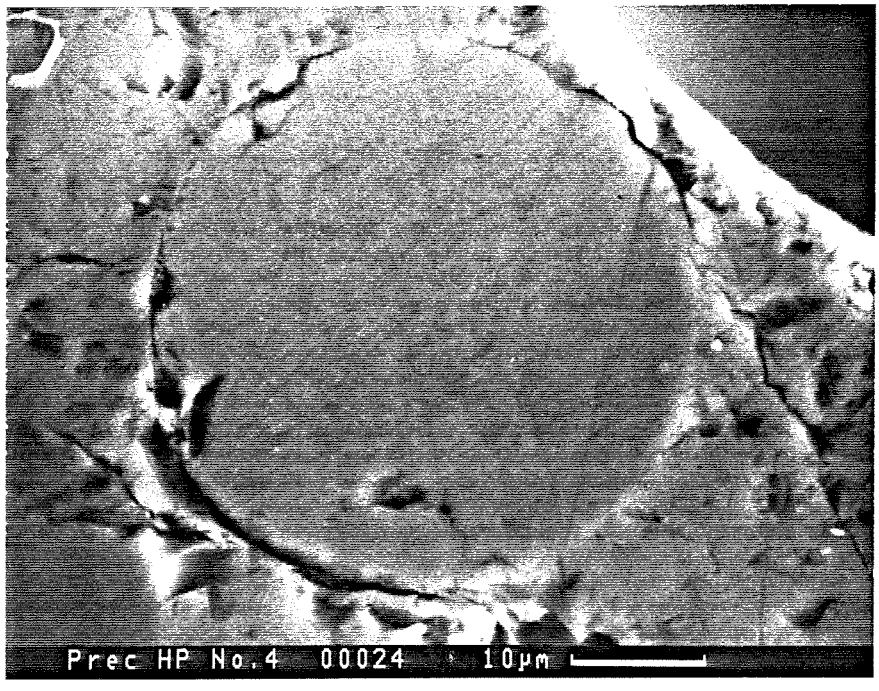

b

Figure 3: (a) high porosity ion exchanged (b) high porosity $CaCO_3$ precipitated.

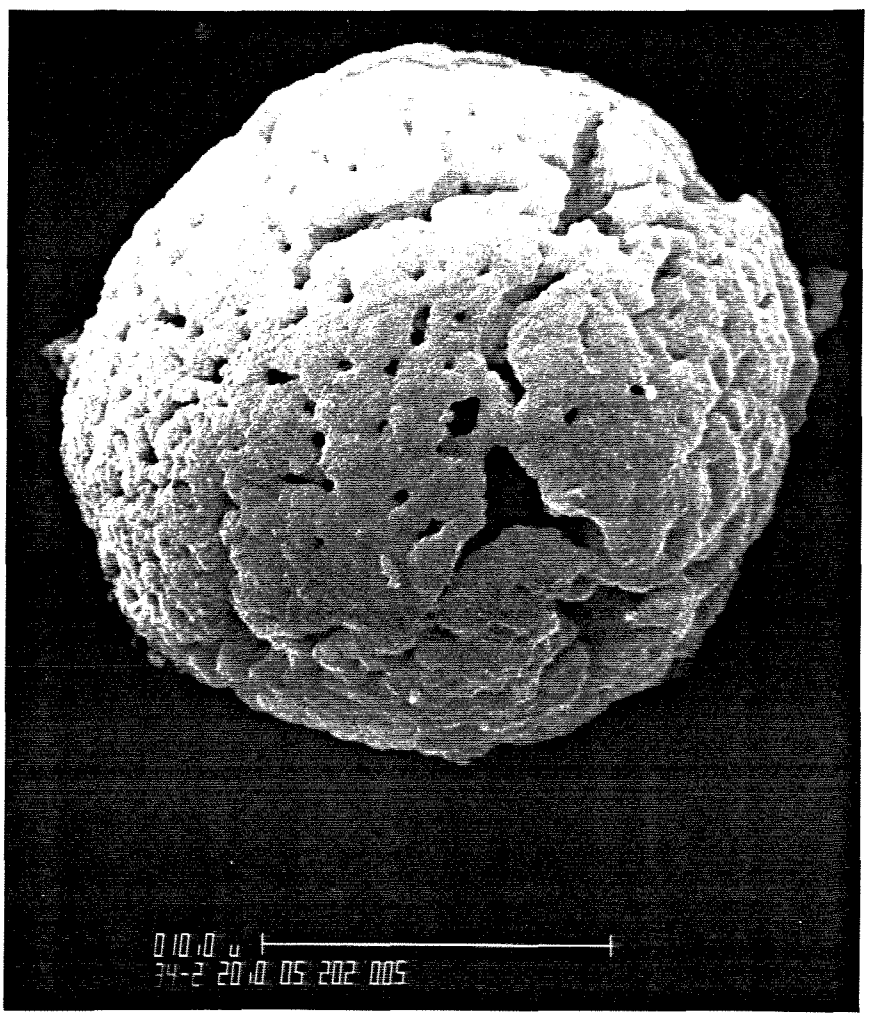

a

Figure 4: SEM-SE micrographs of residual ash after complete combustion of low porosity synthetic char particles in air at 800 K. The particles were treated with ion exchanged calcium: (a) outside view (b) inside view.

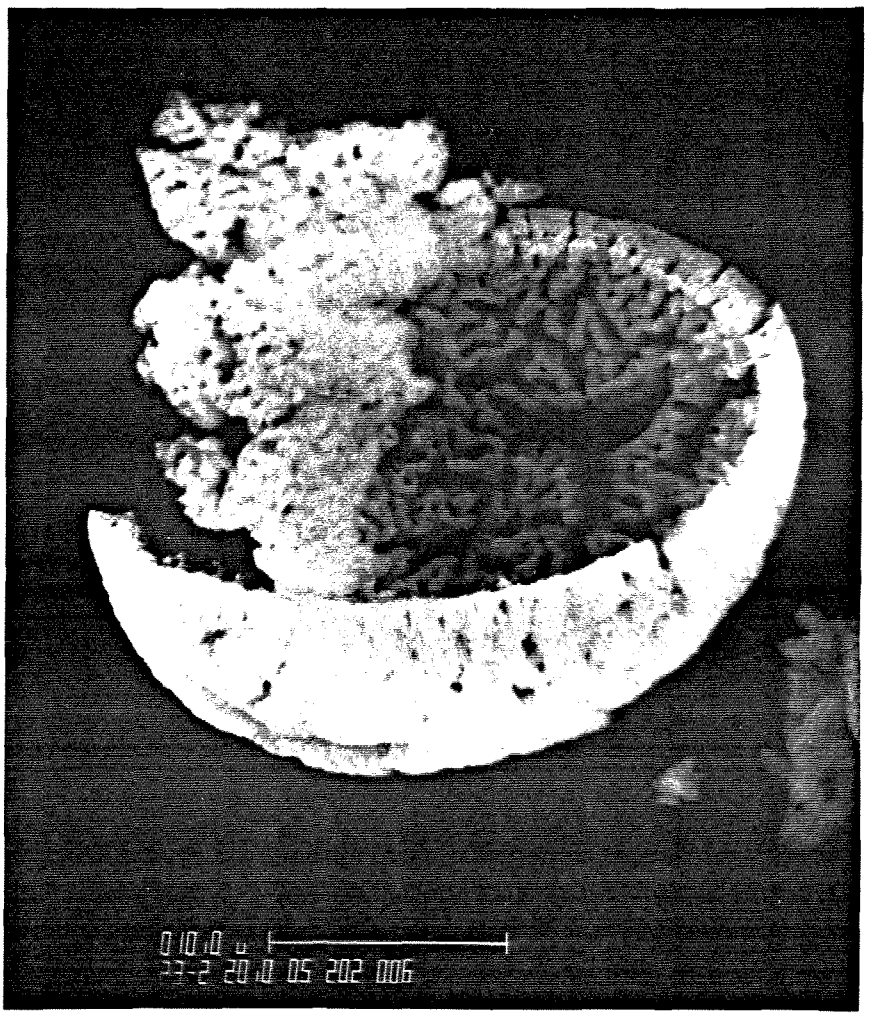

b

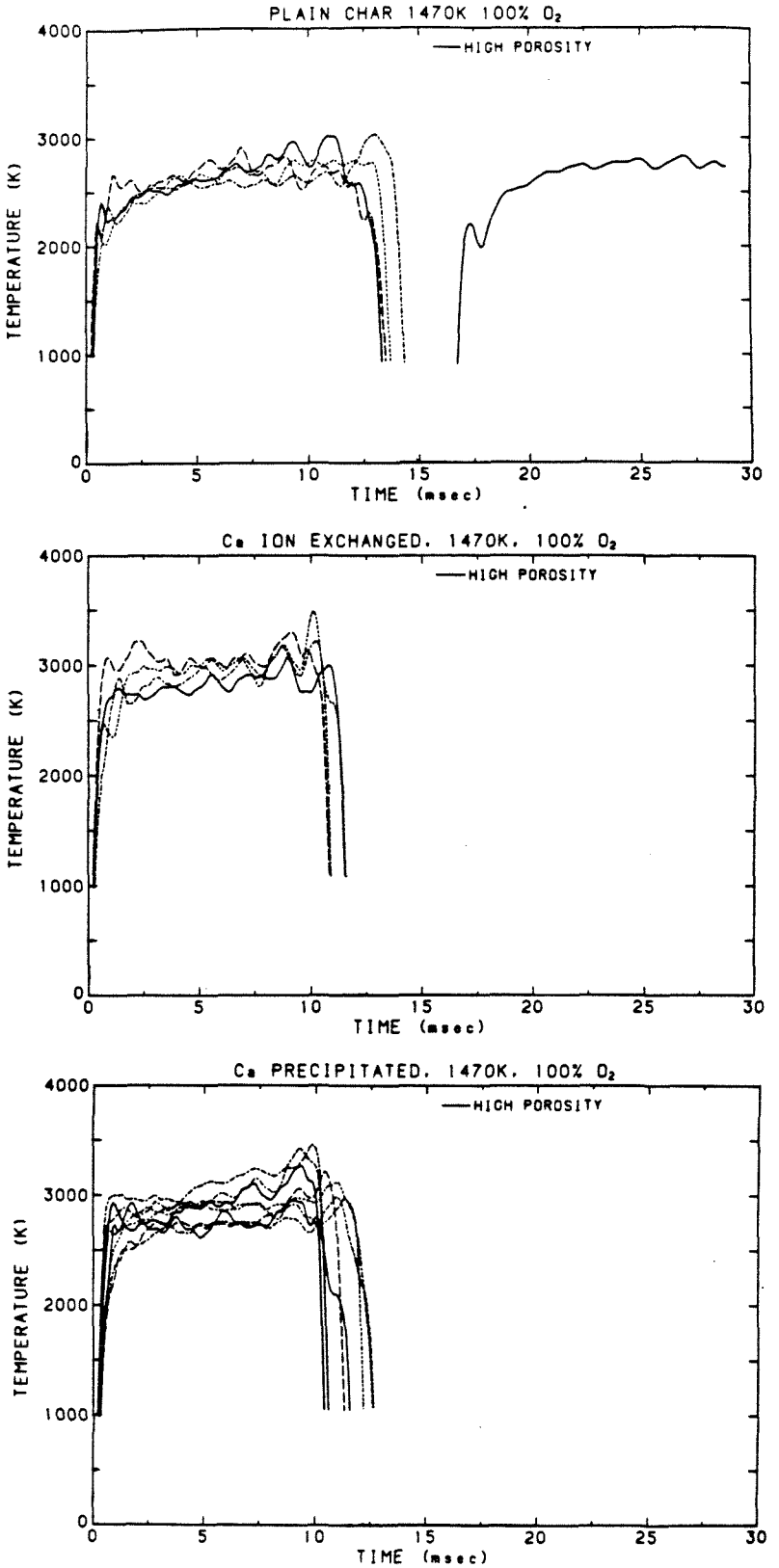

Figure 5: Temperature-time profiles of high porosity particles burning in O_2: (a) plain char, (b) ion exchanged, (c) $CaCO_3$ precipitated.

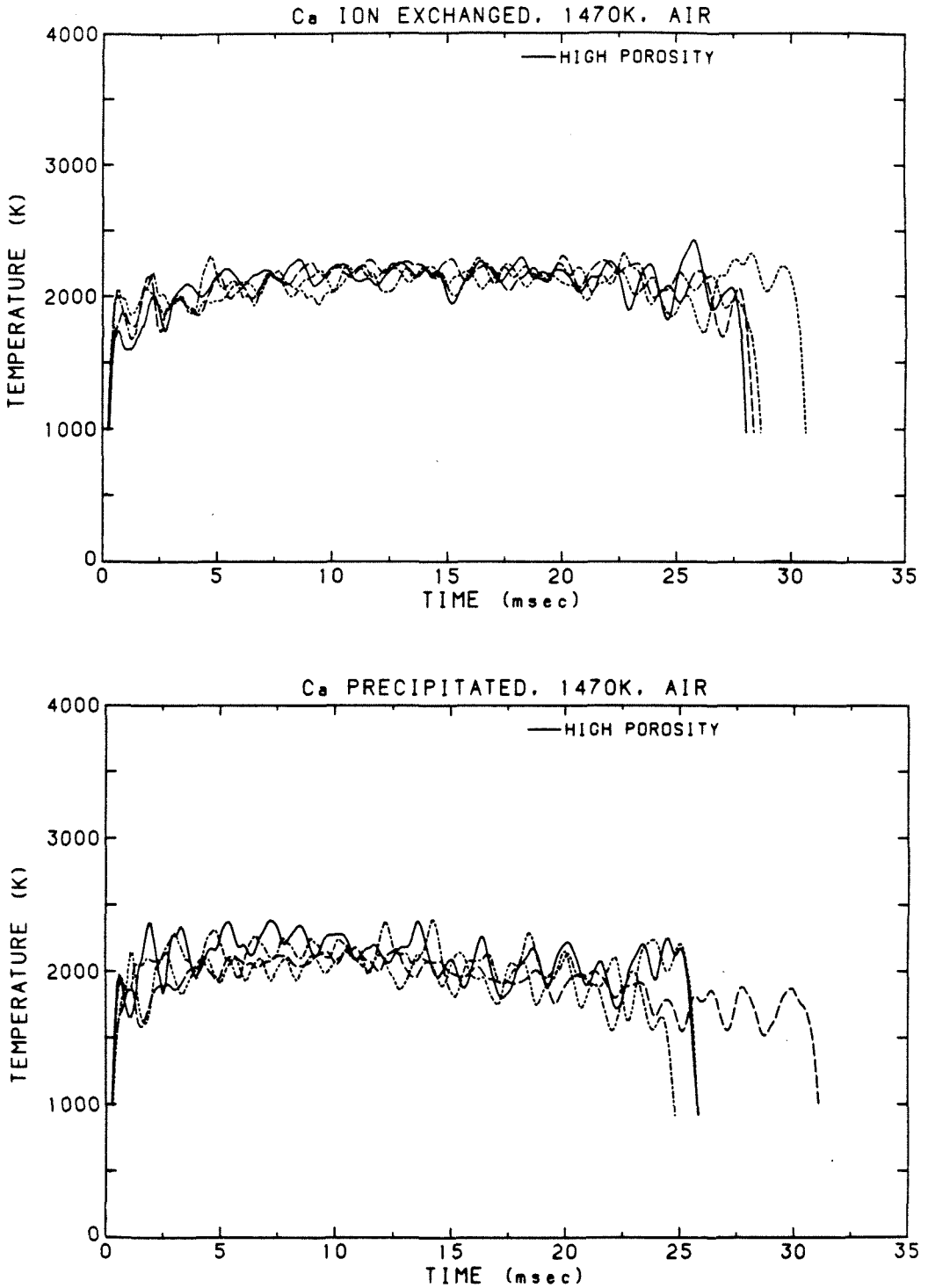

Figure 6: Temperature-time profiles of high porosity particles burning in air: (a) ion exchanged, (b) $CaCO_3$ precipitated.

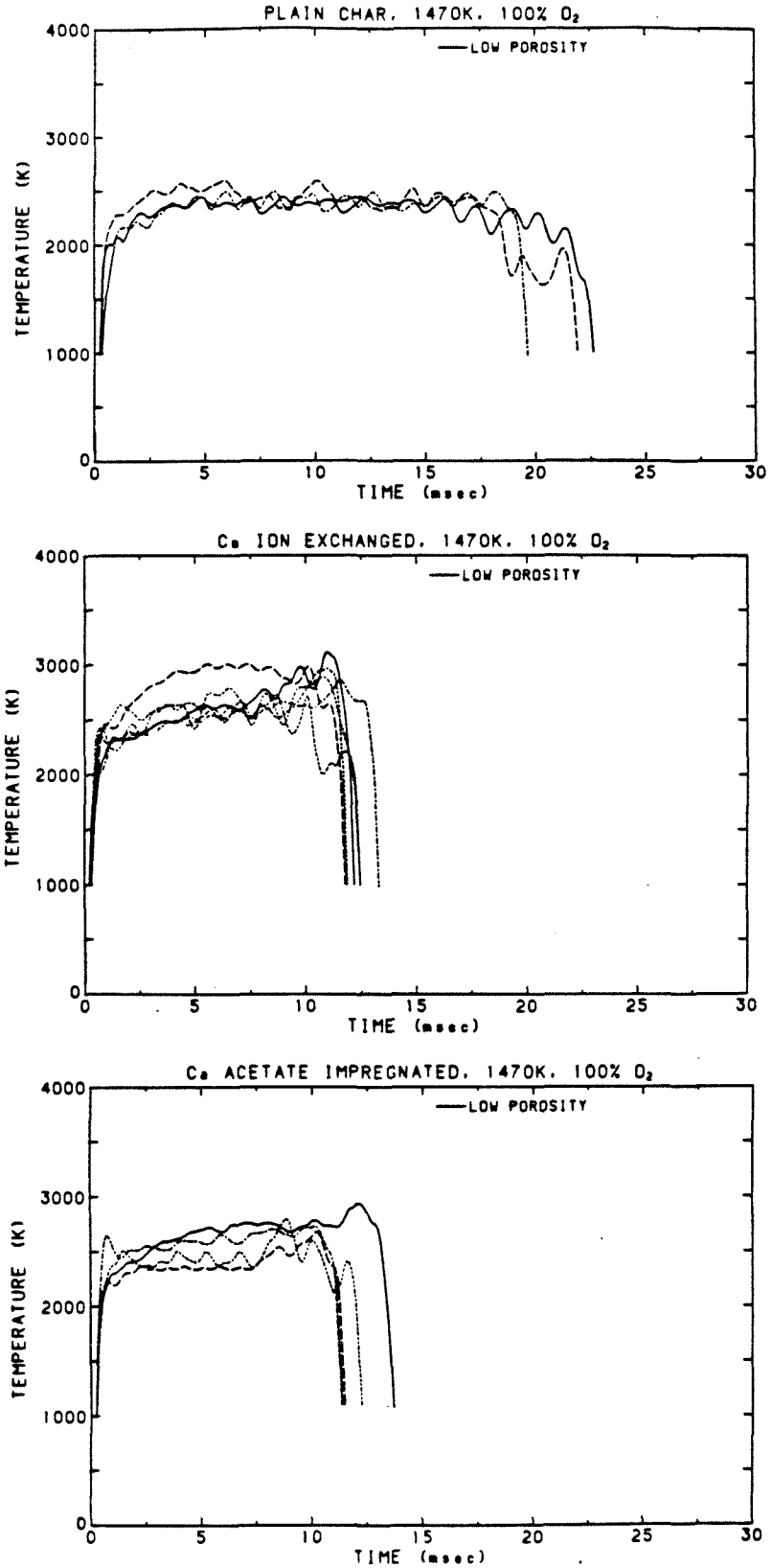

Figure 7: Temperature-time profiles of low porosity particles burning in O_2: (a) plain char, (b) ion exchanged, (c) calcium acetate impregnated.

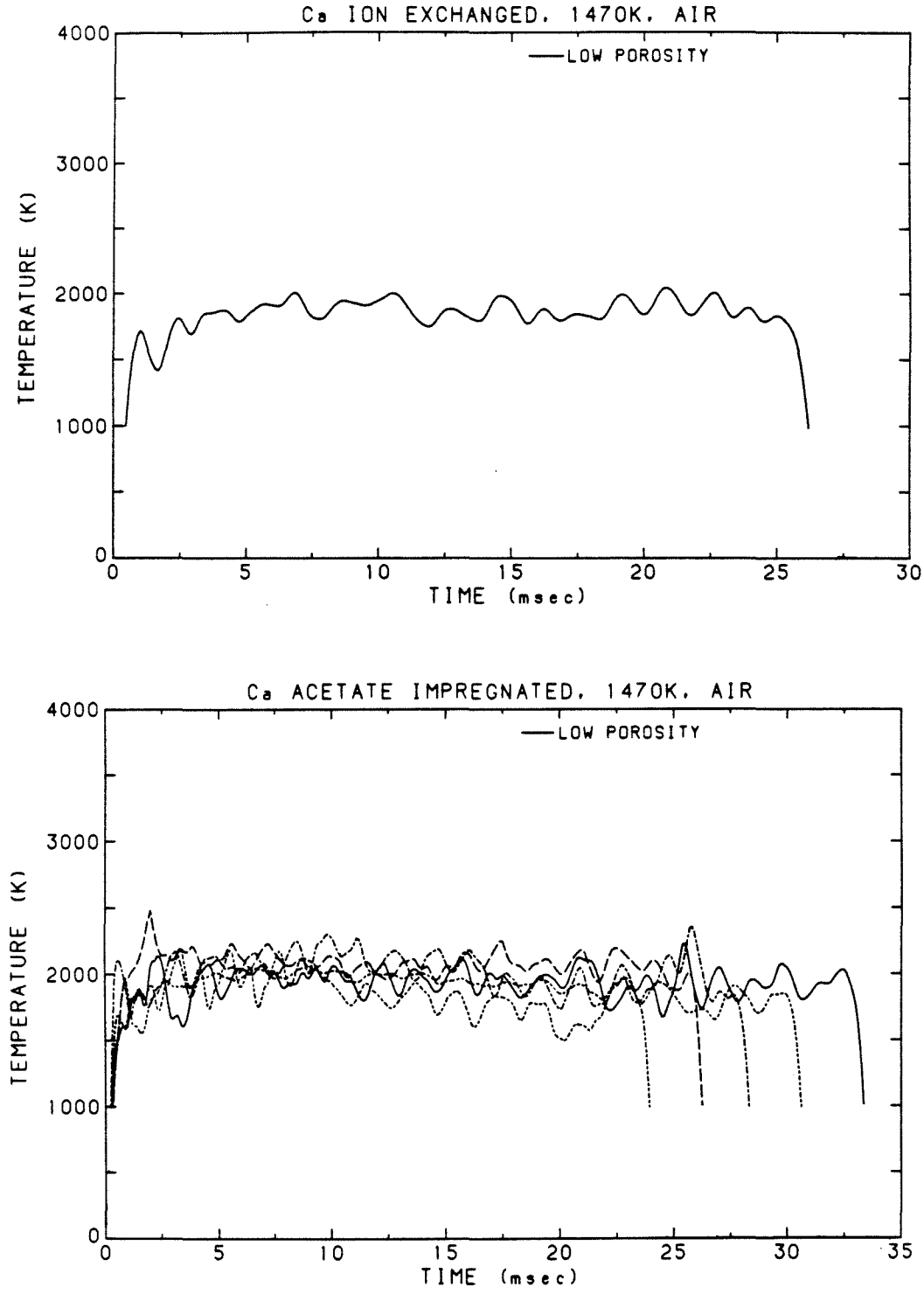

Figure 8: Temperature-time profiles of low porosity particles burning in air: (a) ion exchanged, (b) calcium acetate impregnated.

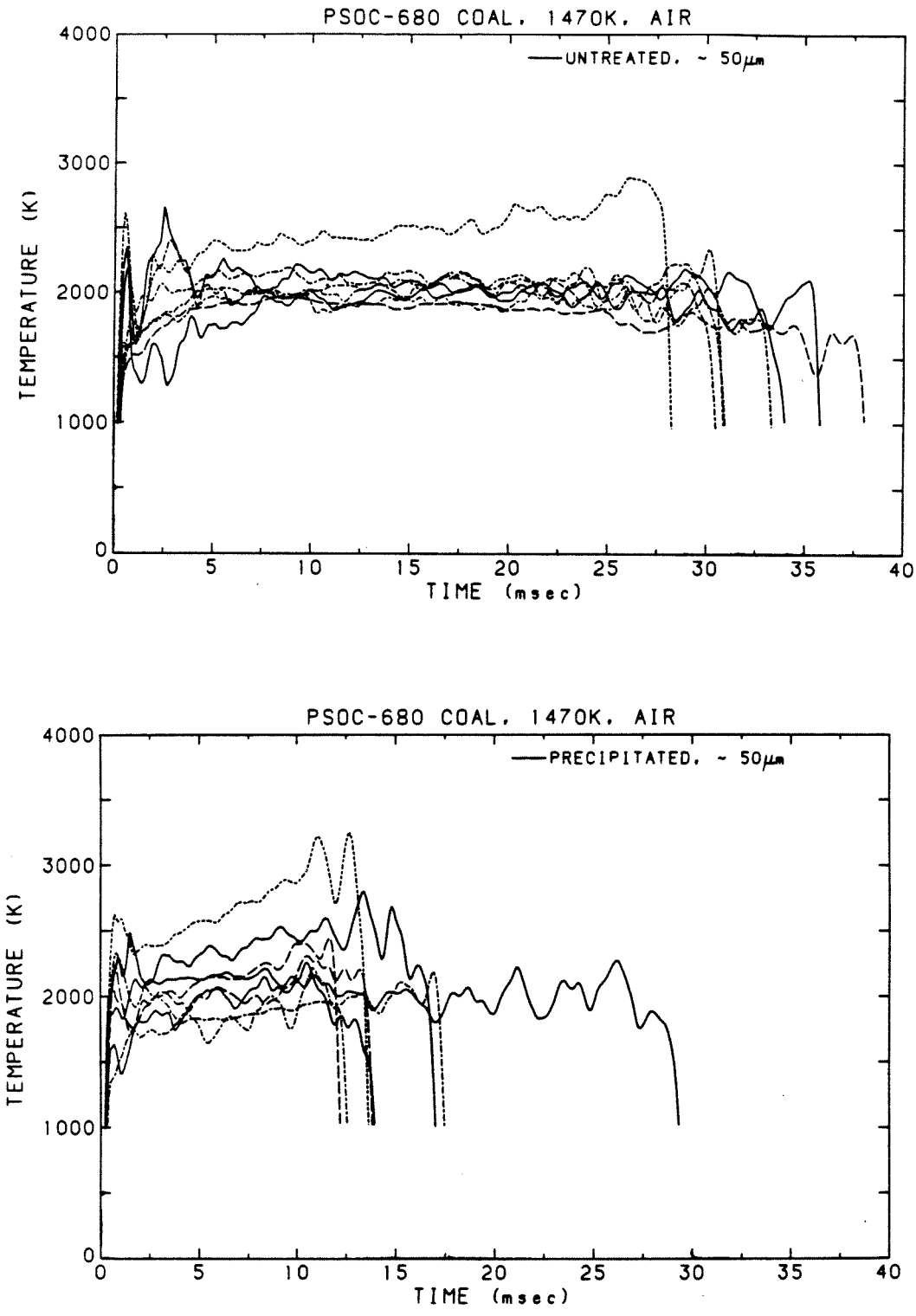

Figure 9: Temperature-time profiles of PSOC-680 coal particles burning in air: (a) untreated coal, (b) $CaCO_3$ precipitated.

Ognuno sta solo sul cuore della terra
trafitto da un raggio di sole
ed è subito sera.

Everyboby stays alone at the heart of the earth
pierced by a solar ray
and before too long it is night again.

Salvatore Quasimodo

APPENDIX 1

Generation of Monodisperse Solid Particles, Theory and Application

1 Introduction

Monodisperse liquid and solid aerosol particles have found many industrial and scientific applications both because of their equal and accurately known size and because of their most easily accounted for spherical shape. Applications range from fundamental aerosol research to calibration of aerosol measuring instruments and to testing of particulate removal devices like cyclones, filters and scrubbers. Many techniques have been devised to produce aerosols like the *spinning-disk* generator, the nebulizer and the atomizer generator, but in most cases the resulting aerosol is not truly monodisperse. The most dependable technique has been developed by Berglund and Liu (1973), based on the instability and break-up of a cylindrical liquid jet. They constructed a vibrating orifice aerosol generator capable of producing monosized particles from a variety of liquid materials. The most important feature of this generator is its ability to produce particles of a predetermined size, the particle size being calculable from the generator operating conditions with an accuracy, according to the authors, of 2% or better. Also, a particle size standard deviation of 1% of the mean droplet diameter is claimed, along with a very steady particle output concentration.

The application of aerosols in the present investigation relates to fundamental

studies of combustion of carbonaceous particles. It aims to take advantage of the monodisperse particle's equal size that enables monitoring of dimensional changes with burnout and the spherical shape that facilitates combustion modelling. The initial material has to be a liquid of mild viscosity to enable flow and atomization and it should be capable of yielding highly carbonaceous materials after drying and curing. Based on previews studies by Fitzer et al. (1969) and by Senior and Flagan (1984), furfuryl alcohol was selected. Based on principles similar to the Berglund and Liu technique, an aerosol generator was designed and constucted.

2 Theoretical Considerations

Any liquid jet is unstable for mechanical disturbances and breaks up into droplets. If the mechanical disturbances are generated at constant frequency and with sufficient amplitude and applied to a jet of constant velocity, the jet may break up into equal size droplets. The likelihood of the monosize droplet break-up depends on the combination of the following parameters: (i) diameter of the jet, (ii) jet velocity and (iii) excitation frequency. Based on theoretical considerations regarding the surface energy, Plateau (1873) and Rayleigh (1879) derived the minimum wavelength, λ_{min}, of excitation for a disturbance to be unstable on an infinitely long liquid cylinder:

$$\lambda_{min} = \pi D_j, \tag{1}$$

where D_j is the diameter of the jet. For an incompressible liquid sprayed into a vacuum, Rayleigh derived the following relationship for the optimum wavelength of the disturbance:

$$\lambda_{opt} = 4.508 D_j. \tag{2}$$

It has been experimentally shown (Schneider and Hendricks, 1964) that uniform size droplets can be produced by varying λ within the following limits:

$$3.5 D_j < \lambda < 7 D_j. \tag{3}$$

The minimum liquid velocity, $V_{j,min}$, necessary to form and sustain a liquid jet flowing from a capillary tube, has been calculated from conservation of energy considerations (Lindblad and Schneider (1965) as:

$$V_{j,min} = \left(\frac{8\sigma}{\rho D_j}\right)^{1/2}, \tag{4}$$

where σ is the surface tension and ρ the density of the liquid. The volume, v_D, of each drop is:

$$v_D = Q/f; \tag{5}$$

here, Q is the volumetric flow rate of the liquid (per sec.) and f is the disturbance frequency (in Hz). Therefore, the diameter of the droplet, d_D, can be expressed as:

$$d_D = \left(\frac{6Q}{\pi f}\right)^{1/3}. \tag{6}$$

Most of the above conditions were verified in the present study.

3 Design of the Aerosol Generator

The aerosol generator described in this work was designed, based on the following criteria: (a) ease of flow of rather viscous fluids; (b) ease of access to the orifice and other generator parts for cleaning purposes, since frequent plugging was expected; and (c) isolation of the parts that are sensitive to chemical solvents from both the flow of the liquid and any associated spills during the cleaning process. A few initial configurations of generators using a piezoelectric ceramic to induce vibrations to the liquid jet were tried with relative success. In Fig. 1 the liquid jet of a generator employing a "homemade" glass nozzle is shown illuminated with a strobe light. By tunning the strobe light with a signal generator to the same frequency as the one exciting the jet, the motion of the droplets can be frozen. The final design of the generator is shown in Fig. 2. Instead of glass extruded nozzles,

the generator employs laser-drilled metallic orifices. These pinholes, supplied by *Melles Griot*, proved to be easier to handle and clean (in an ultrasonic bath) and their diameter known with better accuracy than the glass nozzles. The driving force for the aerosol generation is provided by a silver-plated piezoelectric bimorph element having dimensions (8.9 × 8.9 × 0.53 mm), supplied by *Vernitron Piezoelectric Division* model *PZT-5HS*. The piezoelectric element was attached by means of a conductive silver-based epoxy, provided by *TRA-CON Inc.*, to a stainless steel metallic membrane (100 μm thick). The liquid polymer was fed by a syringe pump to the cavity in the generator between the steel membrane and the orifice and was vibrated by waves generated by the piezoelectric bimorph and transmitted through the membrane. The bimorph was driven by a *Wavetek* function generator capable of providing an ac voltage amplitude of ± 15V. At both sides of the generator's cavity, teflon *O-rings* are used against the orifice and the metallic membrane to seal the cavity and contain the liquid that is under pressure. Teflon *O-rings* were used because of the excellent resistance of this material to chemical solvents, like acetone.

The orifices were spot-welded on small 8.9 mm o.d., 0.5 mm thick washers stamped out of magnetic stainless steel foil. These washers provided rigidity to the orifice and being magnetic, enabled easy removal of the orifice with a small magnet in case of plugging. To help prevent the plugging of the orifice from dried-out polymer particles and strings left over in the lines from previous runs (if the lines had not been cleaned thoroughly), a small tube was inserted in the cavity upstream from the orifice as shown in Fig. 2. This tube was helpful only if the generator was fired downwards, which was the case in the present work. In this case most polymer particles would slide by gravity along the sloped walls of the generator's cavity and would be collected between the tube and the walls instead of sliding all the way to the orifice and plugging it. Orifices in the range of 20 to

100 μm were used to produce droplets having diameters in the range of 40 to 200 μm, for the minimum escape velocity conditions (Eq. 4). Flowrates varied from a fraction of, to a few, cm^3/min and excitation frequencies from a few kHz to a few tens of kHz, the frequency increasing with reducing the size of the orifice. The frequency operating windows for monodisperse droplet generation were determined experimentally using the method of Berglund and Liu. A small air jet was aimed at the string of droplets downstream of the orifice, with velocity enough to deflect the string to a small angle. If there is only one deflected string of drops, i.e., all drops deflect to the same angle, then then it can be concluded that all drops have the same inertia and therefore the same size. If more than one deflected stream arises, satellite streams, then the the resulting droplets are polydisperse.

The droplet dispersion system was designed in a manner similar to the Berglund-Liu generator. A stainless steel cup with a dispersion orifice, centered in the middle, was placed on top of the generator. Provisions of a stream of air to flow between the cup and the generator were made and the air exited coaxially with the droplets from the cup's orifice. The droplets were dispersed in a conical shape.

4 Summary

An aerosol generator capable of atomizing a variety of liquids has been designed and constructed. The generator employs a piezoelectric element to vibrate the liquid inside the generator against the orifice, in contrast to the Berglund-Liu design where the orifice itself vibrates. This way the design incorporates inexpensive piezoelectric elements, and prevents their contact with chemical solvents during the operation and the frequent clean-up periods. All the generator's parts are made of stainless steel and teflon and interchangeable, laser-drilled orifice disks. A droplet dispersion cup and a mechanism for verifying monodispersivity of the drops have been provided.

5 Acknowledgements

Thanks are due to Mark Cohen and Dimitri Papantoniou for their assistance and encouragement in the rather difficult task of atomizing the viscous fluids of the present study. Thanks are also due to Elton Daily and Joe Fontana for the construction of the various parts of the generator.

6 References

1. Berglund, R. N. and Liu, B. Y. H. (1973). "Generation of Monodisperse Standards." *Environmental Science & Technology* **7**, 147.

2. Fitzer, E., Schaefer, W. and Yamada, S. (1969). "The Formation of Glasslike Carbon by Pyrolysis of Polyfurfuryl Alcohol and Phenolic Resin." *Carbon* **7**, 643.

3. Senior, C. L. Flagan, R. C. (1984). "Synthetic Chars for the Study of Ash Vaporization." *Twentieth Symposium (International) on Combustion*, The Combustion Institute, 921.

4. Plateau, (1873). "Statique Experimentale et Theorique des Liquides soumis aux seules Forces Moleculaires." Ref. in Theory of Sound, J. W. S. Rayleigh, 2nd ed., Vol II, 363 (1878). Reprinted dy Dover Publ., New York, N.Y., 1945.

5. Rayleigh, Lord (1879). *Proceedings of the Royal Society* **29**, 71.

6. Schneider, J. M. and Hendricks, C. D. (1964). *Review of Scientific Instruments* **35**, 1349.

7. Lindblad, N. R. and Schneider, J. M. (1965). *Journal of Scientific Instruments* **42** 635.

7 Notation

SYMBOL	DESCRIPTION	UNITS
d_D	particle diameter	cm
D_j	jet diameter	cm
f	frequency	
Q	flowrate	cm^3/s
v_D	droplet volume	cm^3
V_j	jet velocity	cm/s
λ	wavelength	cm
ρ	density of liquid	g/cm^3
σ	surface tension of liquid	dyne/cm

8 List of Figures

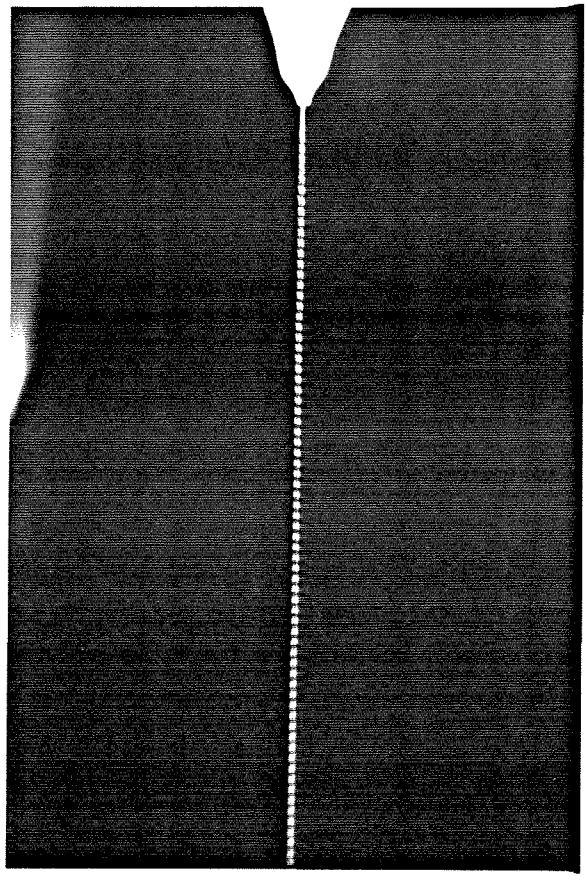

Figure 1: Optical microscope photograph of monodisperse droplet generation illuminated by a strobe light.

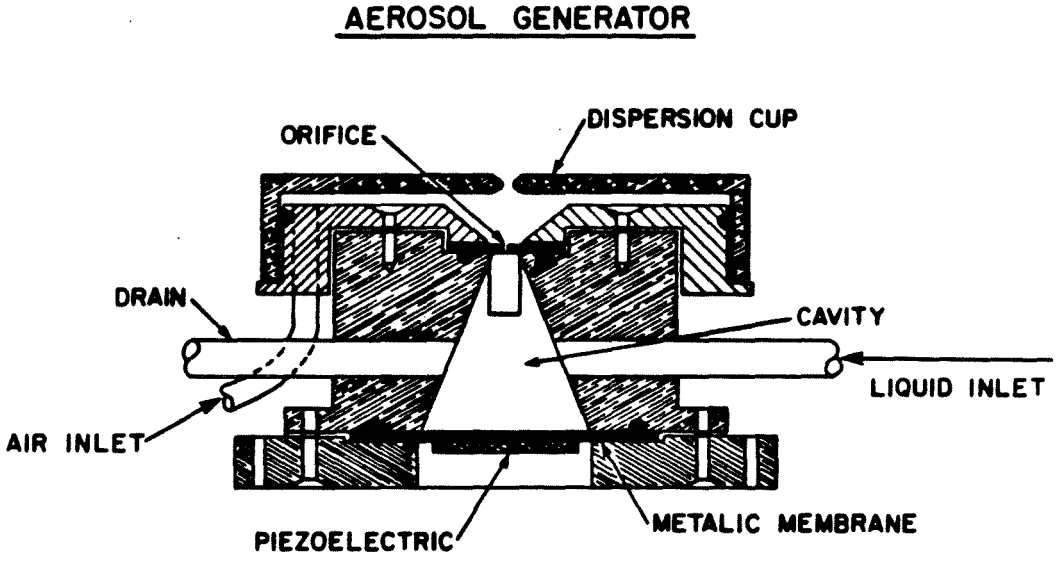

Figure 2: Vibrating liquid column aerosol generator.

APPENDIX 2

Design and Construction of a Three-Stage Thermal Reactor

A thermal rector was constructed in order to dry and cure the droplets produced by the aerosol generator described earlier. The reactor is practically a drying tower where the aerosol is sprayed from the top downwards along the centerline and is collected at the bottom by sedimentation. The design of the reactor was based both on theoretical calculations pertinent to the drying of liquid drops of various sizes and different compositions and on preliminary experiments utilizing a *pyrex* glass drying column wrapped with heating tapes.

Briefly, the theoretical formulation of the problem concerning the drying of liquid drops of diameter d and mass m should take into account the diffusional mass transfer of vapors from the particle to its surroundings and the unsteady particle temperature history:

$$\frac{dm}{dt} = -\pi \left(\frac{6m}{\sigma_p \pi}\right)^{2/3} \sigma_g D(X_s - X_\infty) \tag{1}$$

$$dX/dt = -\frac{N}{\sigma_g Q}\frac{dm}{dt} \tag{2}$$

$$\frac{dT_\infty}{dt} = \frac{1}{C_p m}\left(\frac{dm}{dt}H_0 + h\pi\left(\frac{6m}{\rho_p \pi}\right)^{2/3}(T - T_\infty)\right), \tag{3}$$

where σ_g is the density of the gas, σ_p is the density of the particle, D is the bulk molecular diffusion coefficient, N is the exitation frequency of the aerosol generator which is also equal to the number of drops generated per second, and Q is the gas

flowrate. C is the heat capacity of the drop, H_0 is the latent enthalpy of vaporization of the solvent and h is the heat transfer coefficient calculated as follows:

$$h = Nu\frac{k}{d} \qquad \text{where} \qquad Nu = 0.59(GrPr)^{1/4}; \tag{4}$$

here, Nu Gr and Pr are the Nusselt, Grashof and Prandtl numbers, respectively, and k is the thermal conductivity of the gaseous phase. X_∞ is the mass fraction of the vapors in the surrounding gas and X_s is the saturation vapor pressure at the surface of the drop that can be expressed relatively to temperature in Arrhenius form. For example, for acetone:

$$X_s = \exp\left(-\frac{1/T - 3.06 \times 10^{-3}}{2.48 \times 10^{-4}}\right). \tag{5}$$

The above system of first-order differential equations was solved numerically using a fourth-order Runge-Kutta method with automatic step-size control. A list of the computer code is included at the end of the appendix. From this calculation it was found that a 100 μm diameter acetone droplet requires $\approx$ 4 s to evaporate at room-temperature surroundings. The drying tower functionality, however, had to provide for pyrolysis of the polymer particles; thence, the drying processes had to be enhanced. Based on preliminary experiments, a 2 m long reactor was built.

The main part of the reactor consists of a 1.5 m long stainless steel tube having a diameter of 10.8 cm and a wall thickness of 0.32 cm. At the top of the column a 10 cm long pyrex glass cylindrical window is mounted as shown in Fig. 1. This window served for observing the jet during aerosol generation and verifying monodispersivity of the liquid drops, before every experimental run, using the methods described in Appendix 1. For this purpose a small 1 mm i.d. tube was mounted perpendicularly to the droplet jet, at the side of the aerosol generator holding flange above the observation window. A small jet of N_2, activated only in the absence of dispersion flow, was impinging on the generated droplet string to allow detection of any satellite drops. Provisions for introduction of dilution as well as dispersion gas flows were

incorporated in the design of the top flange of the drying tower, shown in Fig. 1, a 4 cm diameter magnetic stainless steel disk was fitted below the generator replacing the dispersion cup. The disk had a 1.5 mm orifice drilled in its center tapered at an angle of 60° at both sides to facilitate droplet dispersion. Dispersion gas was flowing through the orifice. Dilution gas, used to overcome buoyancy effects in the reactor, was initially introduced tangentially to the top flange, and then it was diverted to a circular tube, with holes, residing in a groove on the inside part of the flange. The gas was diverted from the little holes radially, in respect to the reactor, resulting in a rather uniform radial distribution of the dilution gas at the top of the tower. Finally, a perforated disk was used to deflect the dilution gas to flow axially downwards, surrounding the dispersed jet of droplets.

An additional orifice, having a diameter of 2 cm, was inserted below the observation window to prevent buoyant gases, rising along the reactor walls, from entering into the window area and on one hand, disturbing the jet and on the other hand, coating the window with condensed vapors.

The column was heated in three stages, using *Thermoline* heavy duty samox heating tapes (two per stage) capable of reaching a maximum temperature of 750 K. The resulting stratified temperature profile at the centerline of the reactor exhibited an average temperature of 520 to 550 K in the first and the third stage and 620 to 650 K in the second stage. The centerline temperatures were monitored using *Chromel-Alumel* thermocouples, and the pressure was observed using a manometer. Three coats of 2.5 cm *Caowool* by *Babcock and Wilcox* fiber blanket were used to insulate the reactor and minimize heat loss from the tapes to the surroundings.

A sampling port was inserted at the bottom of the tower. The port, in the shape of a parallelepiped, had two large 10.8 cm holes drilled with shoulders to support filters residing on perforated steel disks. The port was sliding between flanges sealed with *viton O-rings* that resist temperatures up to 500 K. A copper

tube carrying running water was wrapped around the lower part of the column to provide cooling for the *O-rings*. Glass fiber filters were placed in the sampling port only at the beginning of each particle generation run to check for satisfactory particle production. Subsequently, one of the filters was removed to allow sedimentation of particles in the collection stage (described in Appendix 3) below the port. The other filter was kept on so that in the event of orifice plugging or malfunction it would be slid in and would prevent the destruction of the collected sample by any falling large drops of liquid.

Acknowledgements

Thanks are due to Elton Daily and Joe Fontana for advice and technical assistance in all aspects of the construction of the reactor.

References

1. Arpaci V. S., (1966). Conduction Heat Transfer. Addison-Wesley, Reading, Mass.

2. Arpaci V. S., (1986). Convection Heat Transfer. McGraw-Hill, New York.

Notation

SYMBOL	DESCRIPTION	UNITS
C	heat capacity	J/g K
d	particle diameter	cm
D	molecular diffusivity	cm^2/sec
h	heat transfer coefficient	W/m^2K
H_0	enthalpy of combustion	J/g
R_i	rate coefficient	$g/(cm^2sec(atm)^n)$
m	mass of droplet	g
N	frequency	Hz
Q	flowrate	cm^3/s
X	mass fraction	
σ_g	density of the gas	g/cm^3
σ_p	density of the particle	g/cm^3

List of Figures

Detail of the drying tower, the aerosol generator mounting and the observation window.

List of the Program

```
C       ************************************************************
C
C              DRYING TIME FOR A DROP OF POLYMER + SOLVENT
C
C       ************************************************************
C
C       COMPUTER CODE FOR THE STANDARD RUNGE-KUTTA METHOD
C       WITH AUTOMATIC STEP SIZE CONTROL
C       THE CODE CAN BE APPLIED TO GENERAL FIRST ORDER SYSTEMS
C      * Y'=F(T,Y)
C       IN THIS PROGRAM G(X)IS THE EXACT SOLUTION OF THE
C       DIFFERENTIAL EQUATION (IF APPLIED)
C
        IMPLICIT REAL*8 (A-H,O-Z)
C
C       N IS THE NUMBER OF EQUATIONS
C
        DIMENSION U(3),UPLUS(3),UREDU(3),UAST(3),SUM(3)
        REAL*8 D,DD,DDT,M,MFIN
        COMMON XSAT,RO,G,F,CC,HV,HT,DIFF
        OPEN (UNIT=10,NAME='DROP.DAT',TYPE='NEW')
C
C       THE NUMBER OF EQUATIONS N
C
        N=3
        D=0.00001
C
C       THE INITIAL STEP SIZE H
C
        H=0.1
        HMAX=1.0
        DD=0.0
        DDT=0.0
        T=0.0
        PI = 3.141592625
        TW = 298.15
C
C       THE INITIAL DROP DIAMETER
        TYPE 4
  4     FORMAT (3x,'entrer DOpart : ',$)
        ACCEPT *,DO
C
C       THE DENSITY OF THE PARTICLE
        TYPE 5
  5     FORMAT (3x,'enter RO : ',$)
        ACCEPT *, RO
C
C       THE AIR . FLOWRATE ,G
        TYPE 7
  7     FORMAT (3x,'enter G : ',$)
        ACCEPT *, G
C
C       THE PIEZOELECTRIC EXITATION FREQUENCY , F
        TYPE 8
  8     FORMAT (3x,'enter F : ',$)
        ACCEPT *, F
C
C       THE LATENT HEAT OF VAPORIZATION
        TYPE 9
  9     FORMAT (3x,'enter HV : ',$)
        ACCEPT *, HV
```

```
C
C       THE HEAT TRANSFER COEFFICIENT
        TYPE 10
  10    FORMAT (3x,'enter HT : ',$)
        ACCEPT *, HT
C
C       THE HEAT CAPACITY
        TYPE 11
  11    FORMAT (3x,'enter CC : ',$)
        ACCEPT *, CC
C
C       THE DIFFUSION COEFFICIENT
        TYPE 12
  12    FORMAT (3X,'enter DIFF : ',$)
        ACCEPT *,DIFF
C
C       INITIAL CONDITIONS FOR THE DIFFERENTIAL EQUATIONS
C
        U(1) = (PI/6*(DO**3))                   !the initial droplet mass
        u(2) = 0                                !the initial vapor conc.
        U(3) = TW                               !the initial temperature
C
        WRITE(10,98) DO,RO,Q,F,HV,HT,CC,DIFF
 98     FORMAT(//3x,'DOpart =',f7.5,/3x,'RO =',F6.3,/3x,'Q =',f7.3,/
     $          3x,'F =',f8.1,/3x,'LAT.HEAT=',F8.2,/3x,'HEAT TR.CO.=',
     $          f8.6,/3x,'HEAT CAP.  =',F6.3,/3x,'DIFF =',f6.3)
        WRITE(10,99)
 99     FORMAT(//3X,'LOOP#',11x,'TIME',16x,'M',14X,'Xin#',9X,
     $          'TEMPERATURE')
        LOOP=1
 42     CONTINUE
C
        IF (U(3).LE.265.0) THEN
                U(3) = 265.0
        ENDIF
C
C       THE CONCENTRATION OF VAPOR ON THE PARTICLE SURFACE i.e.
C       THE SATURATION VAPOR PRESSURE AT A GIVEN TEMPERATURE , XSAT
        XSAT = EXP(-(1/U(3)-3.06E-3)/2.48E-4)
C
C       METHOD FOR SELECTION OF STEP
C
        CALL KUTTA (N,T,H,U,UPLUS)
        CALL KUTTA (N,T,H/2,U,UREDU)
        CALL KUTTA (N,T,H/2,UREDU,UAST)
        TYPE *,LOOP,U(3),XSAT
C
        SUMT=0
        DO 20 I=1,N
        SUM(I)=(UPLUS(I)-UAST(I))*(UPLUS(I)-UAST(I))
        SUMT=SUMT+SUM(I)
 20     CONTINUE
        S=SQRT(SUMT)/0.93750
C
C       STEP SELECTION. EXAMINE THREE INTERVALS
C
        DD=D*H
        DDT=D*H/10
        IF(DDT.LE.S.AND.S.LE.DD) GO TO 31
        IF(S.GT.DD) GO TO 33
        IF(S.LT.DDT) GO TO 35


C
 31     DO 32 I=1,N
 32     U(I)=UAST(I)
        T=T+H
        GO TO 40
```

```
C
 33     HNEW=H*((DD/5/S)**0.2)
        H=HNEW
        GO TO 40
C
 35     DO 36 I=1,N
 36     U(I)=UAST(I)
        T=T+H
        HNEW=H*((DD/5/S)**0.2)
        H=MIN(HNEW,HMAX)
        GO TO 40
C
C       LOOP CONTROL
C
 40     LOOP=LOOP+1
C
        WRITE(10,100) LOOP,T,U(1),U(2),U(3)
 100    FORMAT(/3X,I4,6X,F15.9,3X,F15.9,3X,F15.9,3X,F7.3)
        IF (U(1).LT.0.0000000009) GO TO 50
        IF (T.LT.100) GO TO 42
        TYPE *,LOOP
 50     STOP
        END
C
C
C
C
C       SUBROUTINE FOR STANDARD RUNGE KUTTA (4TH ORDER)
C
        SUBROUTINE KUTTA(N,T,H,U,UPLUS)
        IMPLICIT REAL*8 (A-H,O-Z)
        REAL*8 K1,K2,K3,K4,KTOT
        DIMENSION K1(3),K2(3),K3(3),K4(3),KTOT(3),U(3),UPLUS(3)
        DIMENSION UNEW(3)
C
        CALL DERIV(T,U,K1)
        DO 70 I=1,N
 70     UNEW(I)=U(I)+H/2*K1(I)
C
        CALL DERIV(T+H/2,UNEW,K2)
        DO 71 I=1,N
 71     UNEW(I)=U(I)+H/2*K2(I)
C
        CALL DERIV(T+H/2,UNEW,K3)
        DO 72 I=1,N
 72     UNEW(I)=U(I)+H*K3(I)
C
        CALL DERIV(T+H,UNEW,K4)
        DO 73 I=1,N
        KTOT(I)=K1(I)/6.+K2(I)/3.+K3(I)/3.+K4(I)/6.
 73     UPLUS(I)=U(I)+KTOT(I)*H
        RETURN
        END
C
C
C
C       SUBROUTINE FOR THE GIVEN PROBLEM

        SUBROUTINE DERIV (T,Y,YP)
        IMPLICIT REAL*8 (A-H,M,O-Z)
        DIMENSION Y(3),YP(3)
        COMMON XSAT,RO,G,F,CC,HV,HT,DIFF
C
C       CONSTANTS USED IN THE CALCULATION
        D = DIFF                              !the diffusion coefficient
        ROAIR = .001                          !the density of air
        PI = 3.141592654
        FF = F                                !drops/sec
        TW = 298
C
C       FUNCTIONS AND THEIR FIRST DEGREE DERIVATIVES
C
        M    = Y(1)
        X    = Y(2)
        TP   = Y(3)
C
        YP(1) = -(PI)*(6*M/(RO*PI))**(1/3.)*(ROAIR*D*(XSAT-X))
        YP(2) = FF/(RO*G)*((PI)*((6*M/(RO*PI))**(1/3.))*(ROAIR*D*(XSAT-X)))
        YP(3) = -1./(CC*M)*(((PI)*(6*M/(RO*PI))**(1/3.)*(ROAIR*D*(XSAT-X)))
     $          *HV+(HT*PI*((6*M/(RO*PI)**(2/3.))*(TP-TW))))
C
        RETURN
        END
```

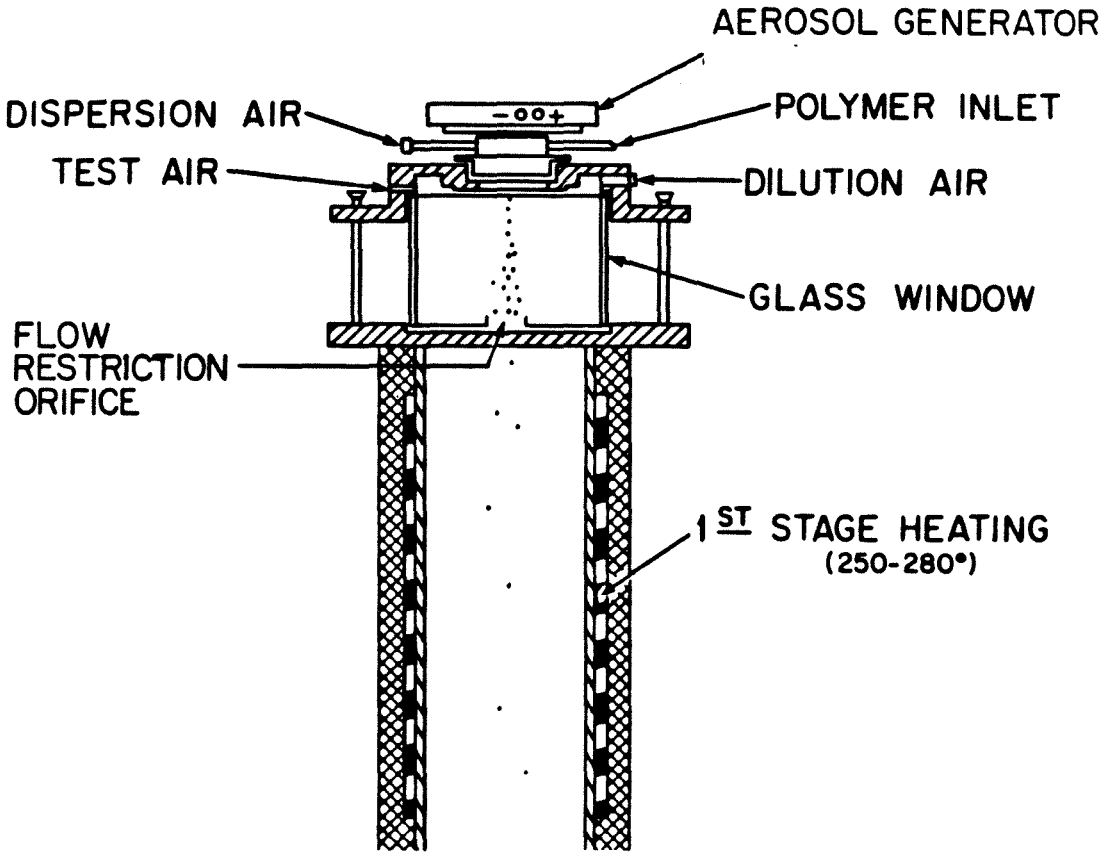

Figure 1: Detail of the drying tower, the aerosol generator mounting and the observation window.

APPENDIX 3

Design and Construction of a Virtual Impactor.

A particle collection system was constructed and incorporated at the very bottom of the drying tower. The aerosol particles, after undergoing solidification through partial pyrolysis, were collected by sedimentation. The requirements that the collection stage must satisfy included resistance to corrosion and high temperatures, air tightness, provisions to allow unobstructed observation of the particles yielded and ease of access for cleaning purposes. Furthermore, it was desirable to avoid collection of small satellite drops (if generated) and prevent deposition of condensing vapors on the collected particles. The design of the collection system was based on the theory of operation of virtual impactors and it was the product of an extensive experimental undertaking.

Theory

The efficiency with which particles of diameter d can be collected by an impactor is a function of the impaction parameter or Stokes number:

$$St = \frac{\sigma_p V d^3 C}{18 \mu w}, \tag{1}$$

where σ_p is the particle density, d is the particle diameter, V is the jet velocity, μ is the viscosity of the gaseous medium, w is the jet diameter and C is the Cunningham slip correction factor given as a function of the mean free path of the gas as:

$$C = 1 + \frac{2\lambda}{d}\left(1.257 + 0.4 \exp\left(-\frac{0.55d}{\lambda}\right)\right), \tag{2}$$

substituting the velocity in terms of the flowrate:

$$V = \frac{Q}{\frac{\pi}{4}w^2} \qquad \text{then} \qquad St = \frac{2}{9\pi}\frac{\sigma_p Q d^2 C}{w^3 \mu}. \tag{3}$$

Solving for the jet diameter it is obtained:

$$w = \left(\frac{2\sigma_p Q d^2 C}{9\pi\mu St}\right)^{1/2}. \tag{4}$$

The collection efficiency depends on the Reynolds number of the impactor jet, the jet to cavity spacing S, and the impactor geometry. However, for a limited range of jet Reynolds numbers ($500 \leq \mathrm{Re} \leq 3000$) for incompressible flows and for length ratios in the range ($0.5 < S/D < 5$), the collection efficiency is a function of the Stokes number alone, $\eta = \eta(St)$. Biswas (1984) performed extensive experiments on a "*Particle Trap Virtual Impactor*" to correlate the collection efficiency to $St^{1/2}$ for various impactor geometries.

Application

The impactor used in the present work was designed based on the specifications given by Biswas to acheive collection of particles bigger than 10 μ with a 75% efficiency. A cavity diameter to jet diameter ratio, w_0/w, of 1.9 and a jet-cavity spacing to jet diameter ratio, S/w, of 2 were used. The "*Particle Trap*" collection stage is shown in Fig.1. Two coaxial funnels are mounted below the sampling port, the lower part of the inner funnel serving as the jet nozzle. A stainless steel cavity entrance is placed at a distance S from the nozzle. A *Pyrex* glass collection cup is mounted below, forming the cavity. The fact that the cup is transparent facilitates observation of the particle yield. The exhaust gases are diverted, in between the funnels, to the exhaust system operating under mild vacuum. The most important feature of the design proved to be the construction of the inner funnel. The problem was that the collected particles were sticky and were not sliding down the walls of the funnel. The most obvious remedy would be to make the slope of the funnel

walls steep. However, even an angle of 65°, which was close to an upper limit for fitting the funnel with the rest of the components, proved to be inadequate. Various techniques were used to alleviate the problem, the most successful of which was adopted as shown in Fig. 1. An additional flange with a circumferential cavity was inserted at the top of the funnel. N_2 gas was intoduced into the cavity and exited through small holes, tilted at an angle of 60° from the vertical, along the inner periphery of the flange. Jets of N_2, at times preheated, emerging from the small holes aided the particles to slide down the funnel walls. This arrangement brought only partial success, working fine for for rather dry particles, like the ones containing carbon black, small particles (8-15 μm) and cenospheres but performed poorly for the most sticky particles like the ones containing high concentrations of PEG. The latter particles were collected on the sides of the funnel. A suggestion of inprovement might be to introduce the N_2 flow tangentially at the top of the funnel in such a way that swirl would result. This way the particles, being entrained in an eddying motion, might be prevented from being deposited on the funnel walls.

Acknowledgements

The encourangement, advice and help of Joe Fontana in all aspects of the design and construction of the impactor is greatly appreciated.

References

1. Marple, V. A. and Liu, B. Y. H. (1974). *Environmental Science and Technology* 8, 648.

2. Biswas, P. (1984). "Impactors for Aerosol Measurements: Developments and Sampling Biases." PhD. Thesis, Caltech.

List of Fiqures

1. The *Particle Trap* virtual impactor collection stage.

Notation

SYMBOL	DESCRIPTION	UNITS
C	Cunningham slip factor	
d	particle diameter	m
Q	gas flowrate	cm^3/sec
S	jet to cavity distance	m
V	gas velocity	m/sec
w	jet diameter	m
w_0	cavity diameter	m
η	collection efficiency	
λ	mean free path length	m
μ	viscosity	N sec/m^2
σ_p	particle density	g/cm^3

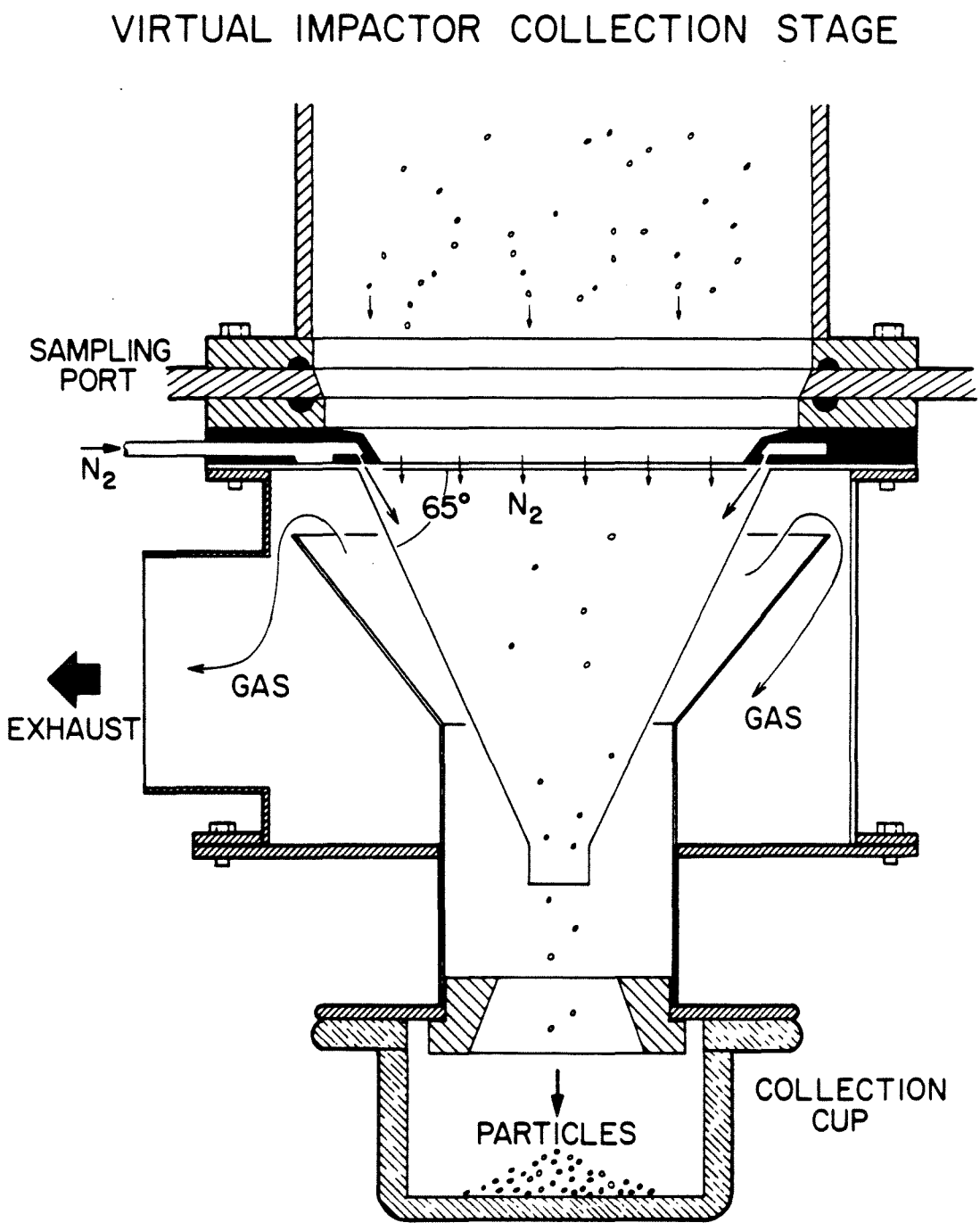

Figure 1: The *Particle Trap* virtual impactor collection stage.

APPENDIX 4

Data Inversion Techniques in Mercury Porosimetry

Basic Principles of Mercury Porosimetry

Mercury porosimetry is a technique used to perform pore size measurements in solids. It complements the pore size distribution analysis from gas adsorption isotherms, which is used to detect pores in the range where capillary condensation accompanies physical adsorption (15 to 200 $\AA$ pore radii). Mercury porosimetry analysis usually covers the range of pore radii between a few microns down to a few tens of Å, depending on the maximum pressure the instrument is capable to achieve.

When Mercury is forced into a cylindrical pore of radius r and length l, under pressure P work is done (force $\times$ displacement) given as

$$W = \pi r^2 P l, \tag{1}$$

This work quantity is equal to the amount of work needed to deform the surface of the mercury surrounding the solid and to force it to assume the shape of the pore. The work neccessary to create this additional area is given as:

$$W = -2\pi r \gamma \cos\theta, \tag{2}$$

where γ is the surface tension of Mercury and θ is the contact angle. The negative sign denotes that the area of mercury external to the pore decreases. Equating

Equations (1) and (2) above the Washburn (1921) equation is derived:

$$P = \frac{-2\gamma \cos\theta}{r}. \tag{3}$$

If it is assumed that the contact angle is constant and approximately equal to 140° and that γ_{Hg} is about 480 dynes/cm, then Equation (3) can be simplified to:

$$r = \frac{75000}{P}. \tag{4}$$

Pore size distributions can be obtained, assuming that $D_v(r)$ and $D_s(r)$ are the volume and surface pore size distribution functions defined as the volume (or surface) per unit interval of radius. Then:

$$dV = D_v(r)dr \tag{5}$$

Differentiating equation (4) gives:

$$Pdr + rdP = 0, \tag{6}$$

which combined with Equation (5) yields:

$$D_v(r) = \frac{P}{r}\frac{dV}{dP}, \tag{7}$$

where the negative sign has been eliminated, since decreasing volumes are measured. Similarly, the surface pore size distribution function can be calculated as follows:

$$D_s(r) = \frac{dS}{dV}\frac{dV}{dr}. \tag{8}$$

Assuming cylindrical pores, then: $dS/dV = 2/r$, and

$$D_s(r) = \frac{2}{r}D_v(r). \tag{9}$$

To plot logarithmic pore volume and surface area distributions $dV/d\log d_p$ and $dS/d\log d_p$, respectively, the following proceedure should be used: Equation (6) can

be rewriten in terms of the pore diameters as: $Pdd_p + d_p dP = 0$ and substituting $d\ln d_p = dd_p/d_p$, it becomes:

$$Pd\ln d_p + d_p = 0. \tag{10}$$

Substituting in Equation (5) it is obtained:

$$D_v(d_p) = \frac{2}{d_p}\frac{dV}{d\ln d_p}. \tag{11}$$

However, combination of (5) and (6) results in:

$$\frac{2dV}{d_p D_v(r)} = -\frac{dP}{P}. \tag{12}$$

Inverting the above equation and combining with Equation (11) results in:

$$\frac{d_p D_v(r)}{2} = \frac{PdV}{dP} = \frac{dV}{d\ln d_p}. \tag{13}$$

Finally, for a logarithmic with base 10 distribution:

$$\frac{dV}{d\log d_p} = 2.3P\frac{dV}{dP}. \tag{14}$$

Similarly for the logarithmic area distribution, the following system of equations is manipulated:

$$D_s = \frac{dS}{dr} = \frac{2}{r}\frac{dV}{dr}$$
$$\frac{dS}{d\ln r} = \frac{dS}{dr}\frac{dr}{d\ln r}.$$

Then

$$\frac{dS}{d\ln d_p} = \frac{4}{d}2.3P\frac{dV}{dP}. \tag{15}$$

A computer program has been written to perform the above calculations. The input to the program is the instantaneous pressure and volume intruded in the pores. The program is written in *Basic* and incorporates graphic routines to plot pore volume and surface area distributions. A list of the program has been attached and an example run is shown in Fig. 1.

Acknowledgements

The help of Sandra Bloomhorst in the development of the computer routine is greatly appreciated. Thanks are also due to Scott Northrop for technical assistance in the experiments.

References

1. Lowell S. (1979). "Introduction to Powder Surface Area." Wiley, New York.
2. Scholten, J. J. F., (1967). "Mercury Porosimetry and Allied Techniques," from Porous Carbon Solids edited by R. L. Bond, Academic Press, London.
3. Washburn, E. W. (1921). *Physics Review* **17**, 273
4. Autoscan Porosimeter manual.

Notation

SYMBOL	DESCRIPTION	UNITS
d	pore diameter	cm
D_s	pore surface area distribution	
D_v	pore volume distribution	
l	pore length	cm
P	pressure	psi-μm
r	pore radius	cm
S	pore surface area	cm^2
V	pore volume	cm^3
W	work	ergs
γ	surface tension	ergs/cm
θ	Mercury contact angle	

List of Figures

List of Computer Programs .

```
20 REM Routine to apply corrections to experimental points.
30 REM
40 DIM V(46), P(46)
50 CLS
60 INPUT "What is the name of the input file ";FIL1$
70 INPUT "What is the file name you will write to ";N$
80 OPEN FIL1$ FOR INPUT AS #1
90 FOR X=1 TO 46
100 INPUT #1,P(X),V(X)
110 NEXT X
120 CLOSE #1
130 V(1)=V(1)+.001
140 V(2)=V(2)+.002
150 V(3)=V(3)+.0021
160 V(4)=V(4)+.0023
170 V(5)=V(5)+.0025
180 V(6)=V(6)+.0027
190 V(7)=V(7)+.0028
200 V(8)=V(8)+.0029
210 FOR X = 9 TO 34
220 V(X)=V(X)+.003
230 NEXT X
240  V(35)=V(35)+.0029
250  V(36)=V(36)+.0029
260  V(37)=V(37)+.0028
270  V(38)=V(38)+.0028
280  V(39)=V(39)+.0027
290  V(40)=V(40)+.0026
300  V(41)=V(41)+.0026
310  V(42)=V(42)+.0025
320  V(43)=V(43)+.0024
321  V(44)=V(44)+.0023
322  V(45)=V(45)+.0023
323  V(46)=V(46)+.0022
330 OPEN "O", #1, N$
340 FOR X = 1 TO 46
350 PRINT #1,P(X),V(X)
360 NEXT X
370 CLOSE
380 END
```

```
11 REM Routine that performs inversion of data and plotting
12 REM
13 REM
14 SCREEN 0,0,0
20 KEY OFF
30 CLS
35 INPUT  "NO.OF PRESSURE POINTS";NN
40 DIM R(NN)
42 DIM D(NN)
44 DIM VOLLOG(NN)
46 DIM SURLOG(NN)
50 DIM DV(NN)
60 DIM DP(NN)
70 DIM VOLUME(NN)
80 DIM SURF(NN)
90 DIM LENGTH(NN)
100 DIM SA(NN)
110 DIM VAR(NN)
120 DIM VOL(NN)
130 DIM E$(5)
140 DIM P(NN)
150 DIM V(NN)
160 DIM DLOGD(NN)
170 INPUT "NAME OF DATA FILE";N$
175 INPUT  "MASS OF SAMPLE";M
180 OPEN "I",#1,N$
190 FOR I = 1 TO NN
200 INPUT #1,P(I),V(I)
210 NEXT I
220 REM             CALCULATE RADII CORRESPONDING TO PRESSURE DATA POINTS
230  R(1)=2*90.43/(P(1)+15)
235 D(1) = 2!*R(1)
240 FOR I = 2 TO NN
250 R(I) = 2*90.43/(P(I)+P(I-1))
260 REM                          TO ROUND VALUES OF R OFF
270 R(I) = (INT(R(I)*100000! + .5))/100000!
275 D(I) = 2!*R(I)
280 NEXT I
282 FOR I =1 TO NN
286 NEXT I
290 REM               CALCULATE THE DECIMAL LOGARITHM OF D(I)
300 FOR I = 1 TO NN
310 DLOGD(I) = (LOG(D(I))/LOG(10))
320 NEXT I
330 FOR I = 1 TO NN
350 NEXT I
360 REM                    CALCULATE DELTA V AND DELTA P
370 DV(1) = V(1)/M
380 DP(1)= P(1)
390 FOR I = 2 TO NN
400 DV(I) =( V(I) - V(I-1))/M
```

```
405 IF DV(I) < 0 THEN DV(I)=0
410 DV(I) = (INT(DV(I)*100000! + .5))/100000!
420 DP(I) = P(I) - P(I-1)
430 DP(I) = (INT(DP(I)*100000! + .5))/100000!
440 NEXT I
450 REM                          CALCULATE PORE SIZE DISTRIBUTIONS
452 REM  VOLUME(I) IS DV/DR  ,  SURF(I) IS DS/DR
454 REM  VOLLOG(I) IS DV/DLOG(D)  ,   SURLOG(I) IS DS/DLOG(D)
460 FOR I = 1 TO NN
470 VOLUME(I) = P(I)*DV(I)/(R(I)*DP(I))
480 SURF(I) = 2*VOLUME(I)/R(I)
482 VOLLOG(I) = 2.3*P(I)*DV(I)/DP(I)
484 SURLOG(I) = 8*VOLLOG(I)/D(I)
490 LENGTH(I) = 1000000!*VOLUME(I)/(3.14159*(R(I)^2))
500 NEXT I
501 FOR I = 2 TO NN-1
502 SA(I) =( SURF(I)+SURF(I-1))*(R(I-1)-R(I+1))/(4)
503 VAR(I) = SA(I)
504 NEXT I
505  SA(NN)=(SURF(NN)+SURF(NN-1))*(R(NN-1)-R(NN))/(2)
506 VAR(NN) = SA(NN)
510 PRINT "PLOTS ONLY? (Y/N)": INPUT Z$
520 IF (LEFT$(Z$,1) = "Y") OR (LEFT$(Z$,1) = "y") THEN GOTO 880
530 REM                                   PRINT OUT TABLE
540 LPRINT "  P";:LPRINT TAB(15) "DELTA P";: LPRINT TAB(30) "R";: LPRINT TAB(45)
 "V";: LPRINT TAB(60) "DELTA V"
550 LPRINT " (PSIA)  ";: LPRINT TAB(16) "(PSIA)";: LPRINT TAB(27) "(MICRON)";: L
PRINT TAB(43) "(CM^3)";: LPRINT TAB(60) "(CM^3)"
560 LPRINT
570 LPRINT
580 FOR I = 1 TO NN
590 LPRINT P(I),DP(I),R(I),V(I),DV(I)
600 NEXT I
610 LPRINT
620 LPRINT
630 LPRINT
640 LPRINT
650 LPRINT "DV/DP";:LPRINT TAB(20) "DV/DLOG(D)";:LPRINT TAB(40) "DS/DLOG(D)";:LP
RINT TAB(60) "DELTA SA"
660 LPRINT "(CM^3/PSIA)";:LPRINT TAB(20) "(CM^3/GRAM)";:LPRINT TAB(40) " (M^2/GR
AM)";:LPRINT TAB(60) "(M^2)"
670 LPRINT
680 LPRINT
690 FOR I = 1 TO NN
700 HORI = 0
710 ANS = DV(I)/DP(I) : GOSUB 850
750 ANS = VOLLOG(I) : GOSUB 830
752 ANS = SURLOG(I) : GOSUB 830
754 ANS = SA(I) : GOSUB 830
760 LPRINT
770 NEXT I
780 PRINT "PLOTS? (Y/N)": INPUT W$
790 IF (LEFT$(W$,1) = "Y") OR (LEFT$(W$,1) = "y") THEN GOTO 880
800 CLS
```

```
810 LOCATE 24,1
820 END
830 REM                    THIS ROUTINE DOES A ROUNDING OF NUMBERS
840 ANS = (INT(ANS * 100000! + .5))/100000!
850 LPRINT TAB(HORI) ANS;
860 HORI = HORI + 20
870 RETURN
880 CLS
890 LOCATE 4,10 : PRINT "CHOOSE PLOT:"
900 LOCATE 6,15 : PRINT "A --PORE VOLUME DISTRIBUTION"
910 LOCATE 7,15 : PRINT "B --PORE SURFACE AREA DISTRIBUTION"
920 LOCATE 8,15 : PRINT "C --SURFACE AREA VERSUS RADIUS"
930 LOCATE 9,15 : PRINT "D --VOLUME VERSUS RADIUS
940 LOCATE 10,15 : PRINT "E --END"
950 INPUT A$
960 IF ASC(A$) > 96 THEN A$ = CHR$(ASC(A$)-32)
970 CLS
980 SCREEN 2
990 IF A$ = "A" THEN GOSUB 1080
1000 IF A$ = "B" THEN GOSUB 1350
1010 IF A$ = "C" THEN GOSUB 1580
1020 IF A$ = "D" THEN GOSUB 1950
1030 IF A$ = "E" THEN GOTO 1050
1040 GOTO 880
1050 CLS
1060 LOCATE 24,1
1070 END
1080 E = 0
1090 C = 2
1100 FOR I = 1 TO NN
1110 VAR(I) = VOLLOG(I)
1120 NEXT I
1130 Y$ = "  "
1140 GOSUB 2340
1150 X$ = "DV/DLOGd"
1160 Z$ = "CC/GRAM "
1170 S$ = X$ + Y$ + Z$
1180 SUM = 8+C+7
1190 TOP = INT(10 - SUM/2)
1200 IF TOP > 0 GOTO 1270
```

```
1210 SUM = 8 + C
1220 S$ = X$ + Y$
1230 TOP = INT(10 - SUM/2)
1240 FOR I = 1 TO 9
1250 LOCATE (5+I),3: PRINT MID$(Z$,I,1)
1260 NEXT I
1270 FOR I = 1 TO SUM
1280 LOCATE (TOP + I),1 : PRINT MID$(S$,I,1)
1290 NEXT I
1300 FOR I = 1 TO NN
1305 IF I=NN THEN GOTO 1330
1310 CIRCLE ( 485+145*DLOGD(I),170 - (10^E)*SCALE*VOLLOG(I)),2
1315 LINE (485+145*DLOGD(I+1) ,170 - (10^E)*SCALE*VOLLOG(I+1)) -
          (485+145*DLOGD(I)  , 170 - (10^E)*SCALE*VOLLOG(I))
1320 NEXT I
1330 H$=INKEY$: IF H$ = "" THEN 1330
1340 RETURN
1350 E = 0
1360 FOR I = 1 TO NN
1370 VAR(I) = SURLOG(I)
1380 NEXT I
1390 C = 2
1400 Y$ = "  "
1410 GOSUB 2340
1420 X$ = "DS/DLOGd"
1430 Z$ = "SQ M/GRAM "
1440 SUM = 8 + C
1450 S$ = X$ + Y$
1460 TOP = INT(10 - SUM/2)
1470 FOR I = 1 TO SUM
1480 LOCATE (TOP + I),1 : PRINT MID$(S$,I,1)
1490 NEXT I
1500 FOR I = 1 TO 11
1510 LOCATE (I + 4),3 : PRINT MID$(Z$,I,1)
1520 NEXT I
1530 FOR I = 1 TO NN
1535 IF I=NN THEN GOTO 1560
1540 CIRCLE ( 485+145*DLOGD(I),170 - (10^E)*SCALE*SURLOG(I)),2
1545 LINE (485+145*DLOGD(I+1) , 170 - (10^E)*SCALE*SURLOG(I+1)) -
          (485+145*DLOGD(I) , 170 - (10^E)*SCALE*SURLOG(I))
1550 NEXT I
1560 G$ = INKEY$: IF G$ = "" THEN 1560
1570 RETURN
1580 LOCATE 1,32: PRINT "MASS OF SAMPLE";M
1582 LOCATE 1,10 : PRINT "INCREMENTAL AREA"
1590 E = 0
```

```
1660  PART=0
1670 FOR I=2 TO NN
1680 PART=PART+SA(I)
1690  NEXT I
1700  LOCATE 2,10: PRINT "Total surface in sq m/g:"
1702  LOCATE 2,35: PRINT PART
1720 C = 2
1730 Y$ = "  "
1740 GOSUB 2340
1750 X$ = "SURFACE AREA"
1770 S$ = X$ + Y$ + Z$
1780 SUM = 12+C+6
1790 TOP = INT(10 - SUM/2)
1800 IF TOP >0 THEN GOTO 1870
1810 SUM = 12+C
1820 S$ = X$ + Y$
1830 FOR I = 1 TO 6
1840 LOCATE (7+I),3 : PRINT MID$(Z$,I,1)
1850 NEXT I
1860 TOP = INT(10-SUM/2)
1870 FOR I = 1 TO SUM
1880 LOCATE (TOP + I),1 : PRINT MID$(S$,I,1)
1890 NEXT I
1900 FOR I = 1 TO NN-1
1905 IF I=NN-1 THEN GOTO 1930
1910 CIRCLE ( 485+145*DLOGD(I),170 - (10^E)*SCALE*SA(I+1)),2
1915 LINE (485+145*DLOGD(I+1) , 170 - (10^E)*SCALE*SA(I+2)) -
          (485+145*DLOGD(I)   , 170 - (10^E)*SCALE*SA(I+1))
1920 NEXT I
1930 I$=INKEY$: IF I$ = "" THEN 1930
1940 RETURN
1950 LOCATE 1,32 : PRINT "MASS OF SAMPLE";M
1954  LOCATE 1,10 : PRINT "INCREMENTAL VOLUME"
1960 E = 0
1970 FOR I = 2 TO NN-1
1980 VOL(I) =(VOLUME(I)+VOLUME(I-1))*(R(I-1)-R(I+1))/(4)
1990 VAR(I) = VOL(I)
2000 C = 2
```

```
2010 Y$ = "   "
2020 NEXT I
2030 VOL(NN) =(VOLUME(NN)+VOLUME(NN-1))*(R(NN-1)-R(NN))/(2)
2040 VAR(NN)=VOL(NN)
2070  VSUM=0
2080  FOR I = 2 TO NN
2090  VSUM=VSUM+VOL(I)
2100  NEXT I
2110  LOCATE 2,10: PRINT "Total volume in cc/g is:"
2112  LOCATE 2,35: PRINT V(46)/M
2130 GOSUB 2340
2140 X$ = "VOLUME"
2150 Z$ = "CC/G"
2160 S$ = X$ + Y$ + Z$
2170 SUM = 6 + C + 4
2180 TOP = INT(10-SUM/2)
2190 IF TOP > 0 GOTO 2260
2200 S$ = X$ + Y$
2210 SUM = 6 + C
2220 TOP = INT(10-SUM/2)
2230 FOR I = 1 TO 4
2240 LOCATE (8 + I),3: PRINT MID$(Z$,I,1)
2250 NEXT I
2260 FOR I = 1 TO SUM
2270 LOCATE (TOP + I),1 : PRINT MID$(S$,I,1)
2280 NEXT I
2290 FOR I = 1 TO NN-1
2295 IF I=NN-1 THEN GOTO 2320
2300 CIRCLE ( 485+145*DLOGD(I),170 - (10^E)*SCALE*VOL(I+1)),2
2305 LINE (485+145*DLOGD(I+1) , 170 - (10^E)*SCALE*VOL(I+2)) -
          (485+145*DLOGD(I)  ,170 - (10^E)*SCALE*VOL(I+1))
2310 NEXT I
2320 Q$ = INKEY$: IF Q$ = "" THEN 2320
2330 RETURN
2340 X = 0
2350 FOR I = 1 TO NN
2360 VAR(I) = (10^E)*VAR(I)
2370 IF VAR(I) > X THEN X = VAR(I)
2380 NEXT I
2390 X = INT(X + 1)
2400 IF X>21 THEN GOSUB 2680
2410 IF X>21 THEN GOTO 2340
2420 IF X<2 THEN GOSUB 2810
2430 IF X<2 THEN GOTO 2340
2440 SCALE = 8*INT(21/X)
2450 LABEL = INT(21/X)
2460 FOR I = 1 TO X
2470 LINE (47,170 - SCALE*I)-(50,170 - SCALE*I)
2480 IF SCALE < 16 THEN GOTO 2500
2490 LOCATE (22 - LABEL*I),4 : PRINT I
2500 NEXT I
2510 IF SCALE > 8 THEN GOTO 2550
```

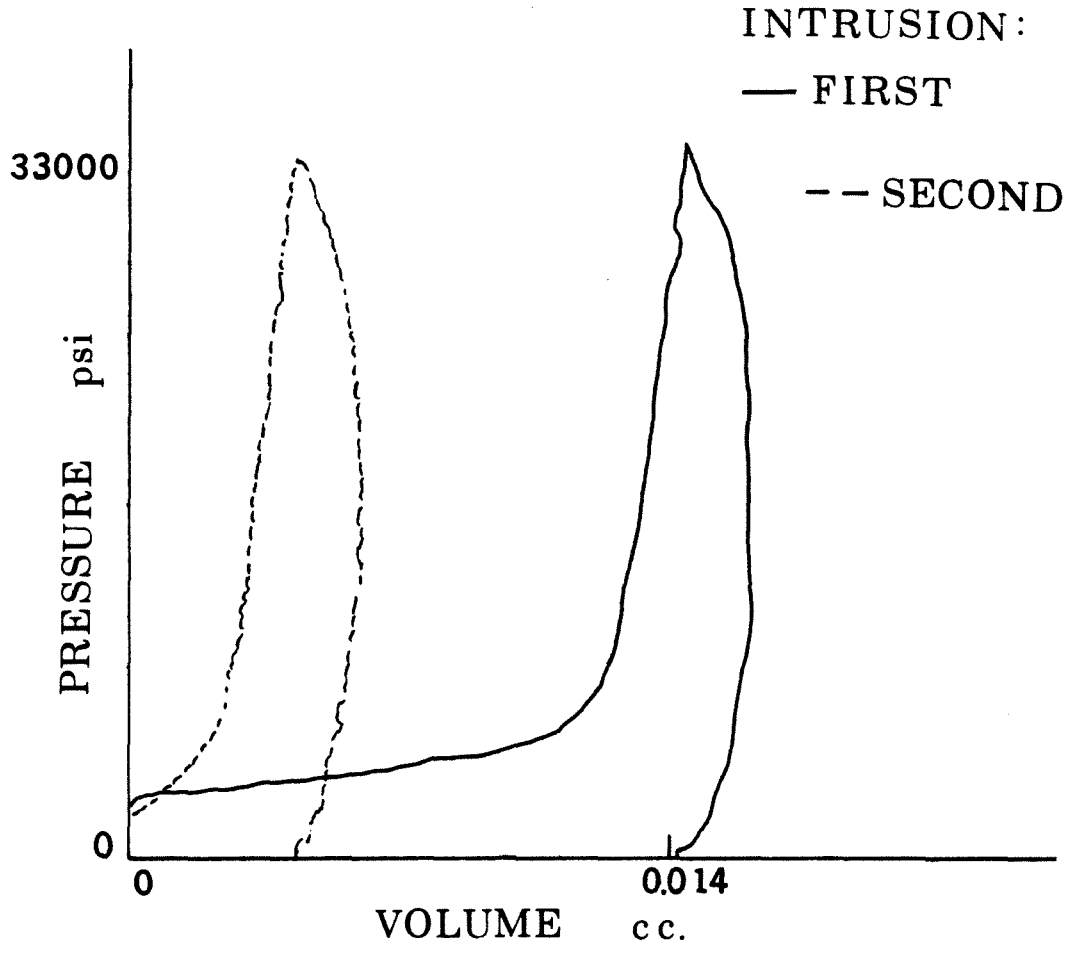

Figure 1: Mercury porosimetry raw data for the PSOC-1451 coal-char pyrolyzed at 1600 K.

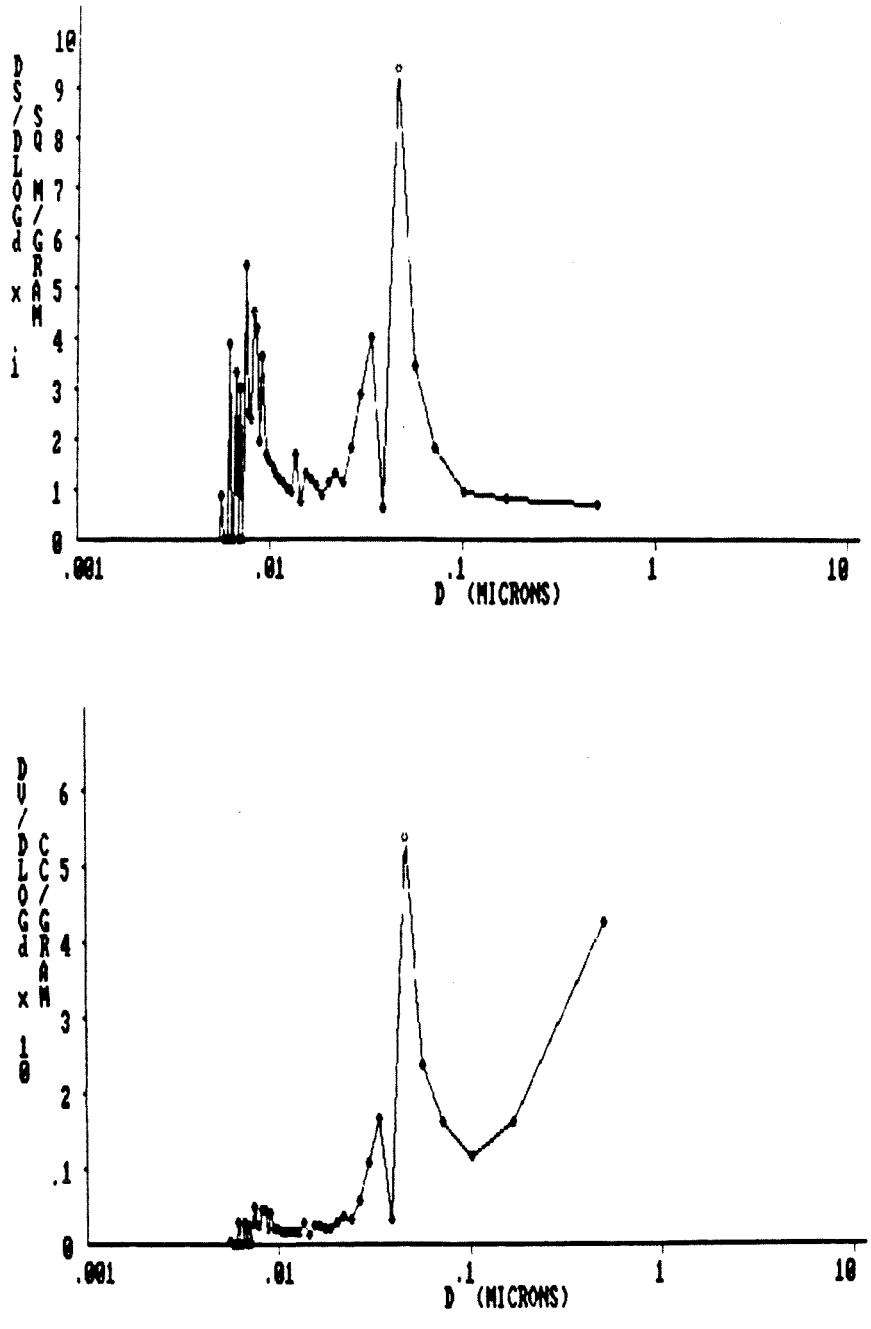

Figure 2: (a) Pore volume distribution and (b) pore surface distribution

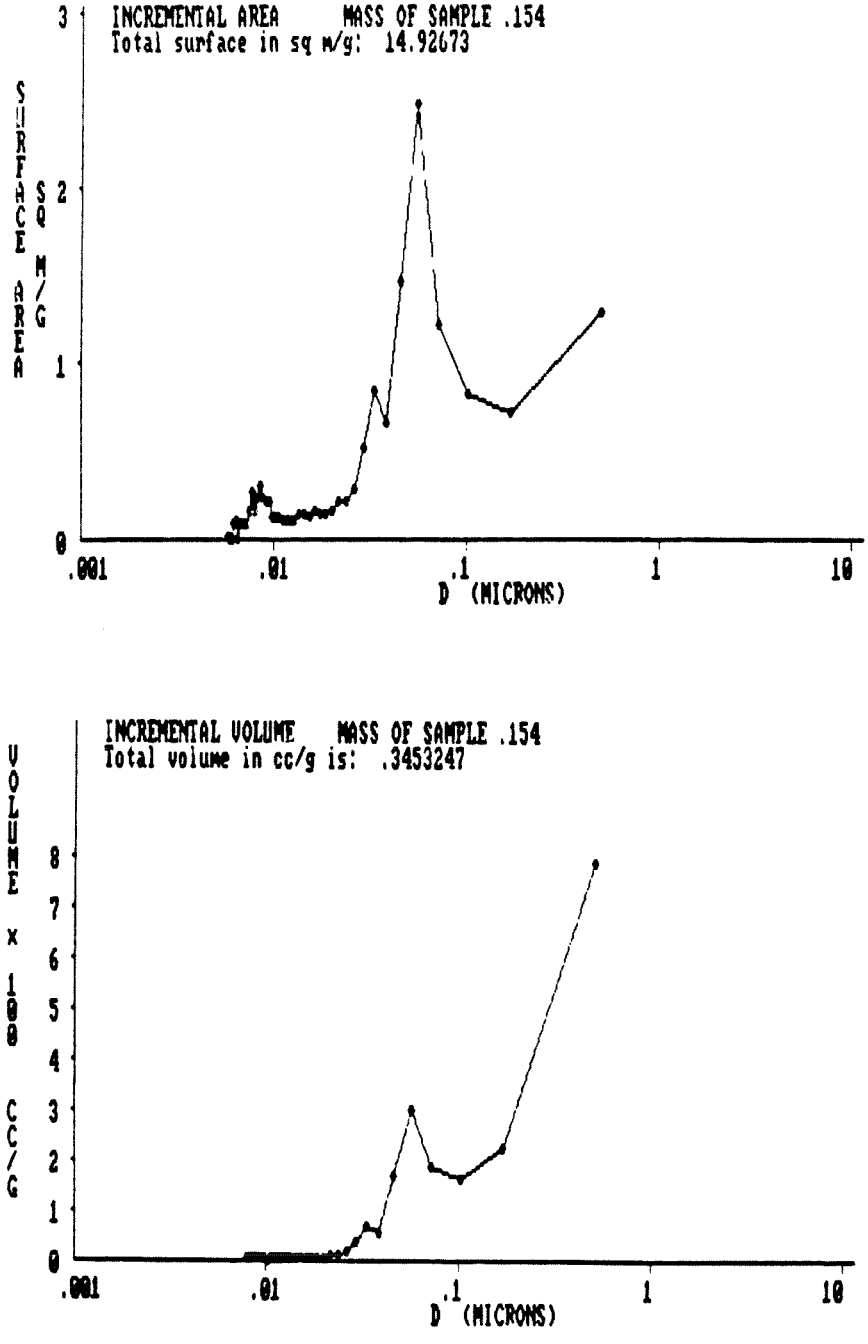

Figure 3: (d) Incremental pore volume distribution and (d) incremental pore surface area distribution.

APPENDIX 5

Corrections applied to the Small Angle X-ray Scattering data.

Small-angle scattering experiments necessitate very exacting procedures, in comparison with the requirements of wide-angle measurements. This is due, primarily, to the necessity of measuring the scattered radiation at angles at close proximity to the undeviated beam, which, in turn, requires very sharp collimation of the incident x-rays. In addition to using a well-engineered apparatus, care must be exercised in the alignment of the components, and long periods of time should be allowed for recording the weakly scattered x-rays. For the analysis of diffuse small-angle scattering it is mandatory that wavelengths other than the desired characteristic radiation (for the present work CuKα with $\lambda = 1.542\mathring{A}$ was used) be removed by the use of a crystal monochromator. However, the use of β-filtered radiation will suffice if no quantitative knowledge of the intensities and reflection profiles is desired.

The experimentally obtained intensities of *SAXS* have been presently corrected for absorption, polarization, air and background scattering, geometry of the incident beam and beam smearing effects.

Polarization factor For monochromatic radiation the polarization factor is given as:

$$1/2(1 + cos^2 2\theta). \tag{1}$$

This factor enters the equation simply because the incident beam is unpolarized.

Absorption factor For samples mounted in the radiation reflection mode the absorption factor is independent of the incident angle, θ (Culity, 1978), because of the balancing of two opposing effects. At small θ the sample area irradiated by the incident beam is large, but the effective depth of x-ray penetration is small. At large θ the irradiated area is small, but the penetration depth is large. The net effect is that the irradiated volume of the sample is constant and independent of θ. Absorption, therefore, depends only on the absorption coefficient of the material examined and causes reduction of all diffracted beams by the same factor and thus does not have to be accounted for in *relative* intensities calculation. The total diffracted intensity, in the reflection mode, is given as:

$$I_D = I_0 \frac{ab}{2\mu}, \tag{2}$$

where μ is the absorption coefficient of the material and a, b denote the volume fraction of the sample containing particles having the correct orientation for reflection of the incident beam and the fraction of the incident energy, which is deffracted by a unit volume, respectively. Here, a, b, and μ can be regarded as constants. For the transmission geometry, the diffracted intensity is given as:

$$I_D = I_0 \frac{abl}{\cos\theta} e^{-\mu l/\cos\theta}, \tag{3}$$

where l is the thickness of the sample. Therefore, after incorporating the polarization factor, P, and the absorption factor, A, the corrected intensity, I_c, is given in terms of the diffracted intensity as follows:

$$I_c = I_D/(PA), \tag{4}$$

Further corrections for background, or parasitic, scattering were made subtracting the scattered intensities generated with the empty sample holder (blank run). Moreover, corrections for the geometry of the incident beam were made for the reflection mode only. This correction was necessitated by the fact that at very small

angles, only a fraction of the incident beam falls on the sample, the rest glancing on the sample holder. As the incident angle θ increases, the width of the irradiated area increases and at a certain θ all of the beam falls on the sample. The width of incident beam on the plane of the sample, w, is given as:

$$w = \frac{2\phi R}{\sin\theta}, \tag{5}$$

where ϕ is the aperture angle of the beam (defined by parallel slits), and R is the radius at which both the x-ray source and the detector revolve around the sample. R, for the *Siemens* diffractometer used was 200.5 mm and the slits used defined an aperture angle $\phi = 0.1°$. For the existing diffractometer-sample holder geometry at incident angles bigger than 2°, all of the incident radiation fell on the sample, therefore, a geometric factor $w_\theta / w_{\theta=2°}$ multiplied only intensities corresponding to $\theta < 2°$.

At last, a correction to account for the fact that the scattering collimation system employed slits instead of pinholes to provide adequate scattered intensity was incorporated. With slit collimation, however, the detector records the scattering from a range of angles rather than from a single angle. Thus, this imperfect collimation leads to a distortion (*smearing*) of the curve of scattered intensity as a function of scattering angle. Several investigators have attempted to correct for collimation errors [2,4,6,7,8]. In this work the method of Schmidt and Hight (1960), which is based on the unsmearing equation of Kratky, Porod and Kahovec (1951), was adopted.

According to Guinier and Fournet (1955), for the geometry of long but infinitely narrow slits, the experimental scattered intensity $I_c(h)$, for a scattering angle h, is related to the perfect collimation scattered intensity $I(h)$ by:

$$I_c(h) = \int_0^\infty W(t) I\sqrt{h^2 + y^2}\, dy, \tag{6}$$

where $W(y)$ is a weighting function, the form of which depends on the collimation

system and $h = 4\pi/\lambda \sin\theta$. For slits of infinite height and negligible width, $W(y) = 1$. For this case, it can be shown [6] that the true intensity $I(h)$ can be determined from the following equation:

$$I(h) = -\frac{2}{\pi}\int_0^\infty \frac{\acute{I}_c(\sqrt{h^2+t^2})}{\sqrt{h^2+t^2}}dt. \tag{7}$$

This equation requires numerical differentiation of the experimental curve. Numerical differentiation, however, can be quite inexact, especially when applied to an experimental curve, which is known only approximately. Schmidt and Hight (1960) have shown that Eq. (7) can be modified to eliminate the need of numerical differentiation. By changing variables $s = \sqrt{h^2+t^2}$ and integration by parts it can be shown that:

$$I(h) = \frac{2}{\pi}\int_h^\infty \frac{ds}{(s^2+h^2)^{3/2}} sI_c(s). \tag{8}$$

Where the true scattered intensity is expressed in terms of the experimental curve itself, equations of the above form can be approximated numerically [9] as follows:

$$\int_h^\infty \frac{sI_c(s)ds}{(s^2-h^2)^{3/2}} = \frac{1}{j^2(\Delta h)^3}\sum_{i=0}^{\infty}\Delta_{ij}^2 sI_c(h_i), \tag{9}$$

with appropriate substitutions:

$$h = j\Delta h$$

$$h_i = (i+j)\Delta h$$

$$\Delta_{ij}^2 = -R_{i+1} + 2R_i - R_{i-1}$$

$$R_i = \Delta h(i^2+2ij)^{1/2}$$

$$\sum_{i=1}^{\infty}\Delta_{ij}^2 = R_1 - \Delta h;$$

the true scattering intensity is given by the following equation:

$$I(\Delta h) = -\frac{2}{\pi}\frac{1}{j^2}\left\{j(2j+1)^{1/2}I_c(j\Delta h) - \sum_{i=1}^{\infty}\frac{1}{\Delta h}(i+1)\left[-\Delta h\left((i+1)^2+2(i+1)j\right)^{1/2}\right.\right.$$
$$\left.\left.+2\Delta h(i^2+2ij)^{1/2} - \Delta h\left((i-1)^2+2(i-1)j\right)^{1/2}\right]I_c((i+j)\Delta h)\right\}.$$

A computer program, included herein, has been writen to implement the above corrections to the scattering curves for samples placed in either the reflection or the transmission modes.

Acknowledgements

The help of Bob Johnson in all aspects of SAXS data aquisition and analysis is greatly appreciated.

References

1. Alexander, L. E. (1969). X-Ray Diffraction Methods in Polymer Science. Wiley-Interscience, New York.

2. Chu, B. and Tan Creti, D. M. (1964). "Infinite Slit Height Corrections in Small Angle X-Ray Scattering." *Acta Crystallographica* **18**, 1083.

3. Cullity, B. D. (1978). "Elements of X-Ray Diffraction" 2^{nd} ed. Addison-Wesley, Reading Mass.

4. DuMond, J. W. M. (1947). *Physical Review* **72**, 83.

5. Glatter, O. and Kratky, O. (1982). Small Angle X-Ray Scattering Academic Press, London.

6. Guinier, A. and Fournet, G. (1955). Small Angle Scattering of X-Rays Chapman & Hall, London.

7. Klug, H. P. and Alexander, L. E. (1974). X-Ray Diffraction Proceedures 2^{nd} ed. Wiley, New York.

8. Kratky, O, Porod, G. and Kahovek, L. (1951). *Zeitschift Elektrochemie* **55**, 53.

9. Schmidt, P. W. and Hight,Jr., R. (1960). "Slit Height Corrections in Small Angle X-Ray Scattering." *Acta Crystallographica* **13**, 480.

10. Tsakalakos, T (1977). "Interdiffusion and Enhanced Elastic Modulus Effects in Composition Modulated Copper Nickel Thin Foils." North Western University, Ph.D. Thesis.

Notation

SYMBOL	DESCRIPTION	UNITS
a	sample volume fraction	
A	absorption factor	
b	incident energy fraction	
h	parameter defined in text	$\mathring{A}^{-1}$
I_0	relative incident intensity	
I_d	relative diffracted intensity	
I_c0	relative corrected intensity	
$I(h)$	relative true intensity	
l	thickness of sample	cm
R	radius of diffractometer	cm
s	parameter of integration	
t	parameter of integration	
w	width of sample	cm
$W(y)$	weighting function	
θ	incident angle	rad
λ	wavelength	$\mathring{A}$
μ	absorption coefficient	1/cm
ϕ	slit aperture angle	rad

```
c       This routine manipulates SAXRS data. Reads a data file then
c       reads the blank file and subtracts the two. Data corrections
c       are also performed.
c
c
        CHARACTER*12 INFIL1,INFIL2,OUTFIL
        REAL TH2(200),TH2R(200),TH2D(200)
        REAL INT(150), INTB(150), INTNET(150), INTSLIT(150)
        REAL INTCOR(250),INTD(150),HINTCOR(150)
        REAL HH(150),HH2(150), SS(150)
        REAL THINIT, STEP, PI,AA
        INTEGER NN, CHOISE
        REAL TOTAL, LM, DH, SUM
        REAL KK
        WRITE(*,10)
        READ(*,40) INFIL1
        WRITE(*,20)
        READ(*,40) INFIL2
        WRITE(*,*) 'ENTER NUMBER OF POINTS: '
        READ(*,*) NN
        WRITE(*,*) 'ENTER: 1 for reflection, 2 for transmision: '
        READ(*,*) CHOISE
        WRITE(*,*) 'ENTER THE INITIAL ANGLE in degrees: '
        READ(*,*) THINIT
        WRITE(*,*) 'ENTER k: '
        READ(*,*) KK
        WRITE(*,*) 'ENTER THE STEP SIZE in degrees: '
        READ(*,*) STEP
        WRITE(*,30)
        READ(*,40) OUTFIL
        OPEN(1,FILE=INFIL1,FORM='FORMATTED',STATUS='OLD')
        OPEN(2,FILE=INFIL2,FORM='FORMATTED',STATUS='OLD')
        OPEN(3,FILE=OUTFIL,FORM='FORMATTED',STATUS='NEW')
C
C       Read and write the diffraction data points and the
C       corresponding points from a blank file and take their
C       difference.
C
        PI = 3.141593
        DO 50  I=1,NN
                READ (1,*) INT(I)
                READ (2,*) INTB(I)
50      CONTINUE
        DO 60  I=1,NN
                INTNET(I) = INT(I)-INTB(I)
            IF (INTNET(I) .LT. 0.0) THEN
                INTNET(I)=0.0
            END IF
60      CONTINUE
        IF (INTNET(I) .LT. 0.0) THEN
                INTNET(I)=0.0
        END IF
C
C       Calculate the corresponding diffraction angles
        DO 80 I=1,NN
                TH2(I) = THINIT +(I-1)*STEP
                TH2R(I) = TH2(I) * 2 * PI / 360.0
C       Make corrections to the relative intensity measurements
C       First make polarization and absorbtion corrections.
C
                AA = EXP (-3.71 / SIN (TH2R(I) / 2.0))
                INTCOR(I) = INTNET(I) / ( (1 + (COS (TH2R(I))) ** 2)
     $                    * (1 - AA))
C       Make geometric corrections for experiments executed in the
C       reflection mode only.
                IF (CHOISE .EQ.1) THEN
```

```
                IF (TH2(I) .LE. 4.0) THEN
                INTCOR(I)=INTCOR(I)*(0.698 /SIN(TH2R(I)/2.0))/20.0
                ELSE
                INTCOR(I)=INTCOR(I)
                CONTINUE
                END IF
              ELSE
              CONTINUE
              END IF
80      CONTINUE
C
C       Perform the correction for the slits
C
C
        DH = TH2R(NN)/(NN * 1.0)
        DO 100 J=1,NN-1
          IF (INTCOR(J) .LE. 0.0) THEN
                GO TO 101
                ELSE
                CONTINUE
          END IF
        SUM = 0.0
        DO 110 I=1,10
        SUM = SUM + 1/DH*(I+J)*(-DH*((I+1)**2 + 2*(I+1)*J)**0.5
     $        + 2*DH*(I**2 + 2*I*J)**0.5
     $        - DH*((I-1)**2 + 2*(I-1)*J)**0.5) * INTCOR(I+J)
110     CONTINUE
        INTSLIT(J) = (2/PI/J**2)*(J*(2*J+1)**0.5*INTCOR(J) - SUM)
101     WRITE(*,*)SUM, INTCOR(J), INTSLIT(J)
100     CONTINUE
C
C       To conpensate for the last point that was not calculated
        INTSLIT(NN)=INTSLIT(NN-1)
C
C
C
C       Create data for Debye, Guinier and Porod plots
C       Parameters for a Debye plot
        DO 120 I=1,NN
                IF (INTSLIT(I) .LE. 0.0) THEN
                  GO TO 120
                  ELSE
                  CONTINUE
                END IF
                INTD(I) = INTSLIT(I)**(-1./2.)
                TH2D(I) = TH2R(I)**2
C       Parameters for Guinier and Porod plots
                HH(I) = 4*PI*(SIN(TH2R(I)/2.0))/1.5417
                SS(I) = SIN(TH2R(I))/1.5417
                HH2(I) = HH(I)**2
                HINTCOR(I) = (HH(I)**3) * INTSLIT(I)
                WRITE (3,70) INTSLIT(I),INTD(I),HINTCOR(I),
     $                       TH2R(I), TH2D(I),
     $                       HH(I), HH2(I)
120     CONTINUE
C       Perform the numerical integration to estimate the range of
C       inhomogeneity lm in this particular material
        TOTAL = 0.00
        TOTAL = HH(1) * INTSLIT(1) + HH(NN) * INTSLIT(NN)
        DO 90 I = 2, NN - 1
                IF ((I / 2) * 2 .EQ. I) THEN
                        TOTAL = TOTAL + 2 * HH(I) * INTSLIT(I)
                ELSE
                        TOTAL = TOTAL + 4 * HH(I) * INTSLIT(I)
                ENDIF
90      CONTINUE
```

```
      TOTAL = (TOTAL * HH(NN)/(NN*1.0)) / 3.0
      WRITE (*,*) TOTAL
      TOTAL = TOTAL + KK / HH(NN)
      LM = 0.0
      LM = TOTAL / KK
      WRITE (*,*) LM
      CLOSE (1)
      CLOSE (2)
      CLOSE (3)
10    FORMAT (' ENTER INPUT FILENAME:'\)
20    FORMAT (' ENTER INPUT BLANK FILENAME:'\)
30    FORMAT (' ENTER OUTPUT FILENAME:'\)
40    FORMAT(A12)
70    FORMAT (F10.2,E11.4,F12.4,2E11.4,2F10.8)
      STOP
      END
```

APPENDIX 6

Data Acquisition Methods in Two-Color Pyrometry.

Data acquisition and analog to digital conversion of the radiation intensity signals generated by the two-channel pyrometer were achieved using a *DEC PDP-11* microcomputer. Data acquisition routines AD2 and ADSET2 (listed in the following pages) were developed and linked to the data base developed by Dale Warren[1]. Sampling is activated by the operator and lasts for 0.2 s. In case that no events occur in this time interval, the operator has to reactivate sampling repeatedly until an event is recorded. To avoid this continous surveillance of combustion events in the drop tube furnace and random sampling with the two color pyrometer, a routine (FPEAK) was developed to sense, display and record oncoming signals automatically.

Briefly the system works as follows: The operator decides the time interval duration he wants to sample up to a maximum of one-quarter of a second. Subsequently, a macro rutine (ADSET2) is activated to convert analog-to-digital signals for the two channels of the pyrometer at maximum possible speed (10 kHz per channel). As soon as the memory buffer is loaded with the data sets from both channels, the routine (FPEAK) is called upon to examine the record of data from one channel only. The comparison is done by contrasting the amplitude of the generated voltages with a preset threshold value, which is dictated by the level of signal-to-noise ratio, that the operator is willing to tolerate. With this method the routine is capable of

finding a signal and of locating the onset and the end of the signal by comparison to the baseline. Furthermore, the location of the peak of the signal can be recorded by monitoring the sign of its first derivative. There is a possibility, depending on the particle feed rate, that more than one signal may be present in one record. In such cases, the beginning of the first signal and the end of the last one will be detected, and both signals, as well as all intermediate events will be recorded. Then the routine returns to the main program, the elapsed time is calculated as well as statistical data; the record is displayed on the screen, through plotting routines, and can be sectioned and stored at the discretion of the operator.

In the event that the routine (FPEAK) does not detect any peaks in the record, an error flag is displayed, operation is returned to the main program and the sampling routine (ADSET2) is activated again to load a new set of data points to the memory buffer. Subsequently, (FPEAK) is called to examine the new record and if no signal is found, an other record is acquired and examined till a signal is detected and displayed. Every record lasts for 200 ms, i.e., would be able to contain 4 to 10 signals, if they were adjacent, since most combustion events in the present study last for 10 to 50 ms. The resolution is 10 data points per millisecond. The effectiveness of the method was verified by using a function generator capable of providing square pulses of variable length and frequency.

A listing of the aforementioned routines follows.

Acknowledgements

The help of Dale Warren and Dimitri Papantoniou in exploring the intricacies of the PDP-11 environment and the data acquisition system is deeply aknowledged.

Reference

Warren D. (1986), "Nucleation and Growth of Aerosols." PhD. Thesis, Caltech.

```
C
C       ROUTINE AD2 (data aquisition)
        DIMENSION IRAW1(1200),IRAW2(1200)
        DIMENSION X(1200),Y(1200)
        BYTE FILE(20),ANSW
        VCON = 10. / 4096.
        KMAX = 1500
        ICH1 = 2
        ICH2 = 3
        TYPE 10, ICH1, ICH2
10      FORMAT(//T10,'Dual A/D Fast Sampling Program -- ',
        1 'Sampling Channels ',I2,' & ',I2 //)
12      TYPE 15
15      FORMAT('$Enter the Number of A/D Samples to Take: ')
        ACCEPT *, KOUNT
        IF (KOUNT.LE.0 .OR. KOUNT.GT.KMAX) GOTO 12
        IDIM=KOUNT
        TYPE 30
30      FORMAT('$Enter threshold (100mv=40) : ')
        ACCEPT *,IEXC
        TYPE 35
35      FORMAT('$Enter # of baseline points: ')
        ACCEPT *,NAVG
40      TYPE 50
50      FORMAT('$Hit RETURN to start sampling:')
        ACCEPT 55, JUNK
55      FORMAT(A1)
59      ITER=0
60      CALL GTIM(TINTB)
61      CALL ADSET2(ICH1,ICH2,KOUNT,IRAW1,IRAW2)
        CALL GTIM(TINTE)
        SEC = ELAPSE(TINTB,TINTE)
        CALL FPEAK (IRAW2,IDIM,IEXC,NAVG,IAVG,ICEN,INS,INE)
        ITER=ITER+1
        TYPE 70, ITER,ICEN,IAVG
70      FORMAT(/T5,'ITERATION=',I3,5X,'PEAK AT :',I4,
     $  5X,'BASELINE SIGNAL :',I4)
        IF (ITER .EQ. 500) GO TO 222
        IF (ICEN .EQ. -1) GO TO 60
        IF (ICEN .EQ. -2) GO TO 60
        IF (ICEN .EQ. -3) GO TO 60
        TYPE 150, SEC, KOUNT
150     FORMAT(' The Elapsed Time is',F10.3,' seconds for',I5 /)
        TYPE 160, INS,INE
160     FORMAT(T5,'SIGNAL STARTS AT:',I4,5X,'SIGNAL ENDS AT:',I4)
        CALL ISTAT(KOUNT,IRAW1,AV1,SD1,SL1)
        AV1 = AV1 * VCON
        SD1 = VCON * SD1
        SL1 = SL1 * VCON
        CALL ISTAT(KOUNT,IRAW2,AV2,SD2,SL2)
        AV2 = AV2 * VCON
        SD2 = SD2 * VCON
        SL2 = SL2 * VCON
        TYPE 200, 1,AV1,SD1,SL1
        TYPE 200, 2,AV2,SD2,SL2
200     FORMAT(' For Channel',I3,' Average=',F8.4,'   St.Dev.=',
        1  F8.4,'  Slope=',F9.5,' Volts')
        DO 7 I=1,KOUNT
          Y(I) = FLOAT(VCON*IRAW1(I))
          X(I) = FLOAT(I)
 7      CONTINUE
        ISTIME = 0.0
        IMIN = 1
        IMAX = KOUNT
```

```
205     IKOUNT=IMAX-IMIN+1
C       CALL RANGES(IKOUNT,X(IMIN),Y(IMIN),XMIN,XMAX,YMIN,YMAX)
        XMIN=X(IMIN)
        XMAX=X(IMAX)
        YMIN=Y(IMIN)
        YMAX=Y(IMIN)
        IF (XMIN.EQ.1) XMIN=0.
        DO 212 I=IMIN,IMAX
          IF (Y(I).LT.YMIN) YMIN=Y(I)
          IF (Y(I).GT.YMAX) YMAX=Y(I)
212     CONTINUE
        YMIN=YMIN-0.001
        YMAX=YMAX+0.001
        CALL VSETS(YMIN,YMAX,XMIN,XMAX,0)
210     CALL VXPLOT(0,X,Y)
        ISTEP = (IMAX-IMIN+1)/100
        IF (ISTEP.LT.1) ISTEP = 1
        DO 220 I = IMIN,IMAX,ISTEP
          CALL VXADD(1,X(I),Y(I))
220     CONTINUE
        CALL VPUT(24,1)
222     TYPE 225
225     FORMAT('$Select M to magnify, S to Save, R to Repeat, ',
        1  'I to Initialize, Q to Quit: ')
        ACCEPT 226,ANSW
226     FORMAT(A1)
        IF (ANSW.EQ.'S') GOTO 240
        IF (ANSW.EQ.'I') GOTO 12
        IF (ANSW.EQ.'Q') GOTO 401
        IF (ANSW.EQ.'R') GOTO 400
        IF (ANSW.EQ.'M') GOTO 229
        GOTO 222
229     TYPE 230
230     FORMAT('$Enter IMIN,IMAX : ')
        ACCEPT *, IMIN,IMAX
        IF (IMIN.GE.IMAX .OR. IMAX.GT.KOUNT) GOTO 229
        GOTO 205
240     CALL ASKFIL(3,FILE)
        CALL ASSIGN(3,FILE)
        DO 300 I=IMIN,IMAX
          WRITE(3,333) VCON*IRAW1(I),VCON*IRAW2(I)
333       FORMAT(' ',2F8.4)
300     CONTINUE
        CLOSE (UNIT=3)
400     CALL VINIT
        GO TO 59
401     STOP
        END
```

```
C
      SUBROUTINE FPEAK(IBUF,IDIM,IEXC,NAVG,IAVG,ICEN,INS,INE)
C
C     THIS ROUTINE IS USED TO DETECT SIGNALS EMITTED BY BURNING
C     COAL PARTICLES AND RECORDED BY A TWO COLOR PYROMETER
C     (THE APPROXIMATE CENTER OF THE PEAK CAN ALSO BE FOUND)
C
C
C
C     METHOD: THE CENTER OF THE PEAK IS DEFINED AS THE POINT WHICH
C         GIVES THE MAXIMUM CORRELATION OF THE SIGNAL AND A WINDOW
C         OF CONSTANT VALUE.
C
C     NOTE: THIS ROUTINE ASSUMES THAT THE FIRST "NAVG" DATA POINTS
C           REPRESENT A ZERO LEVEL IN THE SIGNAL AND THAT THE PEAK
C           OCCURS "IWIN" POINTS BEFORE THE END SPECIFIED BY "IDIM"
C
C     INPUT:     IBUF-   ARRAY CONTAINING THE SIGNAL
C
C                IDIM-    LENGTH OF ARRAY
C
C     OUTPUT:    ICEN-   INDEX TO APPROXIMATE CENTER OF THE PEAK
C
C                INS-    FIRST OCCURENCE WHEN SIGNAL EXCEEDS THRESHOLD
C                       STARTING FROM THE BEGINNING OF THE SIGNAL
C
C                INE-    FIRST OCCURENCE WHEN SIGNAL EXCEEDS THRESHOLD
C                       STARTING FROM THE END OF THE SIGNAL
C     ERRORS:    ICEN-    SET TO -1 IF NO PEAK FOUND
C
C     PARAMETERS: NAVG-  # OF POINTS TO FIND AVERAGE OVER ZERO LEVEL
C                        IN SIGNAL
C
C                  IWIN-  WIDTH OF WINDOW TO FIND PEAK
C
C                  IEXC-  ABSOLUTE VALUE THE SIGNAL MUST CHANGE BY
C                         BEFORE SEARCH FOR PEAK IS MADE
C                         100mv IS 41.
C
C
      INTEGER*2  IBUF(IDIM)
C     VIRTUAL    IBUF(IDIM)
C
C     GET ZERO LEVEL FOR START OF SIGNAL
C
      AVG=0.
      DO 10 J=1,NAVG
 10   AVG=AVG+IBUF(J)
      IAVG=AVG/NAVG
C
C     FIND ENDING ZERO LEVEL
C
      AVG=0.
      DO 15 J=IDIM-NAVG+1,IDIM
 15   AVG=AVG+IBUF(J)
      IAVGE=AVG/NAVG
C
      IWIN=IDIM-NAVG*2
C
C     TWO STATEMENTS THAT SET ERROR FLAGS FOLLOW
C
      IF (IWIN .GT. 20) GO TO 19
      ICEN=-2
      RETURN
```

```
      IF (IBUF(IDIM) .LT. IEXC/2)GO TO 19
      ICEN=-3
      RETURN
C
C     FIND STARTING INDEX WHERE SIGNAL EXCEEDS THRESHOLD
C
 19   INS=1
 20   IF ( IABS(IBUF(INS)-IAVG) .GT. IEXC ) GO TO 25
      INS=INS+1
      IF ( INS .LT. IWIN )GO TO 20
      ICEN=-1                              !SET ERROR IF SIGNAL
      RETURN                               !DOESN'T EXCEED THRESHOLD
C
C     FIND ENDING INDEX WHERE SIGNAL EXCEEDS THRESHOLD
C
 25   INE=IDIM
 28   IF ( IABS(IBUF(INE)-IAVGE) .GT. IEXC ) GO TO 30
      INE=INE-1
      GO TO 28
C     INS=INS-IWIN/2
C     INE=INE+IWIN/2
      IF ( INS .LT. 1) INS=1
      IF ( INE .GT. IDIM) INE=IDIM
C
C     LOOK FOR PEAK
C
 30   XMAX=0
      DO 50 K=INS,INE
       TMAX=0
 40    TMAX=TMAX+IABS(IBUF(K)-IAVG)
      IF ( TMAX.LE.XMAX) GO TO 50
      ICEN=K
      XMAX=TMAX
 50   CONTINUE
      RETURN
      END
```

```
;
C
        .TITLE ADSET2 -- TAKES 2 SETS OF A/D READINGS
        .GLOBL ADSET2

;       FORTRAN USAGE:  CALL ADSETS(IC1,IC2,KOUNT,IAR1,IAR2)
;               ICH1 = FIRST A/D CHANNEL NUMBER (0-15 NORMALLY)
;               ICH2 = SECOND A/D CHANNEL NUMBER (0-15)
;               KOUNT = NUMBER OF READINGS TO TAKE
;               IAR1 = FIRST INTEGER ARRAY SPACE FOR RAW A/D VALUES
;               IAR2 = SECONDE INTEGER ARRAY SPACE FOR RAW A/D VALUES
;       NOTE THAT ICH1, ICH2, AND KOUNT ARE INTEGER*2 VARIABLES, AND
;        IAR1 AND IAR2 ARE INTEGER*2 ARRAYS DIMENSIONED TO AT LEAST KOUNT

CDSTAT=170400
GNCHAD=170402
ADDATA=170402

ADSET2::
        TST     (R5)+           ; IGNORE # OF ARGUMENTS
        MOV     @(R5)+,R1       ; R1 = ICH1
        MOV     @(R5)+,R2       ; R2 = ICH2
        MOV     @(R5)+,R0       ; R0 = KOUNT
        MOV     (R5)+,R3        ; R3 = ADDRESS OF IAR1
        MOV     (R5)+,R4        ; R4 = ADDRESS OF IAR2
NEXT:   MOV     R1,@#GNCHAD     ; START CONVERSION
LOOP1:  TST     @#CDSTAT        ; A/D CONVERSION DONE?
        BGE     LOOP1           ; LOOP UNTIL DONE
        MOV     @#ADDATA,(R3)+  ; SAVE RAW DATA IN IAR1
        MOV     R2,@#GNCHAD     ; START ICH2 CONVERSION
LOOP2:  TST     @#CDSTAT        ; A/D CONVERSION DONE?
        BGE     LOOP2
        MOV     @#ADDATA,(R4)+  ; SAVE RAW DATA IN IAR2
        DEC     R0              ; DECREMENT KOUNT
        BNE     NEXT            ; NEXT SAMPLE UNLESS R2=0
        RETURN                  ; ALL DONE
        .END
```

APPENDIX 7

Detailed Analysis of Intraparticle Transport and Gas Phase Equations for the Combustion of a Single Burning Porous Char Particle.

The equations listed in the present appendix are developed based on the model of Loewenberg *et al.* (1987) and Gavalas (1981,1982). The main difference is that the current analysis incorporates provisions for cenospheric particles and particles containing mineral matter. Such a particle is shown in Fig. 1. The present work incorporated the option of using either cylindrical voids or spherical or a combination of both, depending upon the particular char. The axes of the capillaries and the centers of the spherical voids are spacially uncorrelated; thus, consideration of pore overlap between voids of all sizes in the distribution is an implicit feature of the model.

The only heterogeneous reaction considered is

$$C + 1/2O_2 = CO \tag{1}$$

The effective diffusivity within the ash layer can be estimated by assuming that the layer consists of randomly packed, 1.0μ hard-sphere ash particles. A void fraction of 0.25 is assumed as discussed below. A conservative estimate of the diffusional resistance of the ash layer is then determined by considering an ash layer of thickness equal to the (initial) characteristic dimension of the char and using an upper bound

for the oxygen flux based upon observed rates and the assumed stoiciometry given by Equation (2). The result indicates that the diffusional resistance of the ash layer is negligible, thus justifying Assumption (viii).

The model of intraparticle transport developed in this section is also applicable to cenospheric char particles. The cenopshere is modelled as a spherical, carbonaceous shell enclosing a large, single central void. Two limiting cases are treated:

(I) Oxygen diffuses into the char solely through the external surface of the cenosphere shell. The central void inaccessible.

(II) The interior of the cenosphere shell "communicates" to the external surface through several large "blow-holes" in the cenosphere shell (Gavalas *et al.* (1985)). Oxygen penetrates the central void.

Fig. 1. illustrates the most general example of case (II) for a partially combusted cenospheric char particle containing mineral matter. The instantaneous outer radii of the particle and ash layer are denoted $r_{o,p}(t)$ and $r_{o,a}(t)$, respectively. Similarly, the corresponding instantaneous inner radii are denoted $r_{i,p}(t)$ and $r_{i,a}(t)$. Initially, all ash is contained within the char; thus, the initial inner and outer ash radii coincide with the initial particle radii, $r_{o,p0}$ and $r_{i,p0}$. As shown below, case (I) implies that the inner shell radius is constant; thus: $r_{i,a}(t) = r_{i,p}(t) = r_{i,p0}$. Solid, spherical char is a subcategory of case (I) with $r_{i,p0} = 0$. Another special case is synthetic chars, free of mineral matter, which implies: $r_{i,a}(t) = r_{i,p}(t)$ and $r_{i,a}(t) = r_{i,p}(t)$.

Within the char, pseudosteady oxygen concentration is described by:

$$r_{i,p}(t) \leq r \leq r_{o,p}(t) \quad : \quad \frac{1}{r^2}\frac{\partial}{\partial r}\left(r^2 \delta_e(q) \frac{\partial c}{\partial r}\right) = b R_{in}(c, T_p) S(q), \tag{3}$$

with boundary conditions listed below, and the local conversion variable is given by:

$$r_{i,p}(t) \leq r \leq r_{o,p}(t) \quad : \quad \frac{\partial q}{\partial t} = \frac{1}{\rho_T} R_{in}(c, T_p), \tag{4}$$

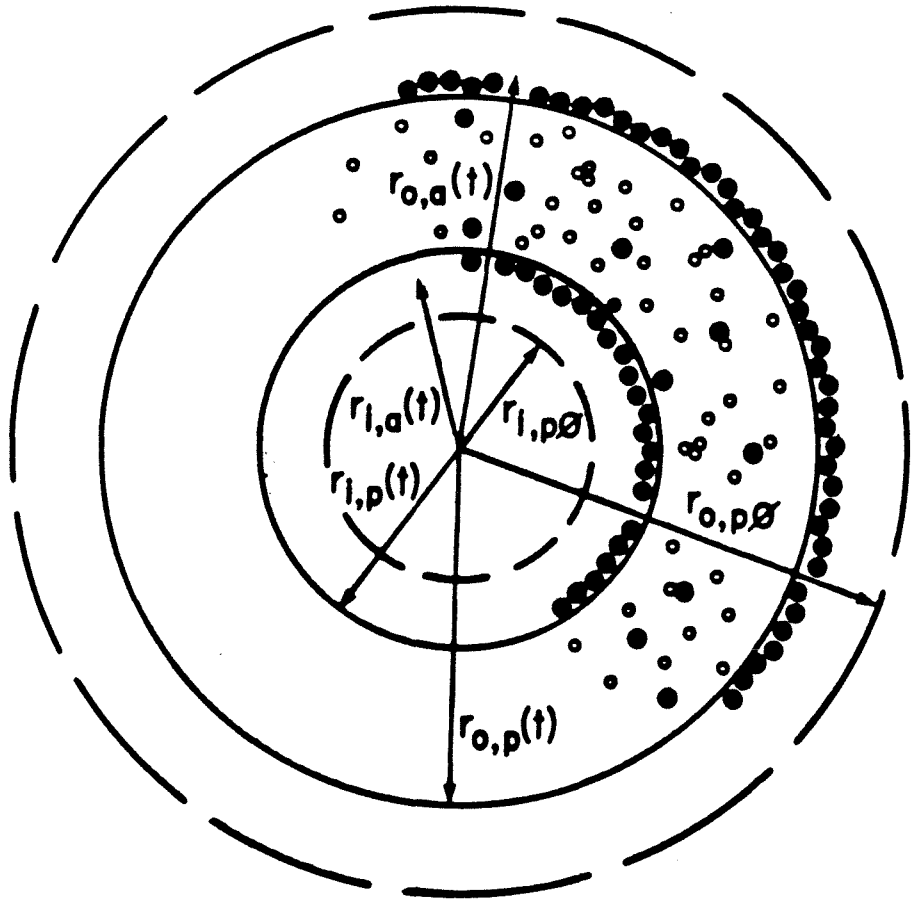

Figure 1: Schematic of the most general case of a burning spherical particle assumed by the model: a cenosphere containing mineral matter.

with the initial condition:

$$t = 0 \quad : \quad q = 0. \tag{5}$$

The oxygen concentration within the outer ash layer is given by:

$$r_{o,p}(t) \leq r \leq r_{o,a}(t) \quad : \quad c = c_s, \tag{6}$$

which follows from Assumption (viii) and serves as the outer boundary condition for Equation (3). For case (II) described above, the oxygen concentration within the inner ash layer is given by:

$$r_{i,a}(t) \leq r \leq r_{i,p}(t) \quad : \quad c = c_s, \tag{7a}$$

which similarly supplies the inner boundary condition for Equation (3). However, if oxygen cannot penetrate the central void (case (I)), no inner ash layer develops during combustion as shown below and the boundary condition at the inner cenosphere surface is:

$$r = r_{i,p0} \quad : \quad \frac{\partial c}{\partial r} = 0, \quad \frac{\partial q}{\partial r} = 0, \tag{7b}$$

The outer particle radius is described by:

$$r = r_{o,p}(t) \quad : \quad r_{o,p}(t) = r_{o,p0}, \quad q < q^* \tag{8a}$$

$$r = r_{o,p}(t) \quad : \quad \frac{dr_{o,p}}{dt} = -\left(\frac{\partial q/\partial t}{\partial q/\partial r}\right)_{r=r_{o,p}}, \quad q = q^*. \tag{8b}$$

The inner particle radius is similarly given by:

$$r = r_{i,p}(t) \quad : \quad r_{i,p}(t) = r_{i,p0}, \quad q < q^*. \tag{9a}$$

$$r = r_{i,p}(t) \quad : \quad \frac{dr_{i,p}}{dt} = -\left(\frac{\partial q/\partial t}{\partial q/\partial r}\right)_{r=r_{i,p}}, \quad q = q^* \tag{9b}$$

The radius of the outer ash layer is given by:

$$r_{o,p}(t) = r_{o,p0} \quad : \quad r_{o,a}(t) = r_{o,p0} \tag{10a}$$

$$\frac{dr_{o,a}}{dt} = \left(\frac{r_{o,p}}{r_{o,a}}\right)^2 \left(\frac{1-\epsilon_a-v_a}{1-\epsilon_a}\right) \frac{dr_{o,p}}{dt} \tag{10b}$$

and the inner ash layer is similarly described:

$$r_{i,p}(t) = r_{i,p0} \quad : \quad r_{i,a}(t) = r_{i,p0} \tag{11a}$$

$$\frac{dr_{i,a}}{dt} = \left(\frac{r_{i,p}}{r_{i,a}}\right)^2 \left(\frac{1-\epsilon_a-v_a}{1-\epsilon_a}\right) \frac{dr_{i,p}}{dt}, \tag{11b}$$

where $1-\epsilon_a$ is the solid volume fraction within the ash layer and v_a is the volume fraction of ash within the char. If $v_a = 0$, the ash radii coincide with the particle radii, as implied by the above equations. The intrinsic rate, $R_{in}(c, T_p)$, is given in terms of grams of carbon and the conservation equations are for moles of oxygen; thus, we introduce the stoichiometric factor, $b = 1/24$.

Equations (8) and (9) result from the observation that, initially, a particle burns with constant size until the surface porosity reaches a critical value, ϵ^*, which causes fragmentation of the local carbonaceous matrix. At that instant, the inner and outer boundaries start receeding with velocities $dr_{i,p}/dt$ and $dr_{o,p}/dt$, respectively, given by Equations (8b) and (9b). The quantity, q^*, is the value of the local conversion variable at the onset of fragmentation (Gavalas, 1981) and is defined by:

$$\epsilon(q^*) = \epsilon^*. \tag{12}$$

We chose ϵ^* equal to 0.8 (Loewenberg *et al.* (1987)), although the results are quite insensitive to the precise value chosen for ϵ^* (Gavalas (1981)). Equations (10) and (11) are derived from a volume balance on the mineral matter contained within the char and are based upon Assumption (vii).

In case (I), oxygen concentration is a monotonically increasing function of radial position, r, for fixed time, t. Then, assuming that the intrinsic rate, $R_{in}(c, T_p)$, is a monotonically increasing function of oxygen concentration (*e.g.*, first-order kinetics) implies that $q(r,t)$ is also a monotonically increasing function of r (for fixed t) according to Equations (3) and (5). Equations (8) and (9) imply that $q(r,t)$ is

bounded above by q^*. Thus, in case (I), $q < q^*$ for all $r < r_{o,p}(t)$ and , in particular, at $r = r_{i,p}(t)$, $q < q^*$. Therefore, according to Equations (9) and (11), we obtain the result:

$$r_{i,a}(t) = r_{i,p}(t) = r_{i,p0} \qquad \text{case (I)}, \tag{13}$$

which indicates that the inner surface neither recedes nor forms an ash layer as claimed above.

Solution of the above equations allows calculation of the total mass flux, F_p^T, at the particle surface:

$$F_p^T = F_p + F_p^* + F_p^v, \tag{14}$$

where F_p is the mass flux at the particle surface, resulting from chemical reaction within the particle, F_p^* is the mass flux due to fragmentation, and F_p^v is the mass flux which results from devolatilization during a brief period in the initial phase of the combustion process. The above mass fluxes can be computed based upon the surface area of the outer ash layer; thus, F_p and F_p^* are given, respectively, by:

$$F_p = \frac{1 - v_a}{b\, r_{o,a}^2} \left[r_{o,p}^2 \delta_e \frac{\partial c}{\partial r}|_{r=r_{o,p}} - r_{i,p}^2 \delta_e \frac{\partial c}{\partial r}|_{r=r_{i,p}} \right] \tag{15}$$

$$F_p^* = \rho^* \frac{1 - v_a}{r_{o,a}^2} \left[r_{i,p}^2 \frac{dr_{i,p}}{dt} - r_{o,p}^2 \frac{dr_{o,p}}{dt} \right], \tag{16}$$

where ρ^* is the density of the carbon matrix at the particle surface and corresponds to local conversion $q = q^*$ and local porosity ϵ^*. The factor $(1 - v_a)$ results from the presence of mineral matter, inert to reaction with oxygen, present within the char. For case (I), $\frac{\partial c}{\partial r}|_{r=r_{i,p}} = \frac{dr_{i,p}}{dt} = 0$ according to Equations (7b) and (13), respectively. The mass flux of volatile species, F_p^v, will be determined in the following section where the dynamic equation for particle temperature is derived.

Equations (6), (7a) and (15) couple the intraparticle equations to the gas-phase equations. The distinction between total mass flux, F_p^T, and mass flux due to chemical reaction, F_p, follows from the argument of Loewenberg *et al.* (1987), that

detached char fragments move out of the particle's sphere of influence in a fraction of a millisecond as a consequence of Stefan flow. Therefore, these char fragments burn in the free stream and have little influence upon the film transport.

An important special case within the framework of Equations (3) - (9) is the high Thiele modulus limit, where the particle burns at nearly constant density and receeding particle surface(s), $r_{i,p}(t)$ and $r_{o,p}(t)$. In this limiting case, the solution approach outlined above can be simplified drastically by exploiting a closed-form solution of the intraparticle problem that was developed by Gavalas (1981) for the regime of strong pore diffusion resistance. Gavalas considered the pseudosteady situation in which the surface velocity, $dr_{o,p}/dt$, has reached a constant velocity. Here, the result is also applied to cenospheric char particles. This approach eliminates the intraparticle conversion variables, reducing the dynamical equations from one hundred or more to five: for the particle temperature, for both shell radii and for both ash layer radii. According to this method, Equations (3) - (9) yield the following solution:

$$dr_{o,p}/dt = -\frac{1}{b^{1/2}\rho_T}\frac{I^{1/2}}{J^{1/2}}, \tag{17}$$

where $I^{1/2}$ and $J^{1/2}$ are simple quadratures which describe kinetic and physical parameters respectively:

$$I = \int_0^{c_*} R_{in}(c, T_p)dc, \tag{18}$$

$$J = \int_0^{q^*} \frac{\epsilon(q) - \epsilon_{T_0}}{\delta_e(q)}dq. \tag{19}$$

The inner particle radius is given by:

$$dr_{i,p}/dt = 0 \qquad \text{case(I)} \tag{20a}$$

$$dr_{i,p}/dt = -dr_{o,p}/dt \qquad \text{case(II)}. \tag{20b}$$

The total mass flux is simply the product of surface velocity and the (initial)

particle density; Equation (14) becomes:

$$F_p^T = \rho_0 \frac{1 - v_a}{r_{o,a}^2} \left[r_{i,p}^2 \frac{dr_{i,p}}{dt} - r_{o,p}^2 \frac{dr_{o,p}}{dt} \right]. \tag{21}$$

The mass flux that results from fragment shedding, F_p^*, is given by Equation (16); therefore, the mass flux given by chemical reaction within the particle becomes:

$$F_p = \frac{(\rho_0 - \rho^*)(1 - v_a)}{r_{o,a}^2} \left[r_{i,p}^2 \frac{dr_{i,p}}{dt} - r_{o,p}^2 \frac{dr_{o,p}}{dt} \right]. \tag{22}$$

Equations (10) and (11) are then required to determine the thickness of the outer (and inner) ash layer(s). The above analytical solution remains coupled to the gas-phase equations through c_s in the upper limit of integration in Equation (18).

Loewenberg *et al.* (1987) compared the results of the above semi-analytical solution with those of the full numerical solution and found fair agreement for Thiele moduli larger than 10 and excellent agreement for Thiele moduli larger than 40. Thus, the simplified intraparticle solution procedure can be successfully employed in the regime of strong pore diffusion resistance. This will be shown again herein by comparison with the results of the full solution of Equations (3) - (9).

The following section is concerned with heat and mass transport from the particle surface to the free stream. In the first part of the section, algebraic expressions for the pseudosteady mass and energy fluxes are derived and evaluated at the particle surface, which serve as a nonlinear boundary condition of the intraparticle problem. In the second part the equation describing the particle temperature is determined. Throughout the gas-phase analysis, the following will be assumed:

(i) The temperature and concentration profiles are at steady state with respect to the dynamical quantities T_p, $r_{o,p}$, $r_{i,p}$, $r_{o,a}$, $r_{i,a}$, and $q(r,t)$.

(ii) The gas-phase oxidation of CO to CO_2 takes place in the free stream and therefore does not appear in the species balances.

(iii) The mass flux that results from the combustion of volatiles (if any) is negligible by comparison to the mass flux resulting from the heterogeneous reaction (2) and similarly does not affect the species balances. However, the initial heating effect from the combustion of volatiles is retained.

(iv) Mass transfer is described by ternary diffusion involving O_2, CO and "inert," the latter including N_2, CO_2 and the combustion products that result from devolatilization. The three binary diffusion coefficients are equal but not constant.

(v) The gas phase is transparent to radiation, neither absorbing nor emitting radiation.

(vi) The fluxes induced by thermal and pressure gradients are insignificant.

Assumption (iii) follows from the observation that devolatilization occurs for only a very brief time allowing negligible conversion. For most of the combustion process, the mass flux of volatiles at the particle surface, F_p^v, and associated energy flux, e_v, are negligible; thus, we shall neglect the coupling to the mass and energy fluxes resulting from reaction (2). Although conversion is slight, significant particle heating is observed during the devolatization period and has a dominant influence upon particle ignition. Having based the mass flux due to chemical reaction within the particle, F_p, upon the area of the outer ash layer according to Equation (15), the gas-phase analysis is the same for all char particles treated herein.

Denoting by Y_i and F_i the mass fraction and mass flux of the i^{th} component (O_2 : i=1, CO : i=2, inert : i=3), we can write the pseudosteady component balances as:

$$r^2 F_i = r_{o,a}^2(t) F_{ip}, \tag{23}$$

where F_{ip} denotes the mass flux of the i^{th} component at the surface of the outer ash layer. The fluxes, F_i, are related by the Stefan-Maxwell equations:

$$\nabla Y_i = \sum_j \frac{1}{\rho_g(T) D_{ij}(T)} (Y_i F_j - Y_j F_i), \tag{24}$$

where the contributions of pressure and temperature gradients have been neglected according to Assumption (vi). Using Assumption (iv) above: $D_{12} = D_{13} = D_{23} = D$ simplifies this equation to :

$$F_i = -\rho_g(T) D(T) \frac{dY_i}{dr} + F Y_i, \tag{25}$$

where $F = \sum_i F_i$ is the total mass flux satisfying:

$$r^2 F = r_{o,a}^2(t) F_p. \tag{26}$$

The stoichiometry of the reaction given by Equation (2) yields the relationships:

$$F_{3p} = 0, \quad F_{1p} = -\frac{4}{3} F_p, \quad F_{2p} = \frac{7}{3} F_p. \tag{27}$$

Introducing (26) and (27) into (25), we obtain by suitable linear combination:

$$\rho_g(T) D(T) r^2 \frac{dZ}{dr} = r_{o,a}^2(t) F_p Z, \tag{28}$$

where

$$Z = \frac{Y_1}{4} + \frac{Y_2}{7}. \tag{29}$$

Equation (25) for component 3 (N_2) reads:

$$\rho_g(T) D(T) r^2 \frac{dY_3}{dr} = r_{o,a}^2(t) F_p Y_3. \tag{30}$$

Division of Equation (28) by (30) gives:

$$\frac{dZ}{dY_3} = \frac{Z}{Y_3} \tag{31}$$

with the free stream boundary condition:

$$Y_3 = Y_{3\infty} \quad : \quad Z = Z_\infty = \frac{Y_{1\infty}}{4} + \frac{Y_{2\infty}}{7}. \tag{32}$$

It follows:

$$Z = \frac{Y_1}{4} + \frac{Y_2}{7} = \frac{Z_\infty}{Y_{3\infty}} Y_3. \tag{33}$$

This equation is solved along with $\sum_i Y_i = 1$ to express Y_2 and Y_3 in terms of Y_1:

$$Y_2 = \frac{7A}{7A+1} - \frac{7(4A+1)}{4(7A+1)} Y_1 \tag{34}$$

$$Y_3 = \frac{1}{7A+1} + \frac{3}{4(7A+1)} Y_1, \tag{35}$$

where A is given by:

$$A = \frac{1}{Y_{3\infty}} \left(\frac{Y_{1\infty}}{4} + \frac{Y_{2\infty}}{7} \right), \tag{36}$$

The pseudosteady energy equation for a gas transparent to radiation is:

$$r^2 \left[-\lambda(T) \frac{dT}{dr} + \sum_i F_i \bar{H}_i \right] = r_{o,a}^2(t) e_p \tag{37}$$

where

$$e_p = -\lambda(T) \frac{dT}{dr} \Big|_{r=r_{o,a}(t)} + \sum_i F_{i,p} \bar{H}_i \tag{38}$$

By using Equations (26) and (30), (37) is rewritten as:

$$r^2 \lambda(T) \frac{dT}{dr} = r_{o,a}^2(t) \left[h(T) F_p - e_p \right] \tag{39}$$

with boundary conditions:

$$\begin{aligned} r = r_{o,a}(t) \quad &: \quad T = T_p \\ r \to \infty \quad &: \quad T \to T_\infty, \end{aligned} \tag{40}$$

where $h(T)$ is given by:

$$h(T) = \frac{1}{3} \left[7\bar{H}_2(T) - 4\bar{H}_1(T) \right]. \tag{41}$$

Using Equations (23),(25),(26) and (27), the balance for component 1 (oxygen) becomes:

$$r^2 \rho_g(T) D(T) \frac{dY_1}{dr} = r_{o,a}^2(t) F_p \left(Y_1 + \frac{4}{3} \right). \tag{42}$$

We divide Equation (42) by Equation (39) to obtain:

$$\frac{\rho_g(T)D(T)}{\lambda(T)}\frac{dY_1}{dT} = \frac{\frac{4}{3}+Y_1}{h(T)-\gamma_p} \tag{43}$$

with boundary conditions:

$$T = T_\infty \quad : \quad Y_{1\infty}$$

$$T = T_p \quad : \quad Y_{1p}, \tag{44}$$

where γ_p is the ratio of energy flux to mass flux:

$$\gamma_p = \frac{e_p}{F_p}. \tag{45}$$

Integrating Equation (39) and invoking (45), it is obtained:

$$\int_{T_\infty}^{T_p} \frac{\lambda(T)dT}{\gamma_p - h(T)} = r_{o,a}^2(t)F_p. \tag{46}$$

Similarly, Equation (43) yields by integration:

$$\ln\left(\frac{Y_{1\infty}+\frac{4}{3}}{Y_{1p}+\frac{4}{3}}\right) = \int_{T_\infty}^{T_p} \frac{\lambda(T)}{\rho_g(T)D(T)}\frac{1}{\gamma_p - h(T)}dT. \tag{47}$$

Equations (46) and (47) are the algebraic expressions for the mass and energy fluxes at the particle surface. The oxygen concentration at the particle surface, c_s, can be expressed in terms of species mass fractions at the particle surface.

$$c_s = \frac{1}{R_g T_p}\frac{Y_{1p}/32}{Y_{1p}/32 + Y_{2p}/28 + Y_{3p}/28}. \tag{48}$$

Equations (34) - (36) then allow c_s to be expressed solely in terms of the mass fraction of oxygen at the particle surface, Y_{1p}. Equations (46), (47) and (48) couple to Equations (6), (7a), and (15) from the intraparticle problem via the quantities c_s and F_p.

The particle energy balance can be written as:

$$\frac{d}{dt}\int_{V_p} \rho\bar{U}\,dV_p = -4\pi r_{o,a}^2(t)(e_p + e_R + e_v), \tag{49}$$

where

$$e_R = \sigma(\varepsilon_p {T_p}^4 - \varepsilon_\infty {T_\infty}^4) \tag{50}$$

is the radiative flux and e_v is the energy flux that results from the combustion of volatiles and is calculated below. In view of the assumed uniform intraparticle temperature profile, (49) is rewritten as:

$$m_p c_{p_c} \frac{dT_p}{dt} = 4\pi r_{o,a}^2(t) \left[F_p \bar{H}_c(T_p) - F_p \gamma_p - e_R - e_v \right], \tag{51}$$

having made the additional approximation: $c_v \simeq c_p$.

The reference states for the enthalpies are chosen as: $\bar{H}_1(T_\infty) = 0$, $\bar{H}_c(T_\infty) = 0$, which implies

$$\bar{H}_2(T) = \frac{1}{28} \Delta H(T_\infty), \tag{52}$$

where ΔH is the heat of reaction (2). Thus, the quantity $h(T)$ defined by Equation (41) is given by :

$$h(T) = \frac{1}{12} \left[\Delta H(T_\infty) + \int_{T_\infty}^{T_p} (\tilde{c}_{p_2} - \frac{1}{2} \tilde{c}_{p_1}) dT \right]. \tag{53}$$

Equation (51) becomes:

$$m_p c_{p_c} \frac{dT_p}{dt} = 4\pi r_{o,a}(t)^2 \left[F_p \int_{T_\infty}^{T_p} c_{p_c} dT - F_p \gamma_p - e_R - e_v \right]. \tag{54}$$

The energy flux, e_v, which results from the combustion of volatiles will be calculated next. The devolatilization process is modelled as a diffusion-limited process in which volatiles, initially uniformly distributed throughout the char, diffuse to the particle surface where, under certain empirically determined conditions, rapid oxidation occurs. Accordingly, the process is described by the unsteady diffusion/heat equation:

$$D_v \frac{1}{r^2} \frac{\partial}{\partial r} (r^2 \frac{\partial u}{\partial r}) = \frac{\partial u}{\partial t} \tag{55}$$

with initial condition:

$$t = 0 \quad : \quad u = u_0, \tag{56}$$

and boundary conditions that depend upon whether the central void (if any) is assumed accessible (case (II)) or not (case(I)) assumed. The boundary condition at the outer surface is:

$$r = r_{o,p0} \quad : \quad u = 0 \tag{57}$$

and at the inner surface:

$$r = r_{i,p0} \quad : \quad \frac{\partial u}{\partial r} = 0 \tag{58a}$$

applies if the central void is inaccessible or the particle is solid, whereas

$$r = r_{i,p0} \quad : \quad u = 0, \tag{58b}$$

if it is penetrated by oxygen, where u is the instantaneous, pointwise density of volatile species, u_0 is the initial (uniform) density, and D_v is the (average) diffusivity of the volatile species through the char. Assumption (iii) allows the use of the initial particle radii, $r_{i,p0}$ and $r_{o,p0}$ in the boundary conditions (57) and (58).

The resulting energy flux is given by:

$$e_v = F_p^v \Delta \bar{H}_v X_v, \tag{59}$$

where F_p^v is the mass flux of volatile species and is obtained by solution of Equations (55) - (58). $\Delta \bar{H}_v$ is the heat of combustion of the volatile species, which depends upon the particular volatile and assumed stoichiometry, and X_v is the extent of volatile conversion at the particle surface. Under conditions of high-temperature and oxygen concentration, complete conversion of the volatiles may occur at the particle surface ($X_v \approx 1$), whereas under other conditions (*e.g.*, $Y_{1,\infty} << 1$), the volatiles may burn only in the free-stream ($X_v \approx 0$), having no influence upon the particle energy balance (Senior (1984)). The quantity, $\Delta \bar{H}_v$, is, in all cases, negative; thus, the energy flux associated with devolatilization is negative and enhances particle heat-up during the initial phase of combustion according to Equation (54).

Equations (55) - (58) are solved by elementary methods to obtain, F_p^v, the flux of volatile species at the particle surface. Inserting the result into Equation (59)

and multiplying by the (exterior) surface area of the particle, $4\pi r_{o,p0}^2$, yields:

$$4\pi r_{o,p0}^2 e_v = \frac{4\pi r_{o,p0}^3}{3} u_0 \Delta \bar{H}_v X_v \frac{6}{\pi^2 \tau_v} \sum_{n=1}^{\infty} \exp(-n^2 t/\tau_v) \tag{60}$$

for spherical particles and

$$4\pi r_{o,p0}^2 e_v = 4\pi r_{o,p0}^2 (r_{o,p0} - r_{i,p0}) u_0 \Delta \bar{H}_v X_v \frac{8}{\pi^2 \tau_v} \sum_{n=0}^{\infty} \exp(-(2n+1)^2 t/\tau_v) \tag{61}$$

for cenospheric particles independent of the assumed accessibility of the central void (case (I) or case (II)). The result for cenospheres incorporates the approximation:

$$\frac{r_{o,p0} - r_{i,p0}}{r_{o,p0}} << 1, \tag{62}$$

thereby neglecting the curvature of the cenosphere shell, which is reasonable for the cenospheres considered in this paper and allows the cenosphere shell to be modelled as a slab with thickness $r_{o,p0} - r_{i,p0}$. The quantity τ_v is the characteristic time for the devolatilization process and is given by:

$$\tau_v = \frac{r_{o,p0}^2}{\pi^2 D_v} \tag{63a}$$

$$\tau_v = \frac{4(r_{o,p0} - r_{i,p0})^2}{\pi^2 D_v} \tag{63b}$$

$$\tau_v = \frac{(r_{o,p0} - r_{i,p0})^2}{\pi^2 D_v} \tag{63c}$$

for a spherical particle, and cenospheres with assumed inaccessible and accessible central voids, respectively. The devolatilization parameters, $u_0 \Delta \bar{H}_v X_v$ and τ_v, are determined from combustion experiments.

Evaluation of the dynamical equations requires the quantites c_s, γ_p and F_p, which are determined for fixed time and instantaneous values of the dynamical quantities, T_p, $r_{i,p}(t)$, $r_{o,p}(t)$, $r_{i,a}(t)$, $r_{o,a}(t)$ and $q(r,t)$. Equation (46) can be written as:

$$\int_{T_\infty}^{T_p} \frac{\lambda(T) dT}{\gamma_p - h(T)} = r_{o,a}(t) F_p(c_s(\gamma_p)), \tag{64}$$

which is an algebraic equation for γ_p and is solved as described in the following.

$F_p(c_s)$ is defined by Equation (15) and is obtained (as a function of c_s) by solution of the boundary value problem given by Equations (3), (6) and (7). Equations (48) in combination with Equations (34) - (36) yield c_s as a rational function of Y_{1p}. Then Equation (47) expresses Y_{1p} in terms of γ_p and thus c_s as a composite function of γ_p. Therefore, F_p, is also a function of γ_p, and Equation (64) (in combination with Equations (3),(6),(7),(15),(34)-(36),(47) and (48)) is solved for γ_p, using a Newton-Raphson scheme. Equation (47) then yields Y_{1p} directly and c_s is found by Equations (48) and (34) - (36), which determines F_p by Equations (3), (6), (7) and (15). The dynamical equations may then be evaluated for a fixed time and ultimately integrated in time as described above.

An important simplification results by the choice of an intrinsic rate linear in oxygen concentration. In this case, the intraparticle equation is linear and F_p is proportional to c_s, thereby simplifying the solution of Equation (64).

1 Notation

SYMBOL	DESCRIPTION	UNITS
A	defined by Equation (36)	
b	stoichiometric coefficient	$(= 1/24)$
c	oxygen concentration	gmoles/cm^3
c_s	oxygen concentration at particle surface	gmoles/cm^3
c_{p_i}	specific heat capacity of i^{th} species	cal/g K
$\bar{c}_p$	average specific heat capacity of particle	cal/g K
$\tilde{c}_{p_i}$	molar heat capacity of i^{th} species	cal/mol K
D	gas-phase diffusion coefficient	cm^2/s
D_v	diffusion coefficient of volatile species	cm^2/s
e	total energy flux	cal/cm^{2}s
e_R	radiative energy flux	cal/cm^{2}s
e_v	energy flux due to volatile combustion	cal/cm^2 s
F^T	total mass flux	g/cm^{2}s
F^v	mass flux due to volatile evolution	g/cm^2 s
F	total mass flux due to chemical reaction	g/cm^2 s
F_i	mass flux of i^{th} species (Eq.(25))	g/cm^2 s
F^*	mass flux due to particle fragmentation	g/cm^2 s
G^T	defined by Equation (74)	
h	defined by Equation (53)	cal/g
$\bar{H}_i$	specific enthalpy of i^{th} species	cal/g
ΔH	molar heat of reaction (Eq. (2))	cal/mol
$\Delta \bar{H}_v$	specific heat of combustion for volatile species	cal/g
I	defined by Equation (18)	
J	defined by Equation (19)	
k_{in}	intrinsic rate coefficient	g/cm^2 s (atm)^n

m	intrinsic reaction order	
m_p	particle mass	g
q	local conversion variable	cm
q^*	value of q at critical porosity, ϵ^*	
r	radial position	cm
$r_{o,p}$	instantaneous outer particle radius	cm
$r_{i,p}$	instantaneous inner particle radius	cm
$r_{o,a}$	instantaneous outer ash radius	cm
$r_{i,a}$	instantaneous inner ash radius	cm
R_{in}	intrinsic rate-per-unit pore surface area	g/cm^2s
R_g	gas constant	
T	temperature	K
ΔT_p^{∞}	temperature rise due to volatile combustion	K
ΔT_p^1	temperature rise during t = $[0,\tau_v]$	K
t	time	s
t_b	burnout time	s
u	concentration of volatiles	g/cm^3
$\bar{U}$	specific internal energy of carbon	cal/g
v_a	volume fraction of ash in carbon matrix	
X_c	conversion based upon carbon mass	
$X_{c,f}$	final conversion	
X_v	extent of volatile combustion	
x_a	mass fraction of minerals	
Y_i	mass fraction of i^{th} species	
Z	defined by Equation (33)	
γ_p	defined by Equation (45)	
δ_e	effective diffusion coefficient	cm^2/s

ϵ	total porosity	
ϵ_a	volume fraction of ash in carbon matrix	
ϵ^*	critical porosity (Eq. (12))	
ε	emissivity	
λ	thermal conductivity of gas-phase	cal/cm s K
ρ_g	density of gas phase	g/cm^3
ρ	particle density	g/cm^3
$\bar{\rho}$	average particle density	g/cm^3
ρ_a	density of ash	g/cm^3
ρ^*	particle density at critical porosity	g/cm^3
ρ_T	true carbonaceous density	g/cm^3
σ	Stefan-Boltzmann constant	
τ_v	time constant for devolatilization	s

SUBSCRIPTS

0	initial value
1	oxygen
2	carbon monoxide
3	nitrogen
∞	at ambient conditions
a	ash
c	carbon
p	at particle surface
v	volatile species

2 References

1. Gavalas, G.R. (1980). "A random capillary model with application to char gasification at chemically controlled rates." *A.I.Ch.E.Jl.***26**, 577.

2. Gavalas, G.R. (1981). "Analysis of char combustion including the effect of pore enlargement." *Comb. Sci. Tech.*, **24**,197.

3. Gavalas, G.R., Loewenberg, M.,Bellan, and J.,Clayton, M. (1985). "Structure and combustion of cenosphere particles." Paper presented at the annual A.I.Ch.E. meeting, Chicago, November 10-15. submitted to *Combustion and Flame.*

4. Libby, P.A., and Blake, T.R. (1979). "Theoretical study of burning carbon particles." *Comb. Flame*,**36**,139.

5. Loewenberg, M., Bellan, J. and Gavalas, G. R. (1987) "A simplified description of char combustion." In Print.

APPENDIX 8

Fuel **67**, 275, (1988).

Physical Properties and Oxidation Rates of Chars from Three Bituminous Coals

Ranajit Sahu[†] Yiannis A. Levendis[‡] Richard C. Flagan[†,‡]

George R. Gavalas[§]

Depts. of Mech.(†), Env.(‡) and Chem.(§) Eng.

California Institute of Technology,

Pasadena, CA 91125, USA

Abstract

Intrinsic oxidation rates of coal chars derived from three bituminous coals were measured at 500 C, and the effects of char formation temperature, conversion, coal particle size and char particle size on the rates were evaluated. Characterization of the various samples by BET surface area, mercury porosimetry, mercury and helium densities, heating values and in some cases elemental analyses were carried out to better understand the roles and interactions of the various parameters. Optical microscopic observations were also made to verify assumptions wherever possible. The results show that apparent and intrinsic rates as well as heating values are reduced with increasing char formation temperature. N_2-BET surface areas increase by an order of magnitude with conversion and exhibit maxima in the range of temperatures considered (1000 K to 1600 K). Of similar-sized chars derived from different sizes of coal particles, those from the smaller coal size fractions had higher apparent reaction rates.

1 Introduction

The relationship between char reactivity and its physical or chemical properties is a subject of longstanding. Several authors have reported on the dependence of the rates of char gasification by O_2, H_2O, and CO_2 on rank or chemical composition of the parent coal,[1-3] mineral matter,[1,2,4,5] and thermal pretreatment.[1,2,4,5] These experimental studies have, in most instances, employed sufficiently low temperatures and have taken other suitable precautions in order to minimize or eliminate intraparticle and external diffusion limitations. In the absence of diffusional effects, the reaction rate divided by the surface area of the char, e.g., the N_2-BET surface area, provides what is known as the "intrinsic rate" or "intrinsic reactivity." It is well known that both total surface area and reactivity vary with the rank of the parent coal and its thermal pretreatment, although both surface area and reactivity have not always been measured.

Once a char has been prepared under specified and carefully controlled conditions, the gasification rate becomes a function of temperature, gas composition, and char conversion only. From the standpoint of process design, the dependence on conversion is as essential as the dependence on gas composition. Rates of char gasification by O_2, H_2O, and CO_2 have been reported as functions of conversion by several authors.[6-9,28] The rate versus conversion curves normalized by the maximum or the initial rate were found, in some cases, to be insensitive to reaction temperature but to vary with the reactant gas. Few workers measured surface area as well as reaction rate as functions of conversion, to determine whether or not that ratio remained constant, although the assumption of constant ratio has been widely employed in modelling work. In a recent investigation[10], oxidation rates of chars from an anthracite and a bituminous coal (hva) were found to be approximately proportional to the surface area determined by CO_2 adsorption at 273K at all conversions. The constancy of the intrinsic rate permitted the analysis of the data by

the random pore model.

In addition to their inherent interest, studies like the ones quoted above are useful in the interpretation of gasification or combustion rates under conditions pertinent to applications. At temperatures typical of practical processes, the reactions of char are quite strongly influenced by external heat and mass transfer and by internal pore diffusion. The interpretation and extrapolation of high-temperature data must somehow take into account pore diffusion and pore growth. Some progress has been made in this area[11,12], but the problem is far from having been satisfactorily treated, especially in regard to swelling coal chars. It is hoped, nevertheless, that in many cases the conversion dependence of pore structure characteristics and relative reaction rates measured under diffusion-free conditions can be approximately applied to high-temperature reaction conditions.

In this paper we report oxidation rates and physical properties of bituminous coal chars subjected to devolatilization for two seconds at 1000-1600K. The focus is on the variation of surface area, reaction rate, and intrinsic reaction rate with conversion under diffusion-free conditions. Other physical properties reported include pore volume distribution, elemental composition and heating value. The effects of devolatilization temperature and particle size of the char and the parent coal are also examined.

2 Experimental Procedure

2.1 *Char Formation*

Chars were made from three bituminous coals with the compositions given in Table 1. At first, the coals were ground in a mechanized mortar and pestle grinder in air for approximately 30 seconds and then sieved on a mechanical shaker for 10 minutes and classified into the following size fractions: less than 45μm, 45 - 53μm, 53 - 90μm, 90 - 104μm, 104 - 125μm and greater than 125μm.

Chars were then generated from the 45 - 53μm and 104 - 125μm size fractions of coal. Fractions of these sizes are narrow enough to minimize the effects of coal size variability while providing adequate sample quantities. The mean sizes 49μm and 114μm were different enough to examine and compare the effects of coal size on subsequent char combustion.

The coals were pyrolyzed in an electrically heated drop-tube furnace. The furnace consists of an alumina tube having 5 cm. internal diameter heated by Kanthal heating elements placed in a radiation cavity 20 cm. long. Coal particles were entrained in a stream of nitrogen at rates of 2 g/hr, using the syringe pump feeder arrangement described by Senior[13] and were injected into the radiation cavity of the furnace through a wide bore (1 cm) water cooled injector. Furnace wall temperatures were measured by thermocouples attached to the outside of the alumina tube. Gas temperatures were measured using a suction pyrometer. Based on both wall and gas temperatures, the particle temperature was deduced from a steady-state thermal energy balance. The carrier gas flow rate was adjusted to achieve residence times of 2 seconds. The devolatilization loss for the coals ranged between 30-50 %, depending on the temperature, and varied from coal to coal.

The chars were collected on a filter. To eliminate any tars that might have condensed, the chars were washed repeatedly with tetrahydrofuran and then dried

at room temperature for 1 hour. Finally, the tar-free chars were sieve-classified into the following size fractions: less than 45μm, 45 - 53 μm, 53 - 90 μm, 90 - 104 μm, 104 - 125 μm, 125 - 147 μm and greater than 147 μm.

2.2 *Rate Measurements with TGA*

A DuPont model 920 electrodynamic balance was used to measure the weight loss of a char sample oxidized at 800 K. In all cases the samples were heated in nitrogen at 50 K/min until the final temperature of 800 K was reached, at which instant oxygen was admitted. The flow rates of the initial nitrogen stream and the oxidizing stream (17 % oxygen by volume) were kept at 100 cm^3/min STP for all runs. This low flowrate was used to avoid entrainment of the extremely low density samples. The sample was placed on a platinum pan and its temperature was monitored with a thermocouple placed directly above. The mass loss, rate of mass loss, and the sample temperature were continuously recorded by a computerized data acquisition system. The initial sample masses were in the range 5 - 10mg.

2.3 *Surface Area and Helium Density Measurement*

Surface areas were measured by a pseudostatic technique by acquiring gas adsoption isotherms using continous addition of adsorbate gas (N_2 at 77 K) as described by Northrop *etal.*[14] BET and capillary condensation analyses were carried out on the resulting isotherms. Calibration of the apparatus was carried out using various standardized samples of alumina and graphite. Helium densities were determined on vacuum-dried samples by helium displacement at room temperature. Sample quantities of at least 0.8 g were used to obtain reliable density values.

2.4 *Mercury Porosimetry*

Pore volume distributions were determined by mercury penetration. An Autoscan porosimeter, Model 33, was used. Low pressure penetration (101 kPa) was implemented to fill the interparticle voids and intraparticle voids with openings larger than 7 μm. High pressure, to a maximum of 227 MPa (30000 psi), was used to penetrate pores having diameters larger than 6 nm. The Washburn equation[15] was used to calculate pore volume distribution as a function of pore radius from pressure and intrusion volume measurements under the assumption of cylindrical pores.

3 Results and Discussion

3.1 *Physical Characteristics*

Apparent densities, σ_A, mercury densities, σ_{Hg}, corresponding to the solid plus pores below 6 nm in diameter, and helium densities, σ_{He}, for the uncombusted chars are listed in Table 2. Total porosity, ϵ_A, and porosity of pores below 64 Å , ϵ, can be estimated from the density values. Pore diffusivities for the initial materials were calculated based on mercury porosimetry, nitrogen capillary condensation and helium density data. Values of mean pore radii r_p were determined from the porosimetry plots or calculated from the microporosity values. In Fig. 1 are shown the volume and surface area distributions for the 1200 K and 1600 K chars of PSOC-1451. These were obtained from mercury intrusion and nitrogen capillary condensation measurements. An interesting feature of the pore volume and area distributions is that chars obtained by devolatilization at higher temperatures (1600 K) developed trimodal distributions, while the low temperature (1200 K) chars developed bimodal ones. As is evident from the surface area curves in the same figure, pores below 100 Å in diameter account for most of the area while contributing very little to the total volume. On the other hand, the presence of the pores above 1000 Å in diame-

ter is manifested in the volume distribution. Therefore the presence of different pore ranges can be inferred by examining both the volume and surface area distributions. For the 1200 K char, the distribution is bimodal, showing appreciable pore volume in the macropore region and significant surface area in the micropore region. The same peaks are also evident for the 1600 K char. In addition there is a distinct peak around 500 Å showing development of accessible porosity in the transitional region. The 1000 K and 1400 K chars for this coal exhibit characteristics similar to the 1200 K char. Chars of the other coals also exhibited similar behaviour. The total pore volume penetrated by mercury, V_{Hg}, along with the pore size distribution is a good indication of the extent of connectivity of the macro and the transitional pores. The corresponding pore area, A_{Hg}, is calculated assuming cylindrical pores. Also listed are initial BET surface areas, heating values and elemental composition, expressed as mass fractions, for some of the chars. Data for partially combusted PSOC-176 1600 K char at 80% conversion are also tabulated. The apparent density of the partially combusted char has diminished, while its porosity and the pore volume have increased.

3.2 *Heating Values*

Higher heating values (HHV) were measured using the 1341 Parr oxygen bomb calorimeter. The results obtained were reproducible to within 250 J/g or about 1%. The values obtained for the PSOC-1451 coal and chars are plotted in Fig. 2 as a function of charring temperature both on a total weight basis and on a dry, ash-free basis. For both cases the heating values decrease with the increase in pyrolysis temperature. The reduction of heating value is obviously related to the loss of hydrogen at higher devolatilization temperatures as shown by the elemental analysis values listed in Table 2. Dulong[16] gives an empirical relationship between coal heating value and C,H,O and S content. Experimental values agree very well with

Dulong's formula as shown in the figure. There appears to be some disagreement for the 1600 K char. This might be due to a small error in the C:H ratio measurement.

3.3 *Rate Calculations*

The variation of sample mass with time in the TGA experiments was normalized with its value at the moment oxygen was admitted. There was some mass loss due to tar release as the sample was heated. The chars formed at relatively low temperature (1000 K and 1200 K) lost considerable mass during this period. For the 1400 K and 1600 K chars, almost all the volatiles were expelled during char formation, so that the loss during the heat-up period was less than 3%.

In Fig. 3 the apparent reaction rate ρ_m is plotted versus carbon conversion. The conversion, X, at any given time is the mass of carbon reacted divided by the mass of initial carbon.

$$X = \frac{m_{initial} - m}{m_{initial} - m_{ash}} \tag{1}$$

The apparent reaction rate normalized per unit instantaneous mass, m, of carbon, ρ_m, is defined as

$$\rho_m = \frac{1}{m - m_{ash}} \frac{dm}{dt} \tag{2}$$

. The mass of ash, m_{ash}, was measured in each run by carrying out oxidation until there was no further mass loss.

Another common way to plot the data is also shown in Fig. 3, where ρ_{m_0} is defined by normalizing with respect to the initial mass.

$$\rho_{m_0} = \frac{1}{m_{initial} - m_{ash}} \frac{dm}{dt} \tag{3}$$

Plotted in this fashion, the reaction rate exhibits a distinct maximum at a certain conversion that varies with char type, and particle size.

Fig. 4 shows the reaction rate ρ_m, as a function of conversion for two sizes of the 1600 K char of PSOC-1451. The two curves are indistinguishable, consistent

with the absence of diffusion limitations concluded from the calculations given in the discussion below. Optical microscope photographs of PSOC-176 1600 K char at conversions of 0, 65 and 90% show that the particle size is independent of conversion as would be expected for regime I reaction.

3.4 *Surface Areas*

The surface area, A_T, for the PSOC-176 1600 K char is shown in Fig. 5 as a function of conversion. The area reported corresponds to the carbonaceous matter inasmuch as the surface area of the ash was measured to be only 2 - 3m^2/g, in good agreement with values reported by Smith and Tyler[17]. It can be seen that the surface area increases rapidly with conversion and at about 60% conversion, reaches a maximum value of 450m^2/g, which is almost higher by an order of magnitude than the initial value 50m^2/g. At higher conversions the area stays constant or decreases slightly. Similar trends have been observed for other coals[18]. Surface areas of the three chars are plotted as a function of char pyrolysis temperature in Fig. 6. The top three curves give the areas of the chars after partial oxidation to 50% conversion, while the fourth curve shows the variation of the uncombusted area of the PSOC-176 char; areas for the other two 1600 K uncombusted chars are also shown. The area of the PSOC-176 char at zero conversion increases with pyrolysis temperature. There are two competing effects that affect surface area. While volatiles and tars released at higher temperatures leave a larger pore volume accessible to nitrogen, thermal annealing and structural reorganization of the carbon matrix at higher pyrolysis temperatures lead to closing of pore mouths and pore coalescence, thus reducing surface area. Which effect will dominate is not predictable *a priori*. In the present case experimental evidence suggests that for PSOC-176, the former does. The surface areas of partially combusted PSOC-176 and 1451 chars initially increase with pyrolysis temperature, reach a maximum and then drop. The high

surface area of the PSOC-176 char indicates that it has more small pores accessible to N_2 at 77 K. In contrast,the surface area of the PSOC-282 char is approximately constant initially but later increases with pyrolysis temperature. Reduction of areas at higher charring temperatures may result from closure of the finer pores because of structural ordering of the carbon that increases with temperature of exposure. This hypothesis is supported by x-ray diffraction studies on semi-anthracite reported by Smith and Tyler[17]. The anomaly presented by the 1000 K char is probably due to the presence of heavy tars in the material.

3.5 *Diffusion Limitations*

Three distinct processes must be examined to ensure that the measured rates are free of diffusional limitations. They are diffusion in the boundary layer between the flowing oxidizer stream and the bed of particles, diffusion through the particle bed, and pore diffusion inside the particles. Each will be examined briefly.

1. Bed Boundary Layer Diffusion: As a very simple approximation, the flow of oxidizer over the pan was modelled as flow past a flat plate, neglecting the effects of the pan walls, pan leading edge and the confining reactor tube walls. For the conditions of the experiment, the Reynolds number (based on average velocity at the reactor temperature and pan length) is about 1.5 and hence the flow is laminar. The time for diffusion across the boundary layer is negligible compared to the characteristic reaction time computed as ρ_m^{-1} (see Table 3). Therefore, it is safe to assume that there is no limitation imposed by diffusion in the bed boundary layer.

2. Bed Diffusion : Although sample quantities were small and spread uniformly over the pan, the effect of bed diffusion could become important at high temperatures. A modified Thiele modulus based on bed parameters and the

apparent reaction rate can be formulated[23] as shown below:

$$K = \dot{N}\frac{H^2}{C_0 D_B}, \tag{4}$$

where $\dot{N}$ is the apparent reaction rate per unit bed volume (g/cm^3-s), C_0 is the oxygen concentration in the ambient (g/cm^3), H is the bed thickness (cm) and D_B is the bed diffusion coefficient (cm^2/s), given by Satterfield[24] as

$$D_B = \frac{D_m \epsilon_0}{\tau}, \tag{5}$$

where D_m is the molecular or bulk binary diffusion coefficient of oxygen in nitrogen at the proper temperature, ϵ_0 is the void fraction of the bed normally in the range 0.35 - 0.4 and τ is the bed tortuosity, commonly taken equal to 2. Bed diffusion is negligible[23] for K $<$ 1. For the 45 - 53 μm size fraction of the PSOC-1451 1600 K char, the sample size was 5 mg. and its apparent particle density was 0.98 g/cm^3. The apparent rate was 25x10^{-6} g/cm^3-s. The pan area was 0.3 cm^2 Hence, the thickness of the bed, H, was 0.017 cm. Assuming a mean particle size of 50 μm, the average bed depth was only 3.4 particles. At 800 K the value of D_m is 1.88 cm^2/s and, therefore, D_B is 0.33 cm^2/s, assuming ϵ_0 to be 0.35. At an oxygen mole fraction of 0.17, C_0 is 6.03x10^{-5} g/cm^3. The resulting Thiele modulus, K, is 3.64x10^{-4}; hence, bed diffusion does not significantly influence the reaction in these experiments.

3. Pore Diffusion : The present chars are extremely porous, having pore openings with length scales ranging from a few microns down to a few angstroms. The type of diffusion taking place covers the range from bulk diffusion in the macropores to Knudsen diffusion in the smaller meso and micropores with a combination of the two in pores of intermediate size. It is essential, therefore, to know the pore size distribution of the material before the pore diffusional resistance can be assessed. In the present study all micro and mesopore diameters were smaller than the mean free path of oxygen, approximately 0.3μm for

the experimental conditions and thus, the diffusivity was that corresponding to Knudsen diffusion[25],

$$D_K = 9.7\text{x}10^3 r_p \left(\frac{T}{M}\right)^{0.5}. \tag{6}$$

For the pores that have diameters comparable to the mean free path of oxygen, the transition regime diffusivity was applied i.e.[26],

$$\frac{1}{D_p} = \frac{1}{D_m} + \frac{1}{D_K}. \tag{7}$$

Finally the total effective diffusivity was calculated by adding the contributions from the different pore sizes, and the resulting values varied from 0.02 to 0.2.

3.6 *Reaction Rates*

As shown in Fig. 3, ρ_m increases sharply during the first 3-4% carbon conversion. The principal reason for this phenomenon is that the gas composition over the bed gradually changes from pure nitrogen to a final mixture of 17% O_2 in nitrogen. Jenkins *etal*..[1] also suggest that oxygen complex formation at the surface and char activation may be important at this early stage of conversion. After this initial delay, the oxygen concentration reaches a steady value and the apparent rate increases slowly with conversion until the completion of combustion.

Following the procedure outlined by Smith,[19] an effectiveness factor η defined as the ratio of actual reaction rate to the rate found in the absence of restrictions due to pore diffusion can be calculated as:

$$\eta\phi^2 \frac{(m+1)}{2} = \frac{\gamma^2 \rho_m \sigma_A (m+1)}{2 D_e C_s}, \tag{8}$$

where ϕ is the pore Thiele modulus and γ is the characteristic length defined as the ratio of particle volume to external area. Thus, the right side of Equation (8) can be

calculated and η can be calculated by the relationships between η and $\eta\phi^2(m + 1)/2$ given by Mehta and Aris[20]. The effectiveness factors calculated for the uncombusted chars, using suitable diffusion parameters, are equal to unity, in agreement with findings by Knill and others[21] for similar conditions. This calculation also shows that there are no pore diffusion limitations. The order of magnitude increase in the surface area after partial combustion indicates the opening of a vast micropore network. A worst-case calculation, assuming that all pores have diameters of 10 Å, yielded an effectiveness factor η, which was still close to unity.

Since the particles oxidize in the kinetically controlled regime I as shown earlier, an intrinsic reaction rate ρ_i can be defined by

$$\rho_i = \frac{\rho_m}{A_T}. \tag{9}$$

Table 3 shows the intrinsic rate of PSOC-176 1600 K char at various degrees of conversion. Values for the areas were taken from Fig. 5 and values of the apparent rate from Fig. 3. It can be seen that after approximately 5% of conversion the intrinsic rate becomes essentially independent of conversion, providing a justification for employing the N_2-BET surface area A_T for the definition of ρ_i. Approximately constant intrinsic rates after the first 5% conversion were obtained for the PSOC-1451 chars as well. The small increase in the rate at the highest conversions could be attributed to experimental error, particularly in the area measurement of very small samples. It could also be due to the decrease in the particle conductivity with increasing porosity, causing local hot spots with high reaction rates.

The fact that the intrinsic rate is nearly constant with conversion makes possible the comparison of the intrinsic reactivities of chars at any conversion for which surface area values are available. In the present study, all rates have been compared at 50% conversion. Figure 7 shows the apparent reaction rate at 50% conversion for the three chars for two size cuts, 104-125μm and 45-53μm . It is evident that the reaction rates of all chars increase with decreasing pyrolysis temperature, pos-

sibly because of the residual volatile matter of higher reactivity or to less complete structural ordering that leaves a larger number of sites available for reaction with oxygen. The figure also shows that the apparent rate is independent of char particle size.

The effect of parent coal size on the apparent combustion rate was investigated for PSOC-1451 chars for the two size cuts 45-53 and 90-104 μm, both produced from coal size cuts 53-90 μm, and from coal fines below 45 μm in diameter. This effect of parent coal size can be quite important, as the fractionation of coal leads to selective segregation of the different maceral types in certain sizes[22]. The presence of macerals of different chemical compositions affects the morphology, structure and reactivity of the char. Figure 8 shows the oxidation rates of chars derived from different size fractions of the parent coal. The oxidation rates of the char fraction derived from smaller coal particles appear to be 10-20% higher. This fraction was characterized by a more pronounced cenospheric structure and higher mineral matter content, the latter possibly causing some catalytic enhancement of the oxidation rate.

Intrinsic reaction rates for two size cuts of the three chars are presented in Fig. 9. The intrinsic rate for two of the chars decreases with pyrolysis temperature, most probably due to the increased structural ordering of the carbon matrix with temperature. The rate of the PSOC-1451 char decreases the least, suggesting minimal structural changes. It is interesting to note that the intrinsic rates of the three chars are equal at the lowest devolatilization temperature but deviate as much as 30% at higher devolatilization temperatures. One reason may be that structural ordering at the lower temperature is minimal in all three chars, while as the temperature increases, changes become more pronounced and differentiated among the chars. The fact that the intrinsic rate follows similar trends with the heating value of the chars suggests that the loss of hydrogen at higher devolatilization temperatures reduces the number of active sites for oxidation. This is in agreement with results reported

by Khan,[27] showing a correlation between hydrogen content and rate of oxidation.

4 Conclusions

Increasing the pyrolysis temperature of three bituminous coals from 1000 K to 1600 K resulted in (i) decrease of the H:C ratio of the resulting char by a factor of 2 to 2.5; (ii) decrease of the heat of combustion of the char by 10-15%; (iii) change in the pore volume and pore surface distributions from bimodal to trimodal with the creation of porosity in the mesopore range. The apparent oxidation rate (at 800K) decreased by about 50% as the pyrolysis temperature increased from 1000 K to 1600 K.

The N_2-BET surface areas of the char increased from 10-50 m^2/g in the first few percent of conversion to 300-500 m^2/g at the highest conversions measured. The surface area at 50% conversion varied irregularly with the pyrolysis temperature.

The intrinsic char oxidation rate defined in terms of the N_2-BET surface area was approximately the same for all coals pyrolyzed at 1000 K but varied with the parent coal for the higher pyrolysis temperatures. The intrinsic reaction rate after the first 5% of conversion was found to be approximately independent of conversion for all chars examined.

Char particles in the same size fraction obtained from coal of different size fractions differ in properties. The cenospheric char produced from the smaller coal particles was 10-15% more reactive than the char of equal size produced from the larger coal particles.

5 Aknowledgements

This work was supported by the US Department of Energy under contract DE-AC2284FC70915. Thanks are due to Mr. P. S. Northrop for help in constructing and testing the BET apparatus and for carrying out some of the surface area measurements. The authors are also grateful to the reviewers for their useful suggestions and comments.

6 References

1. Jenkins, R.G., Nandi, S.P. and Walker, Jr., P.L. *Fuel*, **52**, 1973, 288.

2. Linares-Solano, A., Mahajan, O.P., and Walker, Jr., P.L. *Fuel*, **58**, 1979, 327.

3. Hippo, E and Walker, Jr., P.L. *Fuel*, **54**, 1975, 245.

4. Ashu J.T., Nsakala Y.N., Mahajan O.P. and Walker Jr., P.L. *Fuel*, **57**, 1978, 250.

5. Razouk, R.I., Saleeb, F.Z., and Youssef, A.M. *Carbon*, **6**, 1968, 325.

6. Dutta, S., and Wen, C.Y. *IEC Process Des. Dev.*, **16**, 1977, 20.

7. Dutta, S., and Wen, C.Y. *IEC Process Des. Dev.*, **16**, 1977, 31.

8. Mahajan, O.P., Yarzab, R., and Walker, Jr., P.L. *Fuel*, **57**, 1978, 643.

9. Tseng H.P. and Edgar T.F. *Fuel*, **63**, 1984, 385.

10. Su, J.-L., and Perlmutter, D.D. *AIChE J.*, **31**, 1985, 973.

11. Smith, I.W. *Fuel*, **57**, 1978, 409.

12. Gavalas, G.R. *Comb. Sci. Tech.*, **24**, 1981, 197.

13. Senior, C.L. and Flagan, R.C. *Twentieth Symposium (International) on Combustion,* The Combustion Institute, 1984, 921.

14. Northrop, P.S., Gavalas G.R., Flagan R.C. *Langmuir*, **3**, 1987, 300.

15. Lowell, S. and Shields J. E. Powder Surface Area and Porosity Chapman and Hall, London, 1984, 94.

16. In Chemistry of Coal Utilization 2^{nd} suppl. vol. (ed) M.A.Elliot ,Wiley, London, 1981.

17. Smith, I.W. and Tyler, R.J. *Fuel*, **51**, 1972, 312.

18. Northrop, P.S. *Personal Communication.*

19. Smith I.W. *Nineteenth Symposium (International) on Combustion*, The Combustion Institute, Pittsburg, PA., 1982, 1045.

20. Mehta, B.N. and Aris, R. *Chem. Eng. Sc.*, **26**, 1971, 1699.

21. Knill, K.J., Chambers, A.K., Parkash S., Ungarian D.E., Zacharkiw, R. Presentation at 1986 Spring Meeting of the Canadian and Western States Section of the Combustion Institute.

22. Berkowitz, N. An Introduction to Coal Technology Academic Press, New York, 1979.

23. Weisz, P.B., Hicks, J.S. *Chem. Eng. Sci.*, **17**, 1962, 265.

24. Satterfield, C.N. Mass Transfer in Heterogeneous Catalysis. M.I.T. Press, Cambridge, Mass. 1970.

25. Wheeler, A. *Adv. in Catalysis*, **3**, 1951, 249.

26. Ruthven, D.M. Principles of Adsorption and Adsorption Processes Wiley, London, 1984, p.133.

27. Khan, M.R. *ACS Div. Fuel Chem. Preprints*, **32**, No. 1, 1987, 298.

28. Tseng H.P. and Edgar T.F. *Fuel*, **64**, 1985, 373.

7 List of Figures

8 List of Symbols

SYMBOL	DESCRIPTION	UNITS
A_{Hg}	specific Mercury area[N_2-BET]	m^2/g
A_T	specific total area	m^2/g
C_g	ambient oxygen concentration	g/cm^3
C_s	oxygen concentration at particle surface	g/cm^3
d	particle diameter	cm
D_B	bed diffusivity	cm^2/sec
D_K	Knudsen diffusivity	cm^2/sec
D_m	molecular diffusivity	cm^2/sec
D_p	pore diffusivity	cm^2/sec
H	bed thickness	cm
K	modified bed Thiele modulus	
m	true order of reaction	
M	molecular weight	g/g-mole
n	apparent order of reaction	
N	bed density	g/cm^3
p_{O_2}	ambient partial pressure of oxygen	
r_p	mean pore radius	cm
T_g	ambient temperature	K
T_p	particle temperature	K
V_{Hg}	specific Mercury pore volume	cm^3/g
X	burnoff	
γ	characteristic particle dimension	cm
ϵ_0	bed void fraction	
ϵ	porosity below 6 nm.	
ϵ_A	total porosity	

η	effectiveness factor	
ρ_m	apparent reaction rate	g/g-sec
$\rho_{m,D}$	diff. controlled apparent reaction rate	g/g-sec
ρ_i	intrinsic reaction rate	g/cm^2-sec
σ_A	apparent density	g/cm^3
σ_{Hg}	Mercury density	g/cm^3
σ_{He}	true(Helium) density	g/cm^3
τ	tortuosity	
ϕ	Thiele modulus	
χ	ratio of ρ_m to $\rho_{m,D}$	

TABLE I: COAL DATA

COALS	282	176	1451
RANK	Bit. HVB	Bit. HVB	Bit. HVA
MOISTURE (%)	5.7	0.8	2.5
ASH (%)	6.8	6.5	13.5
CARBON (%)	75.0	78.4	71.5
HYDROGEN (%)	5.3	5.4	4.7
OXYGEN (%)	8.7	5.5	7.0
NITROGEN (%)	1.7	1.3	1.3
SULFUR (%)	1.6	2.9	1.3
VOLATILE MATTER (%)	35.7	40.2	33.5
HEATING VALUE (DRY BASIS) cal/g	7407	7910	6965

TABLE II: PROPERTIES OF COALS AND CHARS

TYPE OF COAL OR CHAR	σ_A (g/cm^3)	σ_{Hg} (g/cm^3)	σ_{He} (g/cm^3)	ϵ_A % <7μm	ϵ % <32 Å	PORE V_{Hg} (cm^3/g)	PORE S_{Hg} (m^2/g)	S_{BET} (m^2/g)	C (%)	H (%)	C/H	HEATING VALUE (cal/g)
PSOC 282 COAL	0.66	1.07	—	~38	—	0.75	15.7	—				7407
PSOC 282 1000 K	0.6	1.35	1.63	63	17	0.96	11.9	—				
PSOC 282 1200 K	0.52	1.4	1.59	67	12	0.90	13.8	—				
PSOC 282 1400 K	0.61	1.55	1.53	60	~0	1.0	15.1	—				
PSOC 282 1600 K	0.63	1.55	1.84	66	16	0.94	15.0	15.3				
PSOC 176 COAL	1.25	1.4	1.25	11	~0	0.08	6.8	9.5				7910
PSOC 176 1000 K	0.68	1.4	1.34	49	~0	0.74	12.9	17.5				
PSOC 176 1200 K	0.60	1.43	1.39	57	~0	1.47	16.37	20				
PSOC 176 80% CONV. AT 500° C	0.48	1.76	—	~72	—	1.53	14.7	—				
PSOC 176 1400 K	0.65	1.68	1.63	61	~0	1.62	26.93	31				
PSOC 176 1600 K	0.76	1.8	1.85	51	3	0.81	28.02	56				
PSOC 1451 COAL	1.18	1.42	—	17	—	0.14	7.9	—				6965
PSOC 1451 1000 K	1.084	1.8	1.28	18	~0	0.4	14.8	—	66.8	2.8	1.9	6242
PSOC 1451 1200 K	1.0	1.8	1.50	33	~0	0.43	11.6	—	69.9	1.8	3.1	6123
PSOC 1451 1400 K	0.9	1.86	1.50	40	~0	0.57	11.4	—	71.0	1.1	5.6	5965
PSOC 1451 1600 K 53-90μm FROM FINES	0.76	1.85	1.85	59	~0	0.78	20.9	—	73.4	0.9	6.8	5594
PSOC 1451 1600 K 53-90μm FROM 53-90μm	0.98	1.81	1.85	47	2	0.46	14.7	27.8				
PSOC 1451 1600 K 53-90μm FROM 90-125μm	1.26	1.9	1.85	32	~0	0.40	14.5	—				
PSOC 1451 1600 K 125-147μm FROM 90-125μm	0.92	1.5	1.85	47	19	0.35	14.9	—				

TABLE III: VARIATION OF RATES WITH CONVERSION FOR PSOC-176 1600K CHAR

CONVERSION %	APPARENT RATE ρ_m (g/g-sec)	INTRINSIC RATE ρ_i (g/cm^2-sec)
5	1.9×10^{-3}	7.0×10^{-10}
10	2.06×10^{-3}	7.2×10^{-10}
15	2.34×10^{-3}	7.1×10^{-10}
20	2.52×10^{-3}	7.15×10^{-10}
25	2.67×10^{-3}	7.11×10^{-10}
30	2.84×10^{-3}	7.1×10^{-10}
35	2.96×10^{-3}	7.12×10^{-10}
40	3.15×10^{-3}	7.3×10^{-10}
67	3.64×10^{-3}	7.9×10^{-10}
90	3.71×10^{-3}	8.0×10^{-10}

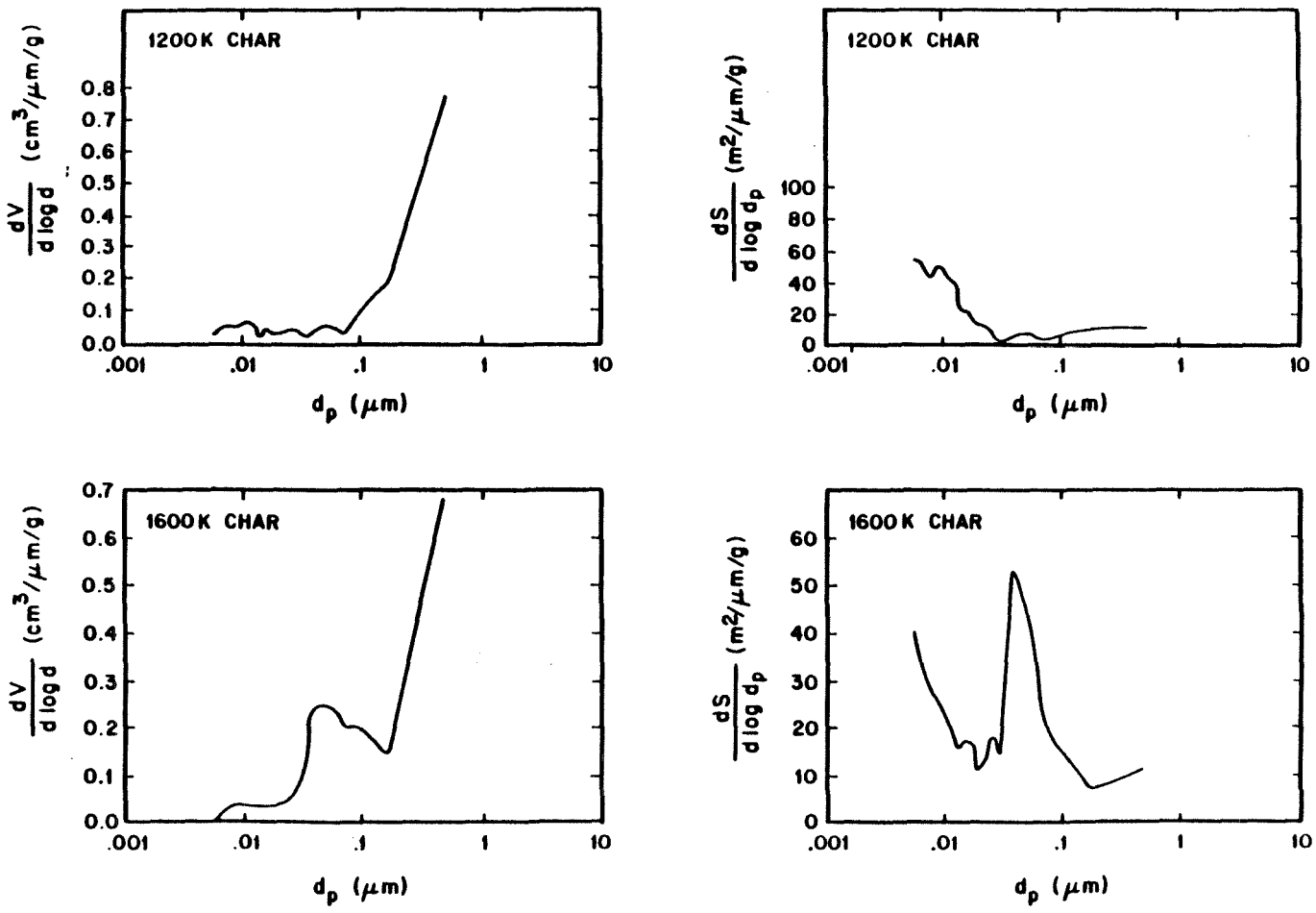

Figure 1: Pore volume and surface area distributions for PSOC-1451 chars (a) 1200 K (b) 1600 K.

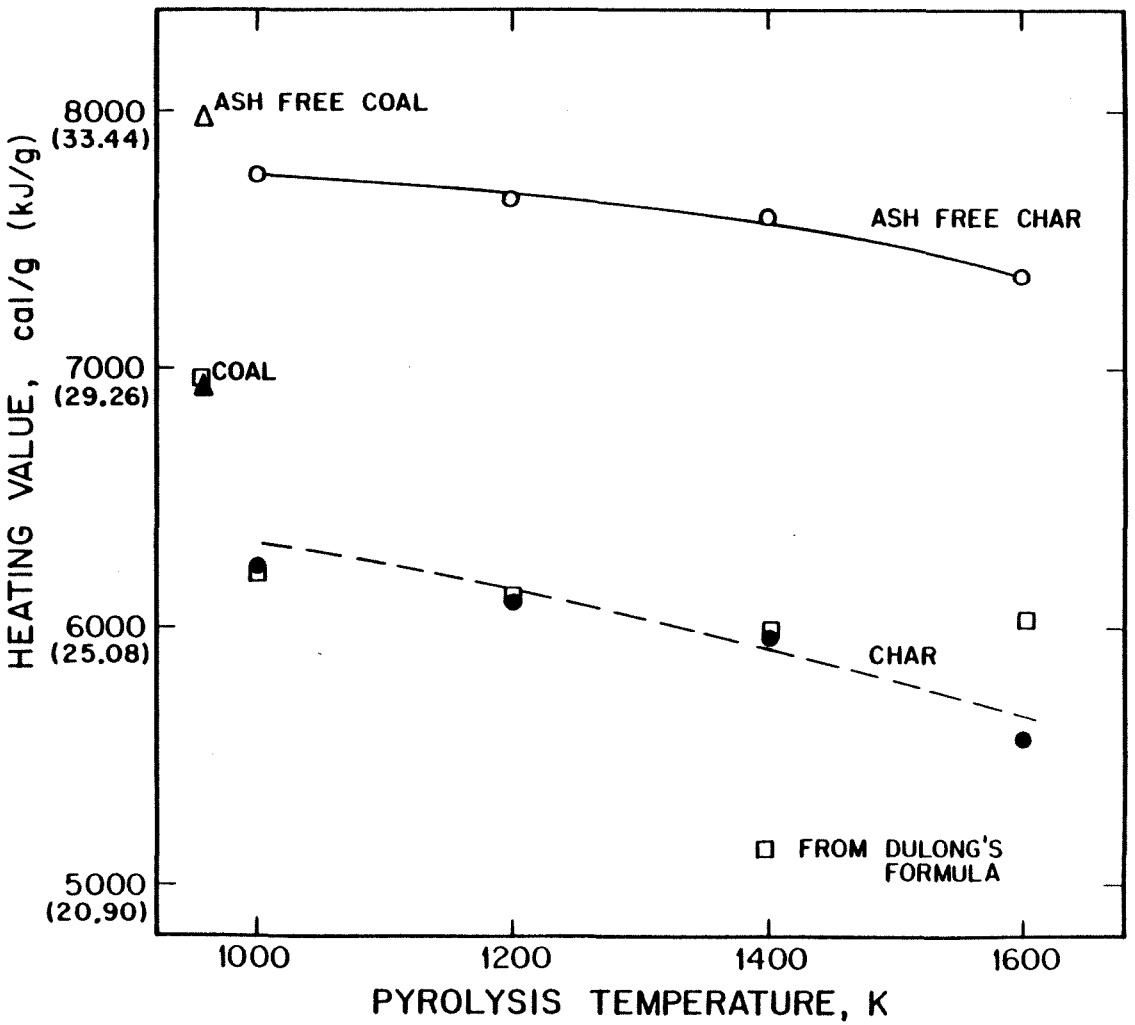

Figure 2: Heating Values of PSOC-1451 coal and chars versus pyrolysis temperature.

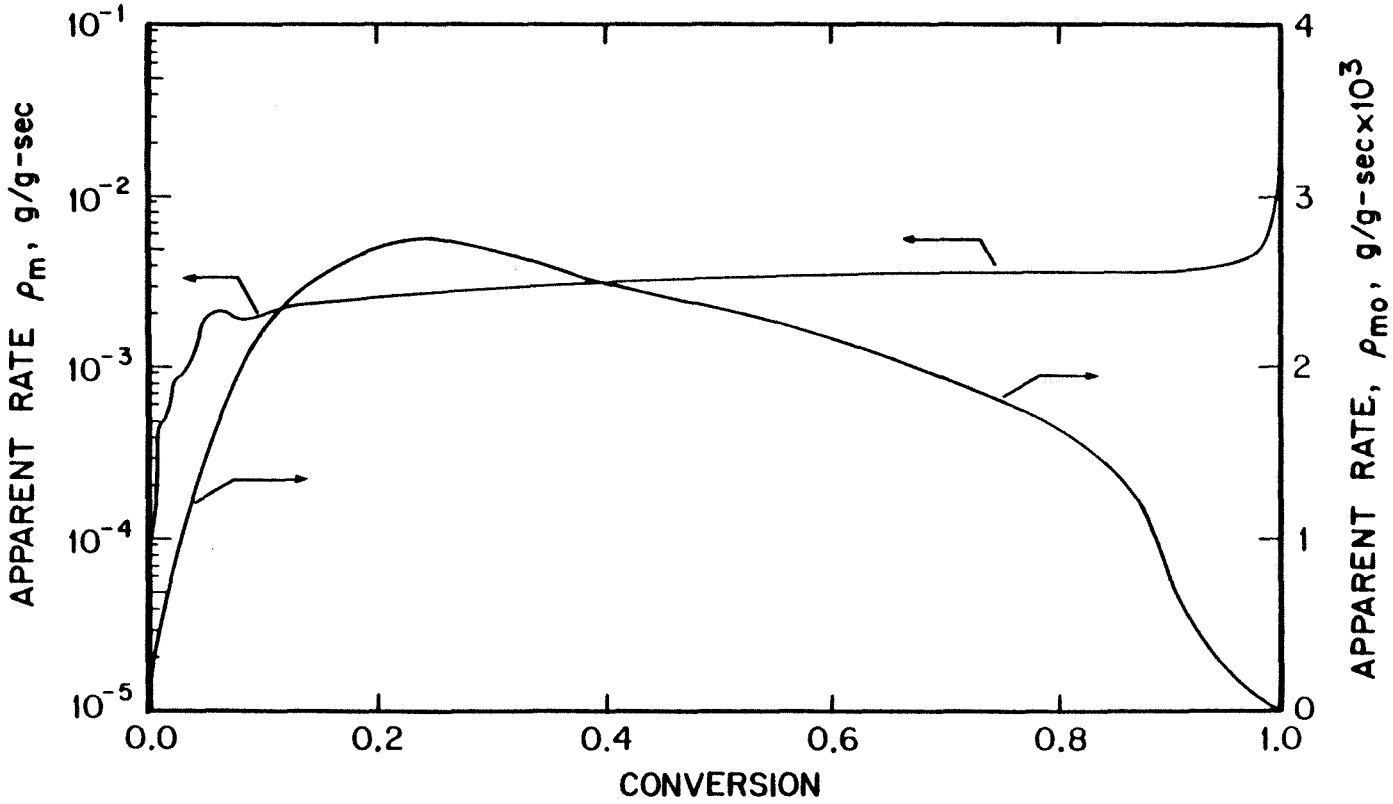

Figure 3: Apparent rates, ρ_m and ρ_{m_0}versus conversion, X for PSOC-176 1600 K char.

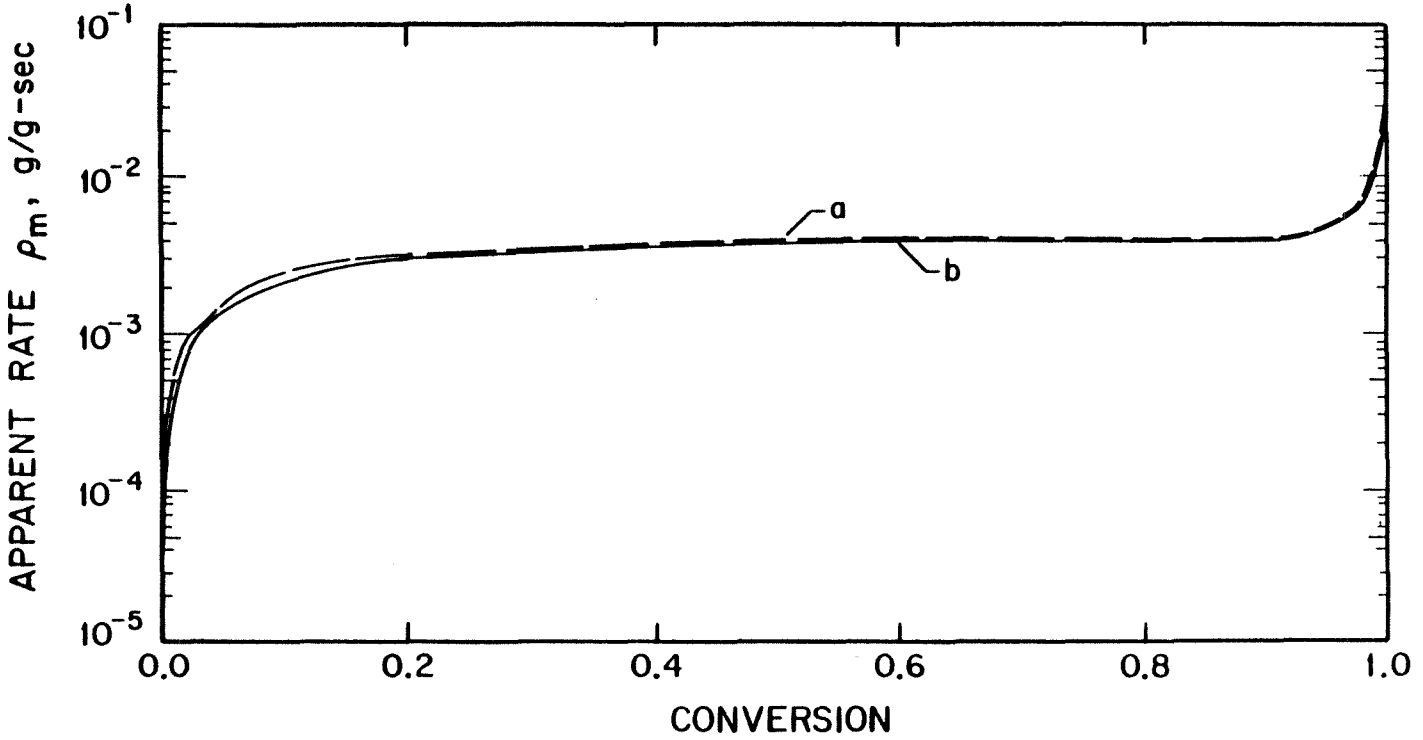

Figure 4: Apparent rates, ρ_m versus conversion, X, for PSOC-1451 1600 K char, sizes 45-53(a) and 104-125(b) μm.

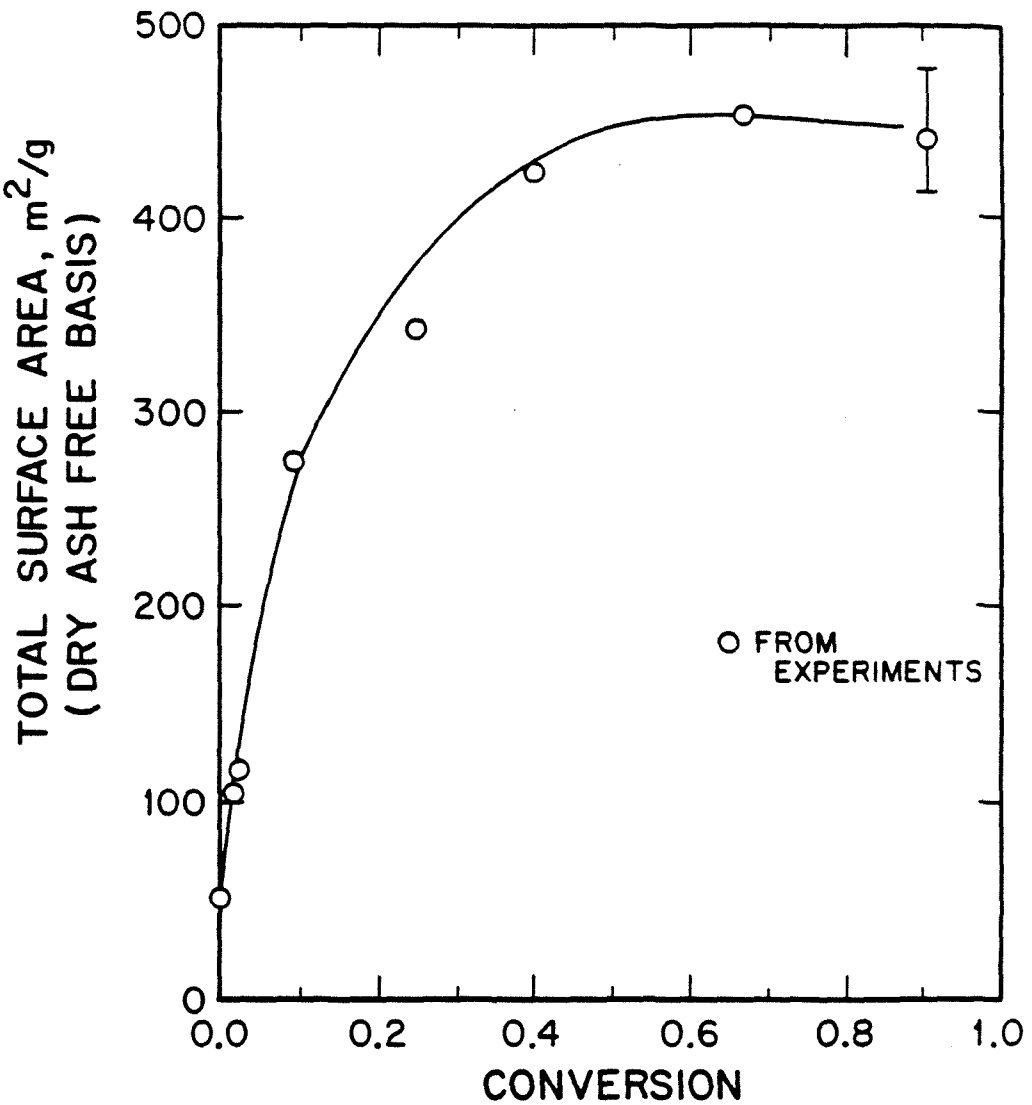

Figure 5: Surface areas of PSOC-176 1600 K char versus conversion. Line is smooth fit.

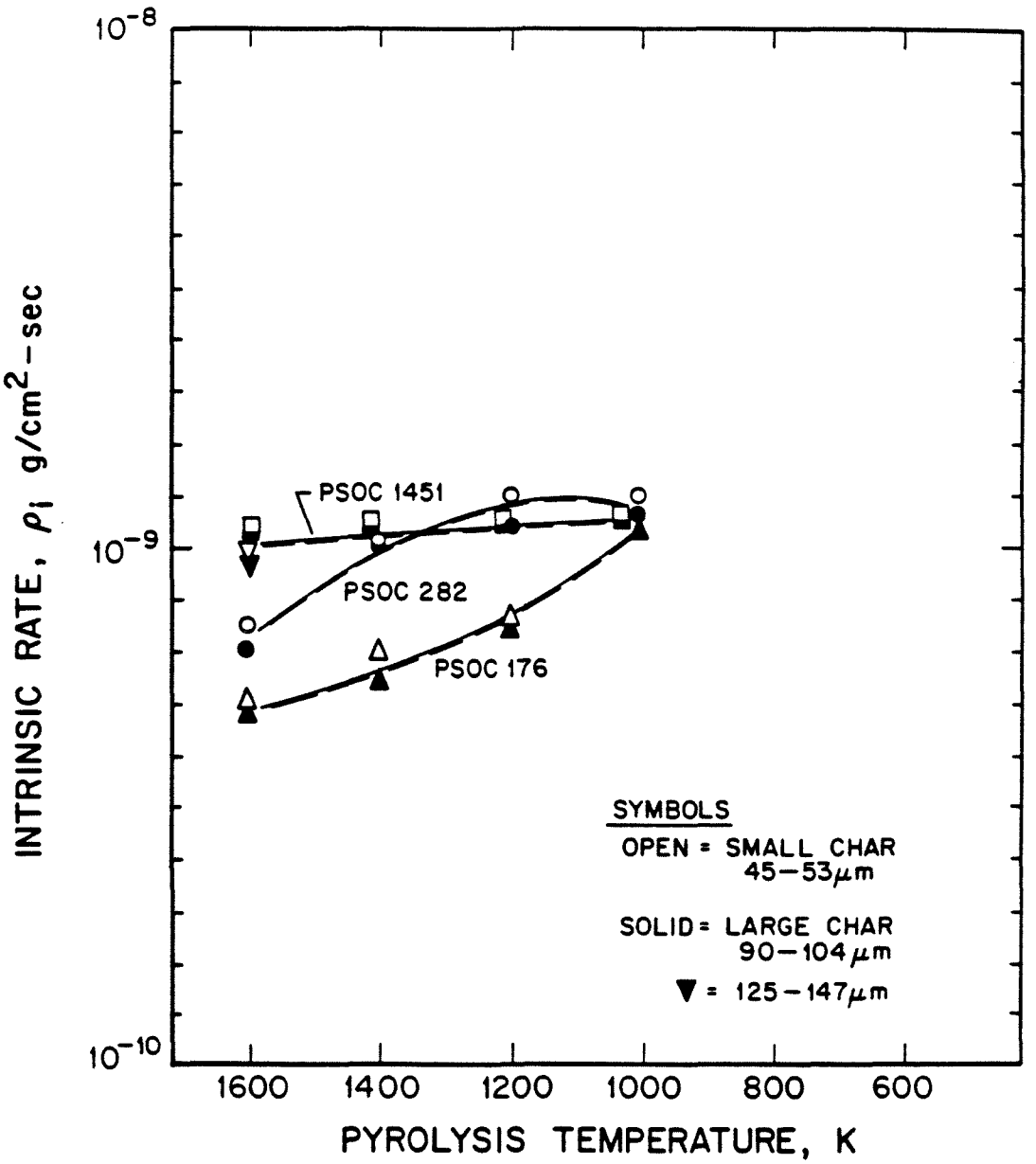

Figure 6: Initial surface areas and surface areas after 50% conversion for all chars versus pyrolysis temperature.

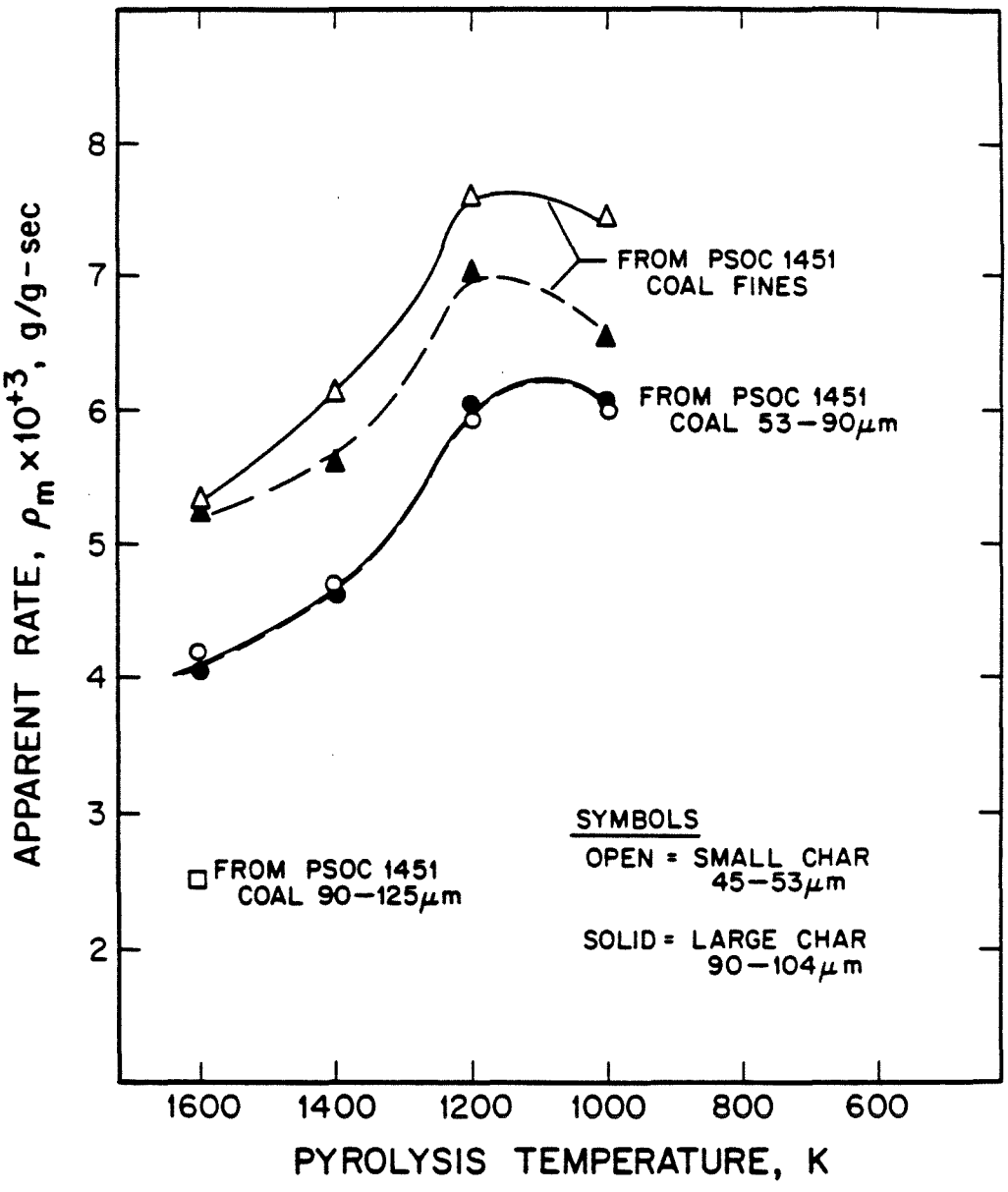

Figure 7: Apparent reaction rates at 50 % conversion for 45-53 and 104-125 μm sizes of all chars versus pyrolysis temperature.

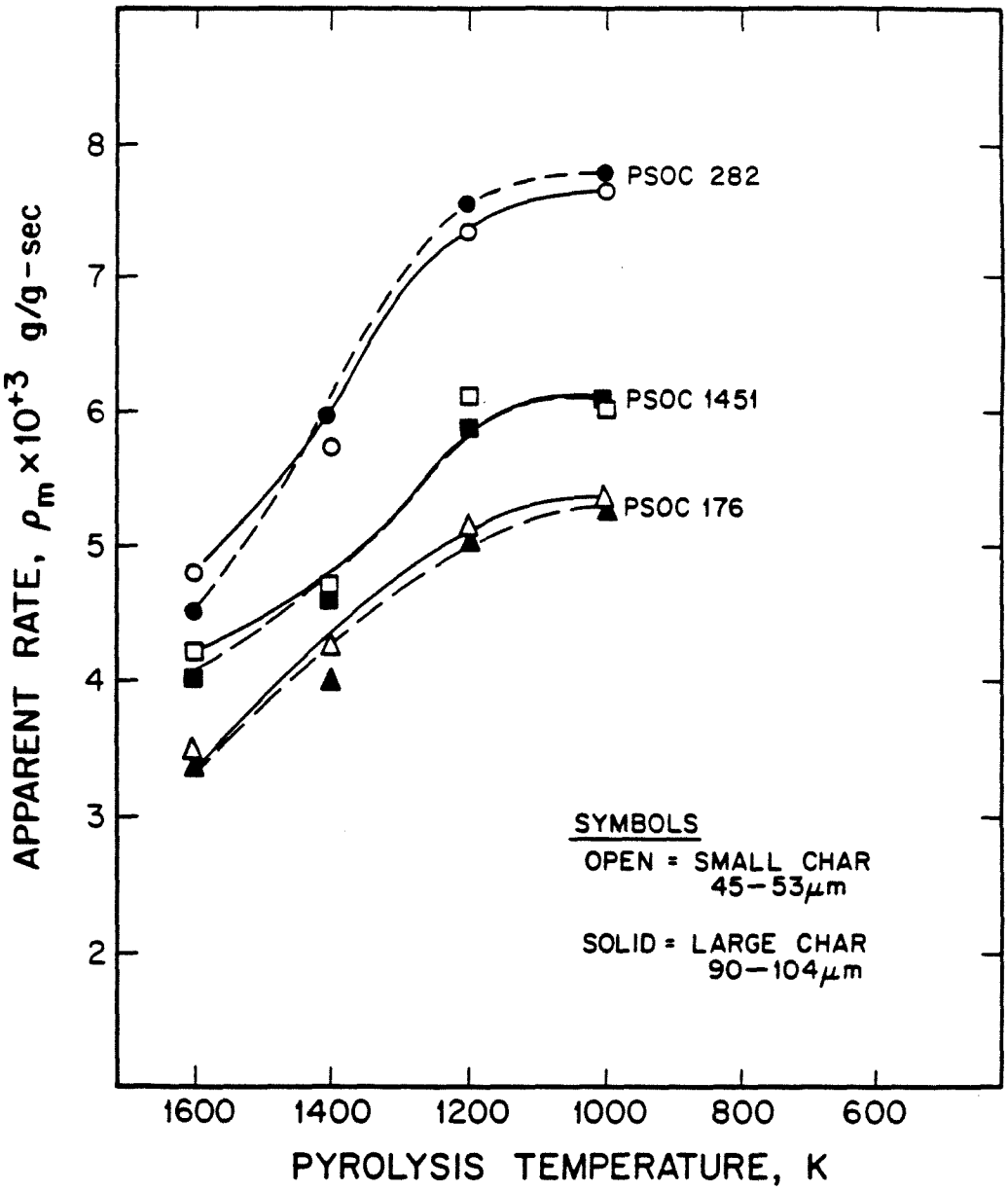

Figure 8: Apparent reaction rates at 50 % conversion for 45-53 and 104-125 μm char sizes derived from PSOC-1451 coal sizes (a) less than 45 μm and (b) 53-90 μm versus pyrolysis temperature.

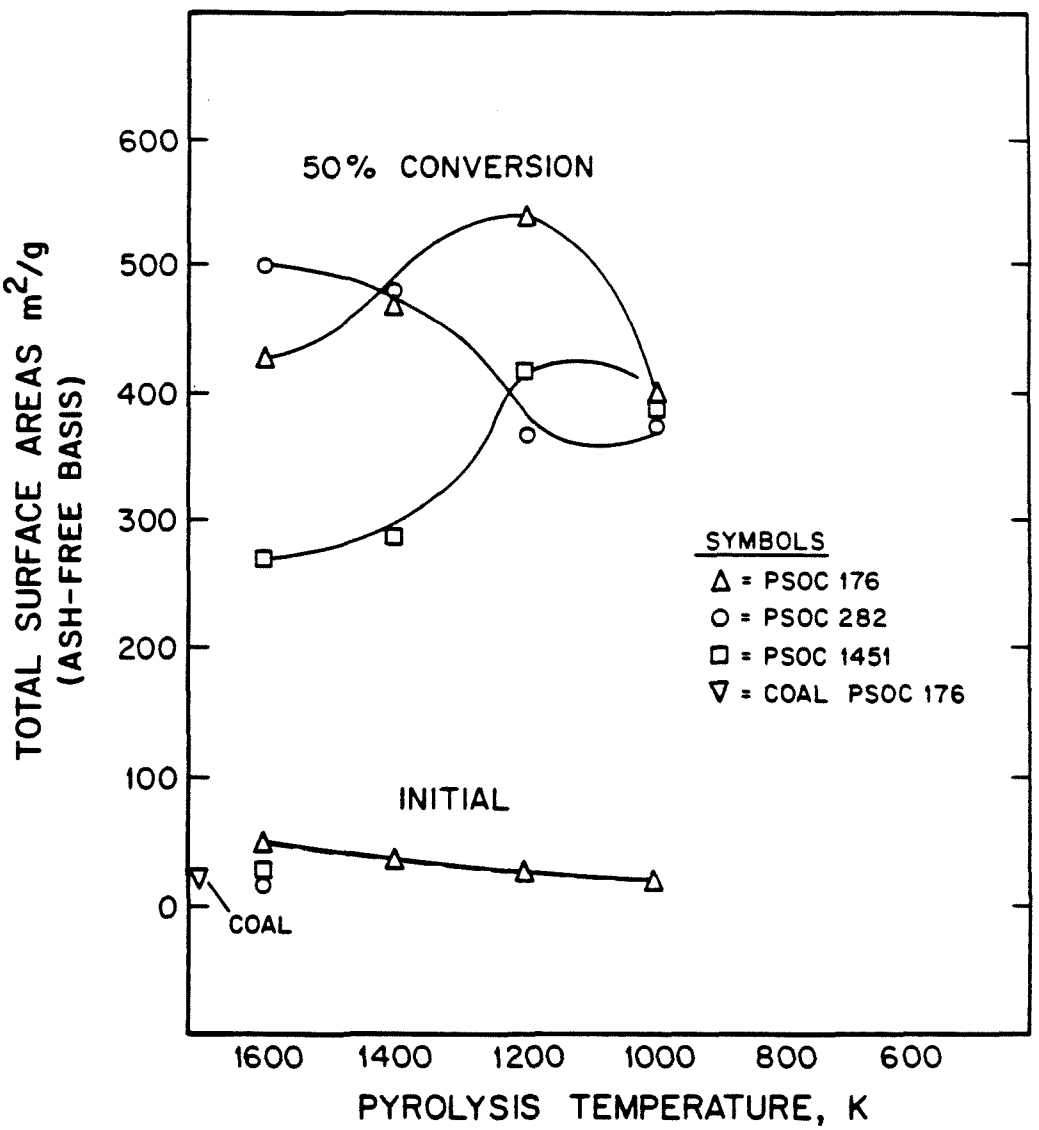

Figure 9: Intrinsic reaction rates at 50 % conversion for 45-53 and 104-125 μm sizes of all chars versus pyrolysis temperature.